For Reference

NOT TO BE TAKEN FROM THIS ROOM

Ex libris
Universitatis
Albertaensis

QUAECUMQUE VERA

The University of Alberta
Printing Department
Edmonton, Alberta

THE UNIVERSITY OF ALBERTA

TURBULENT IMPINGING JETS

by

©

SPYRIDON BELTAOS

A THESIS

SUBMITTED TO THE FACULTY OF GRADUATE STUDIES AND RESEARCH
IN PARTIAL FULFILMENT OF THE REQUIREMENTS FOR THE DEGREE
OF DOCTOR OF PHILOSOPHY

DEPARTMENT OF CIVIL ENGINEERING

EDMONTON, ALBERTA

FALL, 1974

Digitized by the Internet Archive
in 2024 with funding from
University of Alberta Library

https://archive.org/details/Beltaos1974

To the Memory of my Mother

ABSTRACT

The impingement of turbulent jets is studied both experimentally and analytically. This work involves mainly impingement upon solid, smooth boundaries, however, a simple case of a jet impinging against a uniform stream is also considered. Three distinct flow regions exist in this phenomenon; the free jet region, the impingement region and the wall jet region. Emphasis has been placed in studying the impingement region which is the most interesting for practical applications and the least studied owing to its complexity. The relatively simple case of axisymmetric impingement is studied first. Detailed explorations of the time-average velocity and pressure fields are performed and semi-empirical methods are proposed to predict the velocity and pressure fields and the wall shear stress in the impingement region. Experimental data of previous works in the wall jet region are re-analyzed and shown to comply with a simple similarity analysis. The results are summarized and average values of pertinent coefficients are obtained. The more complex cases of plane and circular jets impinging obliquely are studied next and semi-empirical methods are proposed to predict the wall pressure in the impingement region. The wall shear stress in this region is predicted by extending the previous method to account for the effects of obliqueness. Relatively simple methods to predict the velocity field and wall shear stress in the wall jet region are developed and are shown to agree with previous and present experimental results. These studies refer to cases where

ABSTRACT

The impingement of turbulent jets is studied both experimentally and analytically. This work involves mainly impingement upon solid, smooth boundaries, however, a single case of a jet impinging against a uniform stream is also considered. Three distinct flow regions exist in this phenomenon: the free jet region, the impingement region and the wall jet region. Emphasis has been placed in studying the impingement region which is the most interesting for practical applications and the least studied owing to its complexity. The relatively simple case of axisymmetric impingement is studied first. Detailed explorations of the time-average velocity and pressure fields are performed and semi-empirical methods are proposed to predict the velocity and pressure fields and the wall shear stress in the impingement region. Experimental data of previous works in the wall jet region are re-analyzed and shown to comply with a simple similarity analysis. The results are summarized and average values of pertinent coefficients are obtained. The more complex cases of plane and circular jets impinging obliquely are studied next and semi-empirical methods are proposed to predict the wall pressure in the impingement region. The wall shear stress in this region is predicted by extending the previous method to account for the effects of obliqueness. Relatively simple methods to predict the velocity field and wall shear stress in the wall jet region are developed and are shown to agree with previous and present experimental results. These methods refer to cases where the height of impingement is sufficiently large to allow the assumption that the jet is a point source of momentum. In order to understand the physics of the problem when the impingement height is "small", axisymmetric impingement at heights comparable to the jet diameter is also studied in detail. It is shown that significant differences exist in the impingement region whereas the wall jet region remains unaffected of "small" or "large" height considerations. Further, the development of a circular jet in a uniform, opposing stream is studied as an impingement problem. A semi-empirical method is developed to predict the flow field, based on turbulent jet theory and potential flow considerations. Finally, as an application of knowledge gained thus far, a criterion for scour from jets is developed and is shown to agree with previous experimental results.

ACKNOWLEDGEMENTS

The author is indebted to Professor N. Rajaratnam for his advice, constructive criticism and encouragement throughout the course of this work.

Thanks are extended to Mr. S. Lovell, who performed a good portion of the measurements and to Messrs. D. McGowan and R. Gitzel who provided valuable assistance in preparing the experimental set-ups.

Drs. R. Kellerhals and R. Gerard who reviewed parts of the manuscript and made helpful suggestions are gratefully acknowledged.

Gratitude is also expressed to the National Research Council of Canada for supporting this work through a grant to Professor Rajaratnam (A-3365) and through scholarships awarded to the author.

Further, the author is grateful to his wife, Mrs. L. Beltaos, for preparing computer programs and translating some of the foreign literature.

TABLE OF CONTENTS

CHAPTER PAGE

I INTRODUCTION 1

II REVIEW OF LITERATURE 7

2.1 Stagnation Flow Problem 7

2.2 The Classical Wall Jet 10

2.3 Turbulent Impinging Jets 14

2.4 Summary 29

III EXPERIMENTAL EQUIPMENT AND TECHNIQUES 32

3.1 Experimental Set-Up 32

3.2 Experimental Techniques 36

3.2.1 Nozzle Velocity 36

3.2.2 Velocity and Pressure Measurements in the Impingement Region - Pitot Cylinder . 40

3.2.3 Measurement of Wall Shear Stress 52

IV AXISYMMETRIC IMPINGEMENT 55

4.1 Introduction 55

4.2 Experiments and Experimental Results 55

4.3 Analysis of Results 67

4.3.1 Impingement Region 67

4.3.2 Wall Jet Region 78

4.4 Summary 87

V AXISYMMETRIC IMPINGEMENT OF DEVELOPING JETS 88

5.1 Introduction 88

5.2 Experiments 90

5.3 Experimental Results and Analysis 94

5.3.1 Free Jet Region 94

5.3.2 Impingement Region 99

5.3.3 Wall Jet Region 130

5.4 Summary 135

TABLE OF CONTENTS (Cont'd)

CHAPTER PAGE

VI OBLIQUE IMPINGEMENT OF PLANE TURBULENT JETS 136
- 6.1 Introduction 136
- 6.2 Experiments 136
- 6.3 Results and Analysis 137
  - 6.3.1 Free Jet Region 137
  - 6.3.2 Impingement Region 141
    - 6.3.2.1 Wall Pressure 141
    - 6.3.2.2 Wall Shear Stress 155
    - 6.3.2.3 Maximum Velocity, u_m 163
  - 6.3.3 Wall Jet Region 167
- 6.4 Summary 182

VII OBLIQUE IMPINGEMENT OF CIRCULAR TURBULENT JETS 184
- 7.1 Introduction 184
- 7.2 Experiments 187
- 7.3 Analysis and Results 188
  - 7.3.1 Impingement Region 188
    - 7.3.1.1 Wall Pressure 190
    - 7.3.1.2 Wall Shear Stress 212
  - 7.3.2 Wall Jet Region 223
- 7.4 Summary 251

VIII CIRCULAR TURBULENT JET IN AN OPPOSING, INFINITE STREAM 253
- 8.1 Introduction 253
- 8.2 Experiments 256
- 8.3 Analysis and Results 257
  - 8.3.1 Velocity Similarity Function 258
  - 8.3.2 Velocity Scale 262
  - 8.3.3 Penetration Length 265
  - 8.3.4 Length Scale 266

TABLE OF CONTENTS (Cont'd)

CHAPTER PAGE

8.3.5 Geometry 269

8.3.6 The Question of Infinitely Wide Streams 272

8.4 Summary 274

IX SUMMARY 276

* * * * * * * * * * * * * *

REFERENCES 279

APPENDIX A - A CRITERION FOR SCOUR 285

A.1 Introduction 285

A.2 Theoretical Considerations 285

A.3 Comparison with Experiments 292

A.4 Summary 297

APPENDIX B - ERROR ANALYSIS OF PITOT CYLINDER TECHNIQUE . 298

APPENDIX C - ANNULAR SHEAR LAYER 303

APPENDIX D - DERIVATIONS 311

LIST OF TABLES

TABLE PAGE

2.1 RANGE OF INITIAL PARAMETER 31

4.1 DETAILS OF THE EXPERIMENTS (Ch. IV) 56

4.2 VELOCITY SCALE - SUMMARY 83

5.1 RANGE OF EXPERIMENTS 92

5.2 VALUES OF C_{fm} 127

6.1 RANGE OF EXPERIMENTS 137

6.2 EXTENT OF IMPINGEMENT REGION 155

6.3 VALUES OF η_c 163

7.1 RANGE OF EXPERIMENTS 187

7.2 VALUE OF $\overline{b}_{90}$ 210

7.3 MAXIMUM SHEAR STRESS ($x > 0$) 221

7.4 SKIN FRICTION FACTOR 230

7.5 EXPERIMENTAL VALUES OF $h(\phi, \theta)$ 238

B.1 ERROR ANALYSIS $dp_o/dx = 0$ 301

B.2 ERROR ANALYSIS $dp_o/dx \neq 0$ 301

LIST OF FIGURES

FIGURE PAGE

1.1 SKETCH OF FLOW REGIONS 2

2.1 PLANE STAGNATION FLOW 8

2.2 CLASSICAL WALL JET 8

2.3 TURBULENT IMPINGING JET 15

3.1 SET-UP FOR PLANE JETS 33

3.2 CHAMBER SUSPENSION - PLANE JET 34

3.3 PLANE JET SET-UP 35

3.4 CIRCULAR JET SET-UP 37

3.5 SET-UP FOR COUNTER JET EXPERIMENTS 38

3.6 APPLICATION OF BERNOULLI THEOREM 39

3.7 THE PITOT CYLINDER 39

3.8 CALIBRATION FACTORS K_1, K_2, K_3 (1/8 in. Probe) . . 42

3.9 CALIBRATION FACTOR K (1/8 in. Probe) 43

3.10 CALIBRATION FACTORS K_1-K_2 AND K_3-K_2 (i/8 in. Probe) 44

3.11 CALIBRATION FACTORS K_1, K_2, K_3 (0.04 in. Probe) . 46

3.12 CALIBRATION FACTORS K_1, K_2, K_3 (Wind Tunnel Probe) 47

3.13 STATIC TAP SPACING - PLANE JETS 49

3.14 STATIC TAP SPACING - CIRCULAR JETS 50

3.15 PLATE AND TAPS - OBLIQUE IMPINGEMENT 51

3.16 VALVE AND MANOMETER 51

3.17 PATEL EQUATIONS FOR SMOOTH WALLS 53

LIST OF FIGURES (Cont'd)

FIGURE PAGE

4.1 DEFINITION SKETCH 57

4.2 VELOCITY PROFILES IN REGIONS I AND II 58

4.3 DIMENSIONLESS VELOCITY PROFILES IN REGIONS I AND II 58

4.4 VELOCITY SCALE - REGIONS I AND II 60

4.5 LENGTH SCALE FOR VELOCITY PROFILES 61

4.6 VARIATION OF uv WITH x AND r 62

4.7 TYPICAL PRESSURE PROFILES - REGION II 64

4.8 DIMENSIONLESS PRESSURE PROFILES 65

4.9 WALL SHEAR STRESS VARIATIONS 66

4.10 DIMENSIONLESS WALL SHEAR STRESS 66

4.11 VARIATION OF u_c/u_{cf} 68

4.12 VARIATION OF p_c/p_s AND p_T/p_s 68

4.13 LENGTH SCALE FOR PRESSURE PROFILES 73

4.14 DIMENSIONLESS WALL PRESSURE 73

4.15 VARIATION OF v_m 77

4.16 BOUNDARY LAYER THICKNESS - REGION II 79

4.17 LENGTH SCALE, WALL JET REGION 81

4.18 VELOCITY SCALE, WALL JET REGION 82

4.19 VELOCITY SCALE, WALL JET REGION 84

4.20 WALL SHEAR STRESS, WALL JET REGION 86

5.1 DEFINITION SKETCH 89

LIST OF FIGURES (Cont'd)

FIGURE PAGE

5.2 RELATIVE STAGNATION PRESSURE 93

5.3 VELOCITY FIELD, FREE JET REGION 95

5.4 SIMILARITY IN SHEAR LAYER, FREE JET REGION 96

5.5 RADIUS OF CORE 97

5.6 LENGTH SCALE FOR SHEAR LAYER 98

5.7 VELOCITY FIELD, IMPINGEMENT REGION 101

5.8 SIMILARITY IN SHEAR LAYER, IMPINGEMENT REGION . . . 102

5.9 WALL PRESSURE 103

5.10 DIMENSIONLESS WALL PRESSURE 105

5.11 AXIAL PRESSURE 107

5.12 THE PRESSURE FIELD 108

5.13 AXIAL VELOCITY 110

5.14 VARIATION OF uv 111

5.15 VELOCITY SCALE u_m 113

5.16 VARIATION OF u IN THE CORE 115

5.17 VARIATION OF C WITH H/d 118

5.18 VARIATION OF v_1 121

5.19 SIMILARITY OF v IN THE CORE 123

5.20 LENGTH SCALE, IMPINGEMENT REGION 125

5.21 VARIATION OF v_m 125

5.22 WALL SHEAR STRESS, IMPINGEMENT REGION 128

5.23 LENGTH SCALE, WALL JET REGION 132

LIST OF FIGURES (Cont'd)

FIGURE PAGE

5.24 FRICTION VELOCITY, WALL JET REGION 134

6.1 DEFINITION SKETCH 138

6.2 AXIAL VELOCITY 140

6.3 WALL PRESSURE 142, 143

6.4 WALL PRESSURE SIMILARITY 145, 146

6.5 STAGNATION PRESSURE 148

6.6 MINIMUM PRESSURE 148

6.7 LENGTH SCALE FOR WALL PRESSURE 150

6.8 ECCENTRICITY OF STAGNATION POINT 151

6.9 ECCENTRICITY FOR POTENTIAL JET 151

6.10 WALL SHEAR STRESS 156

6.11 WALL SHEAR SIMILARITY, IMPINGEMENT REGION $\phi < 130°$. 160

6.12 WALL SHEAR - $\phi > 130°$ 161

6.13 MAXIMUM WALL SHEAR STRESS 162

6.14 TYPICAL VARIATION OF u_m , IMPINGEMENT REGION . . . 164

6.15 SIMILARITY OF u_m , $\phi < 130°$ 166

6.15a SIMILARITY OF u_m . $\phi > 130°$ 168

6.16 EVALUATION OF u_{max} 169

6.17 CONSTANCY OF FRICTION FACTOR 171

6.18 LOCAL SKIN FRICTION FACTOR, WALL JET REGION 173

6.19 LENGTH SCALE, WALL JET REGION 175

LIST OF FIGURES (Cont'd)

FIGURE PAGE

6.20 VELOCITY SCALE, WALL JET REGION 178

6.21 THE FUNCTION $C_u(\phi)$ 179

7.1 DEFINITION SKETCH 186

7.2 WALL PRESSURE CONTOURS 191, 192

7.3 WALL PRESSURE SIMILARITY . . . . 194 to 196

7.4 LENGTH SCALE b 198

7.5 SIMILARITY OF SYMMETRY PLANE WALL PRESSURE . . . . . 199 to 201

7.6 ECCENTRICITY OF STAGNATION POINT 204

7.7 STAGNATION PRESSURE 204

7.8 LENGTH SCALES b_1, b_2, b_3 205

7.9 VARIATION OF α 206

7.10 SKEWNESS INDEX b_2/b_1 206

7.11 SIMILARITY IN TERMS OF CONTOUR AREAS 209

7.12 WALL SHEAR STRESS MEASUREMENTS 213

7.13 AUXILIARY FUNCTIONS σ_m, q_m 217

7.14 LOCUS OF MAXIMUM WALL SHEAR, SYMMETRY PLANE 217

7.15 SIMILARITY OF WALL SHEAR, SYMMETRY PLANE . . . . . . 218 to 220

7.16 EVALUATION OF $C_*^{(2)}$ 222

7.17 WALL JET SIMILARITY 225

7.18 WALL JET SIMILARITY - SUMMARY 226

LIST OF FIGURES (Cont'd)

FIGURE PAGE

7.19 CONSTANCY OF u_*/u_m 231

7.20 SKIN FRICTION FACTOR - WALL JET 232

7.21 LENGTH SCALE IN WALL JET 234

7.22 VELOCITY SCALE IN WALL JET 236, 237

7.23 CONTROL VOLUME 239

7.24 VERIFICATION OF EQUATION 7.63 243

7.25 THE FUNCTIONS h_1 AND h_2 244

7.26 ASSUMED GEOMETRY OF ISOTACHS 245

7.27 COMPARISON OF THEORY WITH EXPERIMENT 249

7.28 THEORETICAL EVALUATION OF THE FUNCTION $h(\phi, \theta)$ . . . 250

8.1 DEFINITION SKETCH 254

8.2 SIMILARITY OF VELOCITY PROFILES 259

8.3 THREE DIMENSIONAL POINT SOURCE IN A UNIFORM STREAM 260

8.4 VELOCITY SCALE VARIATION 264

8.5 LENGTH SCALE VARIATION 267

8.6 LINEARITY OF y_o/x_p 267

8.7 LENGTH SCALE - GENERALIZATION 269

8.8 FLOW GEOMETRY 270

8.9 VISUALIZATION 271

8.10 PENETRATION LENGTH 273

LIST OF FIGURES (Cont'd)

FIGURE PAGE

A.1 A SCOUR CRITERION 294

C.1 DEFINITION SKETCH 303

C.2 RELATION BETWEEN $\overline{r}_1$ AND $\overline{b}$ 306

C.3 THE FUNCTION $\phi(\overline{x})$ 309

C.4 ENTRAINMENT VELOCITY 310

D.1 VORTEX NEAR A WALL 322

LIST OF SYMBOLS

SYMBOL	DESCRIPTION
a	constant, contour area, coefficient, ellipse semi-axis
A	area, integration constant
b	length scale, ellipse semi-axis
c	constant, coefficient
C	constant, ceofficient
C_f	local skin friction coefficient
C_u	constant related to velocities
d	diameter or width of nozzle
d_o	outside diameter of Preston Tube
d_p	width of potential jet
d_s	maximum diameter of stagnation streamsurface
D	dimension of uniform stream
e	Napierian Base, error
f	function
F	function, constant
g	function
h	function
H	impingement height
k	constant
K	constant, calibration factor, kinematic momentum
ℓ	distance from projection of vortex on wall
m	constant, strength of point source

LIST OF SYMBOLS (Cont'd)

SYMBOL	DESCRIPTION
M	momentum
M_o	initial momentum of jet
n	constant
p	static pressure, static pressure above ambient
P	integrated pressure
q_m	auxiliary function
Q_o	initial discharge of jet
r	space co-ordinate (radial)
R	Reynolds number
s	eccentricity of stagnation point
t	curvilinear co-ordinate
u	longitudinal velocity
u_1	free stream velocity
u_c	centerline value of u
u_m	maximum value of u
u_s	confined stream velocity
u_*	friction velocity
U	free-stream velocity in x-direction
U_o	velocity at nozzle
U_1	velocity inside the chamber
v	velocity in y-direction
v_r	velocity in radial direction

LIST OF SYMBOLS (Cont'd)

SYMBOL	DESCRIPTION
v_z	velocity in vertical direction
v_θ	velocity in angular direction
v_m	maximum value of v
V	free-stream velocity in y-direction
w	velocity in z-direction
x	space co-ordinate
x_p	penetration length
y	space co-ordinate
z	space co-ordinate (vertical)
α	constant, coefficient
β	exponent, constant, coefficinet
Γ	vortex strength
δ	boundary layer thickness
δ_2	"half" thickness of wall jet
Δ	difference, dimensionless pressure gradient
ε	eccentricity of ellipse
ζ	dimensionless space co-ordinate
η	dimensionless space co-ordinate
θ	angular co-ordinate
λ	dimensionless space co-ordinate, speed ratio
μ	viscosity of fluid
ν	kinematic viscosity of fluid

LIST OF SYMBOLS (Cont'd)

SYMBOLS	DESCRIPTION
ξ	longitudinal distance, dimensionless space co-ordinate
ρ	density of fluid
σ	total normal stress
σ_m	auxiliary function
τ	shear stress
τ_t	turbulent shear stress
τ_o	wall shear stress
τ_{om}	maximum of τ_o
ϕ	angle of impingement, function, angle
ψ	Stokes' streamfunction

CHAPTER I - INTRODUCTION

The impingement of a turbulent jet on a solid surface is of interest in many engineering problems, such as paint spraying, jet blast drying, shielded arc welding and in connection with the operation of VTOL aircraft. In the field of hydraulic engineering the impingement of jets is of particular interest in the design of hydraulic outlet works and in other problems related to scour from jets. The phenomenon of scour from jets has attracted the attention of hydraulicians (Refs. 1 - 8) in the last 35 years, however, no satisfactory solution has been obtained so far. The reason for this, appears to be a general lack of appreciation for the mechanics of impingement. It was felt, therefore, that the first step in a logical development of this subject ought to be the systematic study of the impingement problem. The present study is mainly an effort toward systematic evaluation and solution of the problem of turbulent jets impinging on smooth, plane, walls. This problem has been attacked in the past (Refs. 9 - 27) by workers of various engineering backgrounds. The great majority of these works deals with plane or circular jets impinging normally, while very little is known about the oblique impingement which is naturally more interesting from the practical point of view. For purposes of introduction, some very general considerations will be outlined in this chapter whereas a comprehensive review of literature will be presented in the next chapter.

Consider a submerged, turbulent jet impinging normally on a smooth wall, as shown in Figure 1.1. The outline of the jet shown by a solid line, is to be interpreted as the locus of points where velocity

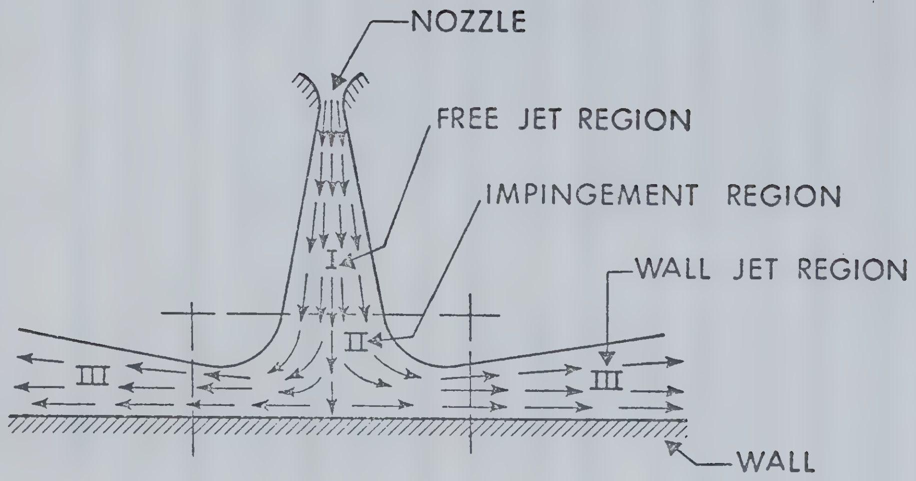
NOZZLE
FREE JET REGION
IMPINGEMENT REGION
WALL JET REGION
I
II
III
III
WALL

FIGURE 1.1 SKETCH OF FLOW REGIONS

becomes negligibly small. At present, it has been established that there exist three distinct flow regions (I, II, III in Figure 1.1). In region I, the flow develops as if the wall did not exist, because wall effects which are transmitted upwards in the form of increased static pressure become negligibly small beyond a certain distance from the wall. This implies that in region I, the flow is identical to the well-known free jet (28),(29) and hence this region is appropriately called the free-jet region. In region II, the effects of the wall are significant. The static pressure assumes values higher than the ambient pressure and intense pressure gradients are set-up in both directions, parallel and normal to the wall. These pressure gradients, in turn, cause the flow to deflect and become eventually parallel to the wall. Region II is, therefore, called the "deflection" or, more frequently, the "impingement" region. After turning, the flow becomes almost parallel to the wall. At the same time, the static pressure drops to ambient values after some distance from the stagnation point and a flow pattern is established which resembles in many respects the classical wall jet. Region III is, therefore, appropriately called the wall-jet region.

A complete study of this problem requires investigation of all three regions. However, the flow characteristics in region I are well known already (28),(29) and all that is needed to know is how far from the outlet this region extends. Region III is a wall-jet type of flow. Considerable theoretical and experimental information is already available for the classical wall jet (Refs. 30 - 35. Reference No. 35 is an extensive bibliography on the subject and contains many references which are not listed here). The objective, therefore, in region III is to

establish the similarities with the classical wall jet and to account for differences that are likely to exist owing to the different geometries that produce the wall jet. Coming to region II, one could see that this is the most complex region of the impinging jet. Here, both components of velocity are of the same order of magnitude and pressure gradients are significant in both directions, hence boundary layer simplifications do not apply. Furthermore, since the direction of the velocity vector and the static pressure at any arbitrary point are not known beforehand, it is obvious that equipment more sophisticated than the ordinary Pitot-tube is necessary. This calls for rather laborious measurements and probably accounts for a general lack of detailed experimental data in this region. At the same time, the impingement region is the most important from the practical point of view, because here the hydrodynamic action on the boundary is most severe, owing to simultaneous existence of large shearing stresses and significant pressure gradients. Hence it is only natural that in the present work emphasis was placed on the study of region II. Region I was studied only in so far as was necessary to verify its free-jet character and to establish its boundary with region II. Intensity of study in region III was dictated mainly by the amount of information already available. It was found that only few experimental data would suffice to complement those already available, hence the main task in region III was to improve upon the analytical solutions proposed earlier, and to extend the theory to more advanced problems, such as oblique impingement.

Given the complexity of the problem, it was considered imperative to proceed in an inductive manner. The simplest case of impingement

is the normal impingement of a plane jet. This was studied by the author as part of his M.Sc. program (25) and the results were published recently (26). The corresponding axisymmetric case, i.e., a circular jet impinging normally, was studied next and the results are presented in Chapter IV. Experimental and analytical results of these works were obtained for impingement heights larger than about ten nozzle diameters (or nozzle widths) which means that the jet was fully developed when approaching the wall (28),(29). It was thought, however, that these results would not apply to smaller heights where the jet is not fully developed, due to the changes in the physics of the problem. In order to explore impingement at small heights, a study of axisymmetric impingement was carried out keeping the impingement height less than 6 nozzle diameters. The results, which verified the expectation of significant differences, are presented in Chapter V. The findings of Chapters IV and V constituded the foundation for additional work on more complex situations. Owing to the relatively minor practical importance of impingement at small heights, the remaining studies were mainly for large impingement heights.

The case of plane jets impinging obliquely was studied next (Chapter VI). Here the number of parameters defining the problem is increased by one, namely the angle of impingement. A further step in complexity is the case of circular jets impinging obliquely. Here, in regions II and III, the flow ceases to be axisymmetric and, therefore, in addition to the angle of impingement, a new parameter must be introduced to account for variations in the direction normal to the plane of symmetry (Chapter VII).

A practical application of the knowledge gained thus far, is given in Appendix A, where a criterion for scour from circular jets impinging normally, is developed. Finally, another problem of impingement is considered (Chapter VIII), namely the development of a circular turbulent jet in a uniform opposing stream. This study is of interest with respect to efficient disposal of effluent discharges. A critical review of literature and some fundamental theoretical considerations are presented in the next chapter, whereas descriptions of experimental set-ups and experimental techniques are given in Chapter III.

CHAPTER II - REVIEW OF LITERATURE

In this chapter, an effort is made to review critically the existing material on turbulent impinging jets. The literature cited herein contains accounts of previous contributions to the author's best knowledge, however, no claim to absolute completeness will be made.

2.1 Stagnation Flow Problem

Consider first a very simple case of impingement, i.e., the case of an infinitely wide, uniform stream, impinging normally on a smooth, plane, wall. This is the well-known stagnation flow problem (36) which affords an exact solution of the Navier-Stokes equations of motion. For simplicity, consider a two-dimensional (plane) flow, the axisymmetric case being analogous to this. With reference to Figure 2.1, the velocity distribution in the frictionless, potential flow outside the boundary layer of thickness δ, is given by (36):

$$U = ax \quad ; \quad V = -ay \tag{2.1}$$

where a is a constant. If p_s is the stagnation pressure and p is the static pressure at an arbitrary point (x, y), then:

$$p_s - p = \frac{1}{2} \rho a^2 (x^2 + y^2) \tag{2.2}$$

For the laminar flow within the boundary layer, it is assumed that:

$$u = x f'(y) \quad ; \quad v = -f(y) \tag{2.3}$$

$$p_s - p = \frac{1}{2} \rho a^2 [x^2 + F(y)] \tag{2.4}$$

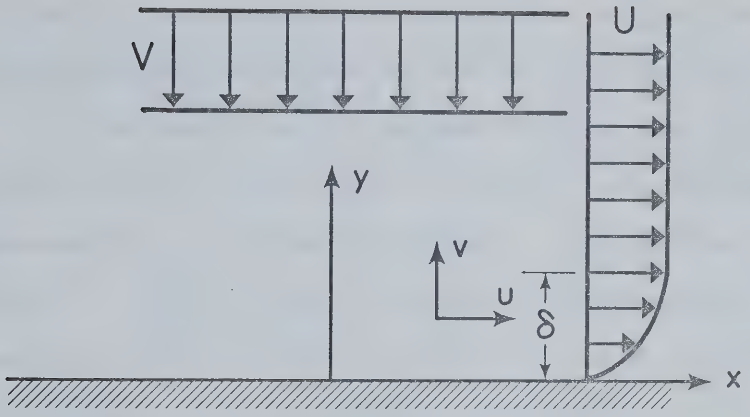

FIGURE 2.1 PLANE STAGNATION FLOW

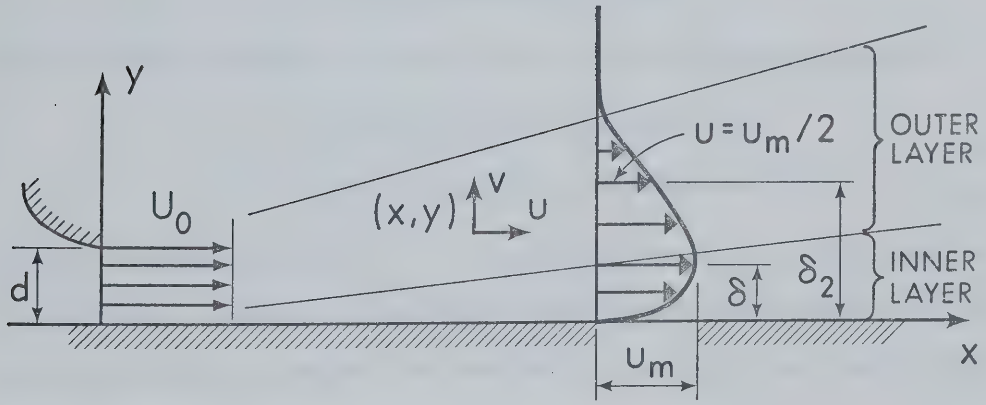
y
U_0
d
(x,y)
v
u
u = u_m/2
OUTER LAYER
INNER LAYER
δ_2
δ
u_m
x

FIGURE 2.2 CLASSICAL WALL JET

In this way, the equation of continuity is satisfied identically and the functions f and F are determined by substitution into the Navier-Stokes equations and subsequent reduction to ordinary differential equations. It is noteworthy that the assumed functional form of the u-component (Equation 2.3) implies that the boundary layer thickness, δ, is independent of x. If the co-ordinate y is normalized by the transformation $\eta = \sqrt{\frac{a}{\nu}}\, y$, then it is shown that the normalized velocity component, u/U, is a function only of η, i.e., the velocity profiles are similar. If δ is defined to be the value of y for which u/U equals 0.99, then δ is given by:

$$\sqrt{\frac{a}{\nu}}\,\delta = \begin{cases} 2.40 \text{ (plane flow)} \\ 1.98 \text{ (axisymmetric flow)} \end{cases} \tag{2.5}$$

The wall shear stress, τ_o, can also be calculated and is given by:

$$\tau_o = \begin{cases} 1.2326\ (\rho\ a\ \sqrt{a\nu})\ x \text{ (plane flow)} \\ 1.312\ (\rho\ a\ \sqrt{a\nu})\ r \text{ (axisymmetric flow)} \end{cases} \tag{2.6}$$

where r is radial distance from the stagnation point. It is seen that τ_o increases linearly with distance from the stagnation point. Naturally the above considerations are meaningful so long as the boundary layer remains laminar. Stagnation flow has been found to occur not only near plane walls, but also near any cylindrical body (36). Considering a turbulent impinging jet, it may be noted that in a small neighborhood of the stagnation point, the approaching stream will have an almost uniform downward velocity (time-averaged). If at the same time the intensity of turbulence is sufficiently reduced, then stagnation flow is likely to occur within this small region.

2.2 The Classical Wall Jet

The problem of the wall jet produced by a two-dimensional or radial nozzle and growing on a smooth wall has received considerable attention (Refs. 30 - 35) and can be considered solved. The now classic work of Glauert (30) appears to be the first theoretical treatment of this problem, including solutions for plane and radial wall jets and for both laminar and turbulent states. In the case of turbulent wall jets, the theory was based on matching separate solutions for the inner and outer layers (see Figure 2.2) using the eddy viscosity model of turbulence. Later experimental investigations have shown that such assumptions are not realistic and, therefore, it was thought instructive to base the following presentation on the work of Schwarz and Cosart (31) which is most appealing for its logical and deductive development.

Consider a plane jet issuing from a two-dimensional nozzle of thickness d, with a uniform initial velocity U_o, growing on a smooth wall as shown in Figure 2.2. In this case the static pressure is constant; the transverse component of velocity, v, is much smaller than the forward component, u, and the transverse extent of the flow is relatively small. Hence the boundary-layer approximation can be applied to the Reynolds' equations of motion, which after simplifications become:

$$u \frac{\partial u}{\partial x} + v \frac{\partial u}{\partial y} = \frac{1}{\rho} \frac{\partial \tau_t}{\partial y} + \nu \frac{\partial^2 u}{\partial y^2} \qquad (2.7)$$

and

$$\frac{\partial u}{\partial x} + \frac{\partial v}{\partial y} = 0 \qquad (2.8)$$

where u, v are the time-average components of velocity, τ_t is the turbulent shear stress and ν, ρ are the kinematic viscosity and density of the fluid respectively. Experiments have confirmed that, much like in the case of a free jet, the flow is self-preserving, i.e.:

$$u/u_m = f(\eta) \quad ; \quad \eta = y/\delta_2 \tag{2.9}$$

where δ_2 is the larger value of y at which $u = u_m/2$. Assuming that the turbulent shear stress obeys a similar relation, if scaled with the maximum local dynamic pressure, then:

$$\tau_t = \rho u_m^2 \, g(\eta) \qquad (2.10)*$$

Using Equations 2.9 and 2.10 and 2.8, Equation 2.7 can be reduced to:

$$\frac{\delta_2}{u_m}\frac{du_m}{dx}\left[f^2 - \frac{df}{d\eta}\int_0^\eta f d\eta\right] - \frac{d\delta_2}{dx}\left[\frac{df}{d\eta}\int_0^\eta f d\eta\right] =$$

$$= \frac{dg}{d\eta} + \frac{\nu}{\delta_2 u_m}\frac{d^2 f}{d\eta^2} \tag{2.11}$$

In order that Equation 2.11 be satisfied for all η, the coefficients of functions of η must be independent of x. Therefore:

$$\frac{d\delta_2}{dx} = \text{const} = C_2 \tag{2.12}$$

---

* Strictly speaking, similarity of shear stress can only be assumed in the form $\tau_t = k(x)g(\eta)$, where $k(x)$ is a function to be determined. It is, however, possible to show [see for example Poreh, Tsuei and Cermak (17)] that $k(x)$ can be taken equal to the wall shear stress, τ_o. Further, by assuming that the defect law holds in the inner layer (Figure 2.2) and comparing to Equation 2.9, one can show that $\tau_o/\rho u_m^2$ is independent of x, i.e., $k(x)$ can be replaced by ρu_m^2.

$$\frac{\delta_2}{u_m}\frac{du_m}{dx} = \text{const} = C_m \tag{2.13}$$

$$\frac{\delta_2 u_m}{\nu} = \text{const} = C_\nu \tag{2.14}$$

A further relation is obtained by integrating Equation 2.7 from $y = o$ to ∞, which yields:

$$u_*^2 = - F \frac{d}{dx} (\delta_2 u_m^2) \tag{2.15}$$

where $F = \int_0^\infty f^2 d\eta = \text{const}$ and u_* is the shear velocity $\sqrt{\tau_o/\rho}$.

Relations 2.12 and 2.13 imply that:

$$\delta_2 = C_2 \bar{x} \qquad \text{and} \qquad u_m = C_u \bar{x}^\beta \tag{2.16}$$

where C_u and β are constants and $\bar{x}$ is a corrected value of x, to account for virtual origin effects. Using the latter and letting C_f to be the local skin friction factor $\tau_o/\frac{\rho u_m^2}{2}$, Equation 2.15 becomes:

$$\beta = - \frac{1}{2} (1 + \frac{C_f}{2FC_2}) \tag{2.17}$$

which also shows that $\tau_o/\rho u_m^2$ is independent of x. Strictly speaking, the exponent β is always less than $-\frac{1}{2}$. However, the term $\frac{C_f}{2FC_2}$ is generally a small quantity, so that as a first approximation:

$$\beta \simeq - \frac{1}{2} \tag{2.18}$$

It is obvious now that with this value of β, relation 2.14 cannot be satisfied simultaneously with 2.12 and 2.13. Yet for values of η greater than about 0.005, the viscous term in Equation 2.7 can be neglected and hence the condition of Equation 2.14 will vanish. For $\eta \lesssim 0.005$,

viscous effects will be significant with a resulting loss of self-preservation. The above quoted limiting value of η was proposed by Schwarz and Cosart (31) on the basis of data in the inner, or boundary, layer. Since $\delta/\delta_2 \simeq 0.150$, it may be stated that self-preservation is lost only in a layer of thickness equal to about 3% of the boundary layer thickness. It is noteworthy that calculations and measurements of the turbulent shear stress (31),(17) have shown that it does not vanish at the locus of maximum velocity ($\eta = \delta/\delta_2$), a fact that precludes use of any eddy diffusivity or mixing length model. This is believed to be due to the asymmetric character of the profile.

For the case of a radial wall jet, analogous considerations are valid, however, here u_m will vary approximately as r^{-1}. The local skin friction factor, C_f, can easily be shown to depend upon the nozzle Reynolds number, $R_o \equiv U_o d/\nu$, by means of dimensional considerations. However, when more complex geometrical configurations are encountered, such as jets impinging normally or at an angle, dimensional analysis will not be very fruitful due to the increased number of parameters. Insight as to dependence of C_f upon initial parameters of the problem can be gained from the following reasoning.

It is assumed that the velocity u obeys a defect-type law in the boundary layer, i.e.:

$$\frac{u - u_m}{u_*} = f_1\left(\frac{y}{\delta}\right) \quad ; \quad \frac{y}{\delta} \leq 1$$

This law is normally valid for turbulent boundary layers on smooth and

rough walls alike. Schwarz and Cosart (31) have indirectly verified its validity in the inner layer of the wall jet on smooth walls, whereas Rajaratnam (34) has found it to hold in the case of rough walls. Applying Equation 2.9 at $y = \delta$, it can be shown that $\delta = \text{const.}\ \delta_2$, therefore, the above equation can be re-written as:

$$\frac{u - u_m}{u_*} = \overline{f}_1(\eta) \quad ; \quad \eta \leq \frac{\delta}{\delta_2}$$

Solving this for u/u_m and comparing to Equation 2.9, it is easy to show that:

$$\frac{u_*}{u_m} = \frac{f(\eta) - 1}{\overline{f}_1(\eta)} = \text{const.}$$

which implies that the friction factor, $C_f = 2\left(\frac{u_*}{u_m}\right)^2$, depends only upon the shape of the functions f and $\overline{f}_1$. These functions are not likely to change with the geometry producing the wall jet, but they can change slightly with R_o the nozzle Reynolds number. Hence it is postulated that C_f depends only upon R_o, being independent of the geometry which produces the wall jet.

2.3 Turbulent Impinging Jets

Consider a turbulent jet, plane or circular, impinging on a smooth wall, as shown in Figure 2.3, where for simplicity the impingement is assumed to be normal. In this figure, d is the width (or diameter) of the nozzle, U_o is the uniform velocity at the nozzle, and H is the impingement height. For oblique impingement, H is defined to be the distance between nozzle and wall, measured along the centerline of the jet. The co-ordinate system x, y (or r) is used for regions I and II, whereas the system x_1 (or r), z is used for region III. The difference between the static pressure at any arbitrary point

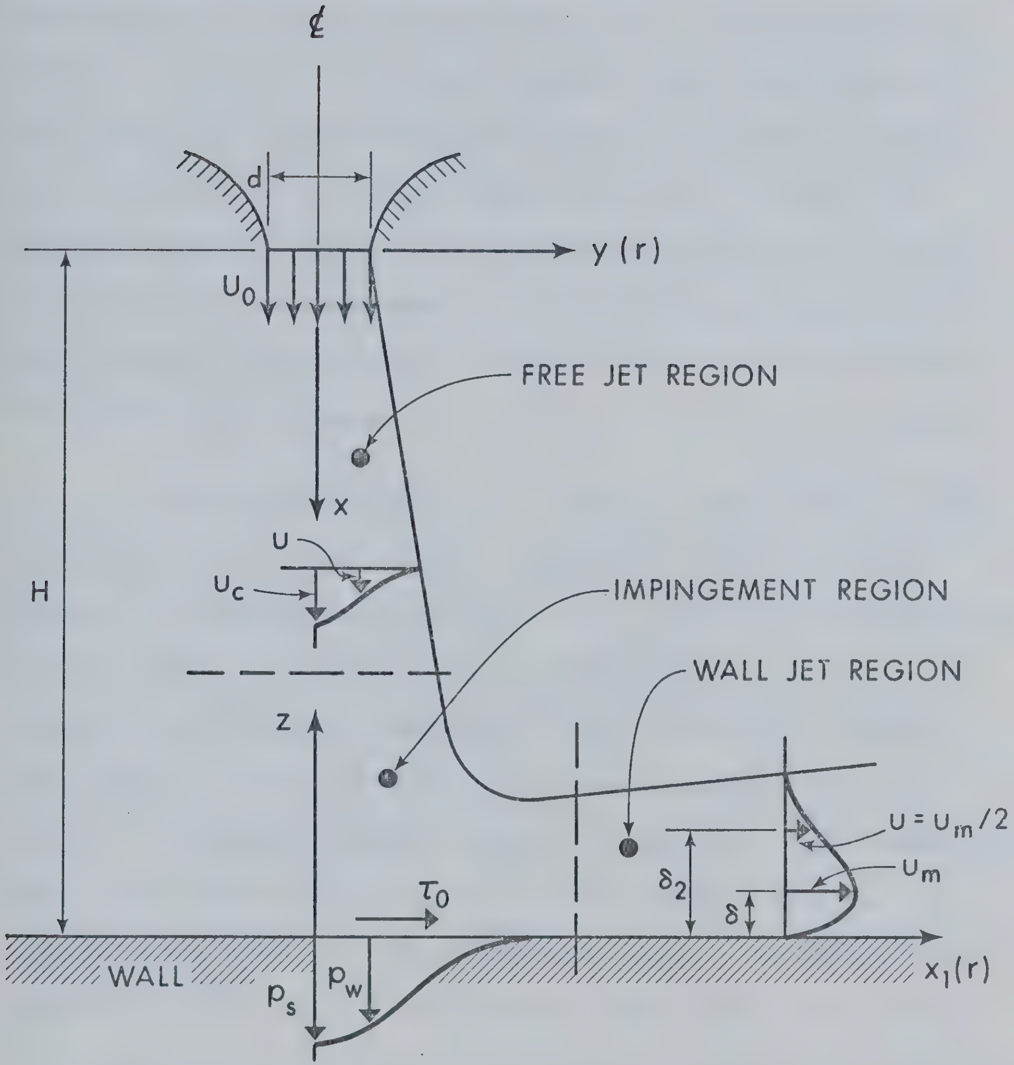
℄
d
y (r)
U_0
FREE JET REGION
x
U
U_c
H
IMPINGEMENT REGION
WALL JET REGION
z
$U = U_m/2$
U_m
δ_2
δ
τ_0
WALL
p_s
p_w
$x_1(r)$

FIGURE 2.3 TURBULENT IMPINGING JET

and the ambient pressure is denoted simply by p, and will be referred to as "pressure". The wall pressure is p_w, p_s is the stagnation pressure and τ_o is the wall shear stress. A short paper by Murray et al, Rouse (9) in 1956 contains the results of a study to determine the flow pattern and some gross characteristics of a circular jet impinging normally. (Values of the parameters defining the problem, such as the angle of impingement ϕ, the dimensionless height H/d and the nozzle Reynolds number $R_o \equiv U_o d/\nu$, are listed, for this, and for the following references in Table 2.1, at the end of this chapter.)

The impingement height H was made so large compared to the jet diameter that the jet could be considered as a point source of momentum. A fundamental contribution of this work (9) is the proposition that when H/d is very large, the two parameters U_o and d do not influence flow properties separately. Rather, they can be combined into a single parameter, known as the kinematic momentum and equal to $\pi d^2 U_o^2/4$ (a reasoning borrowed from free-jet theory). This immediately leads to the realization that there must be a limiting value of H/d, below which the physics of the problem will change. Two questions are, therefore, raised: (i) how does the flow behave when H/d is "small" (i.e., smaller than the limiting value), and (ii) what is the limiting value of H/d. Very generally, it may be stated that the answer to (ii) will be related to the length of the potential core of the jet, whereas the answer to (i) will be related to the distinct physics of an impinging jet and an impinging shear layer for "large" and "small" values of H/d respectively. (In the remaining part of this thesis, the term "impinging jet" without further qualification will denote

large impingement heights.)

It was reported in this paper (9) that the impingement region begins at a distance x_o from the nozzle equal to about 0.8 H, and the well-known irrotational flow solution for this region was presented. Measurements of wall pressure yielded the surprising result that the integral of the wall pressure was about 30% more than the value of the initial momentum of the jet. This was attributed to the occurrence of negative pressures on the wall.

In 1959, Bradshaw and Love (10) presented the results of an experimental study for a circular jet impinging normally. These include data on velocity, static pressure and shear stress in the impingement region. For example, it was shown that the wall shear increases from zero at the stagnation point to a maximum value occurring within the impingement region, decreasing rapidly afterwards. Similarity of radial velocity profiles in the wall-jet region was verified. The length scale δ_2 increased linearly with r whereas the velocity u_m (Figure 2.3) varied approximately in inverse proportion to r. Self preservation in the wall jet begun at $r/H \approx 0.45$.

In the same year, Poreh and Cermak (11) presented the results of an experimental and analytical study on the same problem. The well-known flow development in the free-jet region was verified. Some data are presented in the wall-jet region, however, the choice of velocity scale was made in a manner that would force the profile to assume the shape corresponding to the free jet. Hence, it was necessary to estimate the velocity scale by extrapolation, a procedure that is inaccurate

and similarity of the profiles was not established conclusively. In the impingement region, the wall pressure and radial velocity were measured and the results were presented in a generalized form by means of dimensional analysis which is essentially identical to that of (9). For example, $p_w H^2/M_o$ (M_o = initial momentum of jet = $\rho \pi d^2 U_o^2/4$) is plotted against r/H and a single curve results, showing that $p_w H^2/M_o = f_1(\frac{r}{H})$. The irrotational flow solution was compared against data on wall pressure and was found to be valid within a radial distance of $r/H \lesssim 0.05$ from the stagnation point.

A technical report by Schauer and Eustis (14) in 1963 contains the results of an experimental and analytical study of plane turbulent impinging jets. This includes measurements of wall pressure and one measurement of wall shear in the impingement region. Some data were reported for angles of impingement other than 90° (oblique impingement). The analysis was based on an integral approach which led to rather complex equations that can be solved only implicitly. Furthermore, a large number of rather strong assumptions were introduced, a fact that probably accounts for a large portion of the analysis failing to describe the experimental results. It is worthwhile to examine these assumptions. For the impingement region it was assumed that:

(i) The region extends from the stagnation point equally along the wall and along the centerline of the jet. There is no obvious reason why this should be so and none is given. A weak justification can be furnished only in the case of normal impingement if one refers to the corresponding flow of a potential jet, which again is related to the potential flow of two equal jets imping-

ing against each other. In this case the central streamline between the jets, after impingement, is straight and can be replaced by a wall. Because of the reversibility of potential flows, the pressure distribution on the centerline of the original jets is identical with that along the wall. If the impingement region is defined so that the pressure is greater than, say, 1% of the stagnation value, then the impingement region will extend equally in both directions.

(ii) The stagnation pressure is assumed equal to the centerline dynamic pressure at the boundary between regions I and II. For normal impingement, where the centerline is also a streamline, all the way to the stagnation point, this assumption implies inviscid flow at least near the centerline. For oblique impingement, where the stagnating streamline does not coincide with the centerline, the flow needs to be, in addition, irrotational. These constitute strong simplifications and they do not correspond to reality. For example, for normal impingement it was found (26) that the dynamic pressure at the boundary of regions I and II is about 30% larger than the stagnation pressure.

(iii) A similarity function was used to correlate wall pressures, which is symmetric, about the stagnation point. The data show, however, that for $\phi \neq 90°$, the wall pressure distribution is skew and deviation from the assumed curve becomes significant for $\phi \lesssim 70°$.

(iv) For $\phi \neq 90°$, the stagnation point is removed from the intersection of jet centerline and wall by a certain distance, s. In order to predict this quantity, an equation was borrowed from the corres-

ponding potential flow solution which, however, gives the distance to the center of gravity of wall pressure. This is consistent with the previous assumption of symmetry, but in view of the actual skewness of the wall pressure, it does not correspond to reality.

(v) In order to obtain an extra integral equation, entrainment in the impingement region was neglected. Careful examination of later data (26) shows that significant entrainment continues to take place well into the impingement region.

In the wall-jet region the analysis was based on the following assumptions:

(i) The local skin friction factor $C_f = 2(u_*/u_m)^2$ was assumed to vary with the local Reynolds number $R = \frac{u_m \delta}{\nu}$ according to a Blasius type relationship. Since in the wall jet R is approximately proportional to $x_1^{1/2}$, it is in fact assumed that $C_f \propto x_1^{-1/8}$. This contradicts previous considerations that showed $C_f \propto x_1^{o}$, but in view of the small power of x_1 involved, the discrepancy is not important. Hence, this assumption could be viewed as a source of unnecessary complication.

(ii) It was further assumed that the shear stress τ is given by Prandtl's hypothesis, i.e., $\tau \propto u_m \delta_2 \frac{\partial u}{\partial y}$. This, however, is contradicted by reality as was mentioned before (Sec. 2.2).

In 1964, Tani and Komatsu (15) presented the results of an experimental and analytical study of a circular jet impinging normally. Based on experiments with values of H/d equal to 4, 8 and 12, they reported that the impingement region extends about 1.6d to 3d radially

from the stagnation point and 1.6d to 2.2d above the wall. No distinction was made between "large" and "small" impingement heights. In this work, this constitutes an ommission, because the value $H = 4d$ is smaller than the potential core length (about 6d) and, therefore, one could expect it to be classified as a "small" impingement height. On the other hand, the value $H = 12d$ is about twice the length of the potential core and, therefore, it would rather belong to the "large" impingement height problem. An interesting theoretical contribution is included in this paper and it deserves closer examination. It was assumed that the flow in the impingement region is inviscid but not irrotational. In this case the equations of motion will not contain viscous or turbulence terms, which makes it possible to derive a differential equation for the streamfunction (Stokes) ψ that does not contain other unknowns. The streamfunction was then written as an infinite series expansion (using the co-ordinate system r, z as shown in Figure 2.3):

$$\psi = \frac{1}{2} r^2 [f(z) + r^2 g(z) + r^4 h(z) + \ldots..] \tag{2.19}$$

where $f, g, h, \ldots.$ are as yet unknown functions of z. Substituting Equation 2.19 into the differential equation for ψ it is possible to obtain $g, h, \ldots.$ in terms of only the function $f(z)$. The z-component of velocity, u, is then given by:

$$u = - f(z) + \frac{1}{4} r^2 \left(\frac{d^2 f}{dz^2} - b_2\right) - \frac{1}{8} r^4 \left(A f(z) + \frac{1}{8} \frac{d^4 f}{dz^4}\right) + \ldots \tag{2.20}$$

where $A, b_2, \ldots.$ are integration constants. The meaning of $f(z)$ is made obvious by letting $r = 0$. Then, $u_c = - f(z)$, i.e., $f(z)$ represents the magnitude of the centerline velocity. The function $f(z)$ has

to be evaluated empirically for any given set of initial conditions and this constitutes a weakness of this approach. Furthermore, for large impingement heights the assumption of inviscid flow is justified only in a small neighbourhood of the stagnation point rather than throughout the impingement region, as was pointed out earlier. In Chapter V, however, it is shown that this theory can be employed to advantage for the cases of small impingement heights, where the total pressure head remains constant on the centerline. The results of an experimental study of plane jets impinging normally, were presented by Cola (16) in 1965. One measurement of vertical velocity in the impingement region is included and the results agree with the experimental and theoretical results of Beltaos and Rajaratnam (26).

A paper by Poreh, Tsuei and Cermak (17) in 1967 is a theoretical and experimental study of the wall jet region in the case of axisymmetric impingement. The theoretical development is similar in many respects to that of Schwarz and Cosart (31) which was outlined in Section 2.2. Firstly, it was shown that:

$$u_m \propto r^m \quad ; \quad \delta_2 \propto r^n \quad ; \quad C_f \propto r^{n-1} \tag{2.21}$$

It was not realized that C_f is independent of r (Section 2.2), which would immediately give $n = 1$. The values of the exponents m and n were obtained empirically as:

$$m = -1.1 \quad \text{and} \quad n = 0.9 \tag{2.22}$$

However, a re-analysis of their data (Chapter IV) showed that δ_2 varies linearly with r and if a small virtual origin correction is introduced,

then $\delta_2 \propto \overline{r}$, i.e., $n = 1$. From the integral momentum equation, the following relation can be derived (which is analogous to Equation 2.17 for the plane case):

$$m = -\left(1 + \frac{C_f}{4FC_2}\right) \qquad (2.23)$$

where F is defined as in Section 2.2, and $C_2 \equiv d\delta_2/dr$. It follows that, strictly speaking, $m < -1$. However, from the available data the term $C_f/4FC_2$ can be estimated to be very small in comparison to unity. From dimensional considerations, and using $n = 1$, C_f can be shown to depend only upon the nozzle Reynolds number, R_o, so that it decreases with increasing R_o. This means that for very small values of R_o, negligence of the above term may not be realistic. Assuming then that R_o is not very small, the value of m can be taken as -1. Again, a re-evaluation of the data presented in (17) showed that $u_m \propto 1/\overline{r}$ (Chapter IV). The value of this approximation is not merely academic. From dimensional considerations, the authors of (17) have shown that:

$$\frac{u_m}{U_o}\frac{H}{d} = C_1 \left(\frac{r}{H}\right)^m$$

$$\frac{\delta_2}{H} = C_2 \left(\frac{r}{H}\right)^n$$

If $m = -1$ and $n = 1$ the above expressions will become free of the parameter H. This constitutes a major simplification, especially when considerations of oblique impingement come into play. Then the complexity of the problem will be considerably reduced by knowing that H is irrelevant.

Measurements of turbulent stresses confirmed the conventional boundary layer approximations with respect to normal stresses, and at the same time demonstrated that root-mean square values are also self-preserving with scale u_m. However, due to scatter it was not possible to establish conclusively the similarity of turbulent shear stress variations across the jet, even though a trend toward similarity is clearly demonstrated. It is interesting to note that the turbulent shear stress did not vanish at the point of maximum velocity.

In 1968, Cartwright and Russel (18) presented an experimental and analytical study of a plane jet impinging normally. Measurements were reported mainly for the wall jet region. The law of the wall was verified for the boundary layer. The linearity of δ_2 was also obtained but the exponent of x_1 describing the variation of u_m was given as -0.39, a rather surprising value, since as has already been pointed out (Section 2.2), this exponent cannot be greater than -0.5. Yet, when the data were re-analyzed (Chapter VI) it was shown that an exponent equal to -0.5 is reasonable, if a small virtual origin correction is allowed. In the impingement region only the wall pressure was measured, and a similarity property was obtained by plotting p_w/p_s vs x_1/H.

An interesting numerical study of the plane turbulent jet impinging normally, was presented by Wolfshtein (19) in 1970. It was assumed that the Reynolds stresses are related to the mean strain by a scalar eddy viscosity, which in turn was assumed to depend on the level of energy fluctuations and a length scale. Thus, it was possible to obtain iterative, finite-difference solutions which were compared with

the data of Schauer and Eustis (14). No claim to general validity of the theoretical model was made owing to the arbitrary selection of the length scale. However, this model predicts the correct trends with the exception of the wall shear in the impingement region. This was predicted to be proportional to $R_o^{-0.475}$, whereas later work (26) showed that the wall shear stress in region II is practically independent of R_o. It is noteworthy that the model predicts strong generation of turbulence near the stagnation point, a phenomenon that was also observed experimentally (Ref. 10 of Wolfshtein (19)). Owing to the very small thickness of the wall boundary layer in the impingement region, it is extremely difficult to explore this boundary layer experimentally. Yet, knowledge of boundary layer properties is important, not only in an academic sense, but also from the practical point of view for both scour and heat transfer considerations. In order to estimate boundary layer thickness from data on wall pressure and shear stress, knowledge of the state (laminar or turbulent) of the boundary layer is imperative. The above considerations point toward a turbulent boundary layer, a possibility that is supported by the irrelevance of R_o with respect to wall shear stress. The turbulent counterpart of the classical stagnation flow problem (Section 2.1) has been treated by the same author, Wolfshtein (37).

A systematic experimental study of a circular jet impinging normally was published in 1970 by Hrycak et al (22). The variation of potential core length with R_o was studied extensively. It was demonstrated that for $R_o \leq 4,000$ this quantity normalized with the nozzle diameter, d, depends strongly upon R_o, whereas for $R_o \geq 8,000$ the poten-

tial core length varies only between 6.8d and 6.5d. Next, the free jet laws were verified in the free-jet region. In the impingement region measurements of wall pressure and maximum radial velocity v_m (maximum in a vertical, occurring at the edge of the boundary layer) were presented. No distinction was made between small and large impingement heights, hence no generalization of the results could be achieved. Valuable data on boundary layer thickness were also presented. These were for $H/d = 3$, 7, 10 and 20 but for one only value of Reynolds number ($R_o = 54{,}000$) and were estimated to be accurate to within 15% and 30% for $H/d = 3$ and 20 respectively. It was established that near the stagnation point the boundary layer thickness δ is almost constant. Using the available data on v_m to evaluate the constant a of Equation 2.5, the thickness can be predicted from stagnation flow considerations (Section 2.1). However, the predicted values are about one-half of the measured ones (owing to a numerical oversight, Hrycak et al (22) predicted values that are only 30% less than the actual). In the wall-jet region, u_m was found to vary as $r^{-1.12}$, yet a re-analysis showed that the relation $u_m \propto 1/r$ gives also a good fit (Chapters IV and V). It is noteworthy that these data were for values of H/d ranging between 4 and 20, i.e., for both small and large impingement heights. Yet, when these data were plotted in the form u_m/U_o vs r/d they collapsed in a single curve, thus leading to the expectation that the wall jet region is independent of small or large height considerations. This in turn would imply that the wall-jet region depends only upon the initial momentum of the jet for all impingement heights. Further support to this is furnished by the data of Yakovlevskii and Krashen-

ninikov (27), not only for normal impingement but also for oblique as will be seen in Chapter VII. The length scale, δ_2, was given as $\delta_2/d = \text{const } (r/d)^{0.95}$, the constant being a weak function of H/d. Again, re-analysis showed the linearity of δ_2, i.e., $\delta_2/d = C_2(r/d)$ with C_2 taking values between 0.071 and 0.082 as H/d changes from 2 to 20. This, however, does not necessarily imply dependence upon H/d, because C_2 has been found to vary even for classical wall jets. For example, C_2 varied from 0.056 to 0.085 in the work of Schwarz and Cosart (31) for a plane wall jet. It is believed that this variation is due to varying nozzle conditions which cannot be accounted for at present. A survey of literature by the same authors, Gauntner et al (21) was also published in 1970 and presumably preceeded the above work.

A brief paper by Bradbury (23) in 1972 is an attempt to correlate wall pressure data by means of a rather weak dimensional argument. This correlation is essentially identical to that of Poreh and Cermak in 1959 (11) and can be derived formally by means of dimensional analysis using the assumption of a point source of momentum as set forth by Murray et al, Rouse (9) in 1956. This paper seems to ignore most of the significant research prior to 1972.

A paper by Kamoi and Tanaka (24) in 1972, is mainly an investigation of turbulence properties near the stagnation point for various angles of plane jet impingement. It is again demonstrated that strong turbulence exists near the stagnation point. Measurements of r.m.s. (root-mean-square) values of wall pressure and shear stress showed that

for large impingement heights the r.m.s. is maximum at the stagnation point itself, whereas for small impingement heights the maximum is removed somewhat from the stagnation point. In fact, the authors state that coincidence of r.m.s. maximum with the stagnation point indicates that the boundary layer is turbulent. The state of the boundary layer depends upon the parameter H/d, the impingement angle and the nozzle turbulence level. For normal impingement the critical values of H/d are 8 and 4 for turbulence levels of 0.5% and 3.7% respectively. Time-average values of wall pressure and shear stress were also measured for some runs, however, the shear stress data appear to be suspect because of non-zero values of τ_o at the stagnation point.

In 1973, Beltaos and Rajaratnam (26) presented the results of a systematic experimental and analytical study of plane jets impinging normally. The impingement region was studied in detail, including explorations of the velocity and pressure fields. It was shown that the impingement region begins at $x/H \cong 0.7$. Flow properties were predicted semi-empirically and the analysis will be illustrated in Chapter IV for the axisymmetric case. The wall-jet region was analyzed according to considerations outlined in Section 2.2. It was established that for small values of R_o the exponent of x_1 describing the variation of u_m cannot be taken as -0.5, being definitely smaller than this value.

Finally, a paper by Yakovlevskii and Krashenninikov (27) deals with the wall-jet region for oblique impingement of circular turbulent jets. This will be discussed in greater detail in Chapter VII.

2.4 Summary

A critical review of literature pertinent to the problem of turbulent jet impingement, has been presented in the previous sections. It was shown that previous work was mostly concerned with regions I and III. In region I, flow characteristics have been conclusively verified to be identical with those of a free jet. In region III, an improvement upon the existing analytical approaches has made it possible to effect considerable simplification so long as the Reynolds number, R_o, is larger than a certain limiting value which will be discussed in later chapters. This simplification consists of showing the wall jet development to be independent of the height of impingement. Hence, the velocity and length scales are given by:

$$\delta_2 = \begin{cases} C_2 \, \overline{x}_1 , & \text{for plane jets} \\ C_2 \, \overline{r} , & \text{for circular jets} \end{cases} \qquad (2.24)$$

$$\frac{u_m}{U_o} = \begin{cases} \dfrac{C_u}{\sqrt{x_1/d}} , & \text{for plane jets} \\ \dfrac{C_u}{r/d} , & \text{for circular jets} \end{cases} \qquad (2.25)$$

where C_2, C_u are constants (different for plane and circular jets), and the overbar denotes that distance along the wall must be measured from a virtual origin. Regarding the wall shear stress, it was shown that it is proportional to the local value of the maximum dynamic head i.e., the local skin friction factor is independent of x_1 (or r). This factor depends only upon R_o, i.e.,:

$$C_f = C_f\ (R_o) \tag{2.26}$$

so that $dC_f/dR_o < 0$.

Furthermore, it was pointed out that if H is made very small, the physics of the problem is likely to change, thus bringing out the distinction between "large" and "small" impingement heights. The above considerations are ordinarily valid for "large" heights, however, based on existing data, it was tentatively shown that the wall jet region develops in a unique way, independently of large or small height considerations.

Finally, turbulence measurements (24) show that the state of the boundary layer in the impingement region depends upon the relative height H/d, the angle of impingement, ϕ, and the nozzle turbulence level. Even for the smaller turbulence level investigated (0.5%) the boundary layer will be turbulent for all ϕ so long as $H/d \gtrsim 8$.

Source	Ref. No.	Angle of Impingement ϕ (°)	$R_o \times 10^{-5}$	H/d	Fluid Used	Geometry
Rouse	9	90	——	50,100	Air	Circular
Bradshaw & Love	10	90	1.82	18	Air	Circular
Poreh & Cermak	11	90	.536 - 1.29	8 - 32	Water	Circular
Schauer & Eustis	14	30,50,70,90	.203 - .528	10 - 40	Air	Plane
Tani & Komatsu	15	90	1.05 - 1.67	4,8,12	Air	Circular
Cola	16	90	.34 - .94	44.3	Water	Plane
Poreh, Tsuei & Cermak	17	90	.72 - 3.25	10 - 31	Air	Circular
Cartwright & Russel	18	90	.25 - 1.10	8 - 47	Air	Plane
Hrycak et al	22	90	.006 - 1.0	2 - 30	Air	Circular
Kamoi & Tanaka	24	30 - 90	——	2 - 20	Air	Plane
Beltaos & Rajaratnam	26	90	.053 - .094	14 - 67.5	Air	Plane
Bradbury	23	90	$\lesssim 2$	4 - 19.3	Air	Circular
Yakovlevskii & Krasheninnikov	27	45 - 90	0.69	3.5,10	Air	Circular

TABLE 2.1 RANGE OF INITIAL PARAMETERS

CHAPTER III - EXPERIMENTAL EQUIPMENT AND TECHNIQUES

3.1 Experimental Set-Up

Experiments were conducted with air jets in air using speeds less than 300 fps so that compressibility effects were negligible. Use of air instead of water has the advantage that the necessary experimental set-up is less bulky and much easier to handle.

Circular and plane jets were produced by means of suitably designed nozzles and plenum chambers. The experimental set-up for plane jets is shown in Figure 3.1. The aspect ratio of the nozzle is about 65, so that the flow could be assumed to be two-dimensional in the central portion of the nozzle in the region studied. In the chamber, a series of circular tubes were placed near the entrance and a sequence of five screens was placed further downstream, as shown in Figure 3.1(a). The tubes serve the purpose of "straightening" flow streamlines which tend to become curvilinear after the sudden expansion at the entrance. The screens were provided in order to ensure mixing and thus uniformity of the flow. The flow rate was adjusted by means of a pressure regulatory valve.

To produce impingement, a 1/4 inch thick plexiglass plate, 6 inches wide and 5.75 feet long, equipped with 1 foot high sidewalls, was used. Adjustment of the angle of impingement was made possible by means of a simple suspension system which is outlined in Figure 3.2, whereas Figure 3.3 shows photographs of the plane jet set-up. A circular plenum chamber 3.5 inches in diameter was used for circular jets

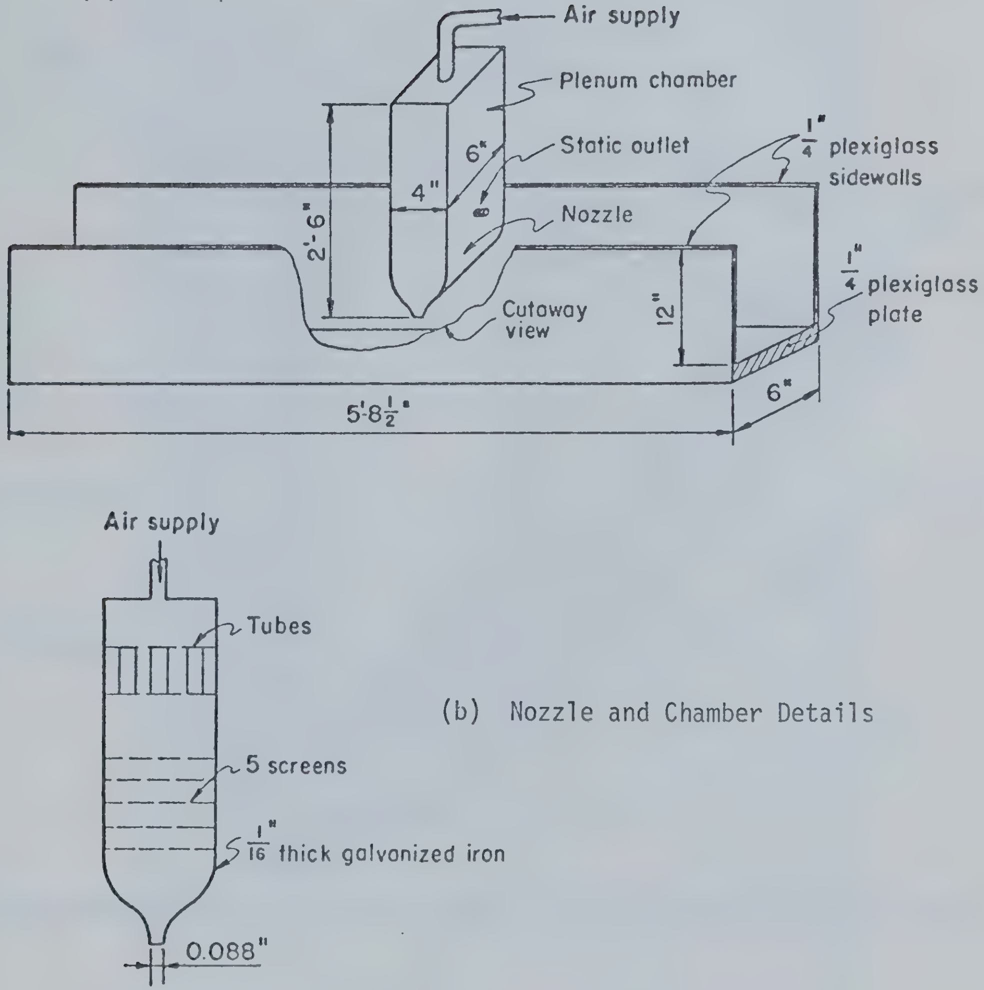
(a) Set-Up

(b) Nozzle and Chamber Details

Air supply
Plenum chamber
Static outlet
Nozzle
6"
4"
2'-6"
Cutaway view
$\frac{1}{4}$" plexiglass sidewalls
$\frac{1}{4}$" plexiglass plate
12"
6"
5'-8$\frac{1}{2}$"
Air supply
Tubes
5 screens
$\frac{1}{16}$" thick galvanized iron
0.088"

FIGURE 3.1 SET-UP FOR PLANE JETS

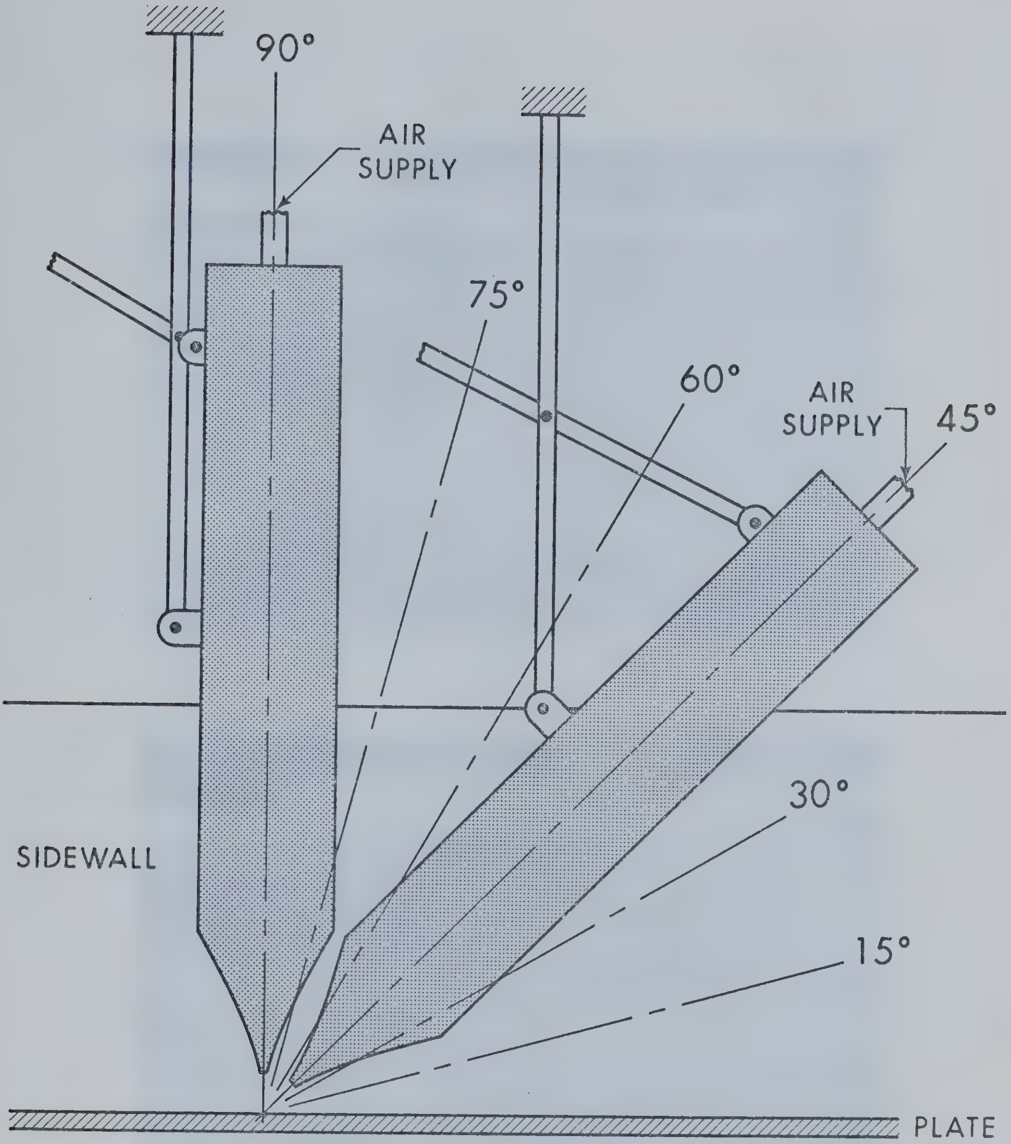
90°
AIR SUPPLY
75°
60°
AIR SUPPLY
45°
30°
SIDEWALL
15°
PLATE

FIGURE 3.2 CHAMBER SUSPENSION-PLANE JET

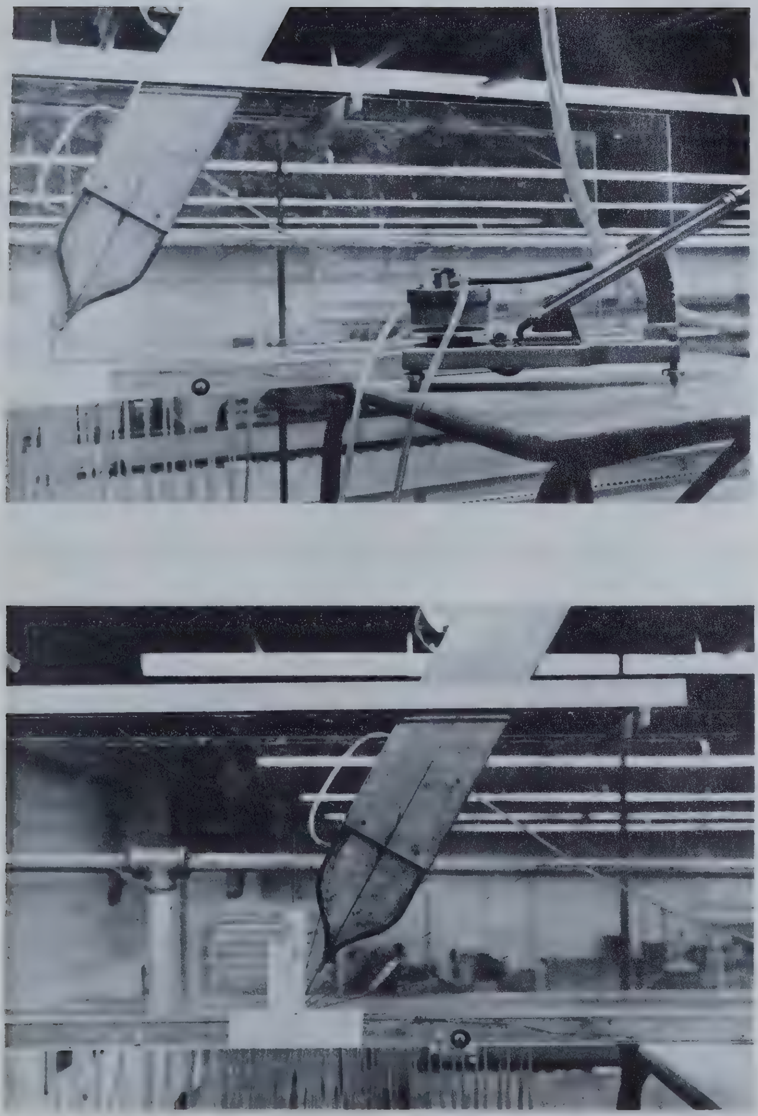

FIGURE 3.3 PLANE JET SET-UP

and the details of construction are much the same as those of plane jets. This was made out of plexiglass and was possible to equip with nozzles of different outlet diameters. In the present experiments two outlet sizes were used, 0.923 and 0.253 inches. Impingement was produced by means of plexiglass plates. The set-up was somewhat different for normal and oblique impingement, as shown in Figure 3.4(a) and (b).

The temperature of the supply air was somewhat less than the room temperature (≃ 68°F) and for this purpose a heater was installed between supply and chamber, so that the air issuing from the nozzle was kept close to room temperatures.

Finally, for studying the circular counterjet, a smaller plenum chamber was built (plexiglass) and was placed along the centerline of a 2 foot square wind tunnel. This chamber was constructed in the same fashion as the previous two but its diameter was only 1.5 inches so as to minimize disturbance to the approaching stream. A nozzle with outlet diameter of 0.20 inches was used so that the ratio of stream dimension to nozzle diameter was made very large (120). To minimize boundary layer effects, the chamber was placed near the entrance of the wind tunnel. This set-up is shown in Figure 3.5.

3.2 Experimental Techniques

3.2.1 Nozzle Velocity

Referring to Figure 3.6, the Bernoulli theorem applied between sections 0 - 0 and 1 - 1, gives:

$$p_1 + \frac{\rho U_1^2}{2} = p_o + \frac{\rho U_o^2}{2} \qquad (3.1)$$

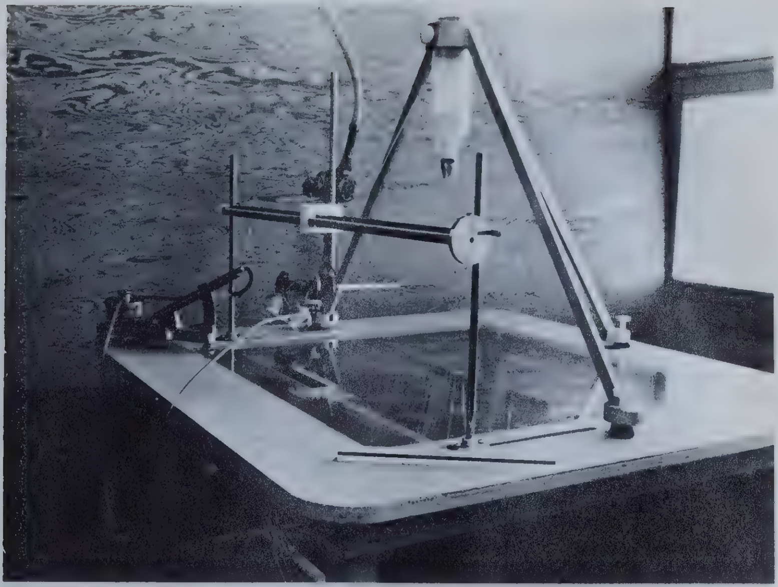

(a) NORMAL IMPINGEMENT

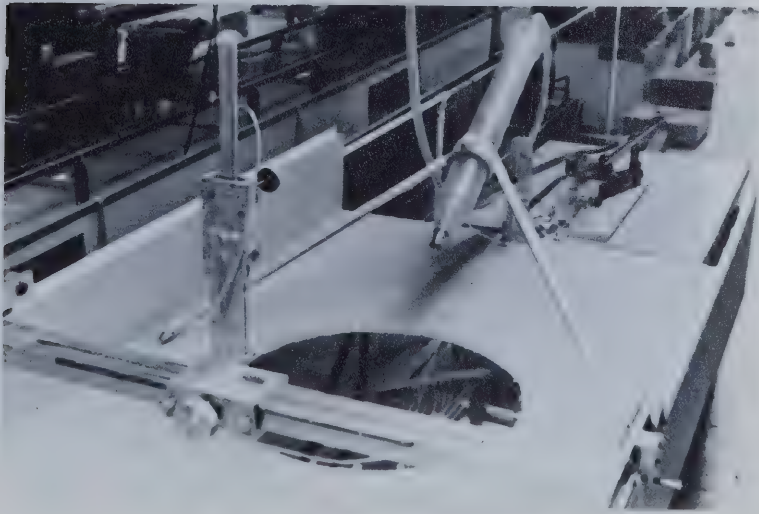

(b) OBLIQUE IMPINGEMENT

FIGURE 3.4 CIRCULAR JET SET-UP

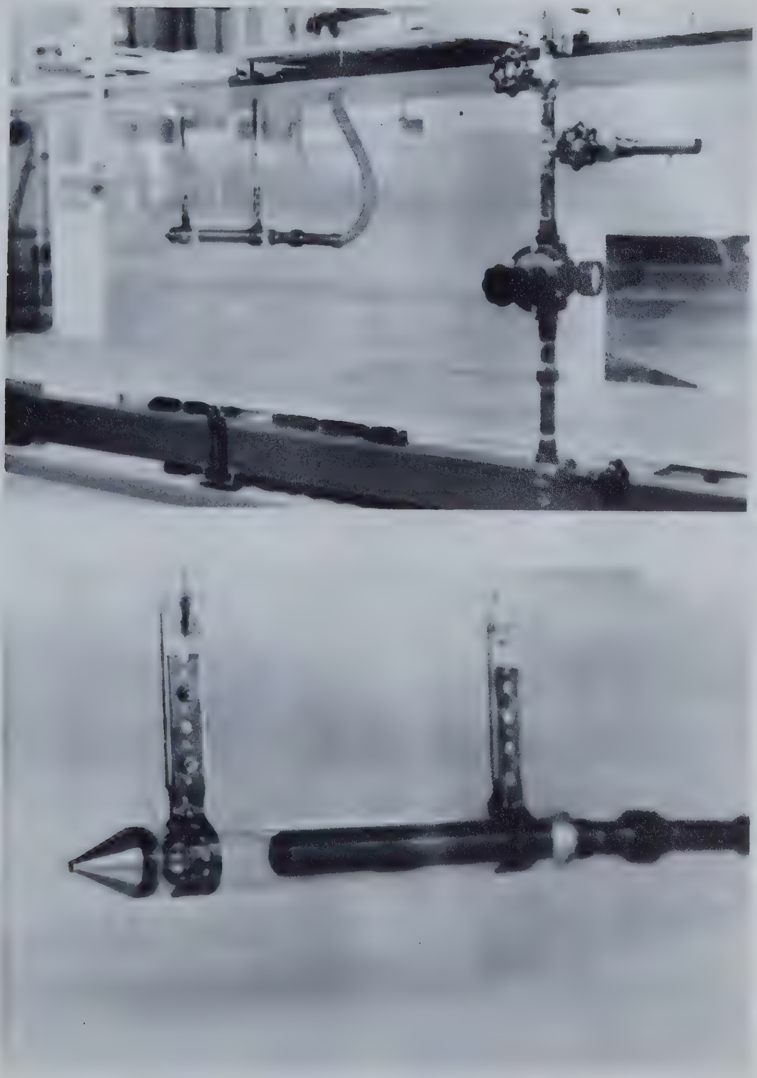

FIGURE 3.5 SET-UP FOR COUNTERJET EXPERIMENTS

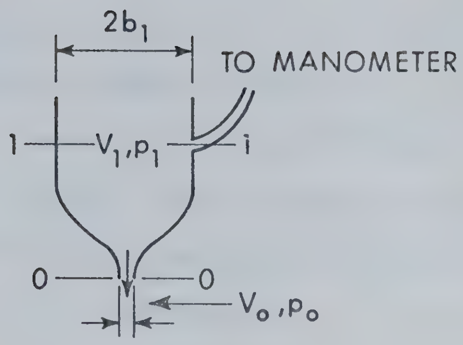
2b1
TO MANOMETER
1
V1,p1
1
0
0
Vo,po

FIGURE 3.6 APPLICATION OF BERNOULLI THEOREM

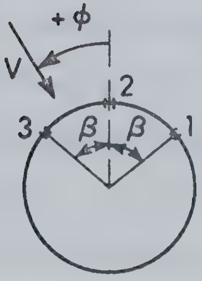

(a) CROSS SECTION

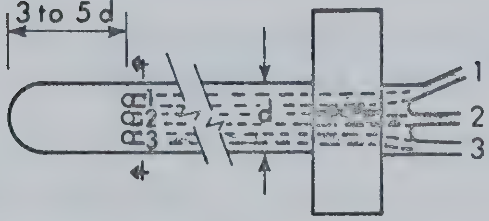
3 to 5 d
1
2
3
d
1
2
3

(b) TOP VIEW

FIGURE 3.7 THE PITOT CYLINDER

where ρ is the mass density of the fluid, p_1, U_1 and p_o, U_o are values of static pressure and velocity at sections 1 - 1 and 0 - 0 respectively. If A_o, A_1 are the flow areas at sections 0 - 0 and 1 - 1, then $(U_1/U_o)^2 = (A_o/A_1)^2$. This quantity is always less than 0.0067 for the present experimental equipment, and therefore, the pressure difference, $\Delta p = p_1 - p_o$, is given by:

$$\Delta p \simeq \frac{\rho U_o^2}{2} \tag{3.2}$$

The validity of Equation 3.2 was checked by comparing manometer heights with nozzle velocity heads at different velocities U_o. No difference was recorded between corresponding readings. A vertical water manometer was used for heads larger than 3 inches. Assuming that reading errors were at most ±0.05 inches, the maximum head recording error would be about 1.6%. Since $U_o \propto \sqrt{\Delta p}$, the maximum error in obtaining U_o would be less than 1%. Thus, the nozzle velocity was measured indirectly by recording the pressure Δp. This procedure has the advantage that U_o may be recorded within seconds at any instant, so that corrections for small supply fluctuations can be applied.

3.2.2 Velocity and Pressure Measurements in the Impingement Region - Pitot Cylinder

In the impingement region the direction of the velocity vector is not known before hand. In addition, the static pressure is higher than the ambient (atmospheric). As ordinary Prandtl-Pitot tubes cannot handle this situation, a Pitot cylinder was used, employing a technique that does not require rotation of the instrument. This technique was developed by the author (25),(38) and is summarized below. The Pitot

cylinder is a cylindrical instrument of small diameter having three orifices near its edge which is rounded (Figure 3.7). For two-dimensional flow, the instrument is placed with its axis perpendicular to the plane of flow so that no gradients exist along the axis. If the orifices 1, 2, 3 (Figure 3.7) are connected to a manometer, three pressure readings, p_1, p_2, p_3, will be obtained respectively which are related to the local values of ϕ, V, and p_o (static pressure). On this principle the instrument can be calibrated so that measurement of p_1, p_2, and p_3 enables calculation of ϕ, V and p_o, and the procedure is:

1. Measure p_1, p_2, p_3.
2. Compute $K = (p_1 - p_2)/(p_3 - p_2)$.
3. From a calibration plot of K vs ϕ, obtain ϕ.
4. From a second calibration plot of K_i vs ϕ, ($i = 1, 2, 3$) obtain K_i.
5. Compute velocity from:

$$\frac{\rho V^2}{2} = \frac{p_j - p_2}{K_j - K_2} \quad ; \quad j = 1, 2 \tag{3.3}$$

6. Compute static pressure from:

$$p_o = p_i - K_i \frac{\rho V^2}{2} \quad ; \quad i = 1, 2, 3 \tag{3.4}$$

Calibration curves for the factors K, K_1, K_2, K_3 and $K_j - K_2$ are shown in Figures 3.8, 3.9 and 3.10 for an instrument 1/8 inch in diameter with a polar angle β between orifices of 45°. This method was found to be satisfactory when applied to plane shear flows (25). It was also found to give satisfactory results in the case of axisymmetric shear

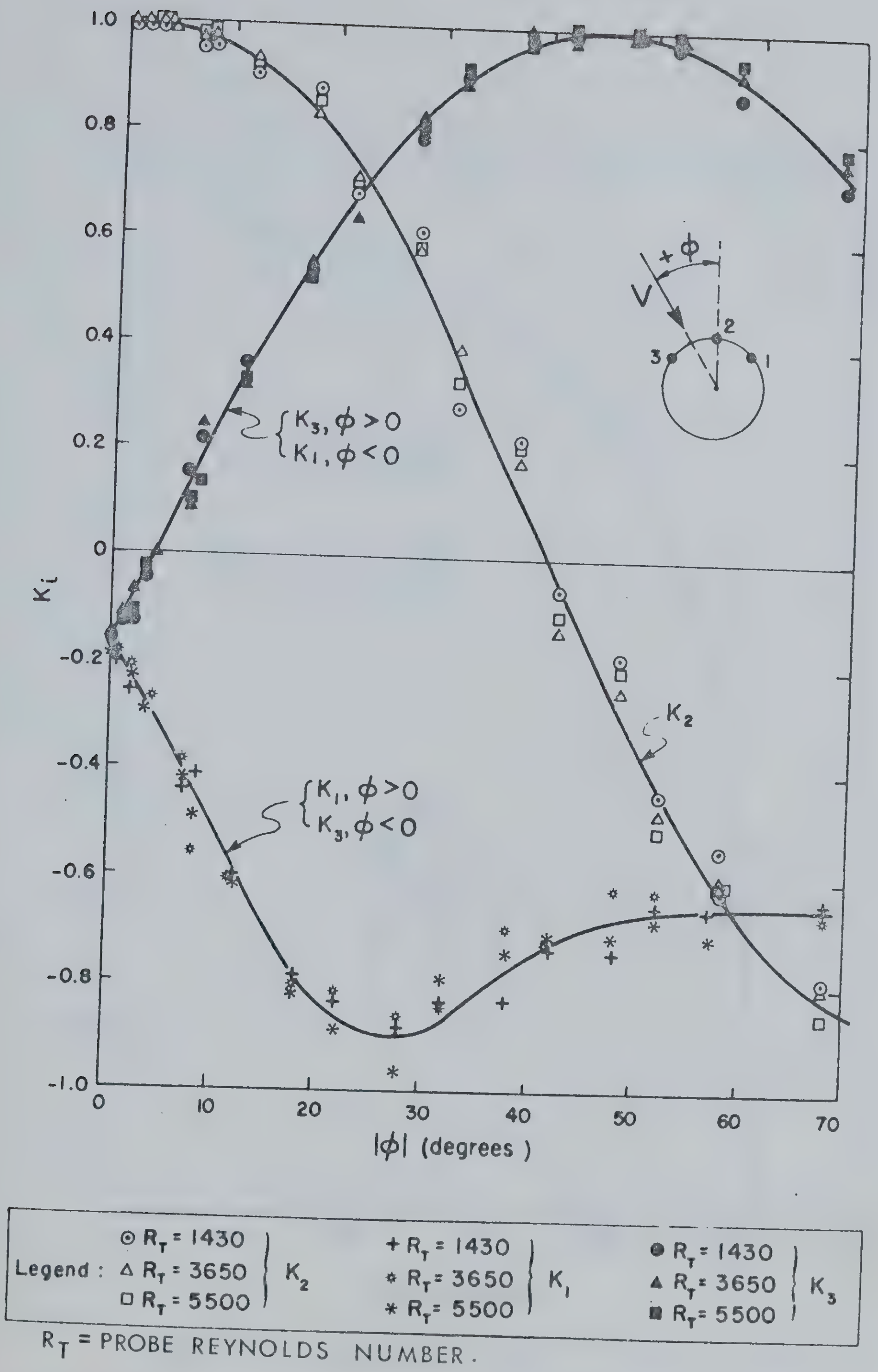

FIGURE 3.8 CALIBRATION FACTORS K_1, K_2, K_3 (1/8 in. Probe)

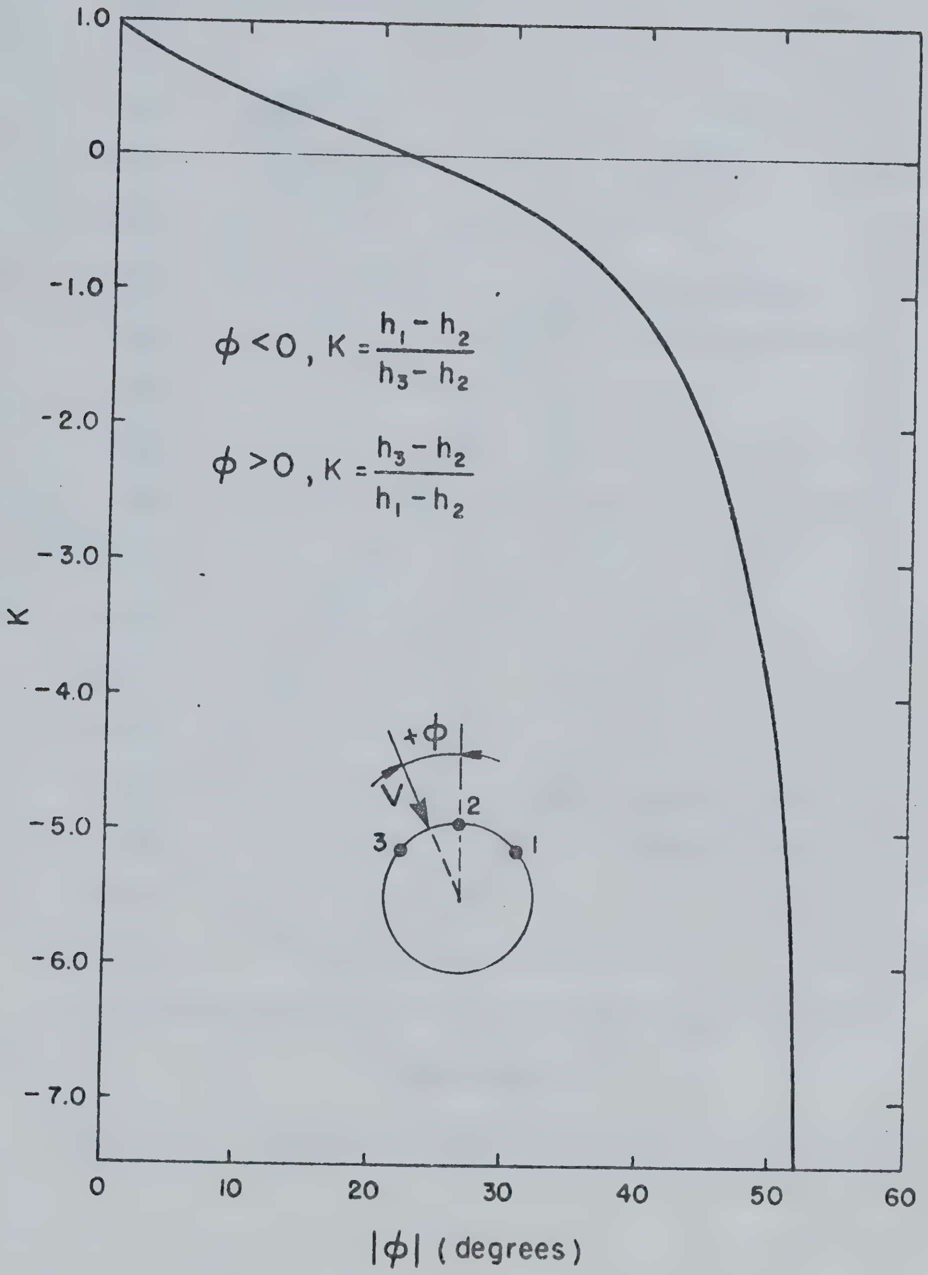

FIGURE 3.9 CALIBRATION FACTOR K (1/8 in. Probe)

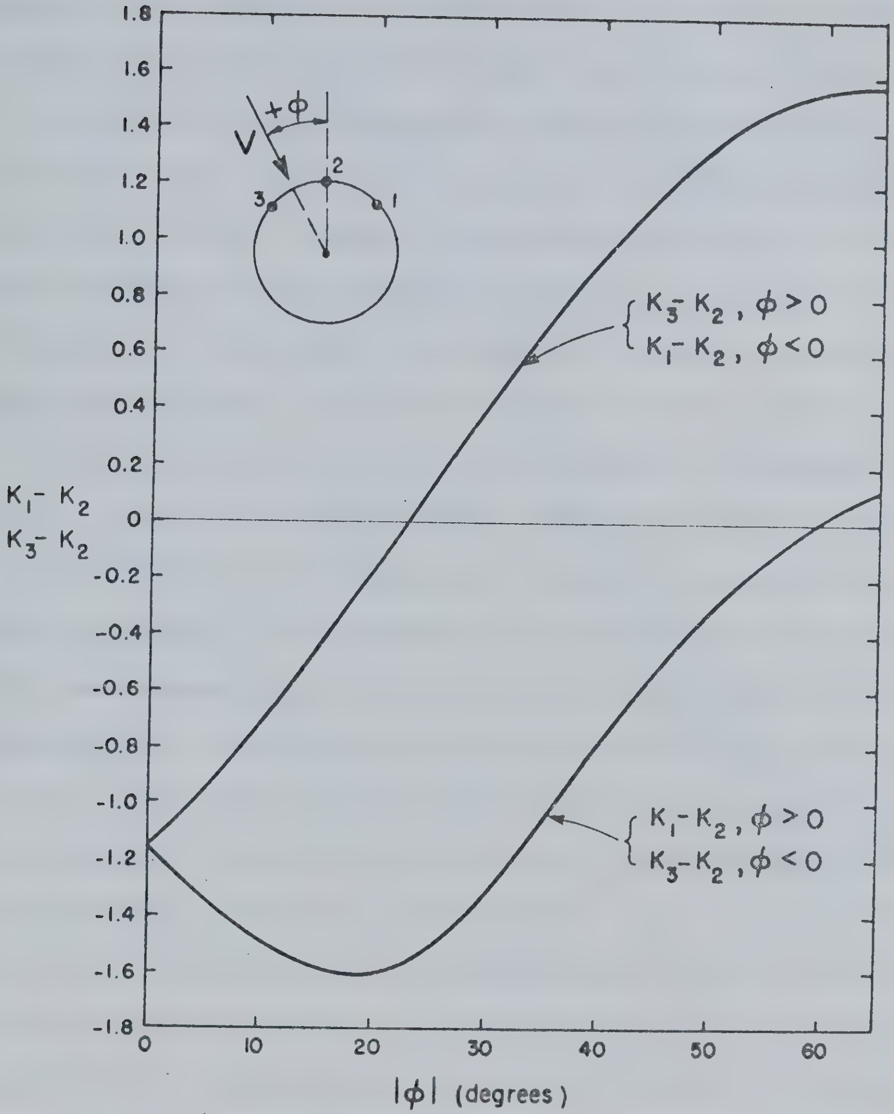

FIGURE 3.10 CALIBRATION FACTORS K_1-K_2 AND K_3-K_2 (1/8 in. Probe)

flows, because here, even though the flow is not two-dimensional, local gradients along the axis of the probe vanish if the probe is oriented with its axis perpendicular to the radial line passing through orifice 2. For the case of large impingement heights, where the width of the jet is much larger than the probe diameter, the 1/8 in. probe yielded satisfactory results. However, when the same probe was used in cases of small impingement heights, erroneous results were obtained, which were attributed to the relatively large size of the probe. In order to overcome this difficulty, a new probe of diameter 0.04 in. was built. Owing to the small size of the probe it was not possible to construct separate orifices. Hence, only one orifice was drilled and each measurement involved rotation by 45° twice so that readings corresponding to 1, 2, 3 could be obtained. This, however, did not slow down the work, because the inside diameter of this probe was considerably larger than the inside diameter of the fine tubing leading to the orifices of the 1/8 in. probe, so that response times were much smaller in this case. As the orifice size can affect the calibration curves, a new calibration was performed, the particulars of which are shown in Figure 3.11. For the factor K_2 in the Figure 3.11, the corresponding curve of the 1/8 in. probe is also shown for comparison. It is seen that the curve is shifted somewhat due to differing relative size of the orifice. For measurements in the wind-tunnel, associated with the counterjet problem (Chapter VIII), a third probe of diameter 0.04 in. and having only one orifice, was built. In this case, however, the relative size of the orifice was made to be close to that of the large probe. Calibration curves for the wind tunnel probe are shown in Figure 3.12.

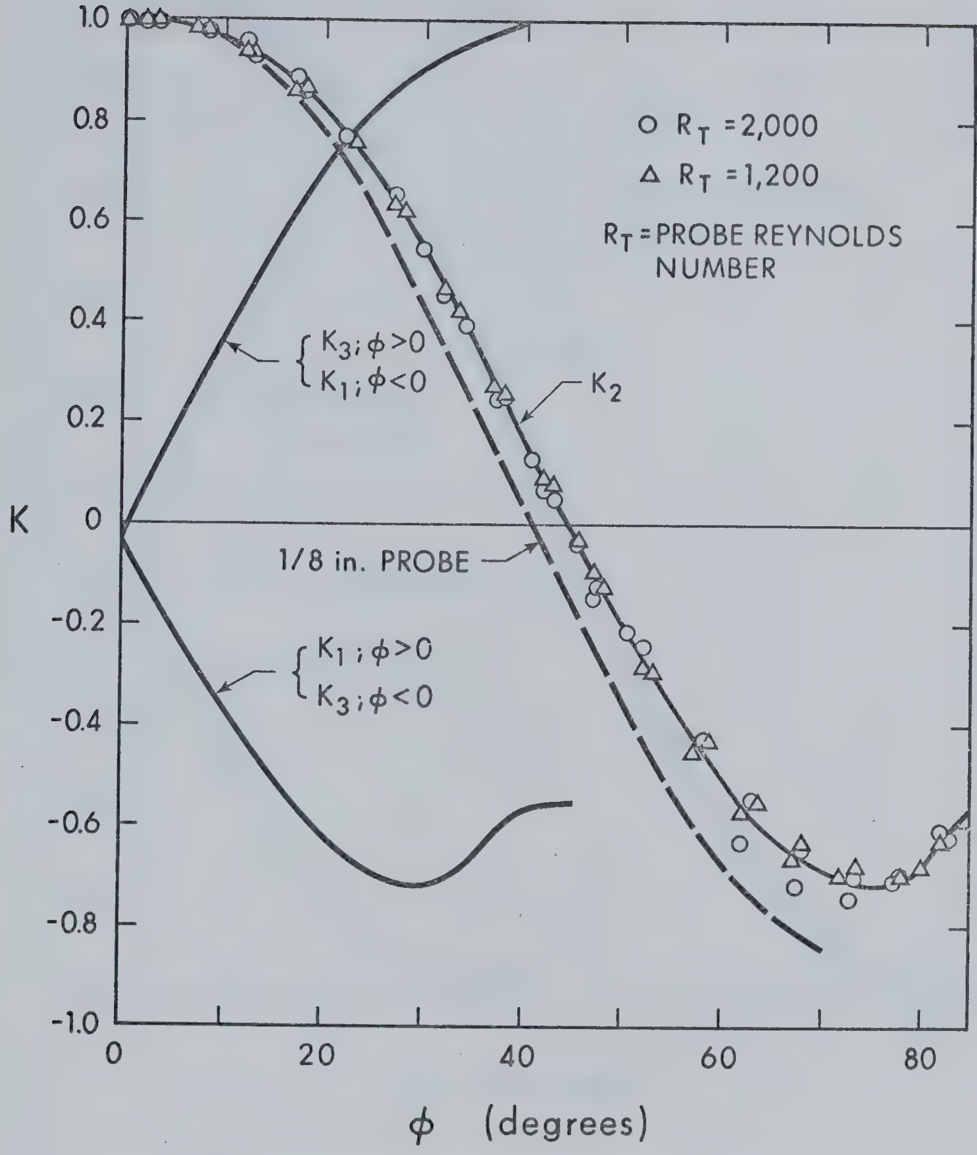

FIGURE 3.11 CALIBRATION FACTORS K_1, K_2, K_3 (0.04 in. Probe)

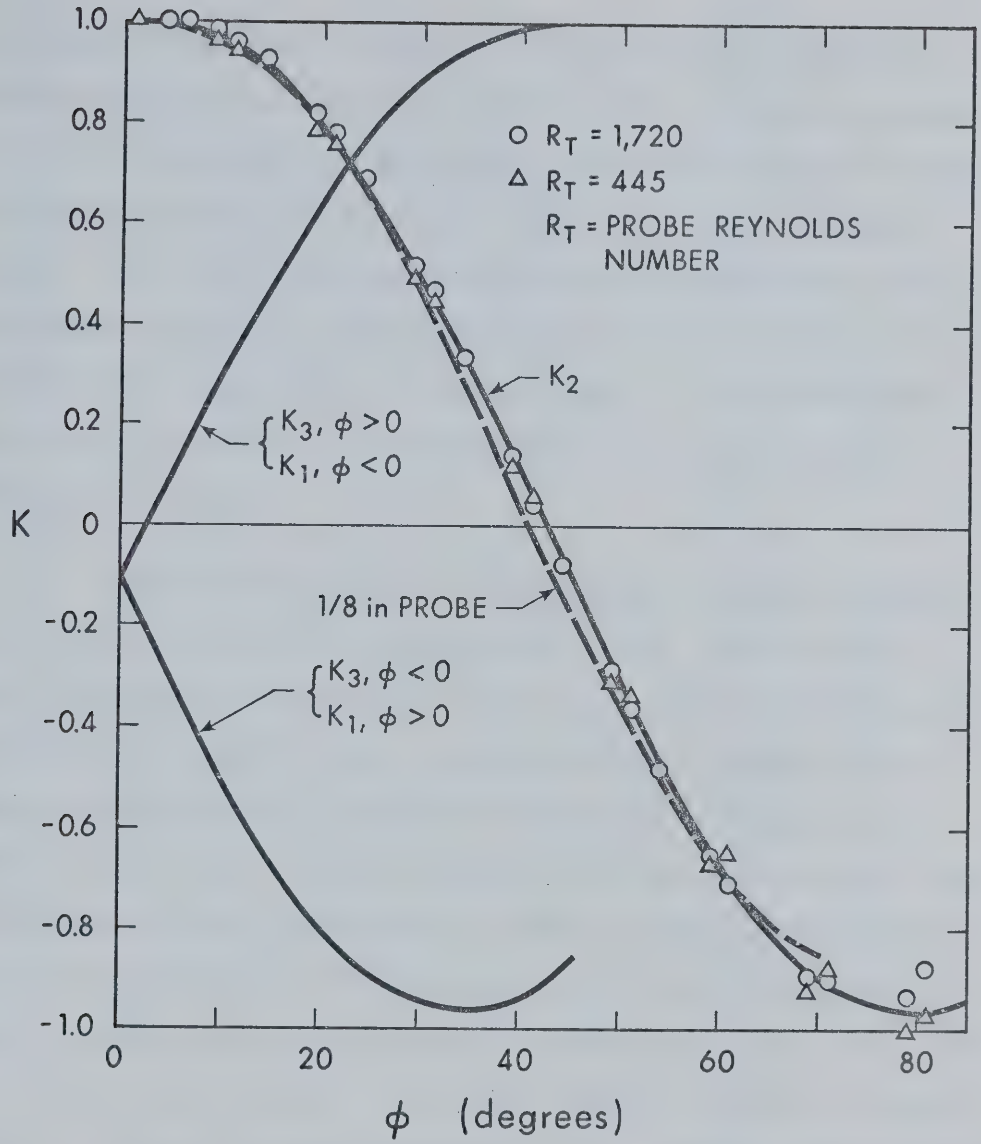

FIGURE 3.12 CALIBRATION FACTORS K_1, K_2, K_3 (Wind Tunnel Probe)

It is seen that in this case (Figure 3.12) the calibration curve for K_2 is almost identical to that of the 1/8 in. probe. In order to estimate effects of probe size to the measurements, an error analysis was performed (Appendix B) using the experimental results for small impingement heights. The percent error depended upon the local transverse gradients of pressure and velocity. The maximum error was 2% for velocity, 3.5% for the static pressure and 1° for the angle ϕ. The percent error in velocity and pressure increases generally for increasing distance from the centerline.

To measure wall pressure, a large number of 1/16 in. diameter static taps were installed on the impinging plates. Details of the spacing for plane jets are shown in Figure 3.13. For normal impingement of circular jets, pressure taps were located along a straight line as shown in Figure 3.14(a). For inclined impingement of circular jets a circular plate 2 ft. in diameter was used, with taps along a radial line. This plate was able to rotate about its center. Radial distributions of pressure were measured at 15° increments of polar angle. These were plotted separately and the co-ordinates of points where $p/p_s = 1.0$, .95, .9, .8, etc. were determined. These were afterwards plotted on the wall plane and contours of equal pressure were drawn. The taps were spaced as shown in Figure 3.14(b) and a close view of this plate is shown in Figure 3.15. Wall pressures yielded vertical water columns generally less than 3 inches, hence, a precision manometer was used which can measure alcohol columns at slopes as small as 1:25. To facilitate the work, a valve was placed between taps and manometer so that it was possible to take readings from different taps by simply turning a knob.

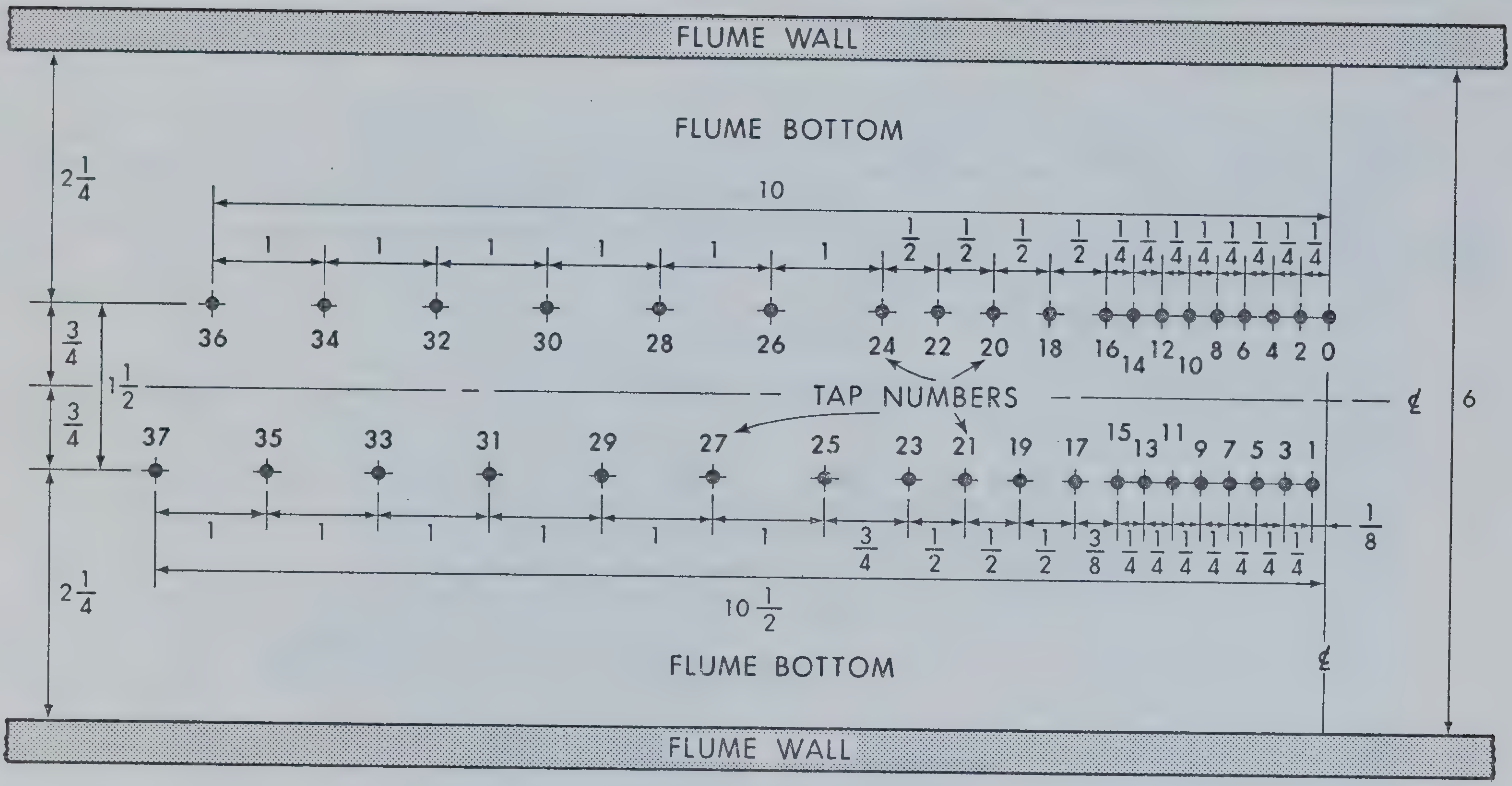
FLUME WALL
FLUME BOTTOM
10
1 1 1 1 1 1
1/2 1/2 1/2 1/2
1/4 1/4 1/4 1/4 1/4 1/4 1/4 1/4
36 34 32 30 28 26 24 22 20 18 16 14 12 10 8 6 4 2 0
TAP NUMBERS
℄
37 35 33 31 29 27 25 23 21 19 17 15 13 11 9 7 5 3 1
1 1 1 1 1 1
3/4 1/2 1/2 1/2 3/8
1/4 1/4 1/4 1/4 1/4 1/4 1/4
1/8
10 1/2
2 1/4
3/4
3/4
1 1/2
2 1/4
6
℄
FLUME BOTTOM
FLUME WALL

Scale in inches

FIGURE 3.13 STATIC TAP SPACING - PLANE JETS

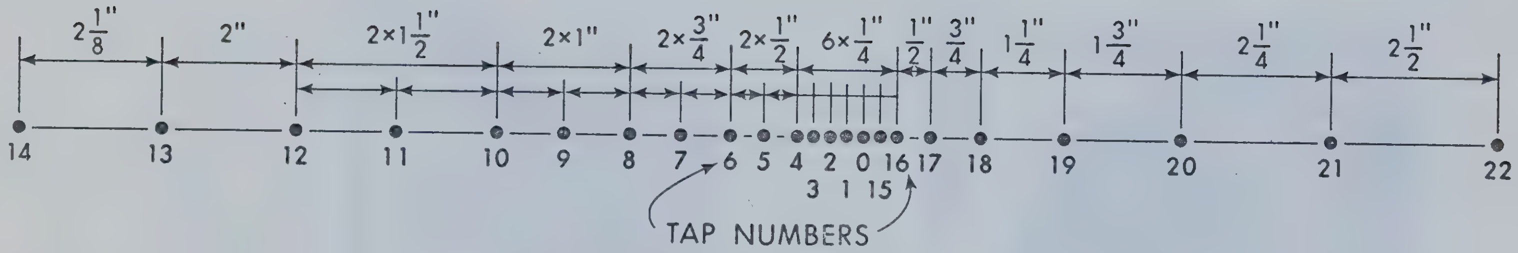
$2\frac{1}{8}''$
2"
$2\times1\frac{1}{2}''$
2×1"
$2\times\frac{3}{4}''$
$2\times\frac{1}{2}''$
$6\times\frac{1}{4}''$
$\frac{1}{2}''$
$\frac{3}{4}''$
$1\frac{1}{4}''$
$1\frac{3}{4}''$
$2\frac{1}{4}''$
$2\frac{1}{2}''$
14
13
12
11
10
9
8
7
6
5
4
2
0
16
17
18
19
20
21
22
3
1
15
TAP NUMBERS

(a) Normal Impingement

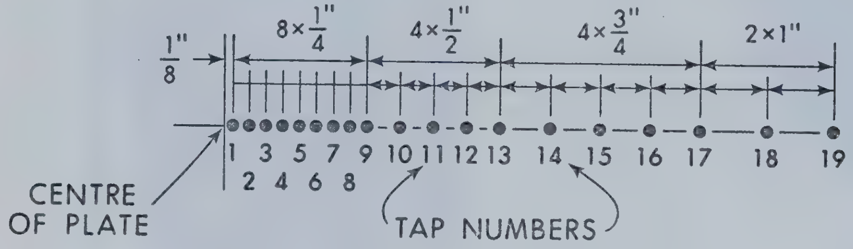
$\frac{1}{8}''$
$8\times\frac{1}{4}''$
$4\times\frac{1}{2}''$
$4\times\frac{3}{4}''$
2×1"
1
3
5
7
9
10
11
12
13
14
15
16
17
18
19
2
4
6
8
CENTRE OF PLATE
TAP NUMBERS

(b) Oblique Impingement

FIGURE 3.14 STATIC TAP SPACING - CIRCULAR JETS

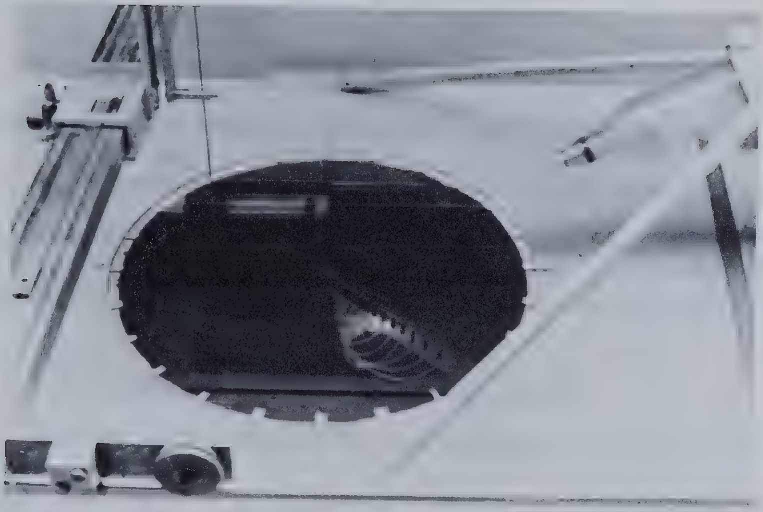

FIGURE 3.15 PLATE AND TAPS-OBLIQUE IMPINGEMENT

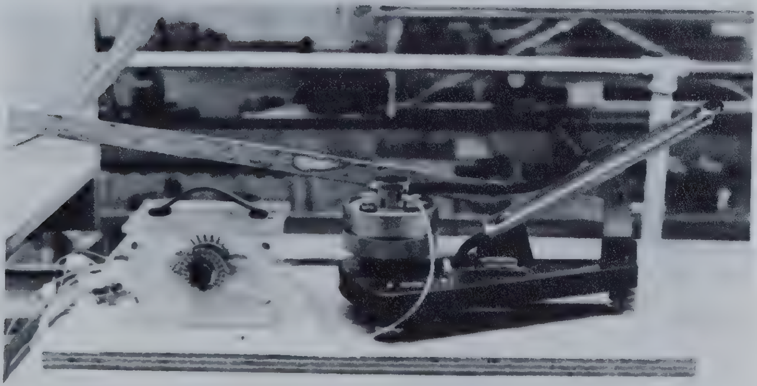

FIGURE 3.16 VALVE AND MANOMETER

Figure 3.16 shows this arrangement.

In the impingement region, a thin boundary layer grows on the wall beginning at the stagnation point. The maximum velocity in the vertical, which occurs at the edge of the boundary layer, was measured using ordinary total head tubes and assuming that the static pressure at this location was equal to the wall pressure in the same vertical.

3.2.3 Measurement of Wall Shear Stress

Preston's technique (39) was employed to measure wall shear stress with the aid of the calibration curves given by Patel (40). This technique is briefly discussed below. For a Preston tube of external diameter d_o resting on a smooth boundary, if Δp is the difference between the total pressure indicated by the tube and the static pressure on the boundary, it could be shown that:

$$\frac{\Delta p {d_o}^2}{4\rho\nu^2} = F\left(\frac{\tau_o {d_o}^2}{4\rho\nu^2}\right) \qquad (3.5)$$

Setting $\Delta p_* = \Delta p {d_o}^2/4\rho\nu^2$ and $\tau_{o*} = \tau_o {d_o}^2/4\rho\nu^2$, Equation 3.5 becomes:

$$\Delta p_* = F\,(\tau_{o*}) \qquad (3.6)$$

Using the equations given by Patel (40) for different ranges of Δp_* and τ_{o*}, Equation 3.6 is plotted in Figure 3.17. This curve is normally valid for zero pressure gradient boundary layers. Certain limitations exist, therefore, when the pressure gradient is not zero, as is the case in the impingement region. Patel (40) suggests that in favourable pressure gradients use of the Preston technique will involve errors less than

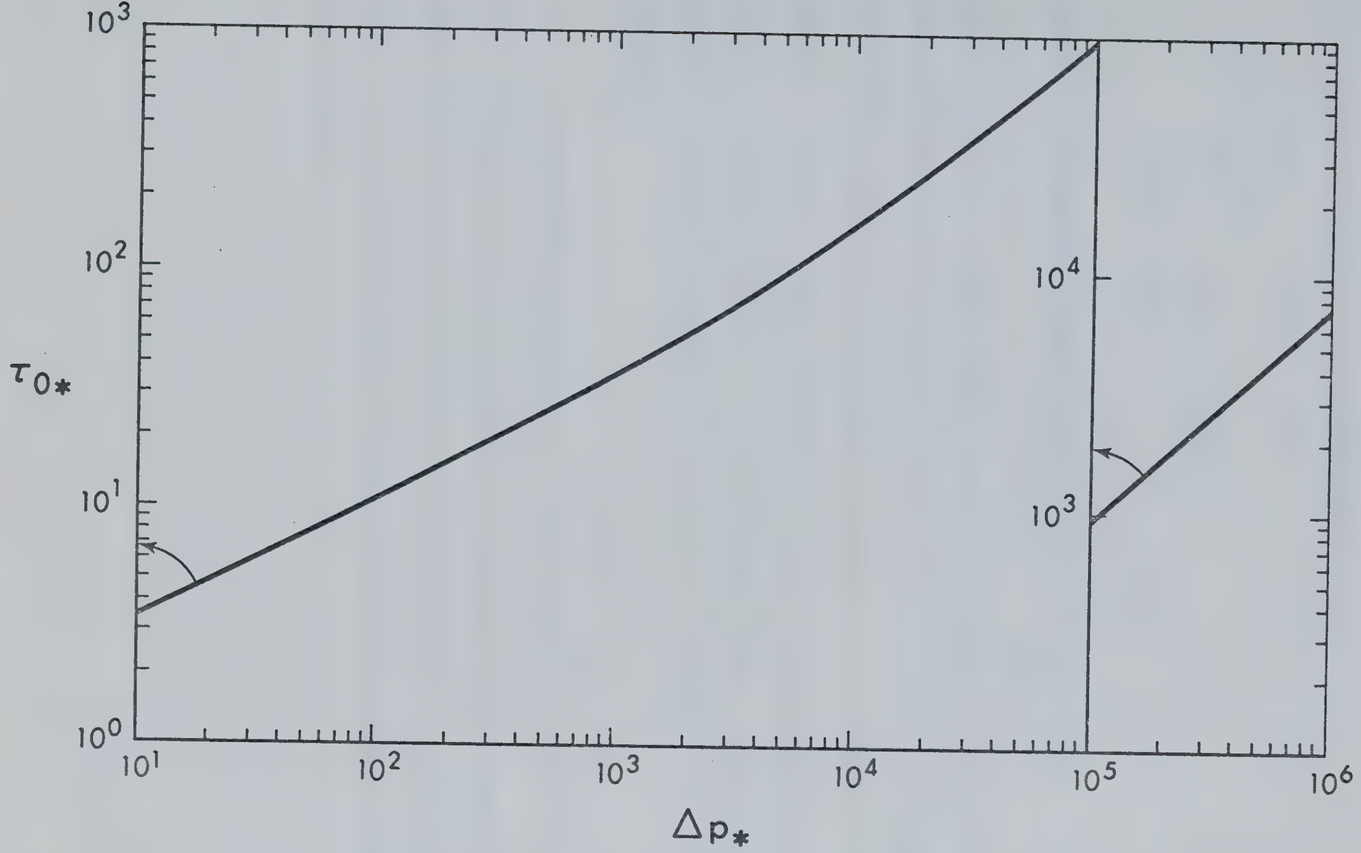

FIGURE 3.17 PATEL EQUATIONS FOR SMOOTH WALLS

6% if the following conditions are satisfied:

$$\text{(i)} \qquad 0 > \Delta > -0.007 \quad \text{or} \quad |\Delta| < 0.007$$

$$\text{(ii)} \qquad u_* d_o / \nu \leq 200 \tag{3.7}$$

$$\text{(iii)} \qquad \frac{d\Delta}{dx} < 0$$

where x is distance along the wall, and $\Delta \equiv \frac{\nu}{\rho u_*^3} \frac{dp}{dx}$; $u_* \equiv \sqrt{\tau_o / \rho}$

These criteria are rough guides rather than absolute restrictions. Condition (i) was derived empirically with the aid of fence readings. Condition (ii) ensures that the tube is located in the region of wall similarity. Condition (iii) is imposed to ensure that the flow is not subjected to re-laminarization. In the present case, the only physically plausible sequence of different flow states is firstly laminar and later turbulent.

Two total head tubes with outside diameters of 0.049 and 0.046 inches were used as Preston tubes in the present set of experiments. These tubes were also used for measuring velocities in the wall jet region, as the static pressure becomes equal to the ambient (atmospheric) in the wall jet.

CHAPTER IV - AXISYMMETRIC IMPINGEMENT

4.1 Introduction

A relatively simple case of impingement is studied in this chapter. Emphasis has been placed in exploring time-average flow characteristics in the impingement region. Data of previous investigators in the wall jet region are re-analyzed according to theoretical considerations outlined in Chapter II and the results are summarized.

4.2 Experiments and Experimental Results

The experimental set-up has been described in Chapter III. Two nozzles of internal diameters of 0.923 and 0.253 inches were used. The velocity at the nozzle was varied between 153 and 293 fps and in this range compressibility effects are known to be negligible. The nozzle Reynolds number R_o was in the range 10^4 to 10^5. The height H was varied from about 15 to 20 inches, thereby varying the ratio H/d from 21.2 to 65.7. On the whole, five experiments were conducted (see Table 4.1) and for description of various symbols see the definition sketch, Figure 4.1. The variation of the u-component of velocity with r at different x-stations, in regions I and II, is shown in Figure 4.2. These profiles are replotted in a dimensionless form in Figure 4.3. From Figure 4.3 it was found that for $\frac{x}{H}$ less than about 0.95, all profiles are described by one curve. (These profiles are said to be similar.) Further, this general curve could be given by the equation:

$$\frac{u}{u_c} = \exp\left(-\,0.693\,\eta_u^{\,2}\right) \qquad (4.1)$$

Run No.	H (in.)	d (in.)	U_o (fps)	H/d	$R_o = \frac{U_o d}{\nu}$	Measured Quantities		
						Region I	Region II	Region III
1	19.55	0.923	153.0	21.2	7.4×10^4	u, u_c, b_u	u, v, u_c, p p_c, b_u, b_p p_w, p_s	—
2	19.55	0.923	196	21.2	9.5×10^4	—	p_w, p_s	—
3	15.66	0.253	267	61.8	3.52×10^4	u, u_c, b_u	u, v, u_c p, p_c, b_u b_p, p_w, p_s	—
4	19.53	0.923	166	21.2	8.04×10^4	—	τ_o, p_w, p_s	τ_o
5	16.625	0.253	293	65.7	6.21×10^4	—	τ_o, p_w, p_s	τ_o

TABLE 4.1 DETAILS OF THE EXPERIMENTS

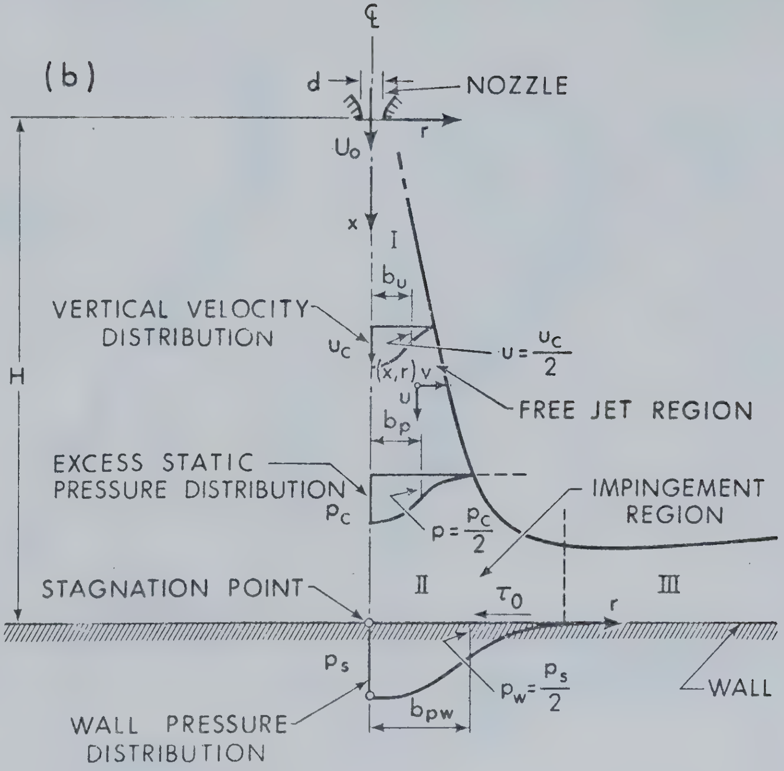
(b)
℄
d
NOZZLE
r
U_o
x
I
b_u
VERTICAL VELOCITY DISTRIBUTION
u_c
$u = \frac{u_c}{2}$
(x,r)
v
u
FREE JET REGION
b_p
EXCESS STATIC PRESSURE DISTRIBUTION
p_c
$p = \frac{p_c}{2}$
IMPINGEMENT REGION
H
STAGNATION POINT
II
τ_0
r
III
p_s
$p_w = \frac{p_s}{2}$
b_{pw}
WALL PRESSURE DISTRIBUTION
WALL

FIGURE 4.1 DEFINITION SKETCH

FIGURE 4.2 VELOCITY PROFILES IN REGIONS I AND II

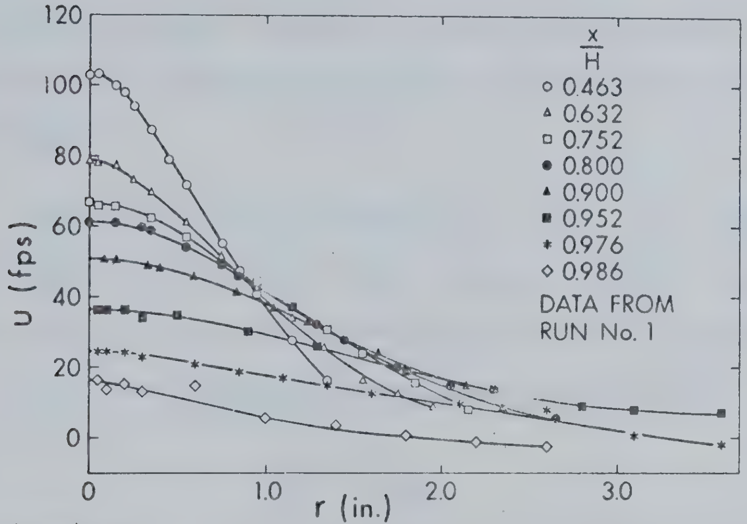

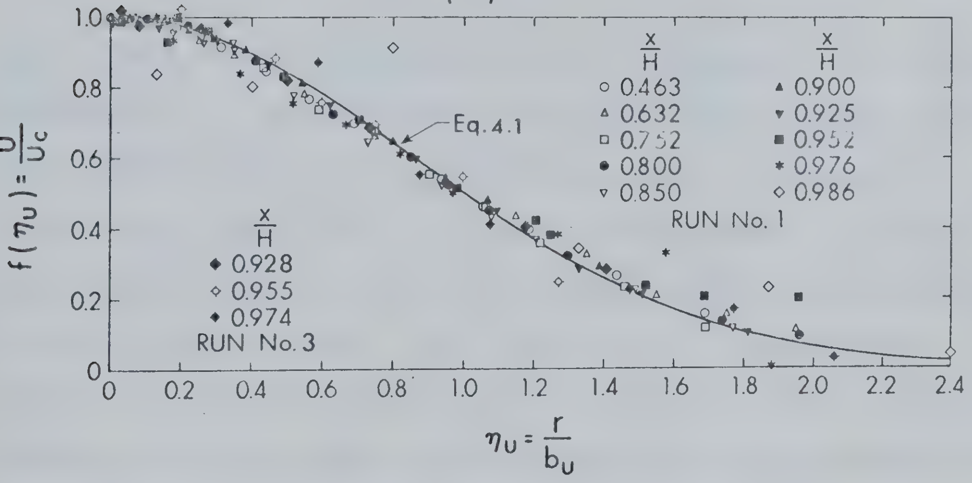

FIGURE 4.3 DIMENSIONLESS VELOCITY PROFILES IN REGIONS I AND II

where u_c is the maximum value of u at any x station, occurring at the centerline, $\eta_u \equiv r/b_u$ with b_u being the value of r where $u = \frac{1}{2} u_c$, and e is the Napierian base. The quantities u_c and b_u are generally known as the velocity and length scales. The data of Figure 4.3 are also well described by the Tollmien solution (28),(29). For values of x/H greater than 0.95, the velocity profiles are no longer similar.

The variation of the dimensionless scale u_c/U_o with x/d is shown in Figure 4.4. For x/H up to about 0.86, U_o/u_c increases linearly with x/d, (the virtual origin appears to be located at the nozzle itself) thus verifying the equation of the free jet:

$$\frac{u_c}{U_o} = \frac{C_1}{x/d} \tag{4.2}$$

where $C_1 = 6.8$ and 6.3 for runs 1 and 3 respectively. This type of variation for C_1 has been noticed before (29). The variation of the dimensionless length scale b_u/H with x/H is shown in Figure 4.5. For x/H up to about 0.86, b_u increases linearly with x, with a slope of 0.093, which is close to the generally accepted value of 0.096 for free circular jets (29). For $x/H \gtrsim 0.86$, b_u increases more rapidly, assuming a maximum value at $x/H \simeq 0.95$. For $x/H > 0.95$, b_u decreases, but in this region the velocity profiles are not similar and b_u is of little practical interest.

In the impingement region, the v component was also measured and Figure 4.6 shows that $\frac{\partial}{\partial r}$ (uv) is approximately independent of x for small values of r. This property is of importance in predicting

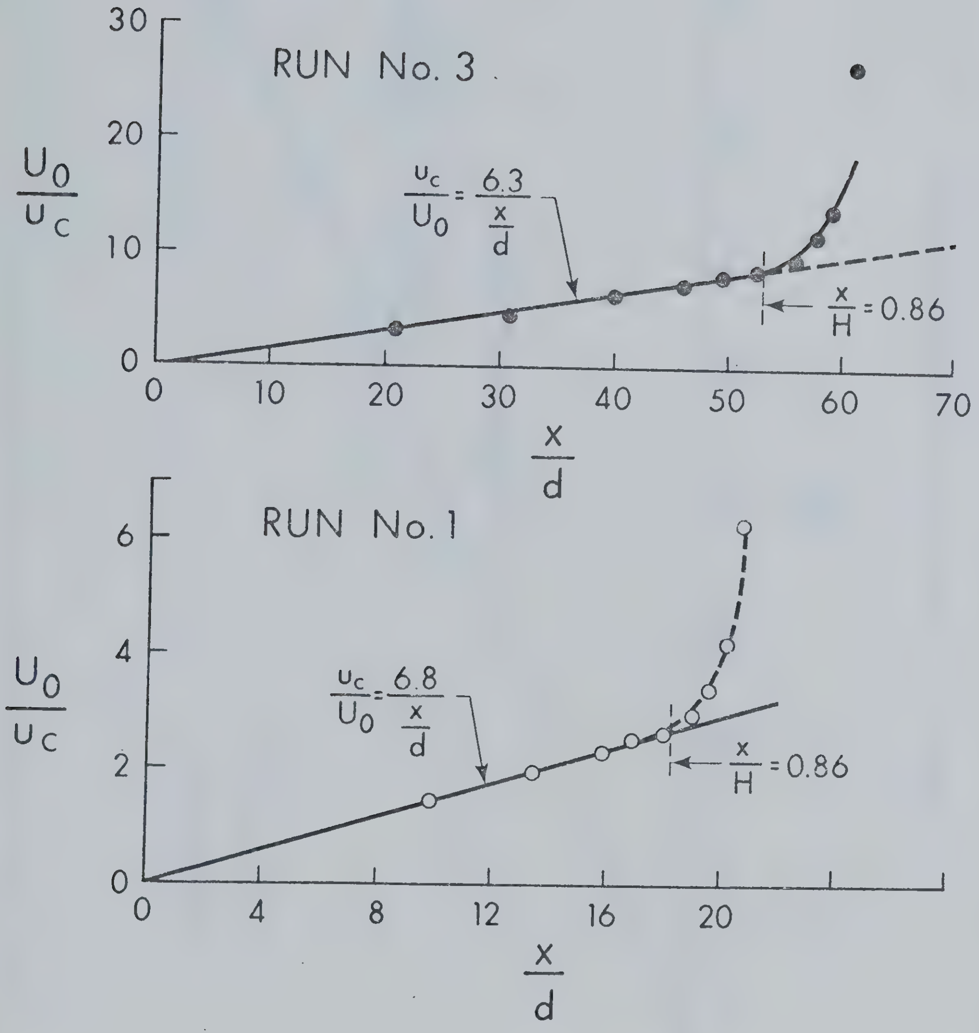

FIGURE 4.4 VELOCITY SCALE - REGIONS I AND II

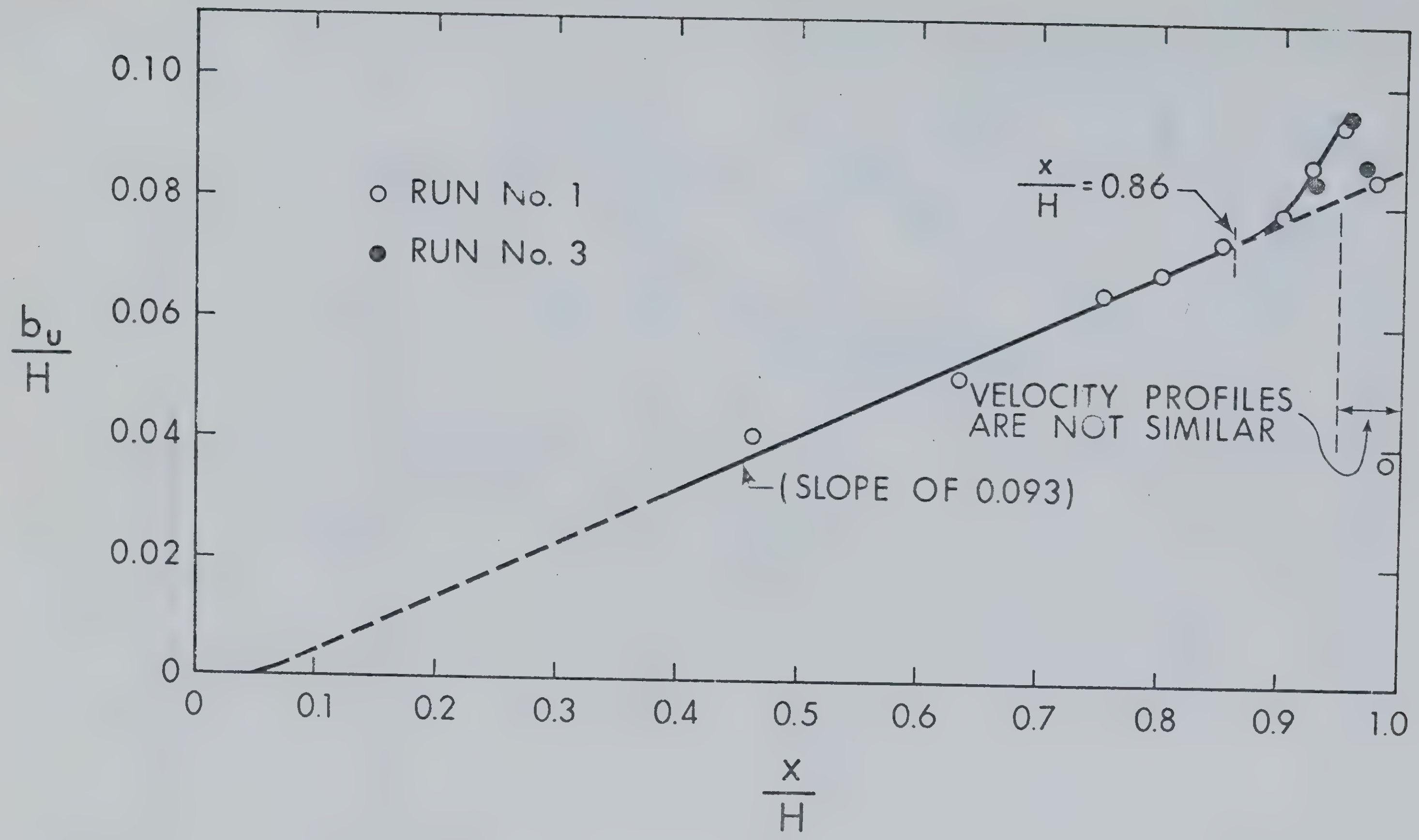

FIGURE 4.5 LENGTH SCALE FOR VELOCITY PROFILES

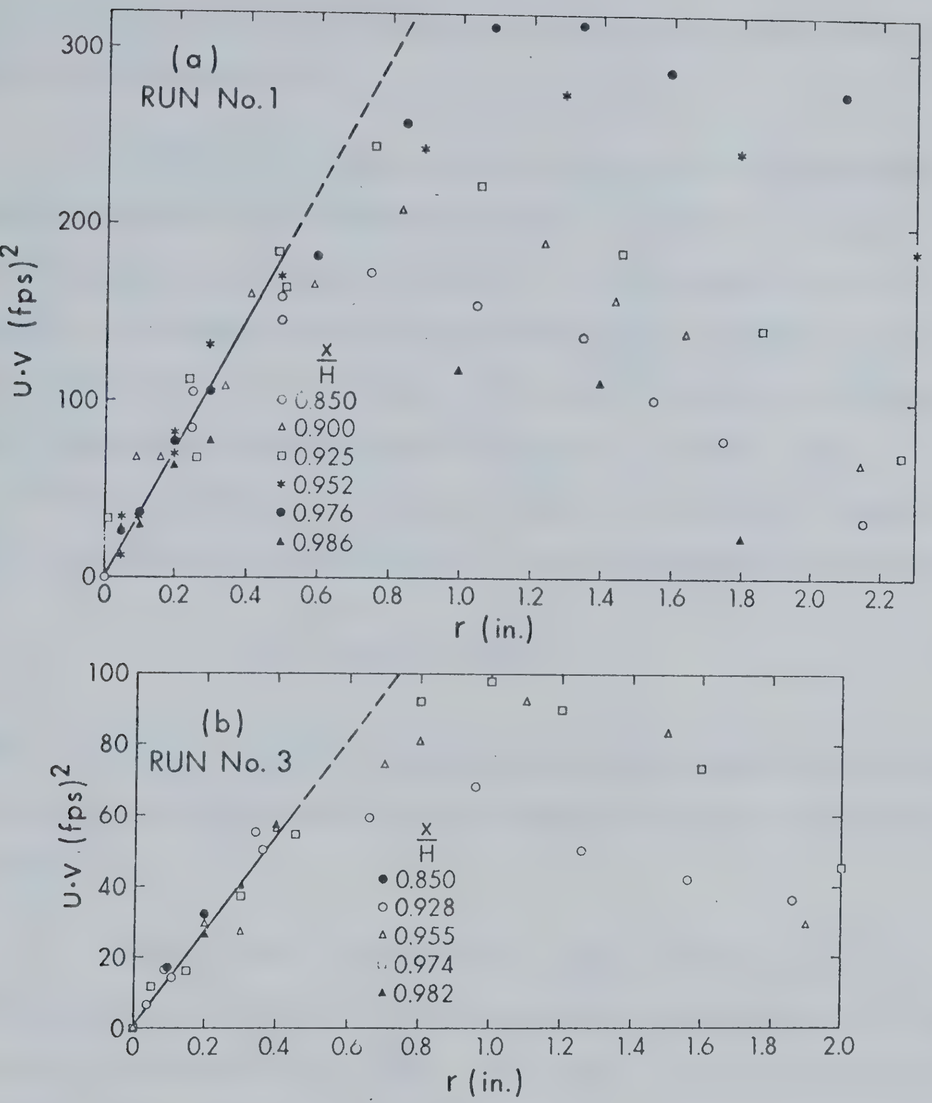

FIGURE 4.6 VARIATION OF uv WITH x AND r

u_c in region II and has been observed earlier by the author (25),(26) for plane impinging jets.

As mentioned before, the static pressure in the impingement region is greater than the ambient pressure and Figure 4.7(a) shows typical pressure profiles in region II. It is seen that for any x station, the pressure decreases continuously from a maximum value of p_c on the axis as r increases. The pressure profiles are replotted in a dimensionless form in Figure 4.8 with p/p_c versus r/b_p, b_p being the value of r where $p = \frac{1}{2} p_c$. It is seen from Figure 4.8 that the pressure profiles are similar and well described by the equation:

$$\frac{p}{p_c} = \exp\left(-\ 0.693\ \eta_p^{\ 2}\right) \tag{4.3}$$

where $\eta_p = r/b_p$. Figure 4.7(b) shows two typical pressure profiles on the wall. It was found that the wall pressures are also well described by Equation 4.3.

In runs 4 and 5, the wall shear stress was measured in the impingement region and Figure 4.9 shows typical variations of $u_*^{\ 2}$, where u_* is the shear velocity, $\sqrt{\tau_o/\rho}$. From Figure 4.9 it is seen that τ_o increases with r up to a maximum value of τ_{om} and then decreases with any further increase in r. When τ_o was replotted with τ_o/τ_{om} versus r/H as shown in Figure 4.10, it was found that the results of runs 4 and 5 and those of Bradshaw and Love (10) are described by one curve for r/H less than about 0.2. This aspect is discussed in greater detail later.

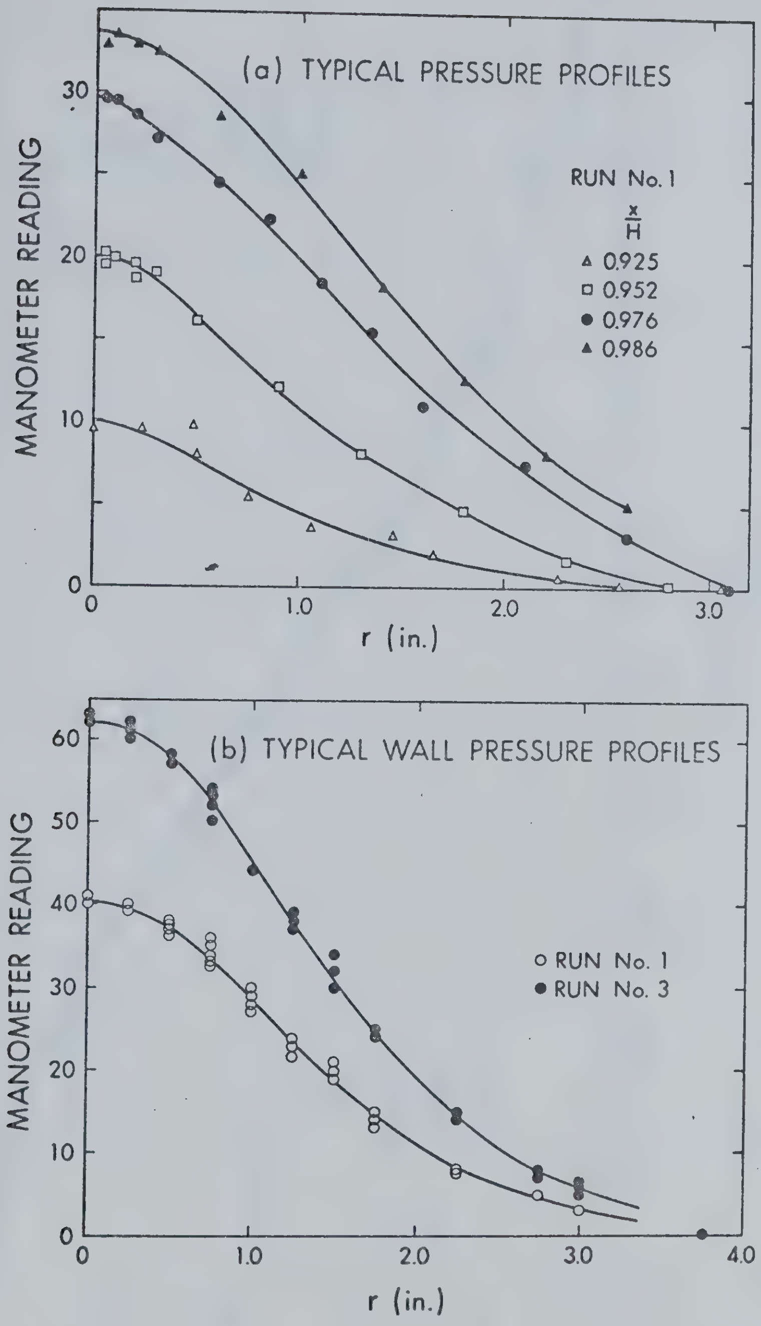

FIGURE 4.7 TYPICAL PRESSURE PROFILES - REGION II

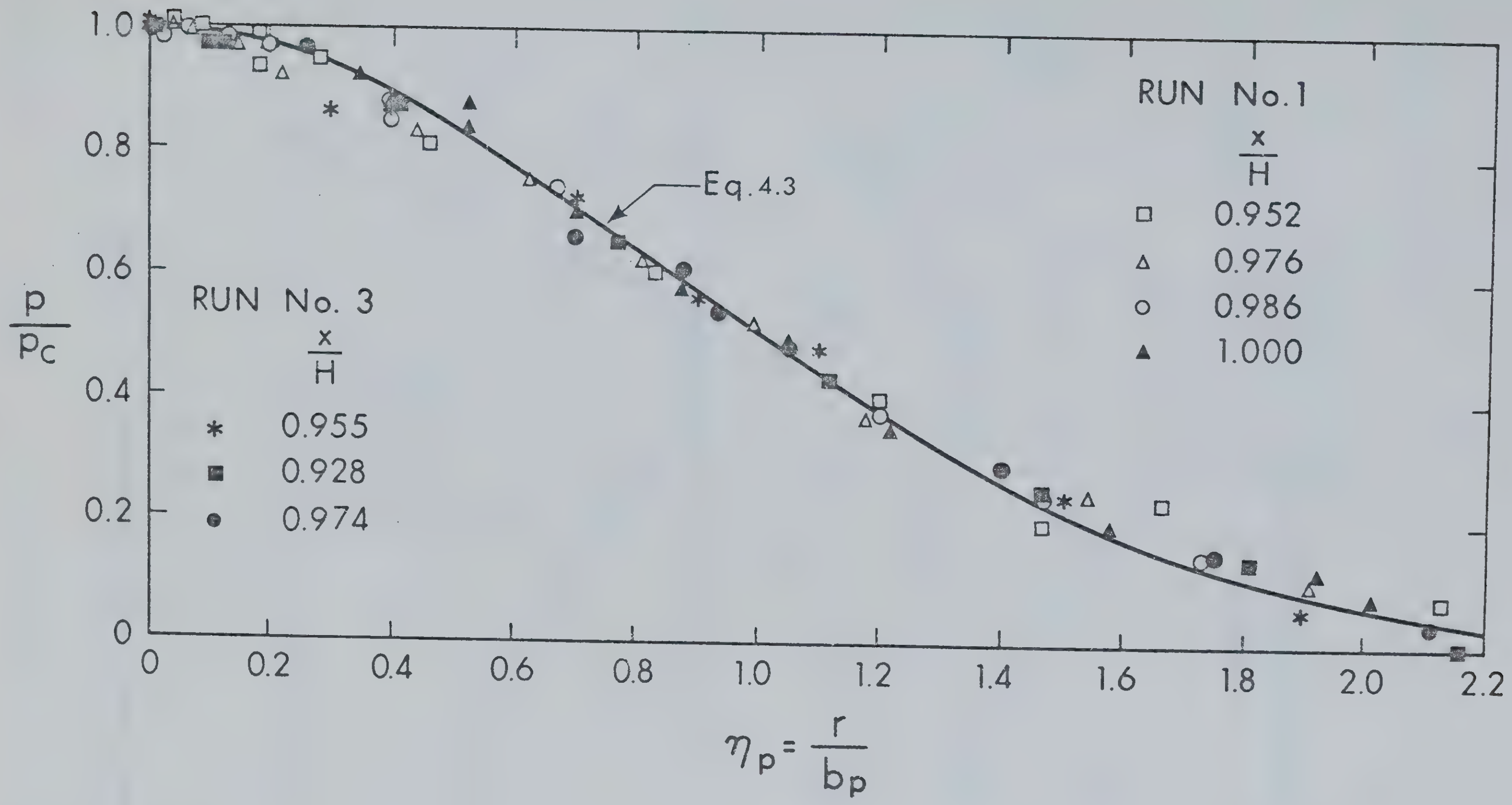

FIGURE 4.8 DIMENSIONLESS PRESSURE PROFILES

FIGURE 4.9 WALL SHEAR STRESS VARIATIONS

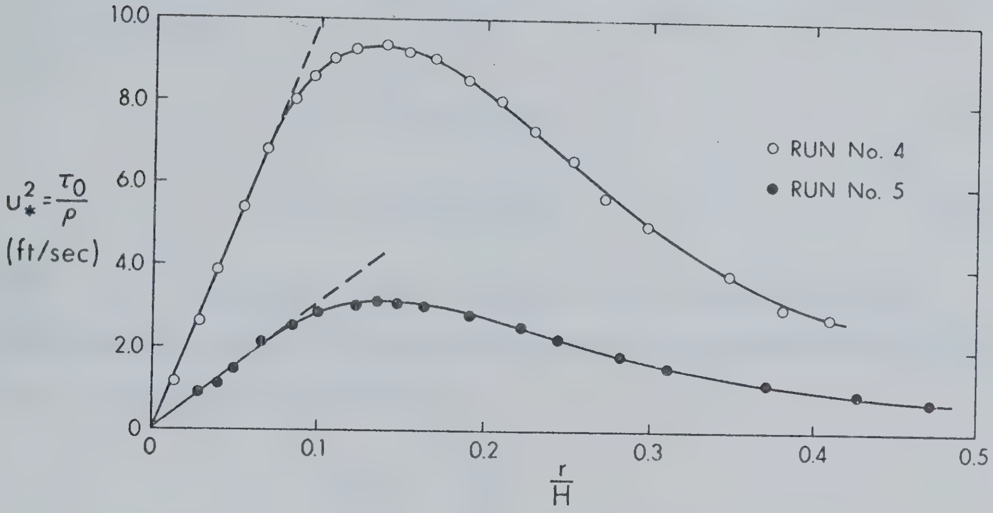

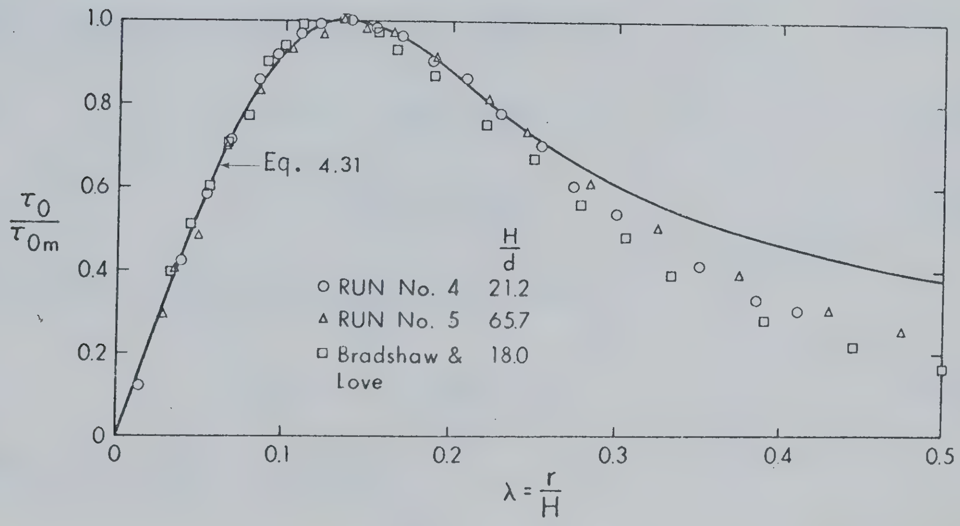

FIGURE 4.10 DIMENSIONLESS WALL SHEAR STRESS

4.3 Analysis of Results

4.3.1 Impingement Region

For the free circular jet it is well known (28),(29),(36) that one could write:

$$u_{cf} = f_1 (M_o, \rho, x) \qquad (4.4.a)$$

$$b_{uf} = f_2 (M_o, \rho, x) \qquad (4.4.b)$$

where M_o is the momentum flux from the nozzle, equal to $\rho \frac{\pi}{4} d^2 U_o^2$. Using the principles of 'Dimensional Analysis' one could reduce Equation 4.4.a to the form of Equation 4.2:

$$\frac{u_{cf}}{U_o} = \frac{C_1}{x/d}$$

For the impinging circular jet, one could write:

$$u_c = f_3 (M_o, \rho, x, H) \qquad (4.5.a)$$

$$b_u = f_4 (M_o, \rho, x, H) \qquad (4.5.b)$$

Equation 4.5.a could be reduced to the form:

$$\frac{u_c}{U_o} \frac{x}{d} = f_5 \left(\frac{x}{H}\right) \qquad (4.6)$$

Combining Equations 4.2 and 4.6:

$$\frac{u_c}{u_{cf}} = \frac{f_5 (x/H)}{C_1} = f_6 \left(\frac{x}{H}\right) \qquad (4.7)$$

The experimental results shown in Figure 4.11 agree with the formulation in Equation 4.7. The beginning of the impingement region could be

FIGURE 4.11 VARIATION OF u_c/u_{cf}

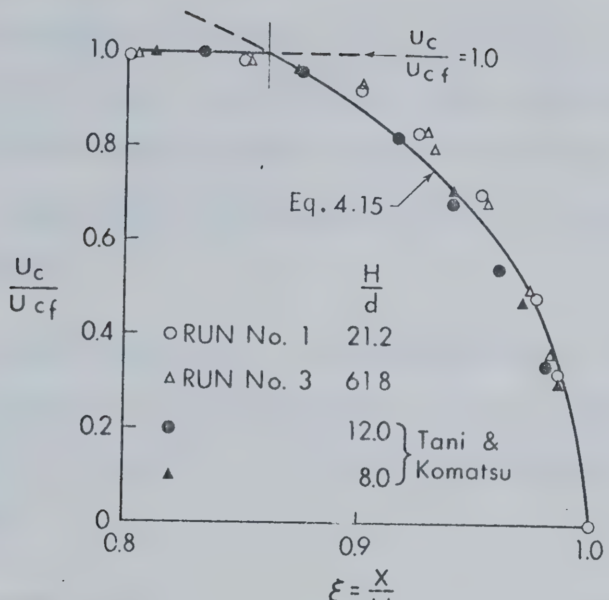

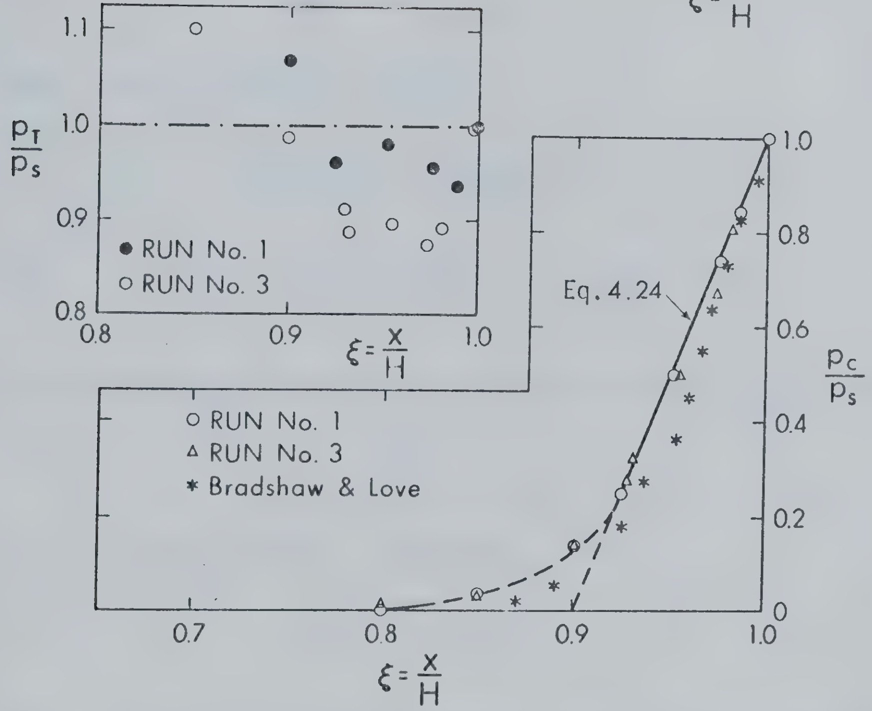

FIGURE 4.12 VARIATION OF p_c/p_s AND p_T/p_s

arbitrarily fixed at that value of x/H where u_c/u_{cf} is equal to, say, 0.98 (or some other convenient value). The start of region II could in principle be fixed from pressure considerations also; but it was found that, since the pressure data scatter more than the velocity data, the velocity criterion is superior.

The functional form of Equation 4.7 is evaluated below. In the impingement region, from Figure 4.7, it was found that $\frac{\partial}{\partial r}(uv)$ does not depend upon x for small values of r. That is, in the neighbourhood of the axis of the jet:

$$(uv) = g_1 (r) \tag{4.8}$$

which could be reduced to the form:

$$g_2 (r) = \frac{1}{r} \frac{\partial}{\partial r} (ruv) \tag{4.9}$$

and
$$g_2 (o) = \left[\frac{1}{r} \frac{\partial}{\partial r} (ruv)\right]_{r = o} = \text{constant} \tag{4.10}$$

Using the equation of continuity, Equation 4.10 can be re-written as:

$$- \frac{d}{dx} \left(\frac{u_c^2}{2}\right) = g_2 (o) = K \tag{4.11}$$

where K is a constant. Integrating:

$$u_c^2 = - 2Kx + K_1 \tag{4.12}$$

where K_1 is an integration constant. Using the formulation of Equation 4.6, Equation 4.12 could be written as:

$$\frac{u_c}{U_o} = K_2 \sqrt{(1 - \xi) + K_3} \tag{4.13}$$

where $K_2 = \sqrt{\frac{2KH}{U_o^2}}$, $K_3 = \frac{K_1}{2KH} - 1$ and $\xi = \frac{x}{H}$. Combining Equations 4.2 and 4.13:

$$\frac{u_c}{u_{cf}} = K_4 \, \xi \sqrt{(1 - \xi) + K_3} \qquad (4.14)$$

where $K_4 = \frac{K_2}{C_1} \frac{H}{d}$.

The present experimental results and those of Tani and Komatsu (15) were used to evaluate K_4 and K_3. It was found that $K_4 \simeq 3.10$ and $K_3 \simeq 0$. With these values, Equation 4.14 becomes:

$$\frac{u_c}{u_{cf}} = 3.10 \, \xi \sqrt{(1 - \xi)} \qquad (4.15)$$

This is shown plotted in Figure 4.11, along with the experimental observations. This curve intersects the $u_c = u_{cf}$ line at $x/H \simeq 0.86$ and this value of x/H is conveniently taken to denote the end of region I and the beginning of region II. Recalling Equation 4.13, it is easy to verify that with a value of $K_3 = 0$ the gradient of u_c at the wall will be infinite. This is physically unacceptable and, therefore, it must be understood that Equation 4.15 cannot apply very near the wall. Rather, one could expect that the irrotational variation ($u_c \propto (H - x)$) would be more reliable when x approaches H. The available data are not sufficiently close to the wall to permit verification of these considerations, however, they do indicate that an irrotational range would not extend further than about 2% of H above the wall.

For the impingement region, considering the axial pressure

excess: $$p_c = g_4 (M_o,\rho,H,x) \tag{4.16}$$

Equation 4.16 could be reduced to the form:

$$\frac{p_c}{\rho U_o^2} \left(\frac{H}{d}\right)^2 = g_5 (x/H) \tag{4.17}$$

and further:

$$\frac{p_s}{\rho U_o^2} \left(\frac{H}{d}\right)^2 = g_5 (1.0) = \text{constant} = K_p \tag{4.18}$$

where p_s is the stagnation pressure. Combining Equations 4.17 and 4.18:

$$\frac{p_c}{p_s} = \frac{g_5 (x/H)}{K_p} = g_6 (x/H) \tag{4.19}$$

The experimental observations shown in Figure 4.12 support the functional form of Equation 4.19.

Regarding the constant K_p, the present experimental results give an average value of 24.7. Previous works indicate values of 24.2, 30.2, 24.0 and 26.1 (Refs. 10, 11, 22 and 23 respectively). Taking an overall average experimental value of K_p as 26, the stagnation pressure is given by:

$$\frac{p_s}{\rho U_o^2} = 26/\left(\frac{H}{d}\right)^2 \tag{4.20}$$

Further, the length scale for pressure could be written as:

$$\frac{b_p}{H} = f_7 \left(\frac{x}{H}\right) \tag{4.21}$$

The experimental results plotted in Figure 4.13 support this formulation. The value of b_p at the wall is $b_{pw} = 0.078$ H. Since the wall pressure profiles agreed with Equation 4.3, one could now transform this equation to the more convenient form:

$$p_w/p_s = \exp(-114\lambda^2) \qquad (4.22)$$

where $\lambda = r/H$. This is compared with experimental results in Figure 4.14 where it is seen that p_w approaches zero at $r \simeq 0.22$ H, which could be conveniently taken as the end of the impingement region. Equating the wall pressure integral to the initial momentum of the jet, the theoretical value of K_p will be 28.5 which agrees with the average experimental value of 26.

In this section a simple method is developed to evaluate the functional form of Equation 4.19. In the impingement region, assuming that the total axial pressure p_T remains constant and equal to p_s (see the inset of Figure 4.13), one could write:

$$p_c = p_s - \frac{\rho u_c^2}{2} \qquad (4.23)$$

Using Equations 4.15 and 4.20, Equation 4.23 is reduced to the form:

$$\frac{p_c}{p_s} = 10\,\xi - 9 \qquad (4.24)$$

where the coefficients have been evaluated using the present experimental results. Figure 4.12 shows that Equation 4.24 is satisfactory for x/H greater than about 0.92. The experimental points of Bradshaw and Love (read from their contour plots) lie somewhat below the plot of Equation

FIGURE 4.13 LENGTH SCALE FOR PRESSURE PROFILES

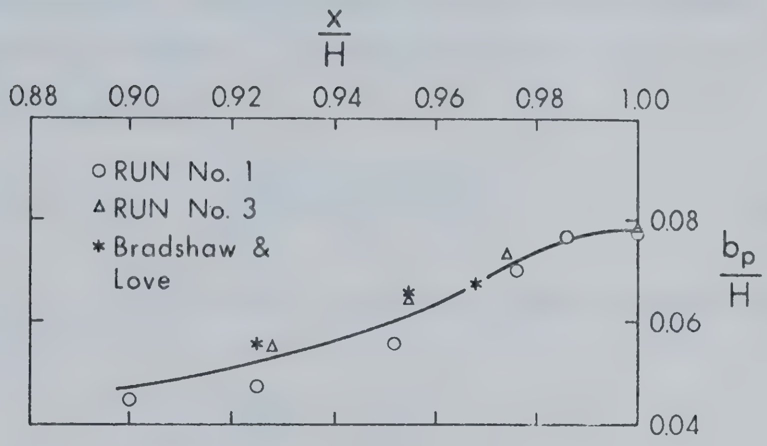

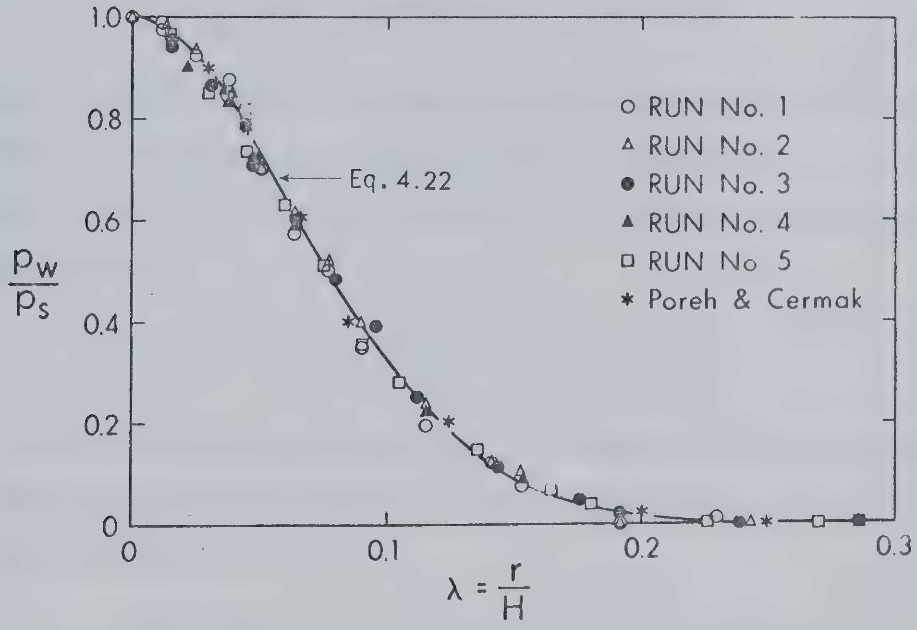

FIGURE 4.14 DIMENSIONLESS WALL PRESSURE

4.24.

The variation of the wall shear stress in the impingement region is predicted as follows. Consider the Reynolds equation of motion in the x-direction:

$$u \frac{\partial u}{\partial x} + v \frac{\partial u}{\partial r} = \frac{1}{\rho} \frac{\partial \sigma_x}{\partial x} + \frac{1}{\rho r} \frac{\partial (r \tau_{rx})}{\partial r} \qquad (4.25)$$

where σ_x and τ_{rx} are the total, normal and tangential stresses respectively, i.e.:

$$\begin{aligned} \sigma_x &\equiv -(\overline{p} + \rho \overline{u'^2}) + 2\mu \frac{\partial u}{\partial x} \\ \tau_{rx} &= \tau_{rx} \text{ (laminar)} + \tau_{rx} \text{ (turbulent)} \end{aligned} \qquad (4.26)$$

where the prime denotes fluctuation and the overbar denotes time-averaged value. Assuming that near the wall the measured pressure p is approximately equal to the sum of time-average static pressure and the normal stress, then:

$$\sigma_x \simeq -p + 2\mu \frac{\partial u}{\partial x} \qquad (4.27)$$

An order of magnitude analysis shows (see Appendix D) that the viscous term is negligible in comparison to p, hence Equation 4.25 can be finally simplified to:

$$u \frac{\partial u}{\partial x} + v \frac{\partial u}{\partial r} = -\frac{1}{\rho} \frac{\partial p}{\partial x} + \frac{1}{\rho r} \frac{\partial (r \tau_{rx})}{\partial r} \qquad (4.28)$$

At $x = H$, the inertial terms vanish, hence:

$$\left[\frac{1}{r} \frac{\partial}{\partial r} (r \tau_{rx}) \right]_{x = H} = \left(\frac{\partial p}{\partial x} \right)_{x = H} \qquad (4.29)$$

But $\tau_{rx} = \tau_{xr}$ and:

$$\left[\frac{1}{r}\frac{\partial}{\partial r}(r\tau_{rx})\right]_{x=H} = \left[\frac{1}{r}\frac{\partial}{\partial r}(r\tau_{xr})\right]_{x=H} = \frac{1}{r}\frac{d}{dr}(r\tau_o)$$

Hence:

$$\tau_o = \int_o^r r\left(\frac{\partial p}{\partial x}\right)_{x=H} dr \tag{4.30}$$

Using the previous findings on pressure distribution, it can be shown (see Appendix D) that the wall shear stress is given by:

$$\frac{\tau_o}{\tau_{om}} = 0.18\,\frac{1 - \exp(-114\,\lambda^2)}{\lambda} - 9.43\,\lambda\,\exp(-114\,\lambda^2) \tag{4.31}$$

where the maximum shear stress, τ_{om}, is given by the expression:

$$\tau_{om} = 0.16\,\rho U_o^2\left(\frac{d}{H}\right)^2 \tag{4.32}$$

and it occurs at $\lambda \simeq 0.14$.

Figure 4.10 shows that Equation 4.31 agrees with the available data so long as $\lambda \lesssim 0.22$. Returning to the neglect of the viscous term from Equation 4.27, it may be argued that its vertical gradient may not be negligible in comparison to the vertical gradient of -p. If this were the case then the coefficient 0.16 in Equation 4.32 would not be constant, but it would depend upon R_o (as can also be verified by dimensional analysis). However, the experimental results show that no dependence upon R_o exists, at least within the range $60{,}000 \lesssim R_o \lesssim 180{,}000$. (This includes the present data and those of Bradshaw and Love (10)). The reason for this result can be traced to the strong turbulence

near the stagnation point, as was outlined in Chapter II.

Considering the boundary layer at the wall, and the maximum value, v_m, of the radial velocity, in any vertical, which occurs at the edge of the boundary layer, $(z = \delta)$, it is of interest to study its variation with r. Dimensional analysis will show that:

$$\frac{v_m}{U_o} \frac{H}{d} = f_8 (\lambda) \tag{4.33}$$

The available data are shown plotted in this form in Figure 4.15, which confirms Equation 4.33. Assuming the Bernoulli equation to hold, it can be shown that:

$$\frac{v_m}{U_o} \frac{H}{d} = \sqrt{2K_p} \left(1 - \frac{p_w}{p_s}\right)^{1/2} \tag{4.34}$$

Equation 3.34 is seen in Figure 4.15 to agree with the data only for the lower values of λ (i.e., $\lambda \lesssim 0.03$). For estimating v_m, the empirical curve drawn through the data (solid line) is more reliable. For values of λ less than about 0.03, Equation 4.34 applies, and recalling Equation 4.22 it is possible to show that in this range v_m can be approximated by:

$$(v_m)_{\lambda \leq 0.03} = \left(\sqrt{228K_p} \frac{U_o d}{H^2}\right) r \tag{4.35}$$

This equation will be compatible with axisymmetric stagnation flow considerations if the constant a (Equation 2.1, Section 2.1) is taken as:

$$a = \sqrt{228K_p} \frac{U_o d}{H^2} \tag{4.36}$$

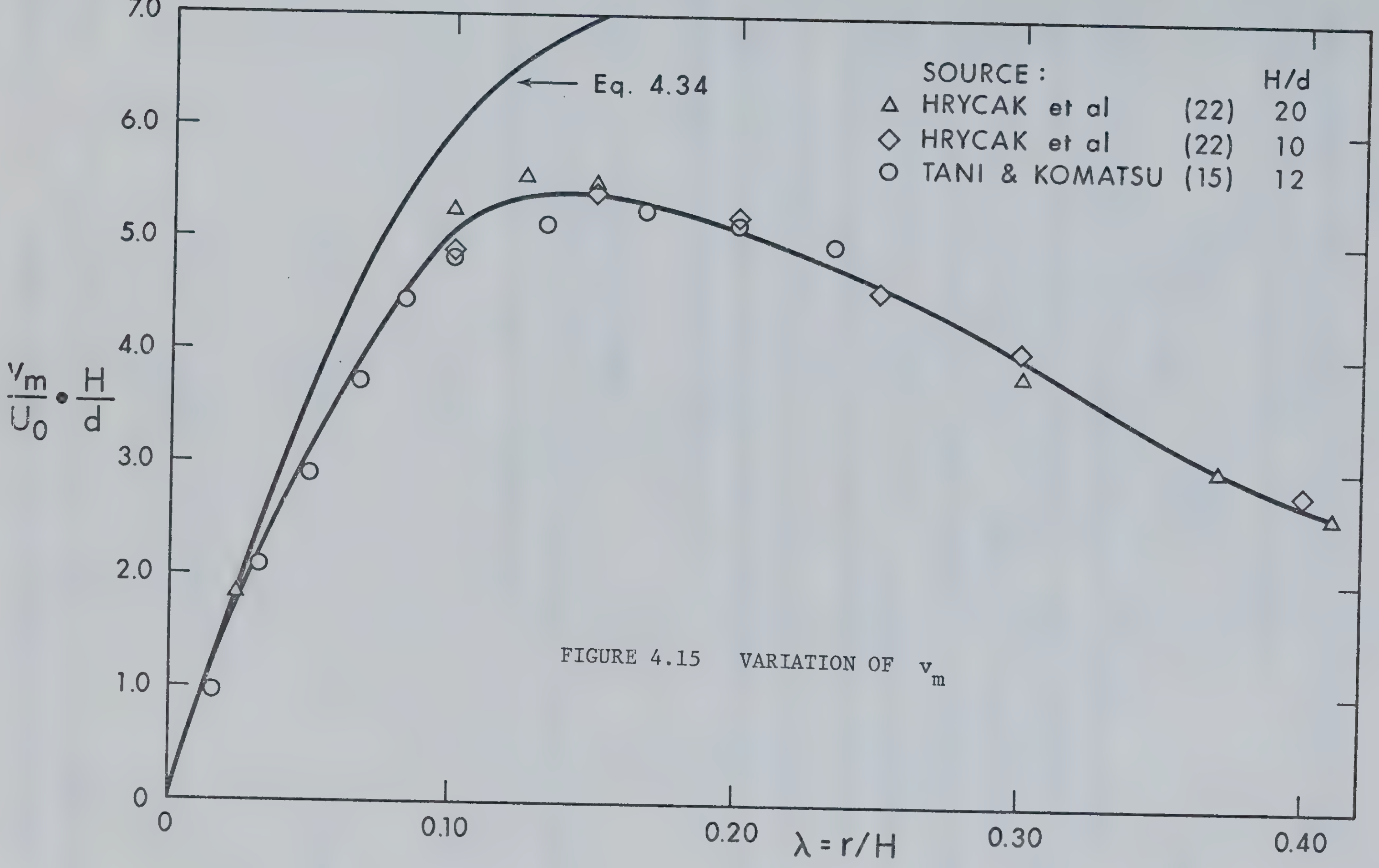

FIGURE 4.15 VARIATION OF v_m

Substituting this into Equation 2.5 (Chapter II) the boundary layer thickness near the stagnation point will be given by:

$$\left(\frac{\delta}{H}\right)_{\lambda \leq 0.03} = \frac{0.225}{\sqrt{R_o}} \qquad (4.37)$$

The data of Hrycak et al (22) are re-plotted in a different form in Figure 4.16. It is seen that initially $\frac{\delta}{H}$ remains approximately constant and equal to about 1.92×10^{-3}. Using $R_o = 54{,}000$, Equation 4.37 will give 0.97×10^{-3}, i.e., about one-half of the measured value. This is not surprixing in view of previous considerations which point to a turbulent boundary layer. The work of Wolfshtein (37) on turbulent stagnation flow shows that if the boundary layer is turbulent, its thickness will be larger than the corresponding laminar value by a factor which depends on the intensity of turbulence.

4.3.2 Wall Jet Region

No data were taken in the wall jet region. However, theoretical considerations (see Chapter II) showed that:

$$\delta_2 = C_2 \, \bar{r}$$

$$\frac{u_m}{U_o} = \frac{C_u}{\bar{r}/d} \qquad (4.38)$$

$$C_f = \frac{\tau_o}{\rho u_m^2/2} = C_f \, (R_o)$$

where $\bar{r}$ is to be measured from a virtual origin, and C_f should be independent of r. Consider first the data of Bradshaw and Love (10). To

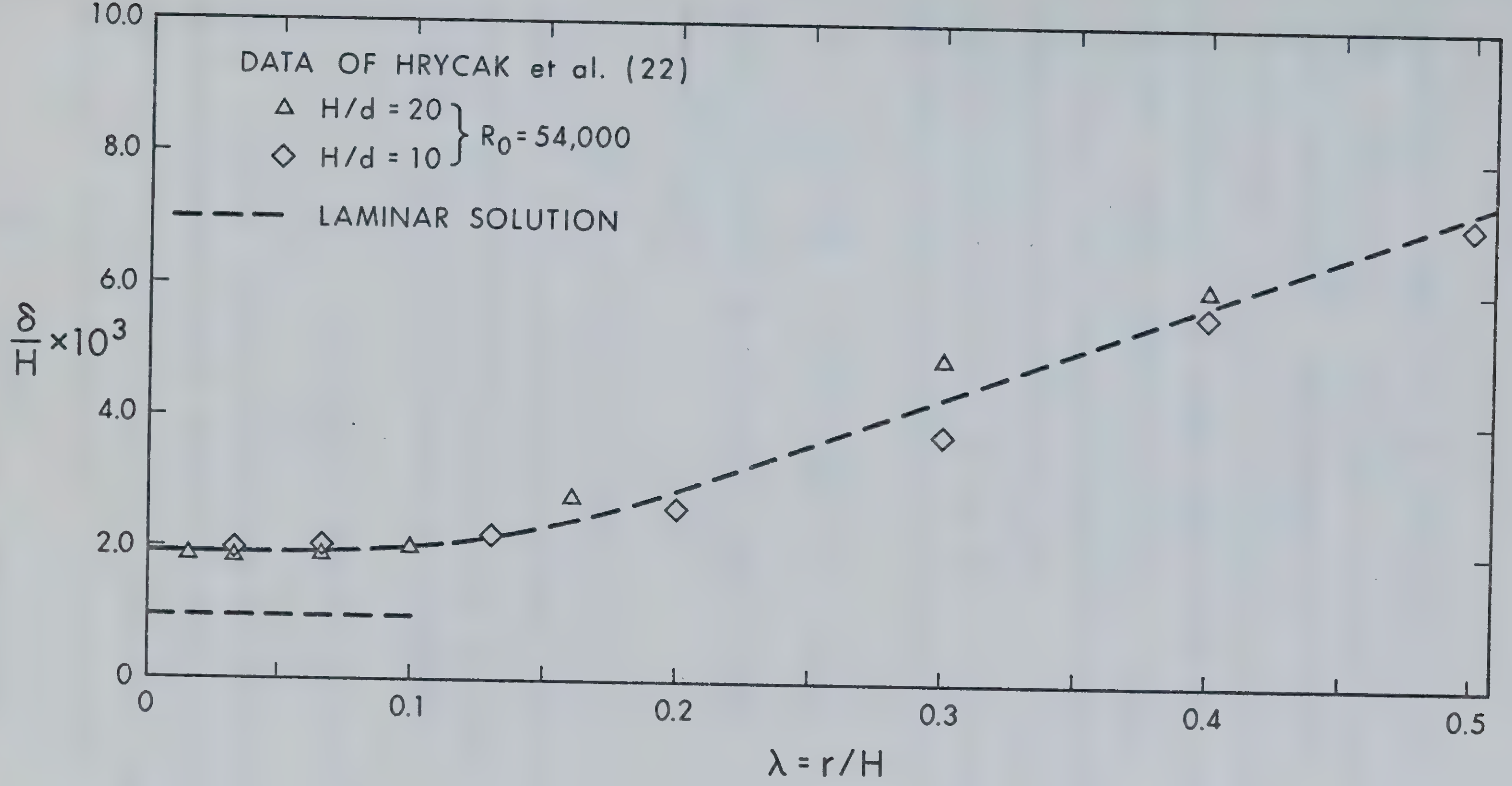

FIGURE 4.16 BOUNDARY LAYER THICKNESS - REGION II

obtain C_2, the data on δ_2 are re-plotted in the form δ_2/H vs r/H in Figure 4.17. Poreh, Tsuei and Cermak (17) gave the relation $\delta_2/H = 0.098\ (r/H)^{0.9}$, which describes their data well. The value of r/H was between 0.5 and 2.5. This relation is also plotted in Figure 4.17 and is seen to give somewhat higher values than those of Bradshaw and Love. Finally, Hrycak et al (22) gave the relation $\delta_2/d = K(r/d)^{0.95}$ for values of r/d ranging from about r to 40. The constant K was 0.0945 for $H/d = 10$ and 0.1025 for $H/d = 20$. This relation is also plotted for the values $H/d = 10$ and $H/d = 20$ in Figure 4.17. The data show that they can be described well by the straight line:

$$\frac{\delta_2}{H} = 0.0792\ (\frac{r}{H} + 0.17) \quad \text{average} \qquad (4.39)$$

i.e., $C_2 = 0.0792$ and the virtual origin is located $0.17\ H$ behind the stagnation point.

For the velocity scale, if the reciprocal of u_m is plotted against r, then a straight line would result. The data of Bradshaw and Love are replotted in the form U_o/u_m vs r/d in Figure 4.18, where the resulting straight line is described by the equation:

$$\frac{u_m}{U_o} = \frac{1.052}{(r/d - 1.8)} \quad \text{(Bradshaw and Love)}$$

i.e., $C_u = 1.052$ and the virtual origin for velocities is located 1.8 d after the stagnation point. Hrycak et al gave the equation $u_m/U_o = 1.4\ (r/d)^{-1.12}$ which is also plotted in Figure 4.18. Again, a straight line can fit the data reasonably well. This results in:

$$\frac{u_m}{U_o} = \frac{0.94}{(r/d - 1.0)} \quad \text{(Hrycak et al)}$$

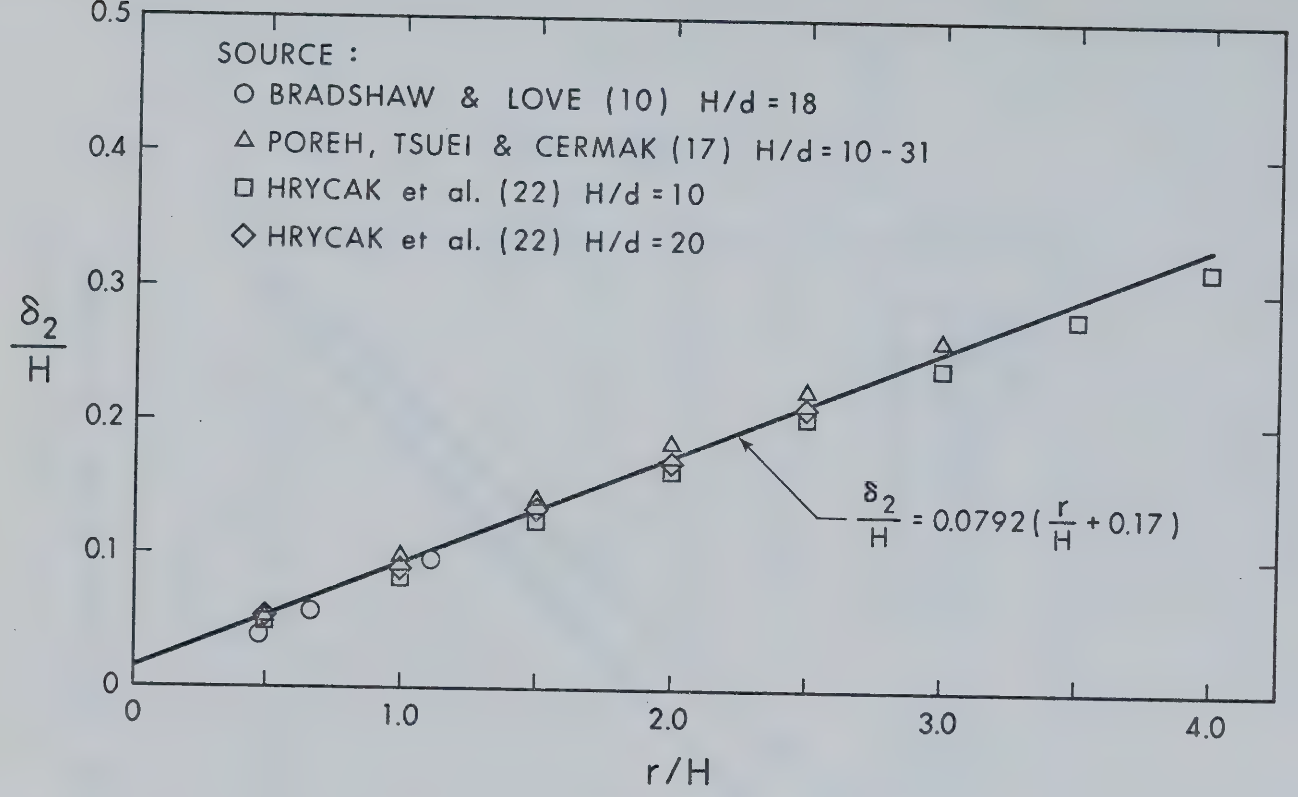

FIGURE 4.17 LENGTH SCALE, WALL JET REGION

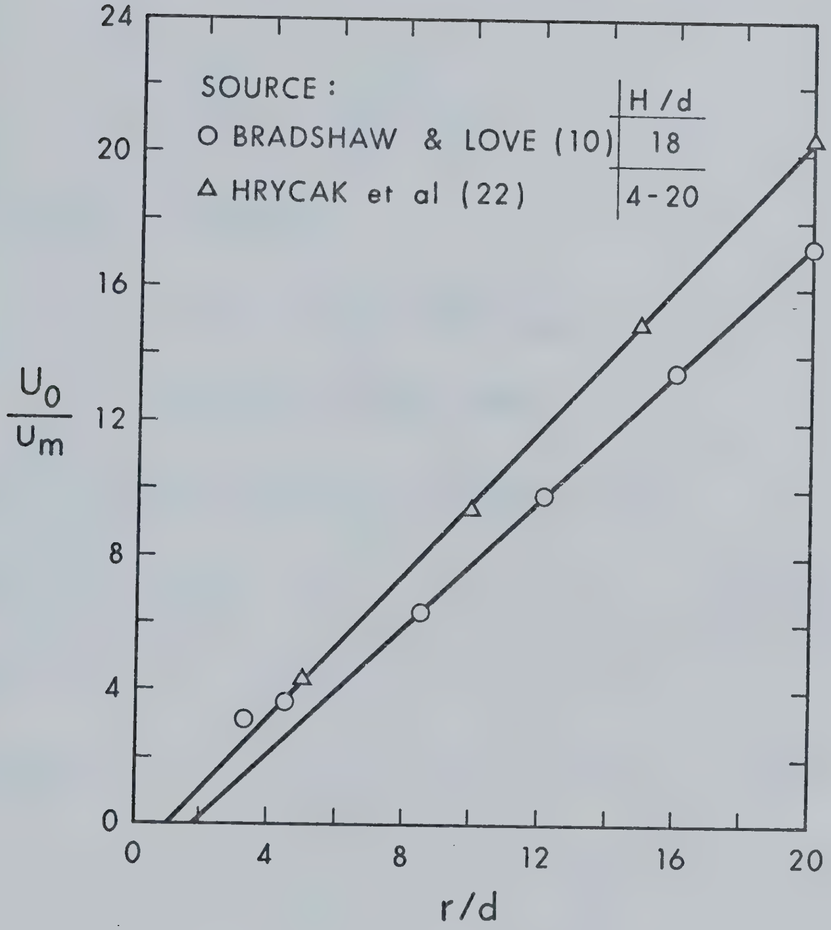

FIGURE 4.18 VELOCITY SCALE, WALL JET REGION

Finally, Poreh, Tsuei and Cermak gave the relation $u_m H/\sqrt{K} = 1.32 \, (r/H)^{-1.10}$, where K is the kinematic momentum of the jet at the nozzle (equal to $\pi d^2 U_o^2/4$). Figure 4.19 shows this relation re-plotted in the form $\sqrt{K}/u_m H$ vs r/H. The resulting straight line has the equation:

$$\frac{u_m H}{\sqrt{K}} = \frac{1.15}{(\frac{r}{H} - 0.14)}$$

which can also be written as:

$$\frac{u_m}{U_o} = \frac{1.02}{(r/d) - 0.14\ (H/d)}$$

(Poreh, Tsuei and Cermak)

The above re-analysis is summarized in Table 4.2 below.

Source	No. of Runs	R_o	H/d	C_u	Locus of Virtual Origin
Bradshaw and Love	1	182,000	18	1.052	+ 1.8 d
Poreh, Tsuei and Cermak	6	72,000 to 325,000	10 to 31	1.020	+ 0.14 H
Hrycak et al	4	—	4 - 20	0.940	+ 1.0 d
Average	11			1.004	+ 2 d

TABLE 4.2 VELOCITY SCALE - SUMMARY

Thus, the velocity scale can be finally written as:

$$\frac{u_m}{U_o} = \frac{1.004}{r/d - 2} \quad \text{(average)} \tag{4.40}$$

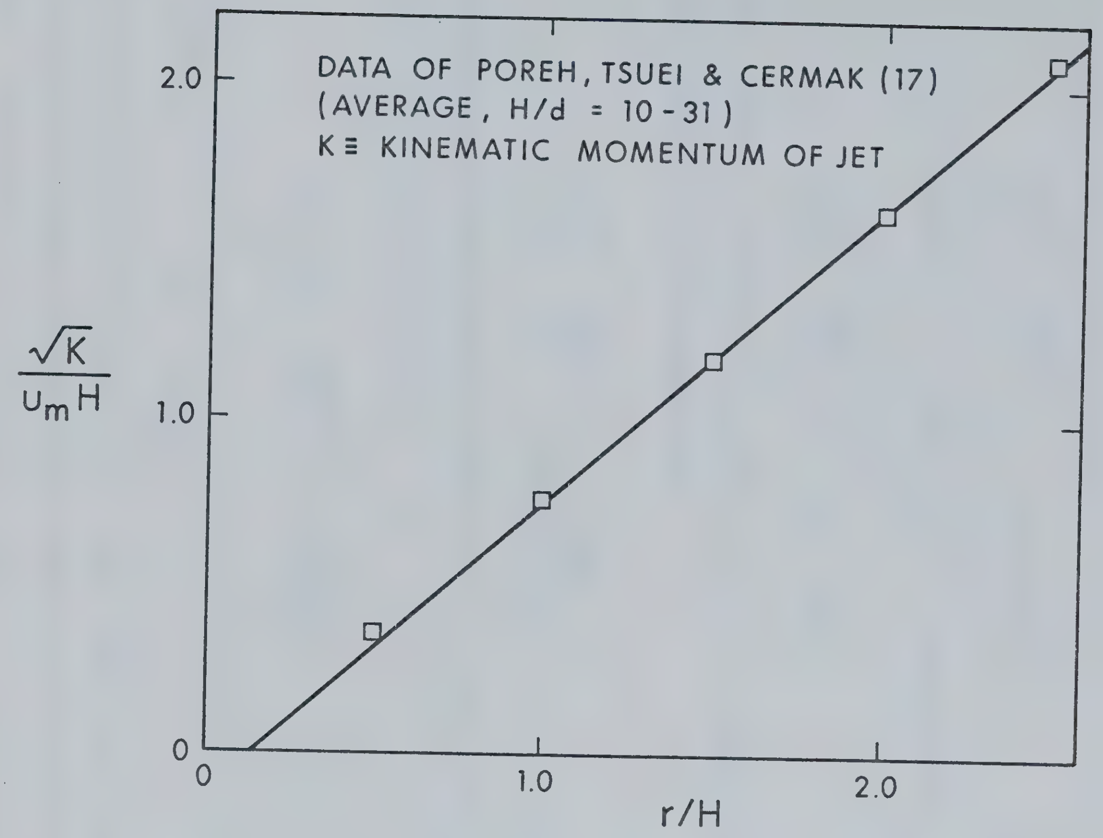

FIGURE 4.19 VELOCITY SCALE, WALL JET REGION

Considering now the friction factor C_f, Poreh, Tsuei and Cermak give the relation (which includes the data of Bradshaw and Love):

$$\frac{\tau_o H^2}{\rho K} \left(\frac{\sqrt{K}}{\nu}\right)^{0.3} = 0.3\ (r/H)^{-2.3}$$

If C_f is independent of r, then $\tau_o \propto r^{-2}$, and a plot of:

$$\left[\frac{\tau_o H^2}{\rho K} \left(\frac{\sqrt{K}}{\nu}\right)^{0.3}\right]^{-\frac{1}{2}} \quad \text{vs} \quad r/H$$

would result in a straight line. This is shown in Figure 4.20 where the drawn straight line has the equation:

$$\frac{\tau_o H^2}{\rho K} \left(\frac{\sqrt{K}}{\nu}\right)^{0.3} = \frac{0.209}{(r/H - 0.14)^2}$$

Recalling the relation found previously for u_m from the same authors, the above can also be written as:

$$\frac{1}{2} \frac{\tau_o}{\rho u_m^2/2} \left(\frac{\sqrt{K}}{\nu}\right)^{0.3} = \frac{0.209}{(1.15)^2}$$

or, finally: $$C_f = 0.328\ R_o^{-0.3} \tag{4.41}$$

which was derived for data lying in the range $72{,}000 \leq R_o \leq 325{,}000$. It remains now to consider the question of where does the wall-jet region begin. The answer lies in finding the value of r beyond which the laws governing the development of the wall jet (Equation 4.38) become valid. Careful examination of the available data showed that the beginning of the wall-jet region ($r = r_o$) can be best defined from considerations of the velocity scale u_m. According to previous findings (Equations 4.33

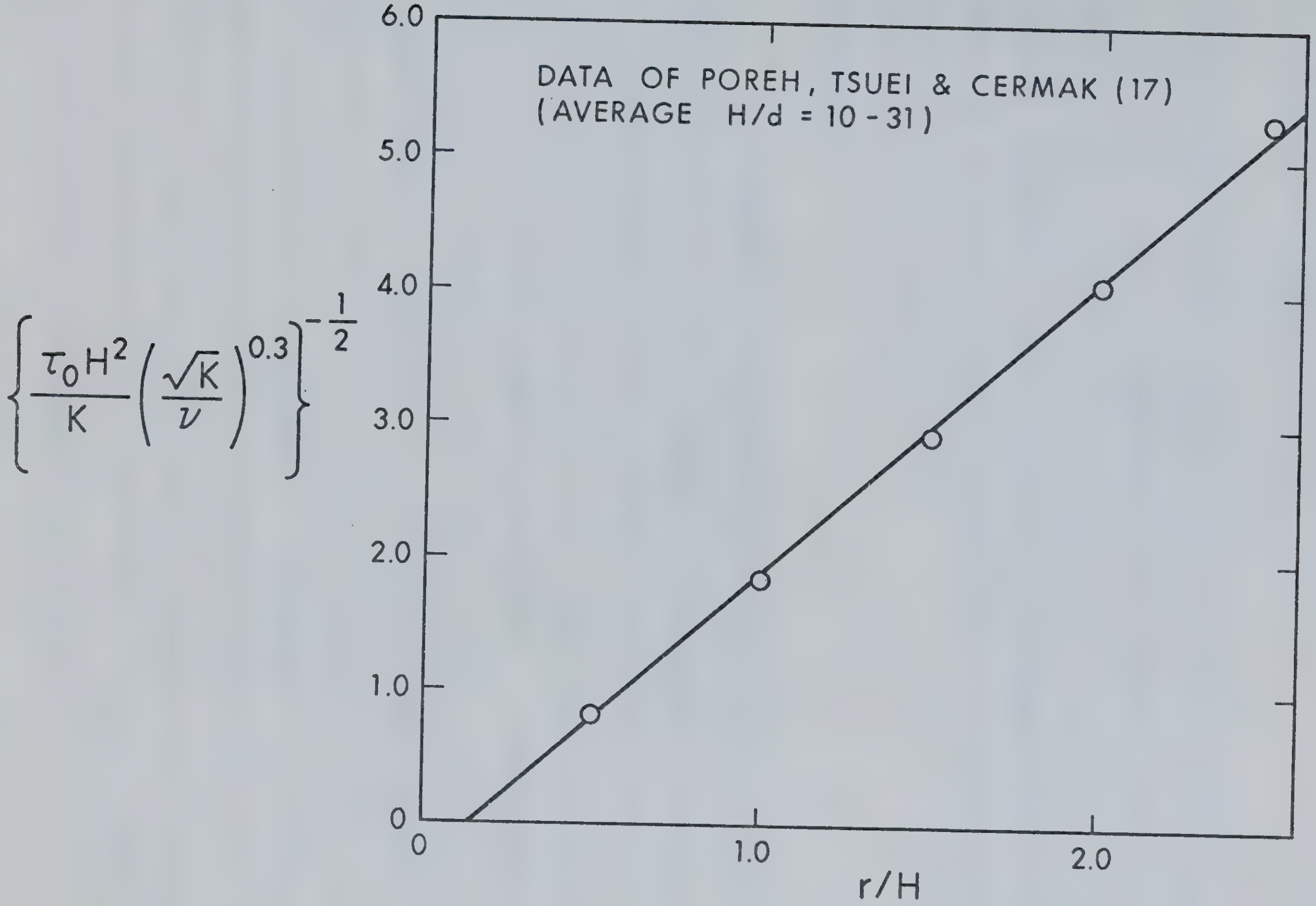

FIGURE 4.20 WALL SHEAR STRESS, WALL JET REGION

and 4.38) u_m can be written as:

$$\frac{u_m}{U_o} \frac{H}{d} = f_m \left(\frac{r}{H}\right) \tag{4.42}$$

for all values of r/H. It follows that r_o must be a fixed portion of H, i.e., $r_o/H = \text{const.}$ Examination of the available data gives an average value of $r_o/H = 0.36$, even though some variation exists among different experiments. Recalling that the impingement region ends at $r/H \simeq 0.22$, it is obvious that the range $0.22 \leq r/H \leq 0.36$ represents a transition between regions II and III.

4.4 Summary

An analytical and experimental study of circular turbulent jets, impinging normally, has been presented in this chapter. The beginning of the impingement region has been located at $x/H = 0.86$ from axial velocity considerations, whereas the end of this region has been located at $r/H = 0.22$ from wall pressure considerations. A semi-empirical method has been developed to predict axial velocity and pressure in the impingement region. Similarity of velocity and pressure profiles in this region has been explored and a satisfactory analytical method to predict wall shear stress has been developed. Existing data in the wall jet region have been re-analyzed and were found to confirm the simple-exponent theoretical considerations of Chapter II. Average values of the constants describing the variations of the length scale, the velocity scale and the wall shear stress, have been obtained and summarized.

CHAPTER V - AXISYMMETRIC IMPINGEMENT OF DEVELOPING JETS

5.1 Introduction

The impingement of fully developed jets was considered in the previous chapter. However, when the nozzle is placed at a small distance from the wall, the physics of the problem is likely to change because in this case the jet is not fully developed when approaching the wall. The study of circular, not fully developed jets impinging normally, is the objective of this chapter. The main quantitative difference between impingement at "small" and "large" heights is that since the latter is fully developed when it enters the impingement region, it can be assumed to originate at a point source of momentum, whereas the former consists of an inner core of uniform velocity equal to U_o and an annular shear layer surrounding the core. This type of geometry depends on both U_o and d and it cannot be described by the previous assumption. This study, therefore, was carried out at impingement heights less than the length of the potential core, i.e., $H/d < 6$. Quantitative flow characteristics are shown in the definition sketch, Figure 5.1. The flow issuing from the nozzle behaves initially as a free jet. At a certain distance from the nozzle, x_o, the static pressure rises above atmospheric, i.e., wall effects begin to be felt. Thus, for $x > x_o$ pressure gradients exist in both directions, x and r. The gradient in the r-direction is set up so that the pressure falls from a maximum value on the centerline to ambient values when r becomes sufficiently large. In the range $0 \leq x \leq x_o$, the flow can be identified to be an axisymmetric shear layer, i.e., for $r \leq r_1$, $u = U_o$;

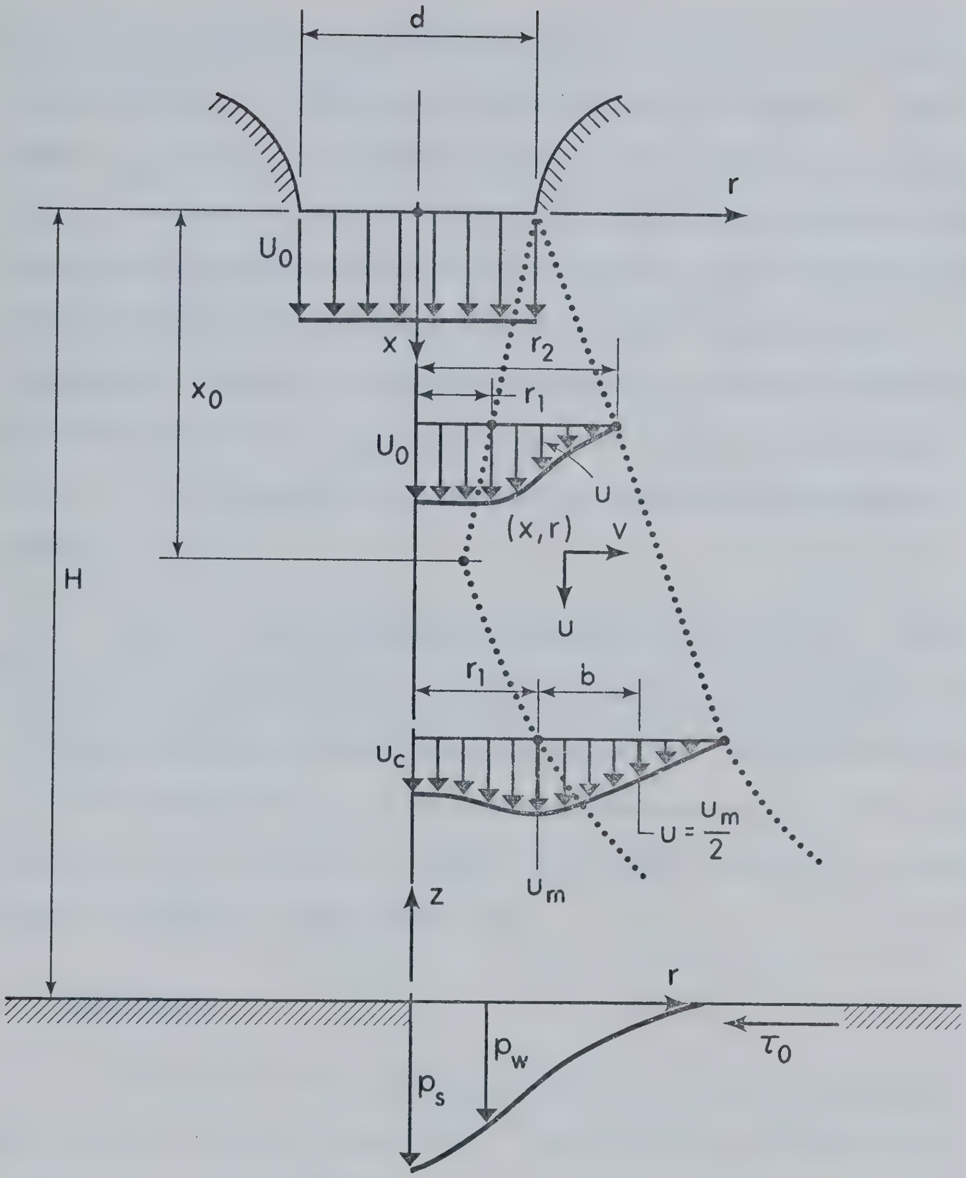
d
r
U_0
x
x_0
r_2
r_1
U_0
u
(x, r)
v
u
H
r_1
b
u_c
$u = \frac{u_m}{2}$
u_m
z
r
p_w
p_s
τ_0

FIGURE 5.1 DEFINITION SKETCH

for $r > r_1$, $\frac{\partial u}{\partial r} < 0$, u approaching zero for $r = r_2$. This region can, therefore, be appropriately called the free jet region. In the range $x_o \leq x \leq H$, u increases initially from a value of u_c at the axis to a maximum of u_m at $r = r_1$ and then decreases again. In this region the difference between the static pressure and the ambient pressure is generally greater than zero and is simply denoted by p. Furthermore, the radial component of velocity, v, becomes comparable to the axial component u, in contrast with the free jet region where $v << u$. It is appropriate, therefore, to call this the impingement region.

If p_c is the centerline pressure then $p_c + \frac{\rho u_c^2}{2} = \text{const} = \frac{\rho U_o^2}{2}$, i.e., the total axial pressure remains constant throughout, which indicates inviscid conditions near the centerline. The wall pressure, p_w has a maximum of p_s at the axis and decreases to zero a few nozzle diameters from the stagnation point. Beyond this distance the flow soon begins to behave as a radial wall jet.

5.2 Experiments

Details of the experimental set-up and measuring techniques have been described in Chapter III. A nozzle with inside diameter of 0.923 in. was used throughout. It was initially intended to carry out experimentation in the range $0 \leq \frac{H}{d} \leq 6$. However, it was found that when H/d was less than about 1.1, some static pressure was transmitted from the wall to the nozzle, its relative magnitude increasing with decreasing H/d. If p_T is the total pressure at the nozzle and p_o is

the static pressure, then $p_T = p_o + \rho U_o^2/2$. The relative static pressure is $p_o/p_T = 1 - \frac{\rho U_o^2/2}{p_T}$. This quantity decreases from 1.0 at $H/d = 0$ to about 0.01 at $H/d = 1.1$. To avoid unnecessary complications only values of H/d greater than 1.1 were considered. Furthermore, it was found that the stagnation pressure p_s, was equal to $\rho U_o^2/2$ so long as H/d was less than about 5.5. For $H/d \gtrsim 5.5$, $p_s < \rho U_o^2/2$, indicating that diffusion effects have penetrated to the centerline of the jet. Thus, only the range $1.1 \leq H/d \leq 5.5$ has been considered in this study. For $H/d \gtrsim 8$ to 10 the flow is that of large impingement height as described in Chapter IV. A transition between large and small impingement heights exists in the range $5.5 \leq H/d \leq \xi_1$ where ξ_1 is an, unspecified as yet, upper limit. Determination of ξ_1 can be achieved from considerations of stagnation pressure. This is given by:

$$\frac{p_s}{\rho U_o^2/2} = \begin{cases} 1.0 & ; \quad 1.1 \leq H/d \leq 5.5 \\ \\ \frac{52}{(H/d)^2} & ; \quad \xi_1 \leq \frac{H}{d} \quad \text{(Chapter IV)} \end{cases} \tag{5.1}$$

Let $\xi = H/d$ and $\overline{p_s} = p_s / \frac{\rho U_o^2}{2}$. An equation for $\overline{p_s}$ can be found in the range $5.5 \leq \xi \leq \xi_1$, using a second degree polynomial approximation and the conditions:

$$\begin{aligned} (\overline{p_s})_{\xi=5.5} &= 1.0 \quad ; \quad (\overline{p_s})_{\xi=\xi_1} = 52/\xi_1^2 \\ \left(\frac{d\overline{p_s}}{d\xi}\right)_{\xi=5.5} &= 0 \quad ; \quad \left(\frac{d\overline{p_s}}{d\xi}\right)_{\xi=\xi_1} = -104/\xi_1^3 \end{aligned} \tag{5.2}$$

Assuming that:

$$\overline{p_s} = a_o + a_1 (\xi - 5.5) + a_2 (\xi - 5.5)^2 \tag{5.3}$$

it is possible to determine a_o, a_1, a_2 and ξ_1 from the conditions 5.2. This procedure gives $a_o = 1.0$, $a_1 = 0$, $a_2 = - 0.0325$, $\xi_1 = 8.3$. With these, Equation 5.3 becomes:

$$\overline{p_s} = 1 - 0.0325 (\xi - 5.5)^2 \tag{5.4}$$

and it is shown plotted in Figure 5.2, in the range $5.5 \leq H/d \leq 8.3$, which constitutes the transition between small and large impingement heights. Detailed measurements of the flow field were made in the first five runs whose particulars are shown below.

Run No.	H/d	R_o	d(in)
1	4.05	53,600	0.923
2	2.21	53,600	"
3	2.21	31,200	"
4	3.08	31,2000	"
5	5.17	53,600	"

TABLE 5.1 RANGE OF EXPERIMENTS

Particulars of supplementary experiments are indicated on figures where these data are plotted.

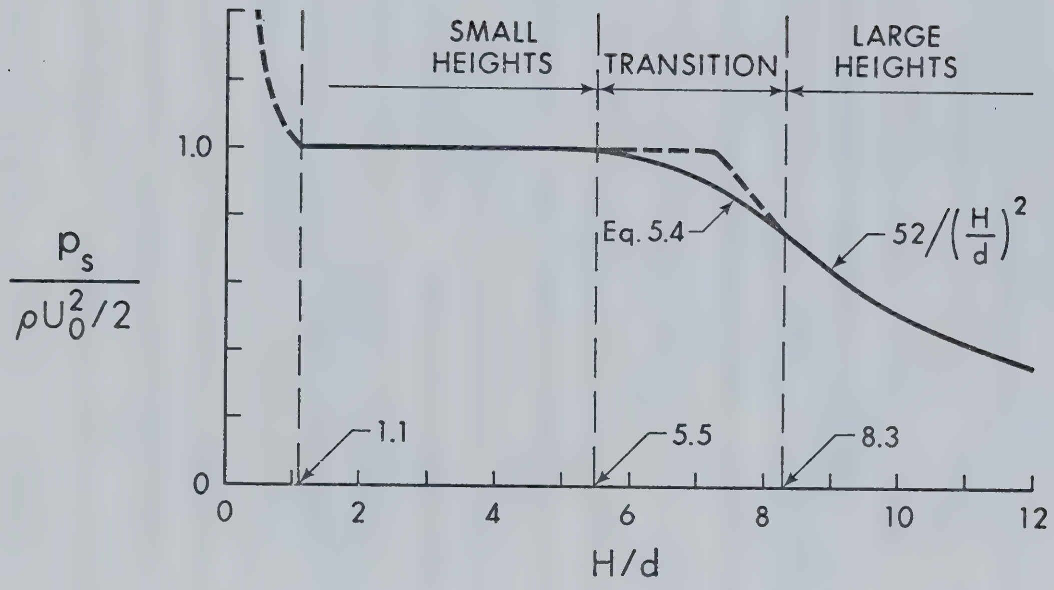

FIGURE 5.2 RELATIVE STAGNATION PRESSURE

5.3 Experimental Results and Analysis

5.3.1 Free Jet Region

Typical velocity distributions in this region are shown in Figure 5.3. It is seen that for $r \leq r_1$, $u = U_o$. From continuity requirements it is easy to show that for $r \leq r_1$, $v = 0$. The v-component is also shown plotted in this figure. It is seen that the above reasoning is supported by the data. For $r > r_1$, u decreases to zero, while v takes on non-zero values and in general $v << u$. These profiles are replotted in Figure 5.4 in the form $\frac{u}{U_o}$ vs η where $\eta \equiv \frac{r - r_1}{b}$ and b is the value of $r - r_1$ for which $u = \frac{1}{2} U_o$. The conventional function $\exp(- .693\ \eta^2)$ applies as is shown in Figure 5.4. The range $r \leq r_1$ is called the potential core, whereas the range $r \geq r_1$ is the shear layer. Annular shear layers have been studied earlier (see (28),(29) for comprehensive accounts). Using the integral momentum equation and the entrainment data of Hill (41), a simple analysis (see Appendix C) showed that r_1 and b vary almost linearly with x, a result that is supported by available data. The analysis of Squire and Trouncer (42) yields complex expressions for r_1 and b which, however, can again be shown to be approximately linear.

The present data on r_1 and b are plotted in Figures 5.5 and 5.6 where they follow straight lines up to a certain value of x/d, their variation changing beyond this value, owing to the presence of the wall. Theoretically, when $x = 0$, $b = 0$ and $r_1/d = 0.5$. However, the data show that this is not the case and only if the x co-ordinate is adjusted by what is commonly known as the virtual origin correction,

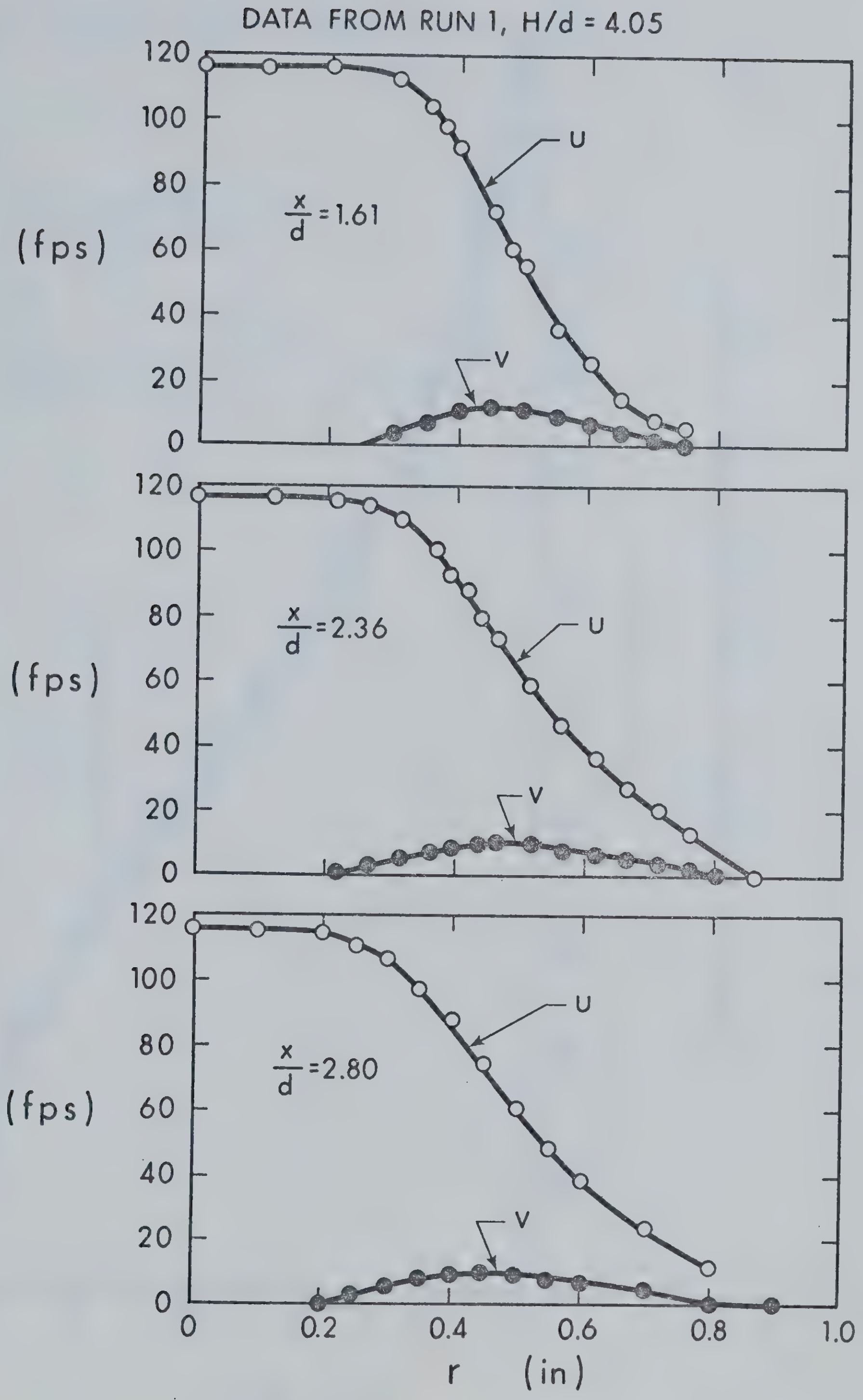

FIGURE 5.3 VELOCITY FIELD, FREE JET REGION

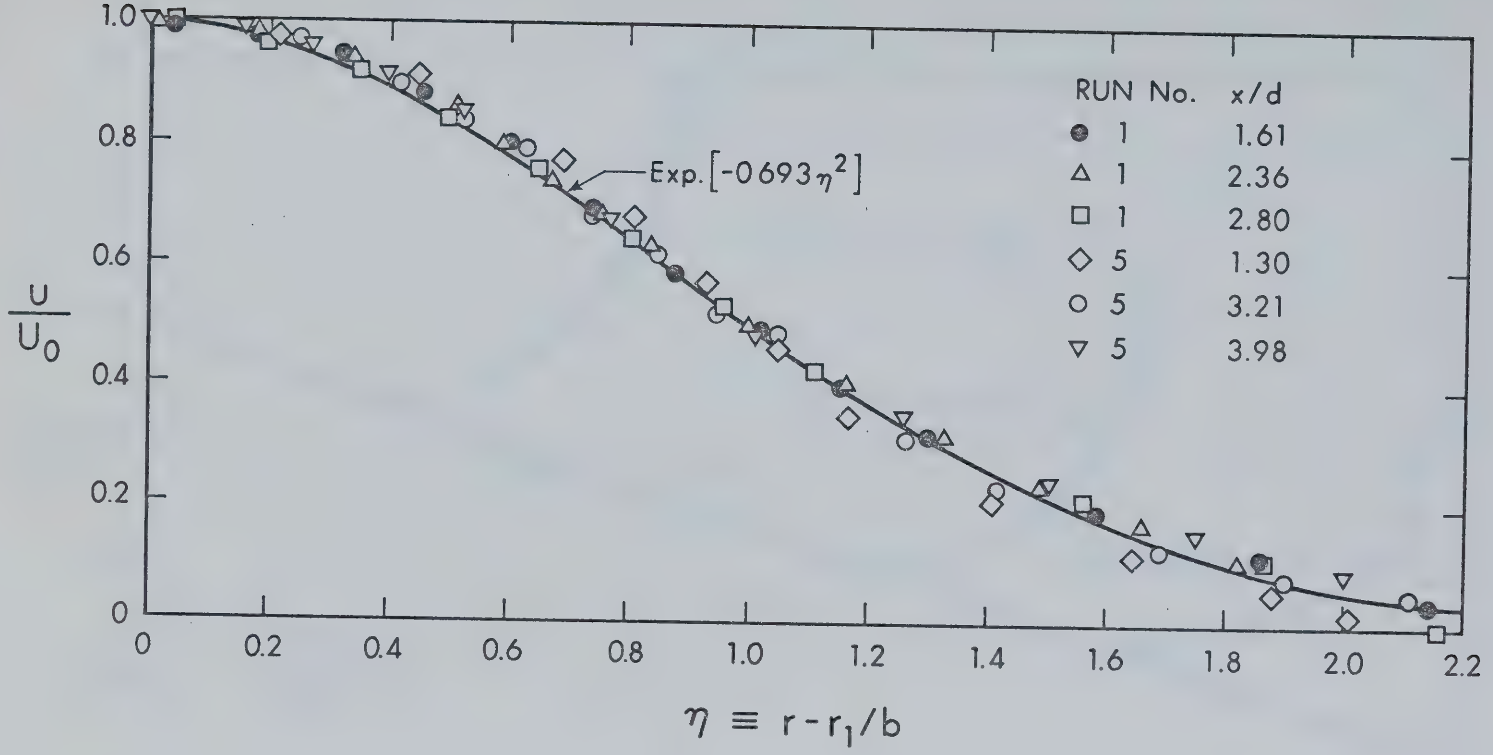

FIGURE 5.4 SIMILARITY IN SHEAR LAYER, FREE JET REGION

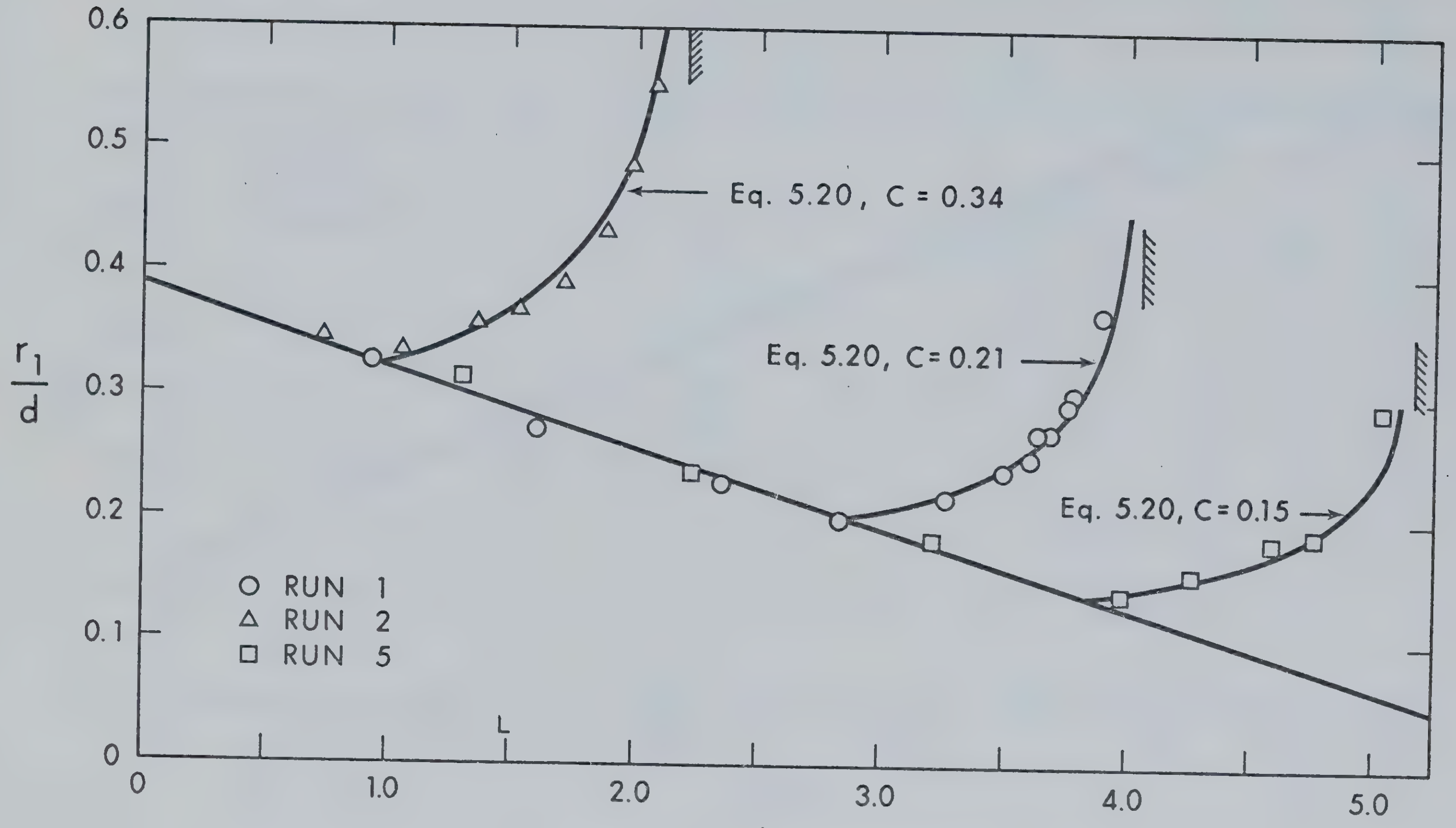

FIGURE 5.5 RADIUS OF CORE

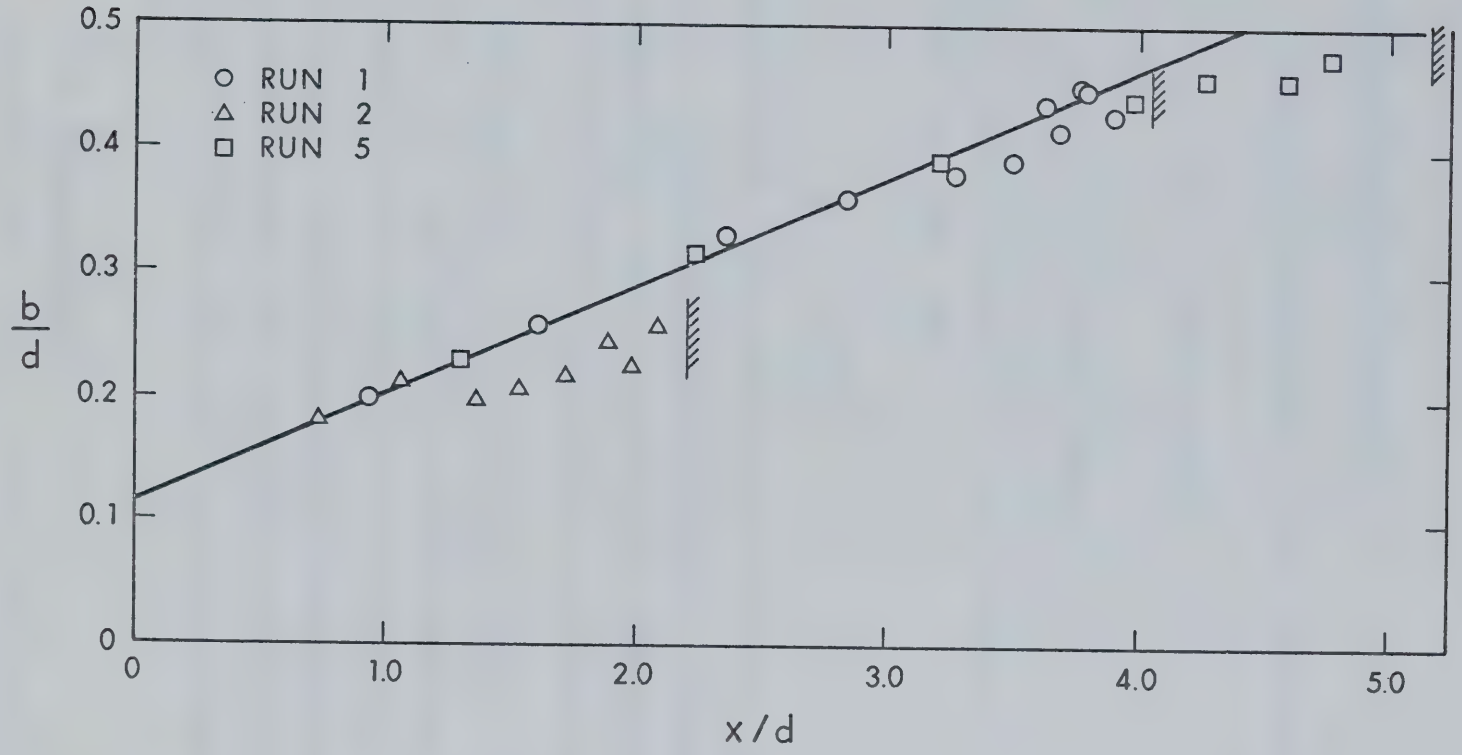

FIGURE 5.6   LENGTH SCALE FOR SHEAR LAYER

would the above conditions be satisfied.

Thus in the free jet region, r_1 and b are given by:

$$\frac{r_1}{d} = 0.39 - 0.065 \frac{x}{d} \tag{5.5}$$

$$\frac{b}{d} = 0.115 + 0.087 \frac{x}{d} \tag{5.6}$$

The virtual origin is located at $x = -1.32d$ so that, if $x_1 = x - (-1.32d) = x + 1.32d$, then:

$$\frac{b}{d} = 0.087 \frac{x_1}{d} \tag{5.6A}$$

According to Equation 5.5, the length of the potential core will be 6d, a value that is commonly accepted for circular jets. Theoretical values for the slopes of r_1/d and b/d are 0.077 and 0.100 respectively (see Appendix C), which compare favourably with the experimental values.

The outer limit r_2 of the jet could be defined as that value of r where $u \simeq o$. Using Figure 5.4, one could deduce that $r_2 \simeq r_1 + 2.3b$. The end of the free jet region could be defined as the value of x where r_1 and b begin to deviate from the linear variation. Figures 5.5 and 5.6 indicate that these limits coincide for each run as would be expected. However, this limit is much better defined for r_1 than for b.

5.3.2 Impingement Region

Beyond the value $x = x_o$, the flow is affected by the wall. This is generally accompanied by an increase in static pressure above

ambient, increase in the v-component of velocity and increase in r_1. At the same time the distribution of u in the core ($r \leq r_1$) is no longer uniform. Typical velocity distributions are shown in Figure 5.7. In the shear layer ($r \geq r_1$) the similarity $\frac{u}{u_m} = f(\eta)$ is preserved as it is verified in Figure 5.8. A complete prediction of the flow field requires knowledge of the quantities, u_c, u_m, r_1, b, p, and u and v in the core. Consider first the static pressure, p. One could generally write:

$$p = f(\rho, U_o, d, H, z, r)$$

or, by dimensional analysis:

$$\frac{p}{\rho U_o^2/2} = f_1(\frac{z}{d}, \frac{r}{d}, \frac{H}{d}) \qquad (5.7)$$

further:

$$\frac{p_w}{\rho U_o^2/2} = f_1(0, \frac{r}{d}, \frac{H}{d}) = f_2(\frac{r}{d}, \frac{H}{d}) \qquad (5.8)$$

$$\frac{p_s}{\rho U_o^2/2} = f_1(0, 0, \frac{H}{d}) = f_2(0, \frac{H}{d}) \qquad (5.8A)$$

and the relative wall pressure is:

$$\frac{p_w}{p_s} = f_3(\frac{r}{d}, \frac{H}{d}) = f_4(\frac{r}{H}, \frac{H}{d}) \qquad (5.9)$$

For large impingement heights, the function f_4 is independent of H/d, as was shown earlier (Chapter IV). Figure 5.9 shows existing data plotted

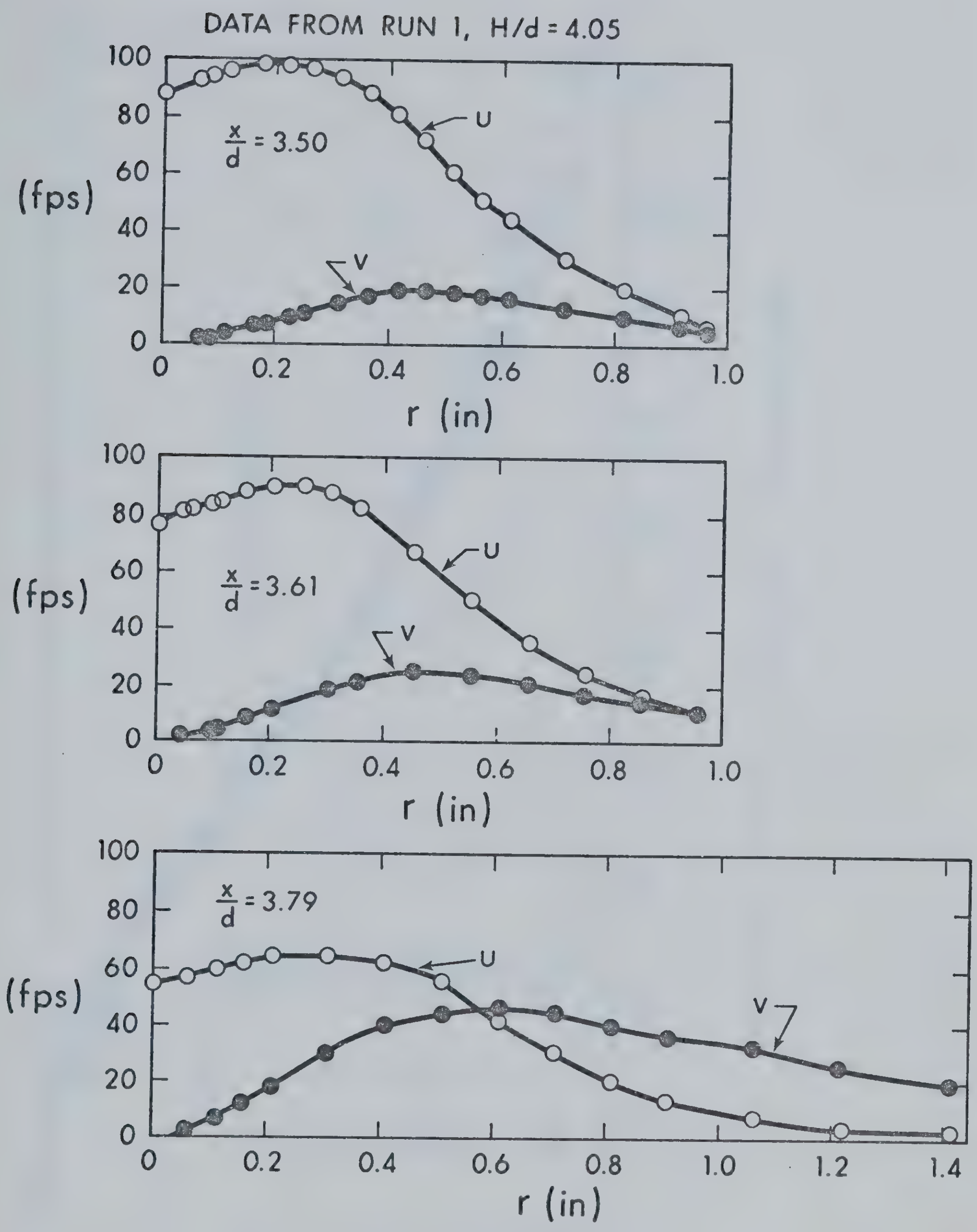

FIGURE 5.7 VELOCITY FIELD, IMPINGEMENT REGION

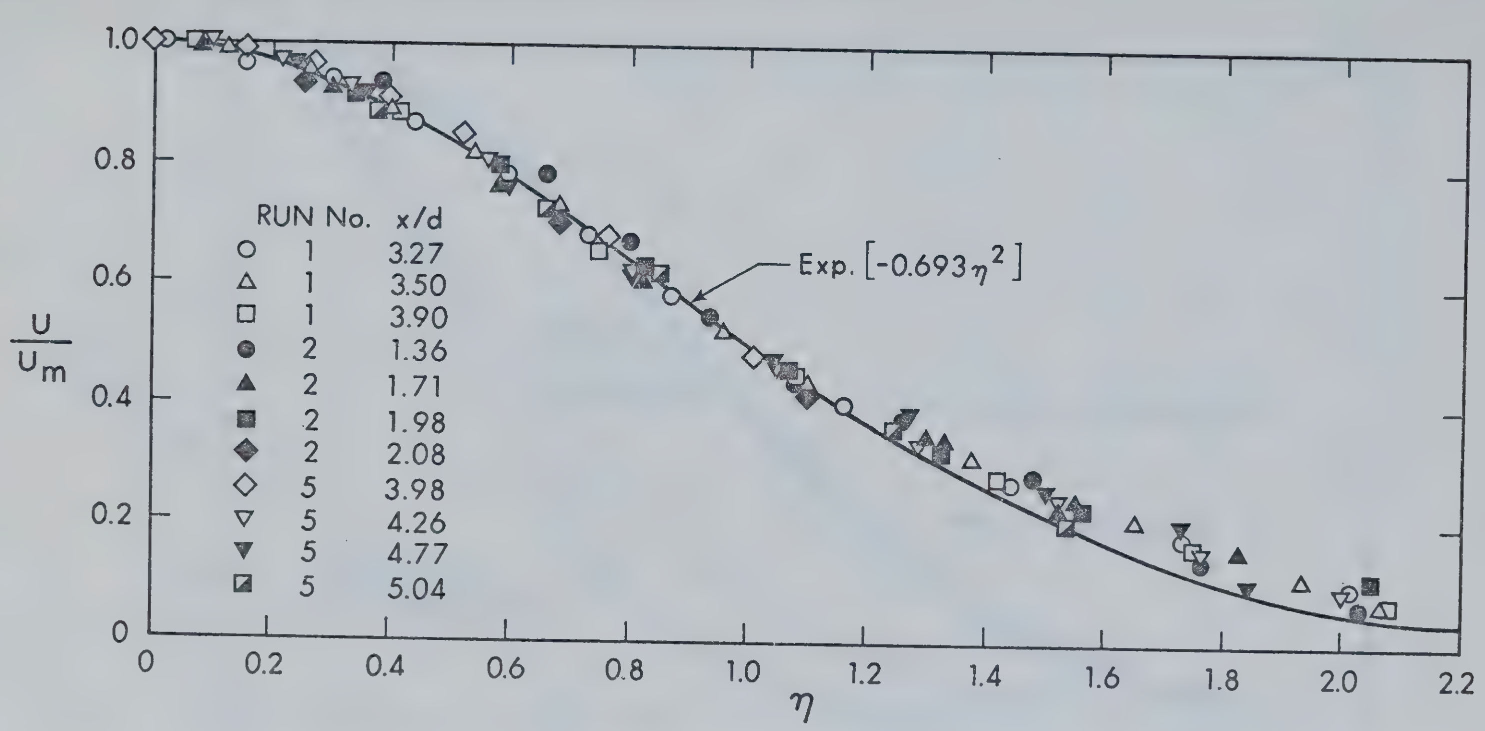

FIGURE 5.8 SIMILARITY IN SHEAR LAYER, IMPINGEMENT REGION

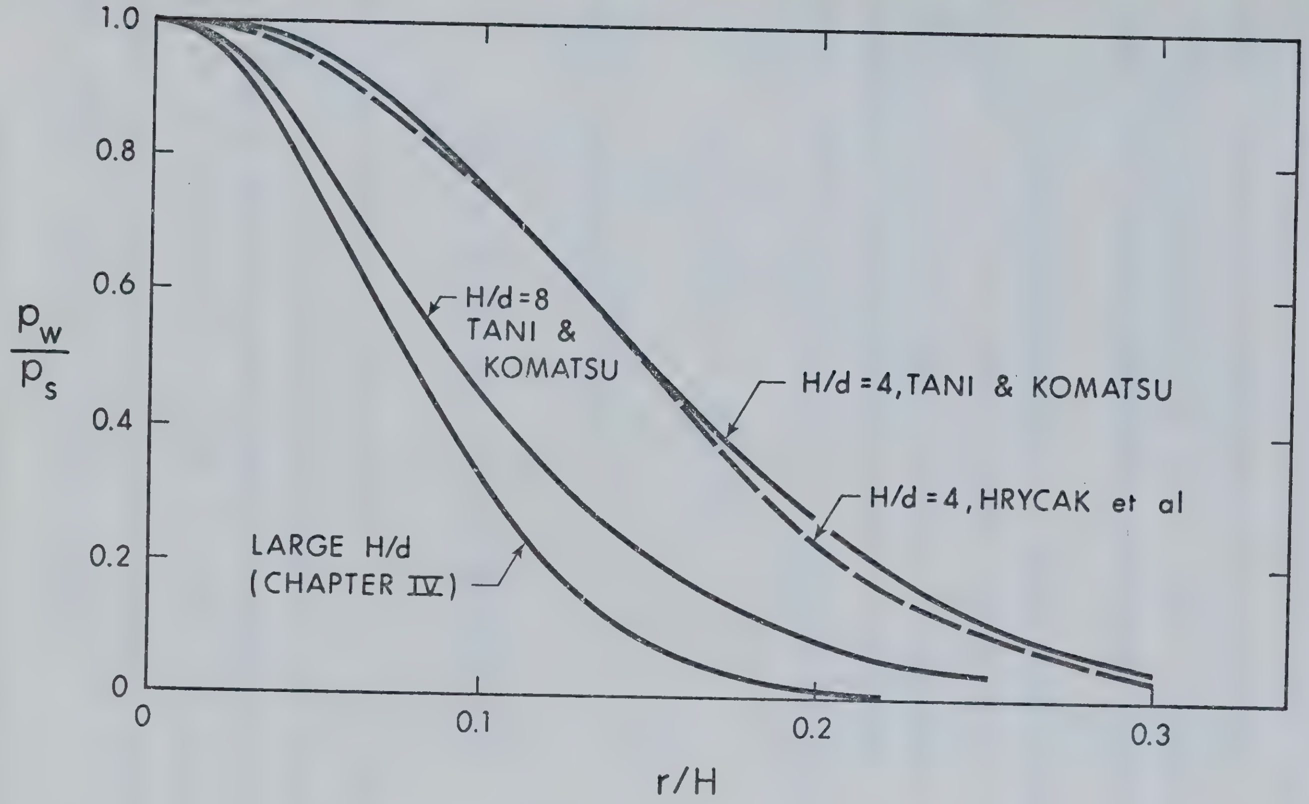

FIGURE 5.9 WALL PRESSURE

in the form p_w/p_s vs r/H for different values of H/d. For $H/d = 8$, p_w/p_s is close to the average curve for large heights, whereas data of different authors (15, 22) for $H/d = 4$ yield practically identical curves, while they are considerably removed from the large height curve.

Consider now Equation 5.8. In the range of interest, $1.1 \leq H/d \leq 5.5$, $p_s/\frac{\rho U_o^2}{2} = 1$, which suggests that unless the functions f_1 and f_2 are of special form, they should be independent of H/d. This expectation is also supported by momentum considerations. Equating the integral of the wall pressure to the initial momentum of the jet:

$$2\pi \int_o^\infty r\ p_w\ dr = \rho \frac{\pi d^2}{4} U_o^2 \tag{5.10}$$

which, using Equation 5.7 reduces to:

$$\int_o^\infty f_1(0, \frac{r}{d}, \frac{H}{d}) \frac{r}{d}\ d(\frac{r}{d}) = \int_o^\infty f_2(\frac{r}{d}, \frac{H}{d}) \frac{r}{d}\ d(\frac{r}{d}) = \frac{1}{4} \tag{5.11}$$

which again suggests that the functions f_1 and f_2 should be independent of H/d unless they are of special form. The available data within the range of small impingement height are plotted in the form $p_w/\frac{\rho U_o^2}{2}$ vs r/d in Figure 5.10. In spite of scatter, the data appear to define a single curve, thus verifying the above reasoning. The Gaussian variation would give here only a fair approximation.

On the basis of the above, it is reasonable to assume that the function f_1, defined in Equation 5.7, is independent of H/d. It follows that the static pressure p at any point in the flow field will be

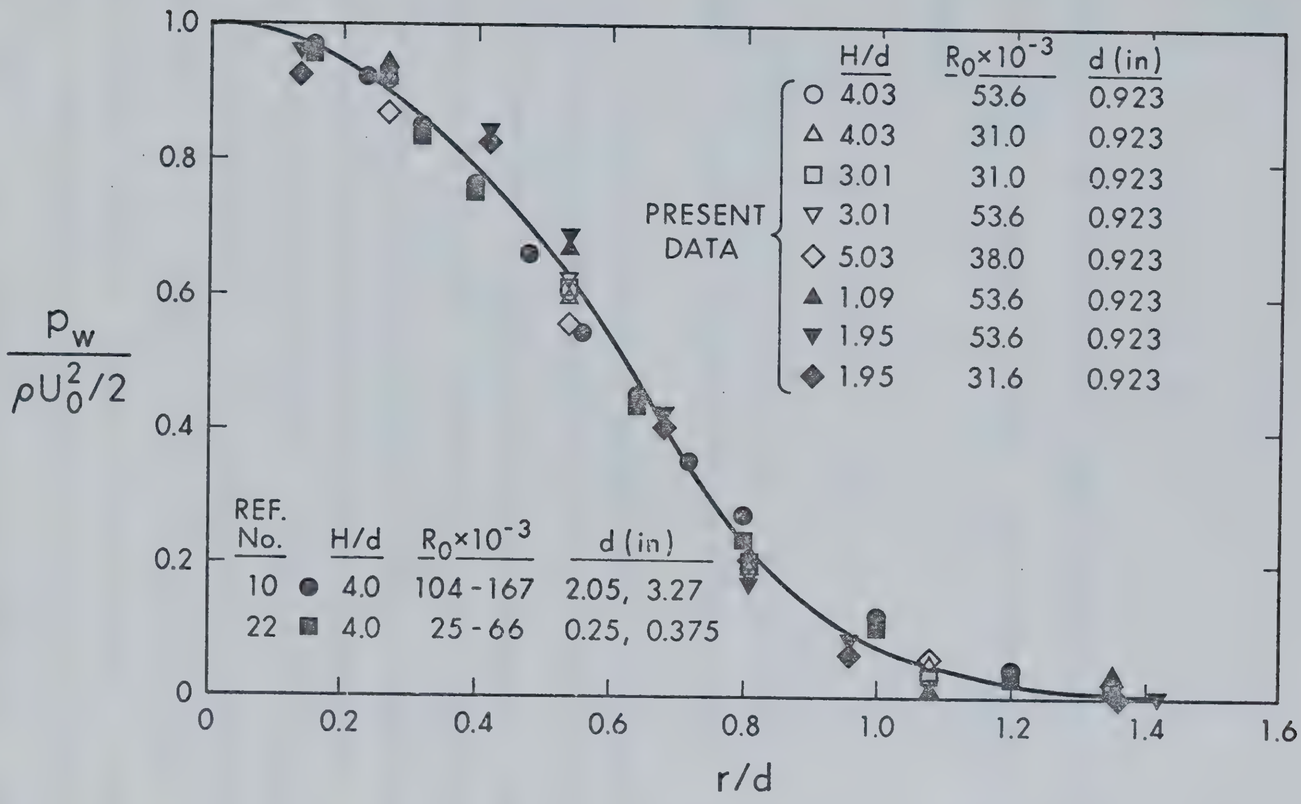

FIGURE 5.10 DIMENSIONLESS WALL PRESSURE

given by:

$$\bar{p} = f_5(\bar{z}, \bar{r}) \tag{5.12}$$

where an overbar has been used to denote dimensionless quantities, i.e., $\bar{p} \equiv p/\frac{\rho U_o^2}{2}$, $\bar{z} = z/d$, $\bar{r} = r/d$. The centerline pressure, p_c, will then be:

$$\bar{p}_c = f_5(\bar{z}, 0) = f_6(\bar{z}) \tag{5.13}$$

This formulation is verified in Figure 5.11, where data for H/d varying between 2.21 and 5.17 are seen to define a single curve.

Finally, the complete pressure field can be constructed, using the present data and Equation 5.12. This is shown in Figure 5.12, where average contours of equal pressure are presented. The physics of this problem is now clear. The effect of the wall (expressed in terms of increased static pressure) extends a certain distance above the wall. This distance does not depend on the height of impingement H but it is proportional to the nozzle diameter d. Thus, with reference to Figure 5.11 it could be stated that the boundary between free jet and impingement regions on the centerline is given by $z/d = 1.2 - 1.4$. This is also supported further by Figures 5.5 and 5.6 where r_1 and b are seen to first deviate from the linear variation at approximately the same value of z/d for all three runs (an average is $\simeq 1.25$). The lateral extent of this region at the wall can be obtained from Figure 5.10 to be $r_o \simeq 1.4d$ which is the value of r where $p_w/\frac{\rho U_o^2}{2} \simeq 0.01$.

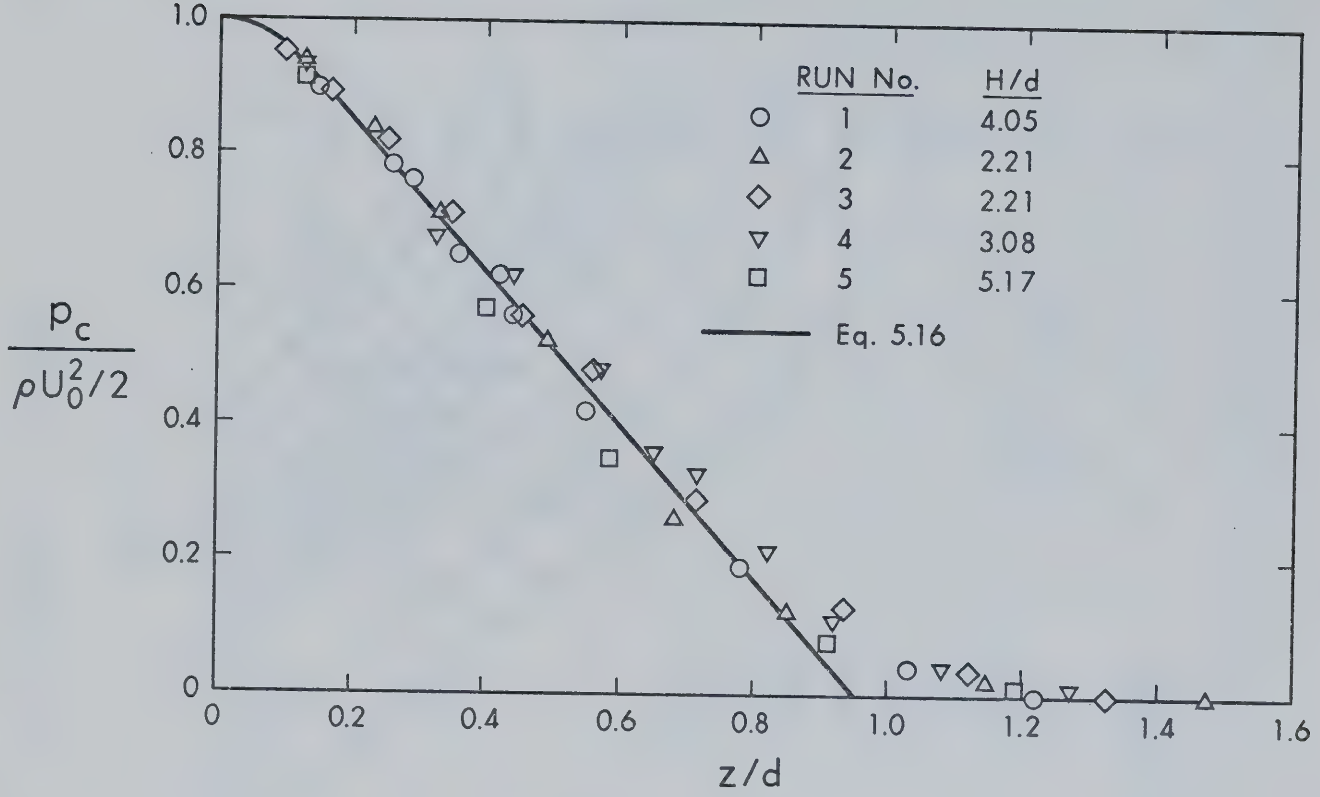

FIGURE 5.11 AXIAL PRESSURE

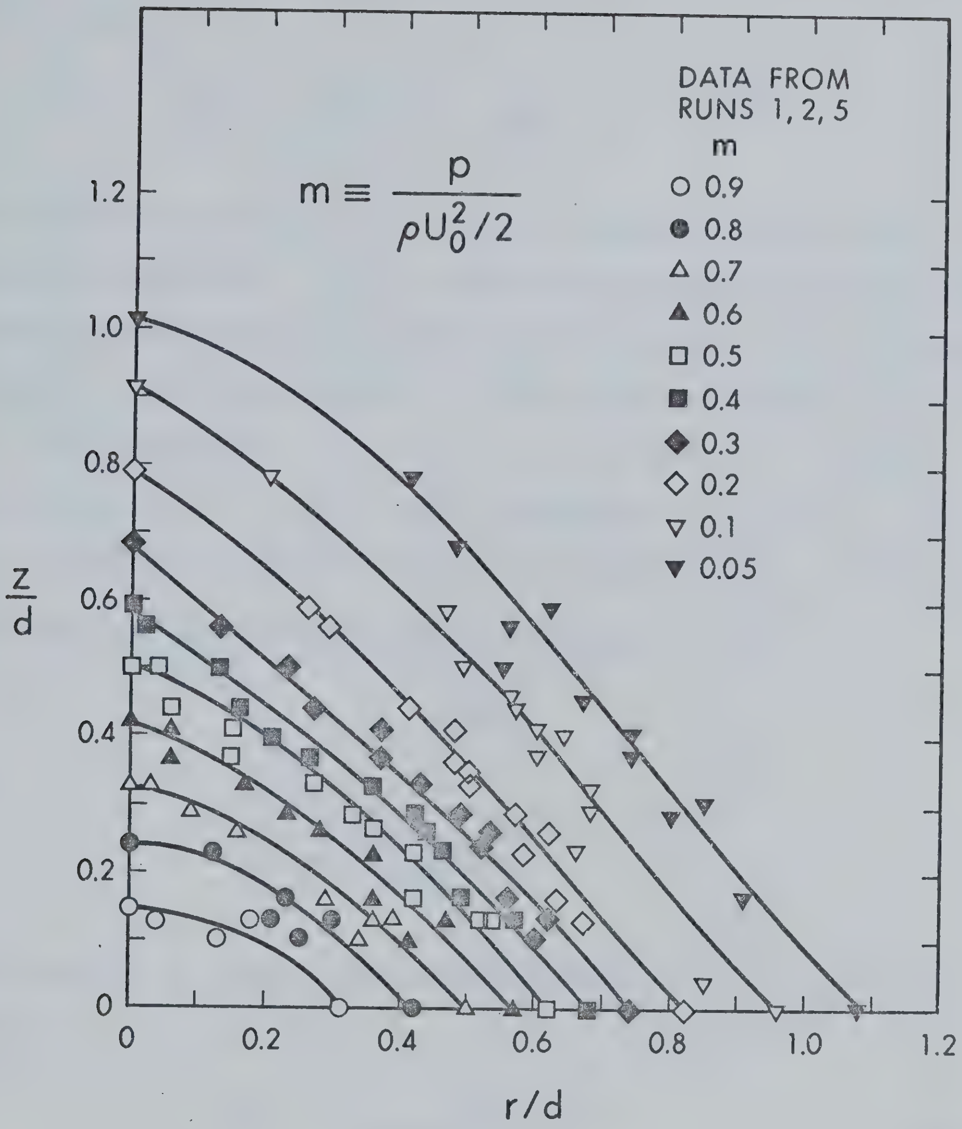

FIGURE 5.12 THE PRESSURE FIELD

Since the total pressure on the centerline is constant, one could write:

$$\frac{u_c}{U_o} = \sqrt{1 - \bar{p}_c} = f(\bar{z})$$

This is verified in Figure 5.13, for H/d ranging from 2.21 to 5.17. To derive an equation for u_c/U_o, an empirical observation is utilized which states that the product uv varies very little with x near the centerline, i.e., for small values of r. This is shown in Figure 5.14 where uv is plotted against r for different values of x/d. It is seen that for $r \lesssim 0.1$ in. uv is almost independent of x (or z). Thus $uv = g(r)$ then $\frac{1}{r}\frac{\partial}{\partial r}(ruv) = g_1(r)$ and $\left[\frac{1}{r}\frac{\partial}{\partial r}(ruv)\right]_{r=o} = g_1(o) = \text{const.}$ The above can be easily transformed (see Chapter IV) to:

$$u_c = c_1 \sqrt{z + c_2}$$

or:

$$\frac{u_c}{U_o} = k_1 \sqrt{\frac{z}{d} + k_2}$$

The constants k_1 and k_2 are evaluated to fit the data and the above becomes:

$$\frac{u_c}{U_o} = 1.07 \sqrt{\frac{z}{d} - 0.07} \tag{5.14}$$

Equation 5.14 is shown in Figure 5.13 to describe the data adequately for $0.1 \lesssim z/d \lesssim 0.8$. For $z/d > 0.8$, there exists a smooth transition between Equation 5.14 and the line $\frac{u_c}{U_o} = 1$. For very small values of z/d a square-root type of variation would give infinite gradient of u_c. This

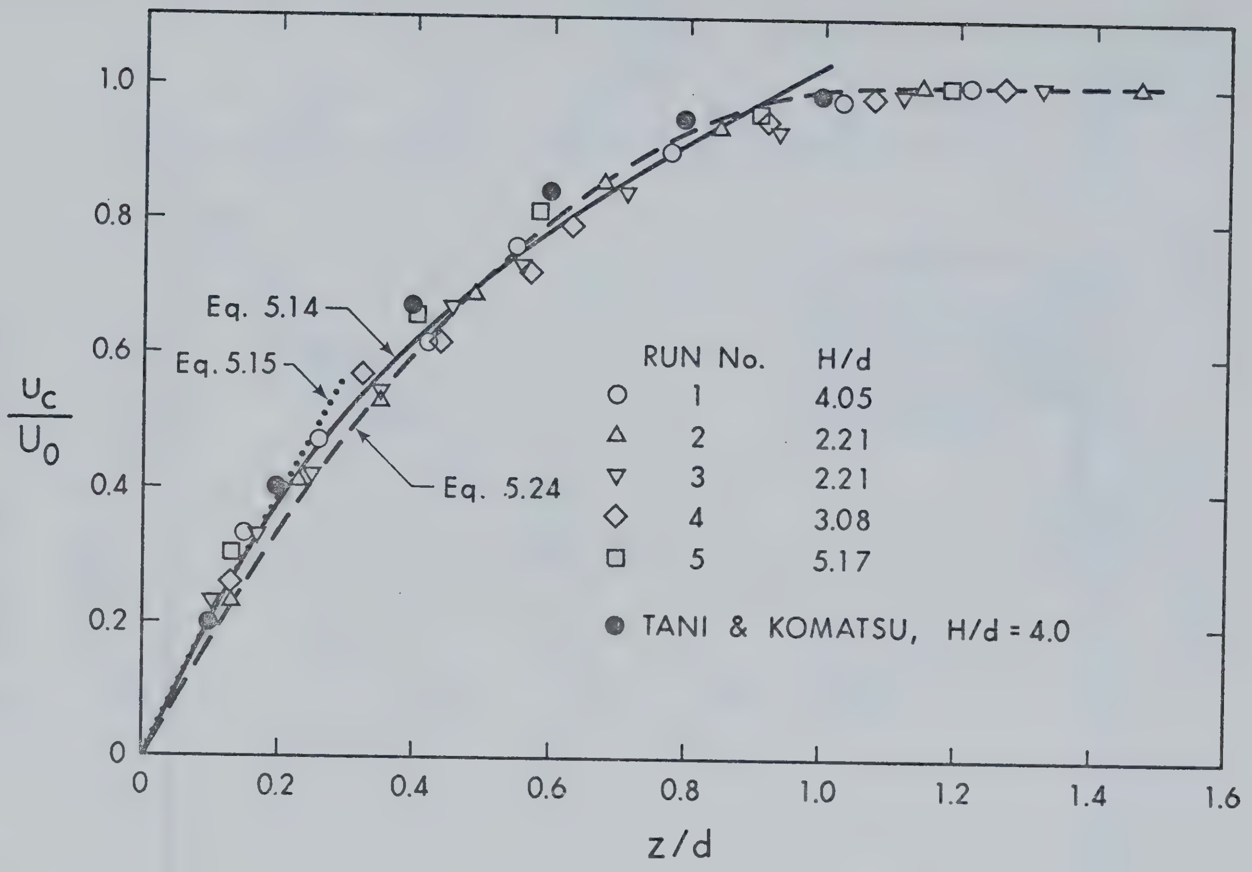

FIGURE 5.13 AXIAL VELOCITY

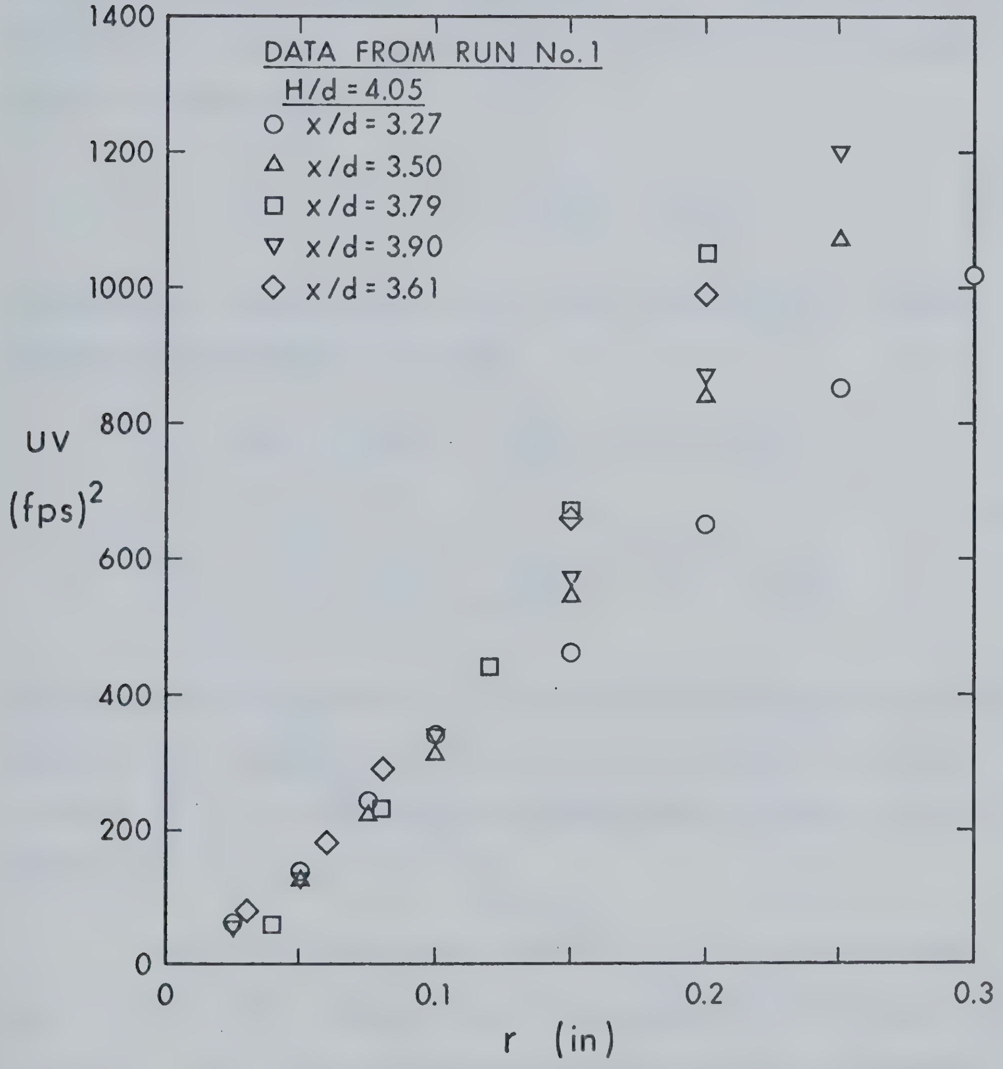

FIGURE 5.14 VARIATION OF uv

is physically unacceptable. If it is assumed that the flow very near the wall is of the stagnation type, then $u_c \propto z$. Matching this with Equation 5.14, so that u_c and $\frac{du_c}{dz}$ are continuous at the matching point one finds that:

$$\frac{z}{d} \leq 0.14 \quad ; \quad u_c/U_o = 2(z/d) \tag{5.15}$$

Consequently, the variation of p_c can be found using the Bernoulli equation which applies on the axis.

$$\begin{aligned} &\text{For} \quad z/d \leq 0.14 \qquad \frac{p_c}{\rho U_o^2/2} = 1 - 4\left(\frac{z}{d}\right)^2 \\ &\text{For} \quad z/d \geq 0.14 \qquad \frac{p_c}{\rho U_o^2/2} = 1.08 - 1.14\frac{z}{d} \end{aligned} \tag{5.16}$$

These are plotted in Figure 5.11 and are seen to describe the data adequately. The variation of u_c can also be described by the simpler relation $\frac{u_c}{U_o} \simeq 1.0\sqrt{z/d}$ with the understanding that this is not to be applied very near the wall.

Considering the maximum velocity u_m, it is assumed that $u_m \propto u_c \propto \sqrt{z/d}$. The constant of proportionality was evaluated as 1.15 ($u_m = 1.15\ u_c$) and this is shown plotted in Figure 5.15 together with the data. A simpler relation can again be taken as $u_m/U_o \simeq 1.15\sqrt{z/d}$. In order now to predict u and v in the core, it will be assumed that in the range $0 \leq r \leq r_1$, the flow is inviscid. This is supported by the constancy of the total pressure on the axis. At the same time, irrotationality cannot be assumed because the total pressure

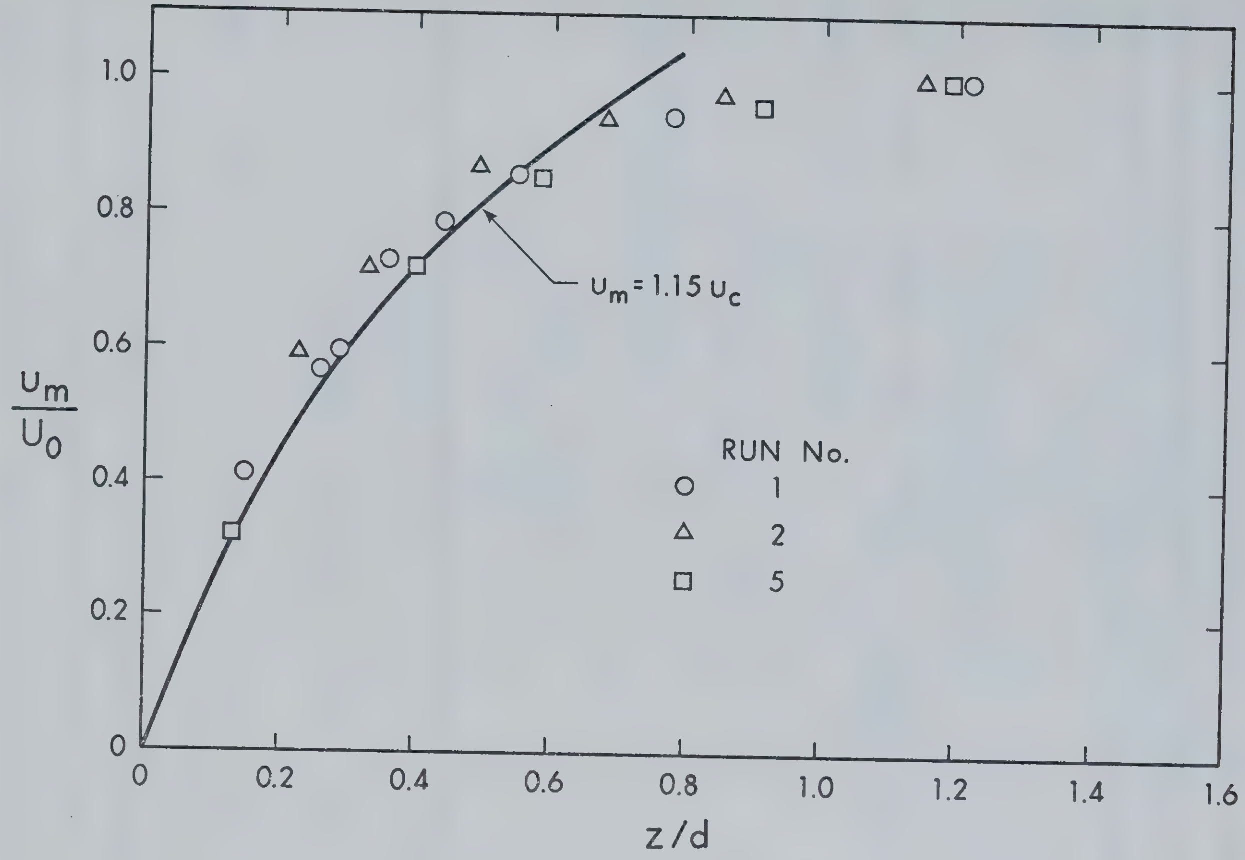

FIGURE 5.15 VELOCITY SCALE u_m

does not remain constant in the radial direction. Under these conditions the solution of Tani and Komatsu (15) will be applicable. Neglecting terms which involve powers of r greater than 4, u is given by (Chap. II):

$$u = u_c + \phi_1(z)\, r^2 + \phi_2(z)\, r^4 \tag{5.17}$$

with $\phi_1(z) = -\frac{1}{4}(u_c'' + C_1)$ and $\phi_2(z) = \frac{1}{8}(C_2 u_c + \frac{1}{8} u_c^{(iv)})$

where C_1, C_2 are constants.

$$\frac{\partial u}{\partial r} = 2\phi_1 r + 4\phi_2 r^3$$

Using the condition $\left(\frac{\partial u}{\partial r}\right)_{r=r_1} = 0$,

$$r_1^2 = -\frac{1}{2}\,\frac{\phi_1}{\phi_2} \tag{5.18}$$

With this and some further manipulation it can be shown that:

$$\frac{u - u_c}{u_m - u_c} = \lambda^2(2 - \lambda^2) \tag{5.19}$$

with $\lambda \equiv r/r_1$.

The data are plotted in the form suggested by Equation 5.19 in Figure 5.16. It is seen immediately that Equation 5.19 is, strictly speaking, a poor approximation. However, if one is interested in finding u rather than $u - u_c$, Equation 5.19 becomes adequate because $u - u_c$ is about an order of magnitude less than u. To demonstrate this, let the subscripts p and a denote predicted and actual values respectively.

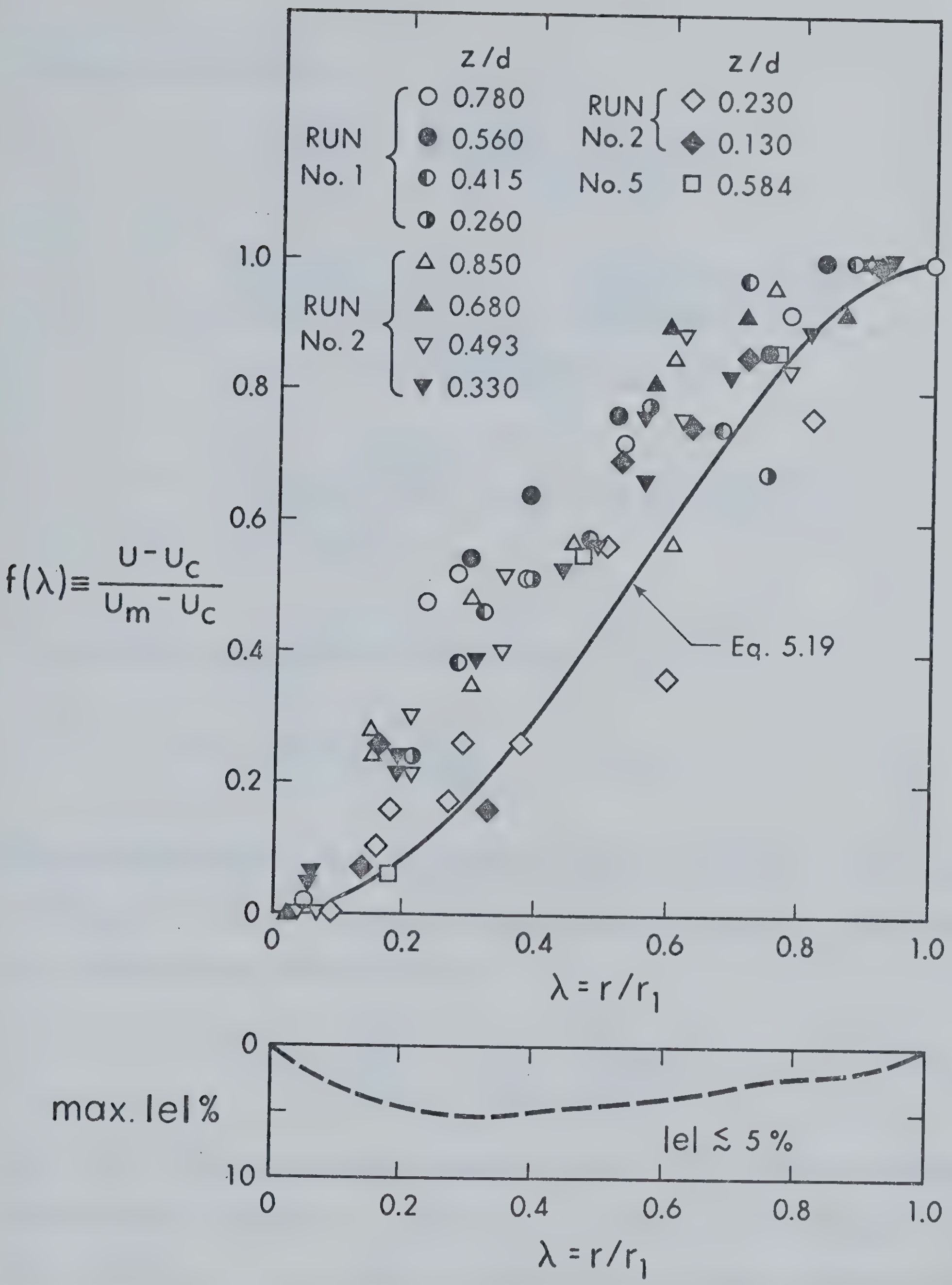

FIGURE 5.16 VARIATION OF u IN THE CORE

Then the error will be:

$$e = \frac{u_p - u_a}{u_a} = \frac{(u_p - u_c) - (u_a - u_c)}{u_c + (u_a - u_c)} =$$

$$= \frac{\left(\frac{u - u_c}{u_m - u_c}\right)_p (u_m - u_c) - \left(\frac{u - u_c}{u_m - u_c}\right)_a (u_m - u_c)}{u_c + \left(\frac{u - u_c}{u_m - u_c}\right)_a (u_m - u_c)} =$$

$$= \frac{\left(\phi_p - \phi_a\right) \frac{u_m - u_c}{u_c}}{1 + \frac{u_m - u_c}{u_c} \phi_a} \quad \text{where} \quad \phi \equiv \phi(\lambda) \equiv \frac{u - u_c}{u_m - u_c}$$

Then the error will be in absolute value:

$$|e| = 0.15 \; \frac{|\phi_p - \phi_a|}{1 + 0.15\phi_a}$$

The maximum value of $|e|$ is plotted against λ beneath the main graph of Figure 5.16 and it is seen to remain less than about 5%. To predict r_1 consider again Equation 5.18:

$$r_1^2 = -\frac{1}{2}\frac{\phi_1}{\phi_2} \propto \frac{C_1 + u_c''}{C_2 u_c + \frac{1}{8} u_c^{(iv)}}$$

With $u_c \simeq \sqrt{z}/d$ as was seen earlier, u_c'' and $u_c^{(iv)}$ can be obtained. If one tries to evaluate C_1 and C_2 so that the above relation fits the variation of r_1, it will be necessary to use very large values of C_1 and C_2. This means that r is described adequately by $r_1^2 \propto \frac{1}{u_c} \propto z^{-\frac{1}{2}}$. Using also some dimensional reasoning the above can be

written as:

$$r_1/d = C(z/d)^{-\frac{1}{4}} \qquad (5.20)$$

where now C depends on H/d, and will be discussed later. This relation is verified in Figure 5.5 with C evaluated empirically. As it could have been expected, Equation 5.20 intersects the free-jet linear variation at a distance z_o from the wall such that z_o/d is independent of H/d. For runs 1, 2, 5 respectively, $z_o/d = 1.21$, 1.19 and 1.34. Taking an average value of $z_o/d = 1.25$, the value of C can be predicted as follows.

$$\text{At} \quad z = z_o \begin{cases} \dfrac{r_1}{d} = 0.39 - 0.065 \left(\dfrac{H-z_o}{d}\right) & \text{(free jet region)} \\[2ex] \dfrac{r_1}{d} = \dfrac{C}{\sqrt[4]{z_o/d}} & \text{(impingement region)} \end{cases}$$

Equating and simplifying with $z_o/d = 1.25$:

$$C = 0.50 - 0.069 \frac{H}{d} \qquad (5.21)$$

This equation is plotted in Figure 5.17 together with the empirical values of C and it is seen to be adequate. The radius of the core, r_1, was determined by means of the relation:

$$r_1^2 \propto \frac{C_1 + u_c''}{C_2 u_c + \frac{1}{8} u_c^{(iv)}}$$

and by observing that this ratio behaves almost as $\frac{1}{u_c}$. This conclusion can be obtained formally by requiring $u_c'' = \text{const.}$ This will yield:

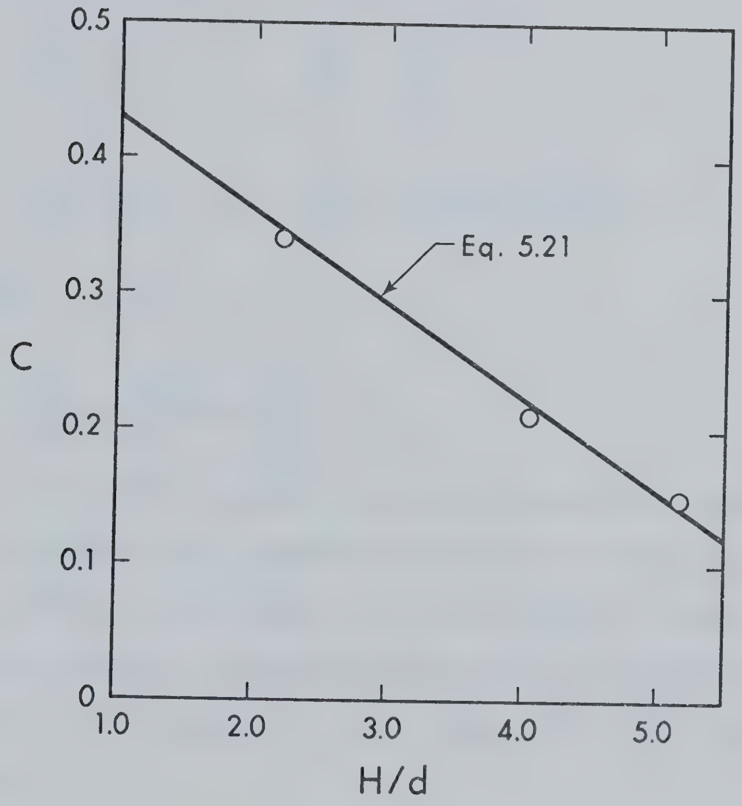

FIGURE 5.17 VARIATION OF C WITH H/d

$$\frac{u_c}{U_o} = \alpha_o + \alpha_1(\frac{z}{d}) + \alpha_2(\frac{z}{d})^2 \qquad (5.22)$$

The coefficients α_o, α_1, α_2, can be determined from the following boundary conditions:

$$\begin{aligned} \frac{z}{d} &= 0 \quad ; \quad \frac{u_c}{U_o} = 0 \\ \frac{z}{d} &\simeq 1.1 \quad ; \quad \frac{u_c}{U_o} = 1.0 \text{ and } \frac{d(u_c/U_o)}{d(z/d)} = 0 \end{aligned} \qquad (5.23)$$

These will give:

$$\frac{u_c}{U_o} = \frac{z/d}{1.10}\,[2 - \frac{z/d}{1.1}] \qquad (5.24)$$

This relation is obviously superior to previous equations for predicting u_c, as shown in Figure 5.13. However, for purposes of predicting r_1 and for later analytical calculations, it is much simpler to work with the square-root relation. It remains now to predict the radial component of velocity, v. Let $\Delta u_c = u_m - u_c$ and $\phi(\lambda) = \lambda^2(2 - \lambda^2)$. By Equation 5.19:

$$u = u_c + \Delta u_c \phi(\lambda) \qquad (5.25)$$

Using this relation and integrating the equation of continuity, it can be shown that (Appendix D, Section D.2):

$$\frac{v/U_o}{r_1/d} = -\frac{1}{2}\, f'(\bar{z})\, F(\lambda) \qquad (5.26)$$

where $f'(\bar{z}) \equiv u_c/U_o$ and $F(\lambda)$ is a function defined by:

$$F(\lambda) = \lambda + \beta(F_1(\lambda) + 2F_2(\lambda))\lambda^{-1}$$

with $\beta = \Delta u_c/u_c \simeq 0.15$ and:

$$F_1(\lambda) = \int_o^\lambda \lambda^2\phi' d\lambda \quad ; \quad F_2(\lambda) = \int_o^\lambda \lambda\phi d\lambda$$

If v_1 is the value of v at $r = r_1$, then:

$$\frac{v_1/U_o}{r_1/d} = -\frac{1}{2} f'(\bar{z})\, F(1) = \text{function of } \bar{z} \text{ only} \tag{5.27}$$

This conclusion is verified in Figure 5.18, where the data define a single curve while H/d is varied from 2.21 to 5.17. If our previous findings with respect to $f'(\bar{z})$ and $F(1)$ are substituted in Equation 5.27, then:

$$\frac{v_1/U_o}{r_1/d} = \frac{0.294}{\sqrt{\bar{z} - 0.07}} \tag{5.28}$$

This is seen in Figure 5.18 to be in fair agreement with the data only for $\bar{z} \lesssim 0.5$. The discrepancy is believed to be due, mainly, to the fact that differentiation of $f(\bar{z})$ is involved. Even though our approximate prediction of u_c is reasonably good when applied to u_c as such, it could be in considerable error when prediction of the gradient is attempted. Nevertheless, the analysis has shown the correct dimensionless grouping of parameters, so that v_1 can be predicted using the empirical curve drawn through the data in Figure 5.18.

Furthermore, dividing Equation 5.26 with Equation 5.27, the variation of v is obtained as:

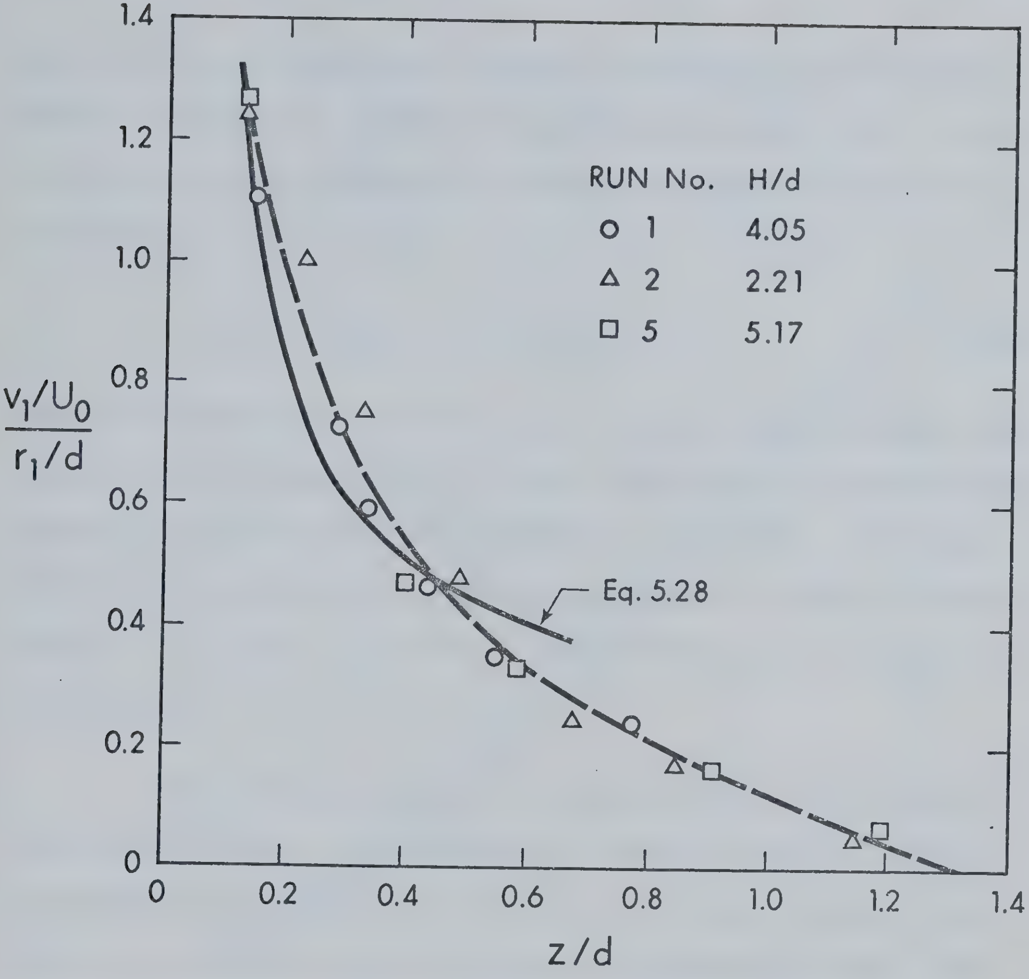

FIGURE 5.18 VARIATION OF v_1

$$\frac{v}{v_1} = \frac{F(\lambda)}{F(1)} = \text{function of } \lambda \text{ only} \tag{5.29}$$

This formulation is verified in Figure 5.19 where the data are seen to define a single curve. Using our previous definition of $F(\lambda)$, it is possible to show that (Appendix D, Section D.2) Equation 5.29 can also be written as:

$$\frac{v}{v_1} = \frac{\lambda}{1.15}\left[1 + 0.15\lambda^2(2 - \lambda^2)\right] \tag{5.30}$$

This is plotted in Figure 5.19 and agrees generally with the data, even though it yields somewhat higher values. Considering the approximations involved in this derivation, the agreement is remarkable. If the flow were not only inviscid but also irrotational, then v would be proportional to r, i.e., $v/v_1 = r/r_1$. This is also shown in Figure 5.19 for comparison.

With these results, it is possible to predict the velocity field within the core. The assumption of inviscid flow and the use of the truncated power series expansion for u has been fruitful, even though this flow model may not be realistic throughout the core. For example, careful examination of the full equations of motion will reveal that some shear stress is likely to develop within the core in the impingement region. At the same time, this flow model is not entirely free of inconsistency. Applying Equation 5.17 at $r = r_1$, this would lead to $u_m - u_c \propto 1/u_c$ which contradicts the relation $u_m - u_c \propto u_c$, that was established before. Yet the former expression yields reasonable answers for not very small values of z/d. It may be stated in conclu-

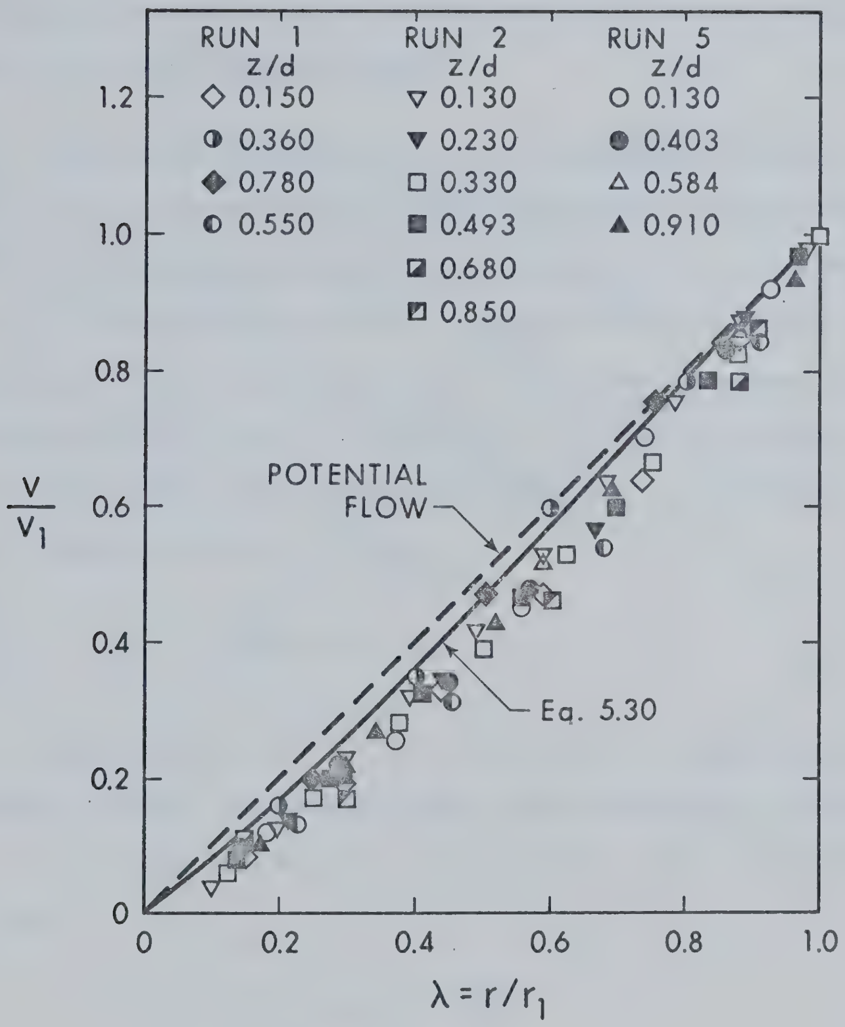

FIGURE 5.19 SIMILARITY OF v IN THE CORE

sion that the inviscid flow model should be regarded as a working hypothesis rather than as an accurate physical representation. It is satisfactory in so far as it has made it possible to analyse the experimental results in a systematic manner.

Considering the shear layer in the impingement region, it is evident that u can be predicted using earlier similarity considerations. For this, it is necessary to know the scales u_m and b. The velocity scale u_m is given in Figure 5.15. In Figure 5.6 it is seen that the length scale b deviates from the linear law in the impingement region. It was shown earlier than $r_1/d = C(\frac{H}{d})f(\frac{z}{d})$, i.e., the two variables H/d and z/d upon which r_1/d depends, are separable. Assuming that a similar relation holds for b, then:

$$\frac{b}{b_o} = \text{function of } z/d \text{ only}$$

with b_o being the value of b at $z = z_o$ (i.e., the beginning of the impingement region). Figure 5.20 verifies this conclusion. The value of b_o can be found from Equation 5.6 by setting $x/d = (H - z_o)/d$, which gives:

$$b_o/d = 0.087(H/d) + 0.006 \qquad (5.31)$$

According to this, the predicted values of b_o/d for runs 1, 2, 5 respectively will be 0.198, 0.358, 0.456, whereas the corresponding experimental values are 0.200, 0.363, 0.445.

After impingement, the flow forms a boundary layer on the wall, beginning at the stagnation point. Denoting the maximum value of v, at

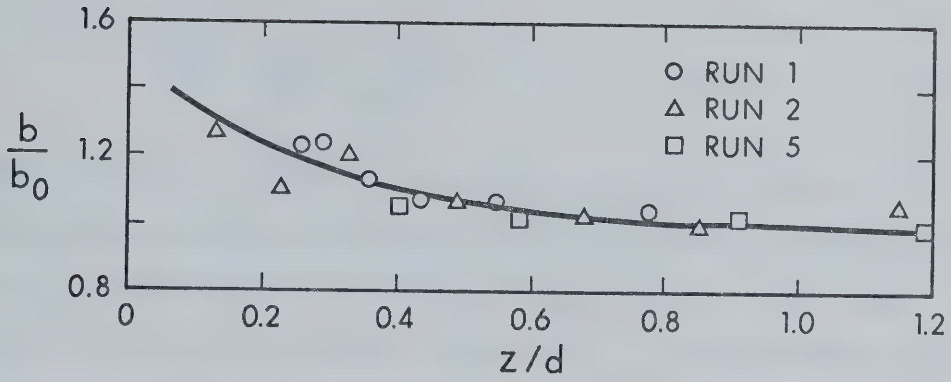

FIGURE 5.20 LENGTH SCALE, IMPINGEMENT REGION

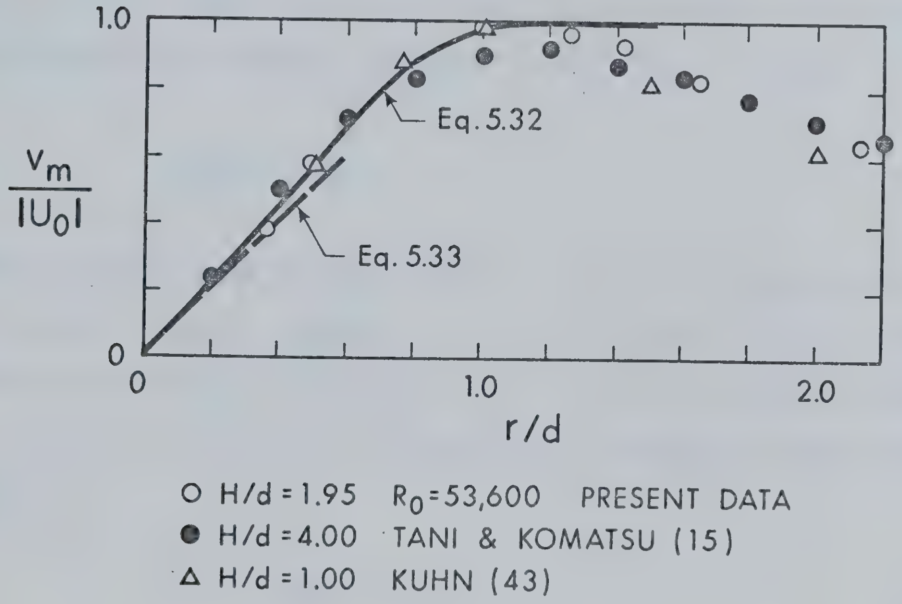

FIGURE 5.21 VARIATION OF v_m

the edge of the boundary layer, by v_m and applying the Bernoulli equation:

$$\frac{v_m}{|U_o|} = \sqrt{1 - \frac{p_w}{\rho U_o^2/2}} \qquad (5.32)$$

Present data on v_m are plotted in Figure 5.21 together with data of other authors (15),(43). It is seen that Equation 5.32 is adequate for $r/d \lesssim 1.0$. Shortly after, the wall jet region begins. It was found earlier (Equation 5.15) that for $z/d \lesssim 0.14$, u_c varies linearly with z with a constant of proportionality (see Section 2.1, Chapter II), $2a = 2|U_o|/d$. That is to say, if ideal fluid stagnation flow occurs in this range, the constant a is equal to $|U_o|/d$, and therefore:

$$\frac{v_m}{|U_o|} = \frac{r}{d} \qquad (5.33)$$

This is also plotted in Figure 5.21 and is seen to be adequate only for $r/d \lesssim 0.14$. Hence, stagnation flow may occur within a small neighbourhood of the stagnation point, with radius 0.14d. Furthermore, using $a = |U_o|/d$ and Equation 2.5 (Chapter II), the boundary layer thickness will be:

$$\frac{\delta}{d} = \frac{1.98}{\sqrt{R_o}} \qquad (5.34)$$

Hrycak's et al (22) data for $H/d = 3$ and $R_o = 54{,}000$, indicate $\left(\frac{\delta}{d}\right)_{r/d \lesssim 1.0} \simeq .017$. At this value of R_o, Equation 5.34 will yield $\frac{\delta}{d} = 0.00835$ which is again (see also Chapter IV) about one-half of the measured value.

Consider now the wall shear stress in the impingement region. Applying the same reasoning as in Chapter IV, it is possible to relate τ_o to the local pressure gradient, i.e.:

$$\tau_o = \frac{1}{r}\int_o^r r\left(\frac{\partial p}{\partial z}\right)_{z=o} dr \qquad (5.35)$$

Since p does not depend upon H/d, τ_o must also be independent of this parameter, i.e.:

$$\frac{\tau_o}{\rho U_o^2/2} = h\left(\frac{r}{d}\right) \qquad (5.36)$$

It follows that the maximum value of τ_o will be:

$$\frac{\tau_{om}}{\rho U_o^2/2} = \text{const} = C_{fm} \qquad (5.37)$$

Dividing:

$$\frac{\tau_o}{\tau_{om}} = h_1\left(\frac{r}{d}\right) \qquad (5.38)$$

This is verified in Figure 5.22, whereas experimental values of C_{fm} are tabulated below.

H/d	R_o	C_{fm}
4.55	53,700	0.0066
4.025	"	0.0066
1.22	"	0.00696
3.64	"	0.00682
1.95	"	0.00710
1.95	30,900	0.00758
4.025	31,000	0.00730

TABLE 5.2

VALUES OF C_{fm}

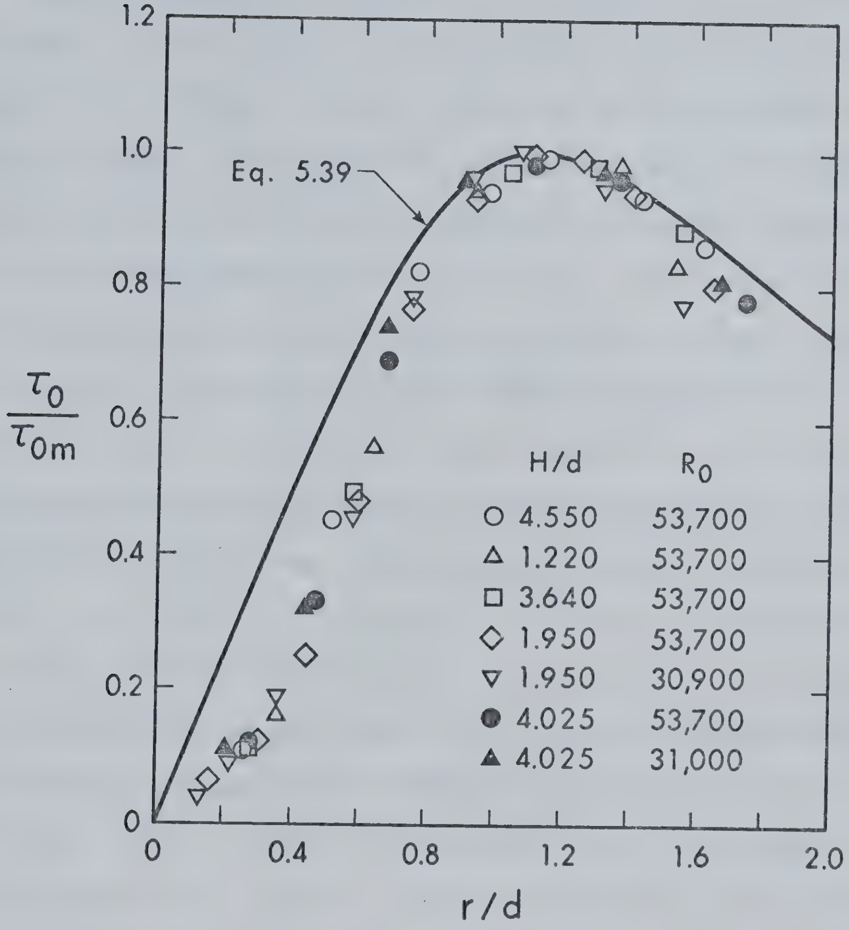

FIGURE 5.22 WALL SHEAR STRESS, IMPINGEMENT REGION

It is seen that C_{fm} is indeed independent of H/d, however, a slight dependence upon R_o seems to be present.

From stagnation flow considerations (Chapter II), it was shown that initially $\tau_o \propto r$. This was found to be the case for large impingement heights (Chapter IV). However, this is not so in the present case, as Figure 5.22 shows, even though a stronger expectation of linearity exists here because there are better chances of the boundary layer being laminar at small impingement heights. This leads to the conclusion that shear stress measurements near the stagnation point are suspect. One source of error is the pressure gradient, which was estimated from Patel's (40) criteria to cause errors larger than 6% for $r/d \lesssim 1.5$. A more significant source of error near the stagnation point is the small thickness of the boundary layer. This was found earlier to be of the order 0.017d, i.e., since $d = .923$ in., $\delta \simeq 0.016$ in. Considering that the outside diameter of the Preston tube was 0.049 in., its center was located outside the boundary layer and, therefore, the present measurements near the stagnation point indicated dynamic heads rather than shear stresses. This is supported by the shape of the shear stress curve at very small r/d, which is roughly of the form $\tau_o \propto r^2$. Since for small values of r, $v_m \propto r$ (Figure 5.21) the dynamic head will be $\rho v_m^2/2 \propto r^2$. The data of Hrycak et al (22) indicate that the center of the Preston tube will be inside the boundary layer for $r/d \gtrsim 2.0$. It follows that the present data on wall shear stress near the stagnation point must be regarded as meaningless. Yet, the data on maximum shear stress τ_{om} are believed to be reasonably accurate. This expec-

tation is supported by the following consideration. The skin friction coefficient, C_{fm}, has an average value of 0.0069 for the present case, whereas for large impingement heights $C_{fm} = 0.32/(\frac{H}{d})^2$. These two variations will become equal at $H/d \simeq 6.8$ which is close to the corresponding value of 7.2 where stagnation pressures for large and small heights become equal. If the theoretical considerations of Appendix D are applied in this case assuming the pressure to be gaussian, the following relation will be obtained:

$$\frac{\tau_o}{\tau_{om}} = 1.47 \left\{ \frac{1}{r/d} [1 - e^{-1.8(r/d)^2}] - \frac{r}{d} e^{-1.8(r/d)^2} \right\} \tag{5.39}$$

This relation is plotted in Figure 5.22 and, in view of the above considerations, it is believed to be more reliable than the data for $r/d \lesssim 0.8$.

5.3.3 Wall Jet Region

In this region the flow assumes the pattern commonly known as the wall jet. In view of previous considerations (Chapter II) the analysis will be merely a demonstration of the fact that this region is independent of the parameter H/d. This can be shown formally (Chapter IV) by assuming that it is influenced by a single kinematic momentum term, $\pi d^2 U_o^2/4$. Thus:

$$\begin{aligned} \delta_2 &= C_2 r \\ \frac{u_m}{U_o} &= \frac{C_u}{r/d} \\ C_f &\equiv \frac{\tau_o}{\rho u_m^2/2} = C_f(R_o) \end{aligned} \tag{5.40}$$

Consider first the velocity scale u_m. The re-analyzed data of Hrycak et al (22), have shown (Chapter IV) that $u_m/U_o = 0.94/(\frac{r}{d} - 1.0)$ for values of H/d equal to 4, 7, 10 and 20. This includes both small and large impingement heights and supports the independent development of the wall jet. For the case H/d = 4, the wall jet region begun at $r_o/d = 2.0$. The results of Yakovlevskii and Krasheninnikov (27) for H/d = 3.5 and 10, also showed no influence of H/d (see also Chapter VII).

Considering the length scale δ_2, Hrycak et al (22) proposed the relation (directly from their data):

$$\delta_2/d = K(r/d)^{0.95} \tag{5.41}$$

where K was given as:

$$K = 0.0864 + 0.00081\ (H/d) \tag{5.42}$$

These were obtained from different experiments using H/d = 2, 4, 10 and 20. Within the range $1.1 \leq H/d \leq 5.5$, K changes from 0.0873 to 0.0908, hence it is permissible to accept an average value of 0.089 and assume K = const, i.e.:

$$\delta_2/d = 0.089\ (r/d)^{0.95} \tag{5.43}$$

This relation is shown plotted in Figure 5.23 for r/d = 4 to 40 which represents the range of experimentation in (22). It is seen that Equation 5.43 can be represented by the linear relation $\delta_2 = .0765r$, i.e.:

$$C_2 = 0.0765 \tag{5.44}$$

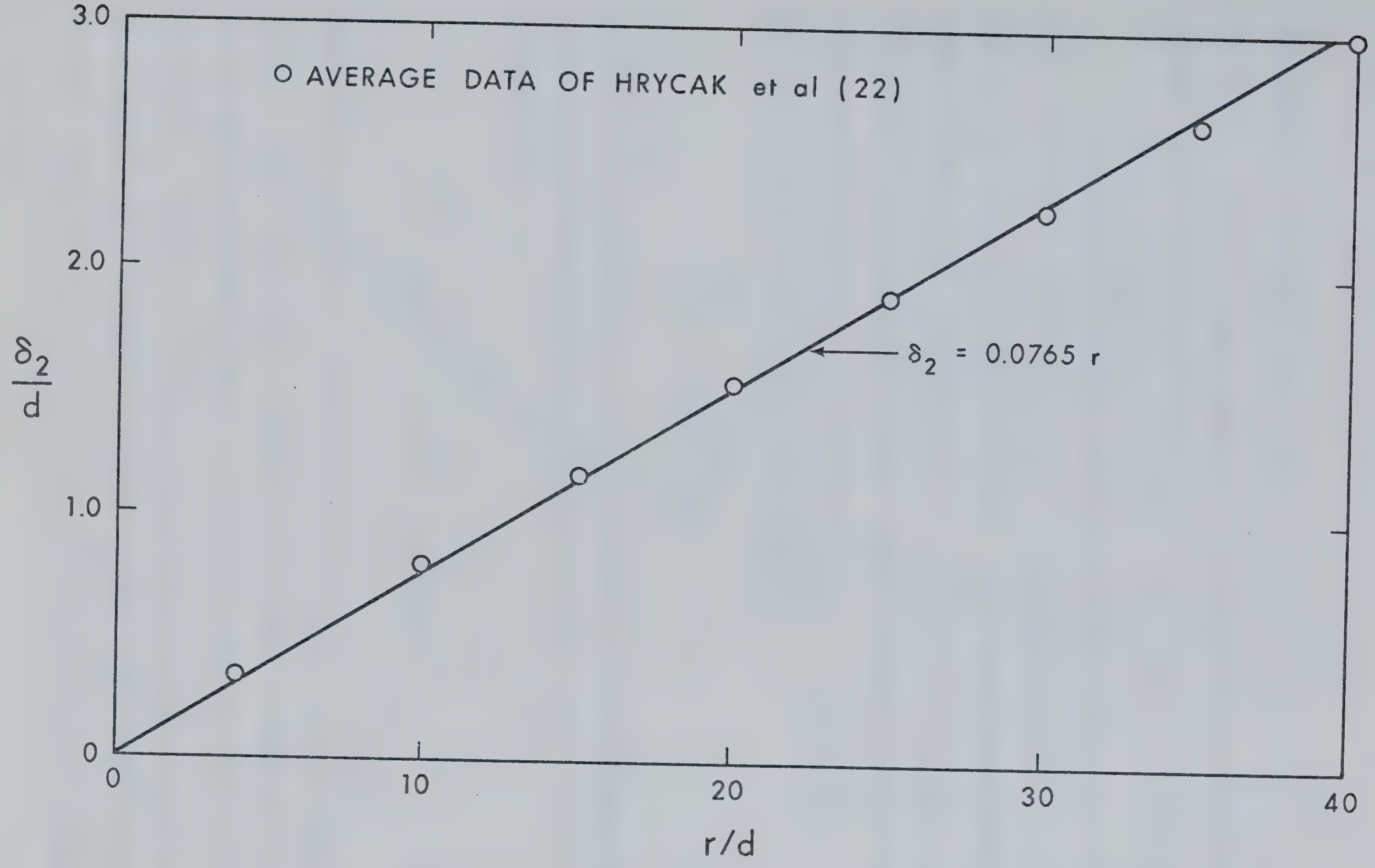

FIGURE 5.23 LENGTH SCALE, WALL JET REGION

The data of (27) show the same trend, but their value of C_2 is slightly lower (C_2 = .075). These values of C_2 are also very close to the average value obtained for large heights, C_2 = .0792 (Chapter IV).

Present data on shear stress are shown in Figure 5.24, where u_*/U_o is plotted against r/d with H/d varying between 1.22 and 4.55 and for R_o equal to 13,800 and 55,300. It is seen that the data define a single curve. Dependence upon R_o cannot be ignored, however, the range of R_o considered is rather small and this dependence cannot be detected in these data. By Equations 5.40, u_* should vary as r^{-1}, and the following relation was found adequate:

$$\frac{u_*}{U_o} = \frac{0.0794}{r/d - 0.3} \tag{5.45}$$

Assuming an average value of C_u = 1.0 (Chapter IV) and neglecting the virtual origin correction, the local skin friction factor C_f will be $2(.0794/1.0)^2$, i.e.:

$$C_f = 0.0126 \quad ; \quad 31,800 \leq R_o \leq 55,300 \tag{5.46}$$

Summarizing this section, it has been shown that the wall jet region begins at $r_o/d \approx 2.0$, and it develops in the same fashion, as in the case of large impingement heights. The only difference lies in the values of r_o and loci of virtual origins which are now related to d rather than to H. A detailed analysis in this region will be presented later (Chapter VII) where the general problem of oblique impingement is dealt with.

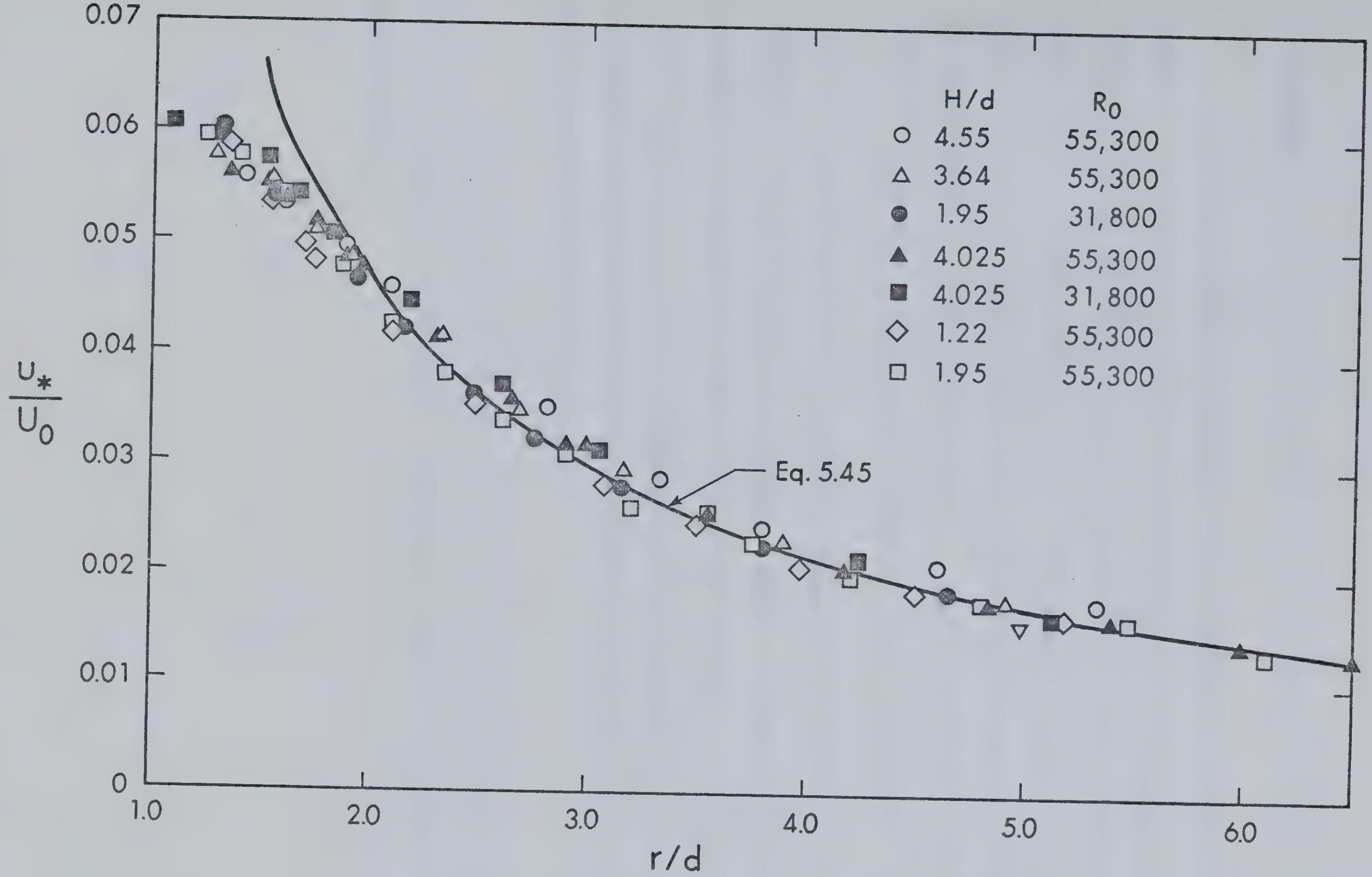

FIGURE 5.24 FRICTION VELOCITY, WALL JET REGION

5.4 Summary

The impingement of developing jets has been considered in this chapter. It was first shown that a given value of H/d can be considered "small" in the interval [1.1, 5.5] whereas it can be considered large if it is greater than about 8.3. The range 5.5 to 8.3 is transitional. Further, it was established that the static pressure, including the wall pressure, is not affected by H. Wall effects extend about 1.25d above the wall and about 1.4d along the wall, regardless of H/d.

It was possible to predict the velocity field in the impingement region, using the inviscid-rotational model as a working hypothesis. Knowledge of the free-jet region is necessary in order to provide information regarding the boundary conditions for the impingement region. An approximate analysis was developed to predict the annular shear layer which yields very simple expressions.

The wall jet region was confirmed to develop independently of H/d, its properties being almost identical to those of large impingement heights.

CHAPTER VI - OBLIQUE IMPINGEMENT OF PLANE TURBULENT JETS

6.1 Introduction

The case of a plane turbulent jet impinging normally has been studied by the author in detail (25),(26). A more general version is obtained if the angle at impingement, ϕ, defined to be the angle between the jet centerline and the wall, is allowed to vary. At present, there is relatively little experimental and theoretical material regarding oblique impingement. Schauer and Eustis (14) have studied mainly the wall jet region. Kamoi and Tanaka (24) were mostly concerned with turbulence characteristics but some wall pressure measurements were included. Mathieu (12) deals with the wall jet region for small angles of impingement ($\phi < 30°$). The present study covers the range $20° \leq \phi \leq 90°$, which is the most important from the practical point of view. In the impingement region, the objectives were to study wall pressure and shear stress, maximum velocity at the edge of the wall boundary layer and to define the limits of this region. No measurements were performed in the wall jet region, however, a simple theoretical treatment is presented and is compared with experimental data of previous investigators.

6.2 Experiments

The experimental set-up has been described in Chapter III. Wall shear stress was obtained using a Preston tube with outside diameter of 0.046 in. and utilizing the calibration curves of Patel (40), as has been explained in Chapter III. A total of 15 experiments were

performed, of which the particulars are summarized in Table 6.1. The symbols appearing in this Table are defined in Figure 6.1.

Run No.	$\phi(°)$	$\frac{H}{d}$	R_o*	Quantities Measured	
				Free Jet Region	Impingement Region
1	60	45.5	12060	u_c	p_w, s, τ_o, u_m
2	60	68.2	12060		"
3	30	45.5	12060		"
4	30	45.5	8550		"
5	30	68.2	8550		"
6	30	68.2	12060		"
7	40	45.5	8550		"
8	40	68.2	12060		"
9	45	68.2	12060	u_c	"
10	45	91.0	12060	u_c	
11	30	91.0	12060	u_c	
12	60	68.2	8550	u_c	
13	60	91.0	12060	u_c	
14	20	68.2	8550	u_c	
15	20	91.0	12060	u_c	

* $R_o \equiv \frac{U_o d}{\nu}$

TABLE 6.1 RANGE OF EXPERIMENTS

6.3 Results and Analysis

6.3.1 Free Jet Region

For normal impingement ($\phi = 90°$), the boundary between free-jet and impingement regions is located at $\xi \simeq 0.7H$ (26). Assuming

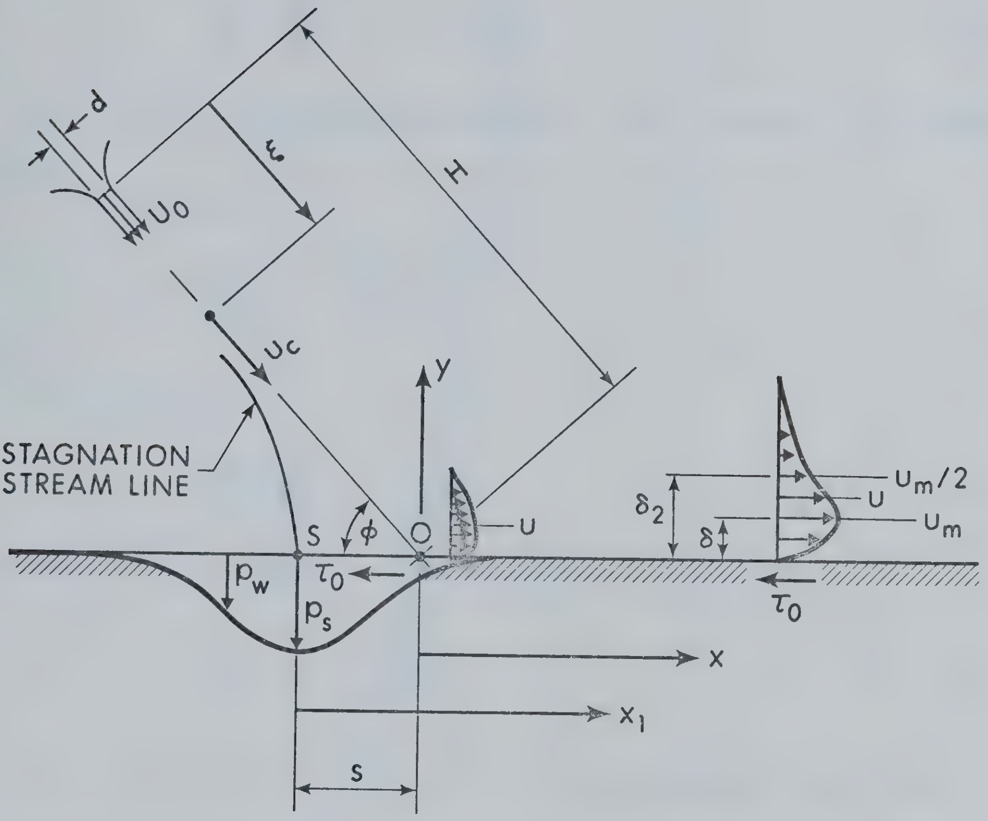
d
U_0
ε
H
U_c
y
STAGNATION STREAM LINE
S
ϕ
O
u
δ_2
δ
$U_m/2$
u
U_m
p_w
τ_0
p_s
τ_0
x
x_1
s

FIGURE 6.1 DEFINITION SKETCH

"large" impingement height, the centerline velocity, u_c, can be written as: $u_c = f(\rho, \rho U_o^2 d, H, \phi, \xi)$. It follows that:

$$\frac{u_c}{U_o} \sqrt{\frac{H}{d}} = f_1(\phi, \frac{\xi}{H}) \tag{6.1}$$

For a free-jet, the corresponding value of axial velocity, u_{cf}, is given by:

$$\frac{u_{cf}}{U_o} = \frac{C_u}{\sqrt{\xi/d}}$$

or:

$$\frac{u_{cf}}{U_o} \sqrt{\frac{H}{d}} = \frac{C_u}{\sqrt{\xi/H}} \tag{6.2}$$

where C_u is a constant. Dividing Equation 6.1 with 6.2:

$$\frac{u_c}{u_{cf}} = f_2(\frac{\xi}{H}, \phi) \tag{6.3}$$

If ξ_o is the value of ξ giving the boundary between free-jet and impingement regions, then one could define ξ_o such that u_c/u_{cf} equals, say, 0.98. Hence:

$$0.98 = f_2(\frac{\xi_o}{H}, \phi)$$

which implies that:

$$\frac{\xi_o}{H} = f_3(\phi) \tag{6.4}$$

All data on u_c are plotted in the form $\frac{u_c}{U_o} \sqrt{\frac{H}{d}}$ vs ξ/H, in Figure 6.2.

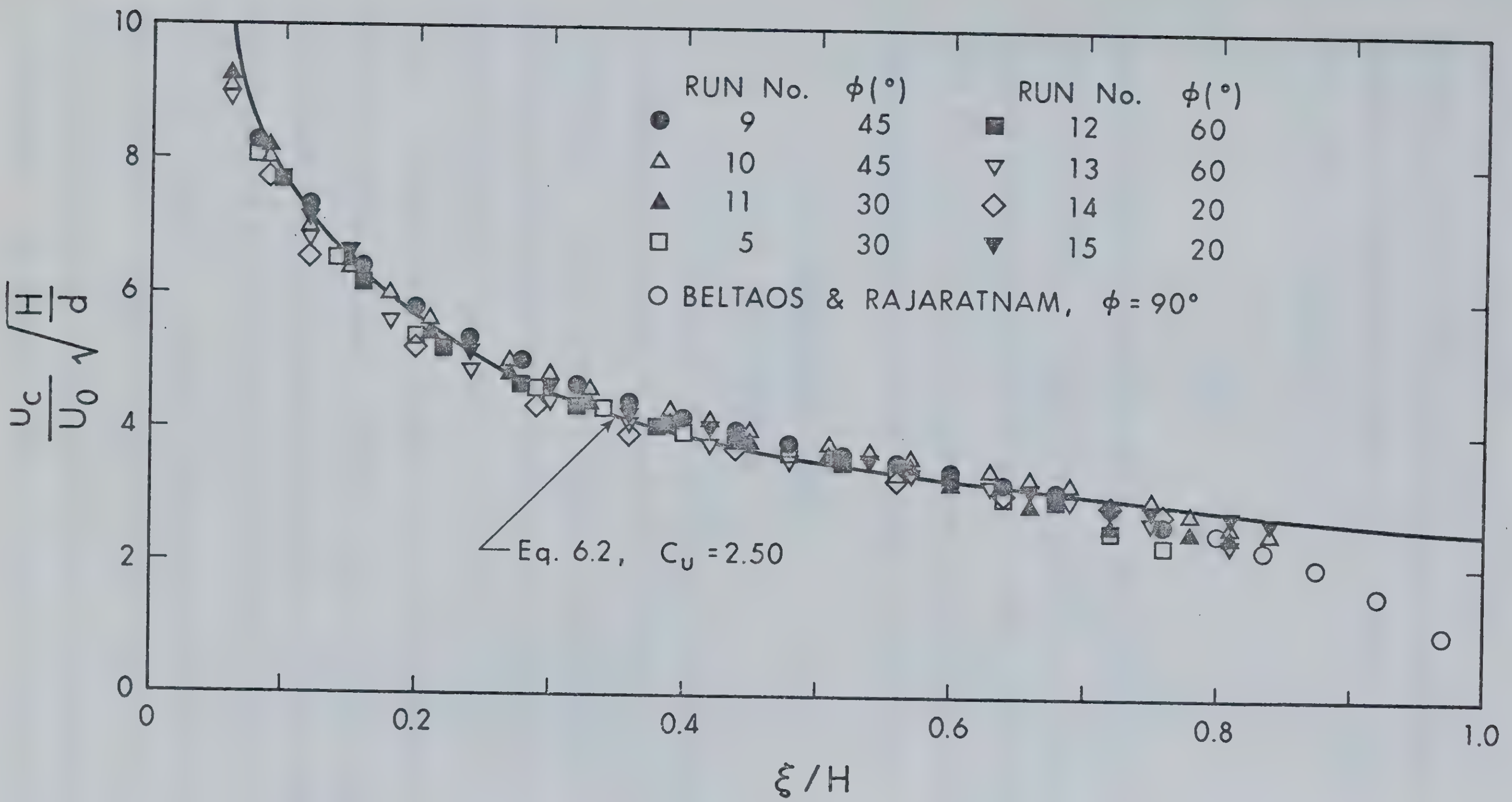

FIGURE 6.2 AXIAL VELOCITY

It is seen, that for $\xi/H \lesssim 0.70$, the data follow the free-jet variation (Equation 6.2) where the constant C_u is taken as 2.50. It follows, that ξ_o/H is independent of ϕ, i.e.:

$$\frac{\xi_o}{H} = 0.70 \tag{6.5}$$

Schauer and Eustis (14) proposed that the distance from the stagnation point to the boundary between these regions is a fixed portion of H. This was verified only for the case $\phi = 90°$ and it obviously contradicts Equation 6.5. The discrepancy is believed to be due to the strong assumptions introduced, as was outlined in Chapter II.

6.3.2 Impingement Region

6.3.2.1 Wall Pressure

Distributions of wall pressure for different angles and heights of impingement are shown in Figure 6.3. The stagnation point, s, which corresponds to the location of maximum wall pressure, is in general removed from the intersection of wall and jet centerline, by a distance s. This is not hard to explain if one considers first the flow of an ideal fluid. In this case, it is known (44) that a stagnation streamline (see Figure 6.1) must intersect a solid boundary at right angles. Assuming that stagnation-type flow occurs at least in a small neighbourhood of the stagnation point for flow of real fluids, as pointed out in (36), then the stagnation streamline will intersect the wall at right angles, which causes the stagnation point to become offset. Figure 6.3 shows that the wall-pressure profiles are skew, the skewness increasing as ϕ decreases. Furthermore, for the angle $\phi = 30°$, the pressure becomes

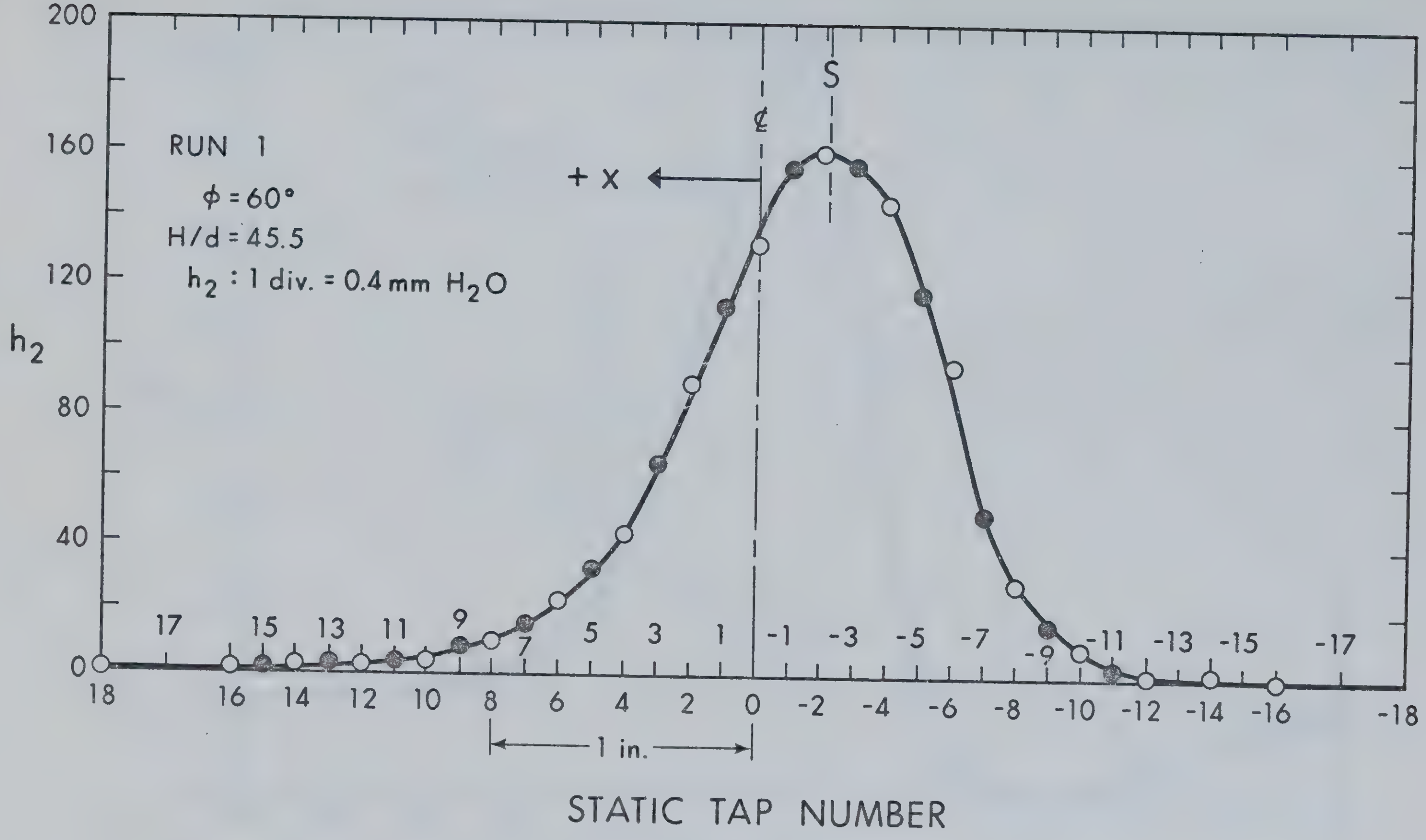

FIGURE 6.3 WALL PRESSURE

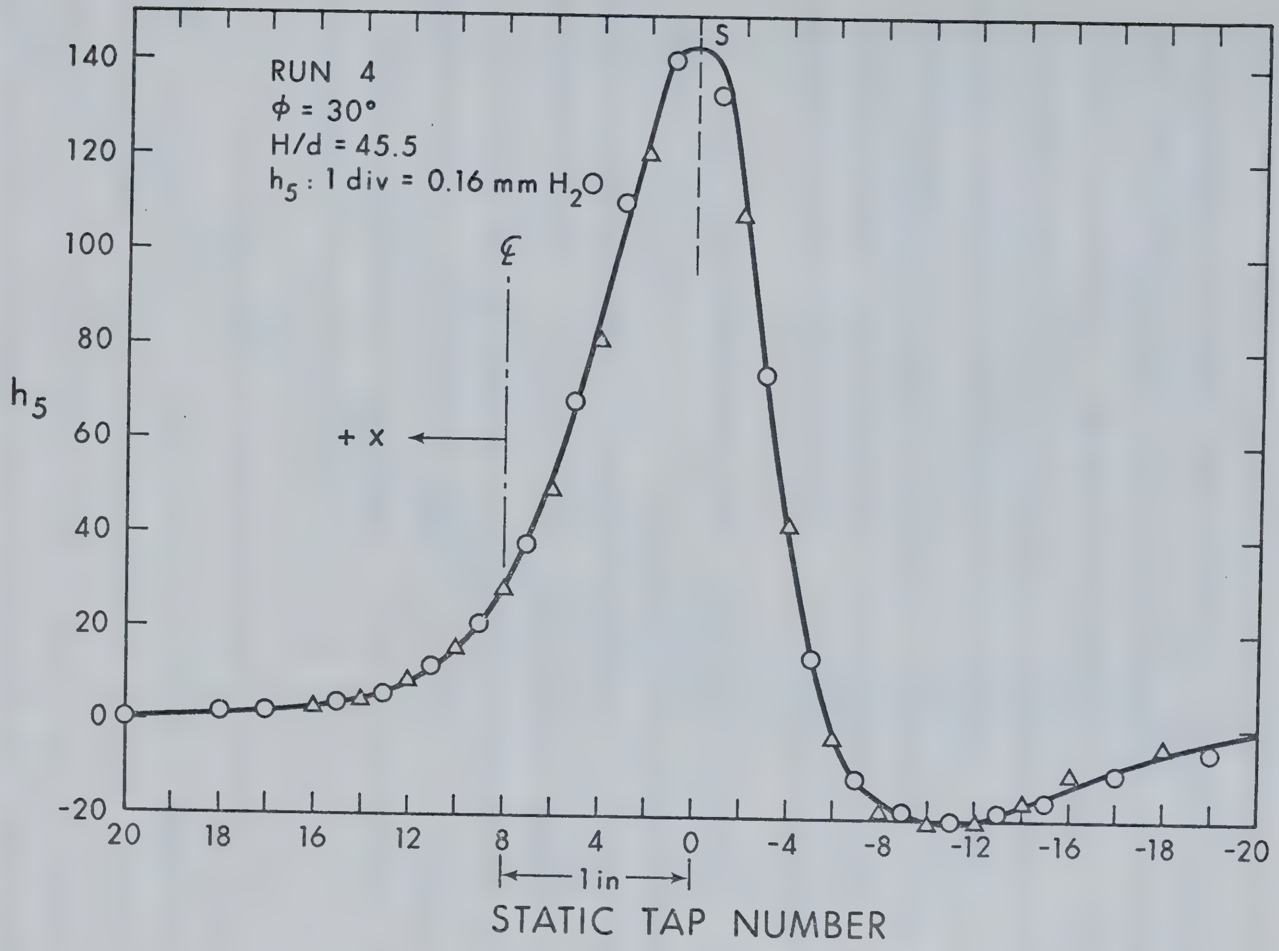

FIGURE 6.3 CONTINUED

negative toward the side of negative x. This is believed to be due to the formation of a vortex. When the angle ϕ becomes sufficiently small, the boundaries of the free jet and the wall jet get so close at the side of negative x, that some of the fluid in the upper layers of the wall jet, which has very low momentum, is entrained into the free jet, thus completing a circulatory motion and forming a vortex. In view of this explanation, it is not surprising that the solution of the corresponding potential flow problem (45) does not predict negative pressures, because it assumes the flow to be irrotational everywhere.

It is now convenient to adopt the following convention. Referring to Figure 6.1, let x_1 be distance along the wall, measured from the stagnation point, so that the positive axis x_1 points towards the right-hand side. In order to avoid use of negative values of x_1 it is observed that the negative axis x_1 will be the same with the positive axis if the impingement angle is made 180° − ϕ. Hence, by referring flow properties in the range $x_1 < 0$, to the case $180 - \phi$, it is possible to use always positive values of x_1.

For pressure profiles that do not exhibit negative values, let b be the value of x_1 for which $p_w = \frac{1}{2} p_s$ (p_s = stagnation pressure). Then, if p_w/p_s is plotted against $\eta \equiv x_1/b$ a single curve results, as shown in Figure 6.4(a). Hence, $p_w/p_s = g(\eta)$ and the function $g(\eta)$ will be the same as that for $\phi = 90°$, which is given by (26):

$$\frac{p_w}{p_s} = g(\eta) = e^{-0.693\eta^2} \qquad (6.6)$$

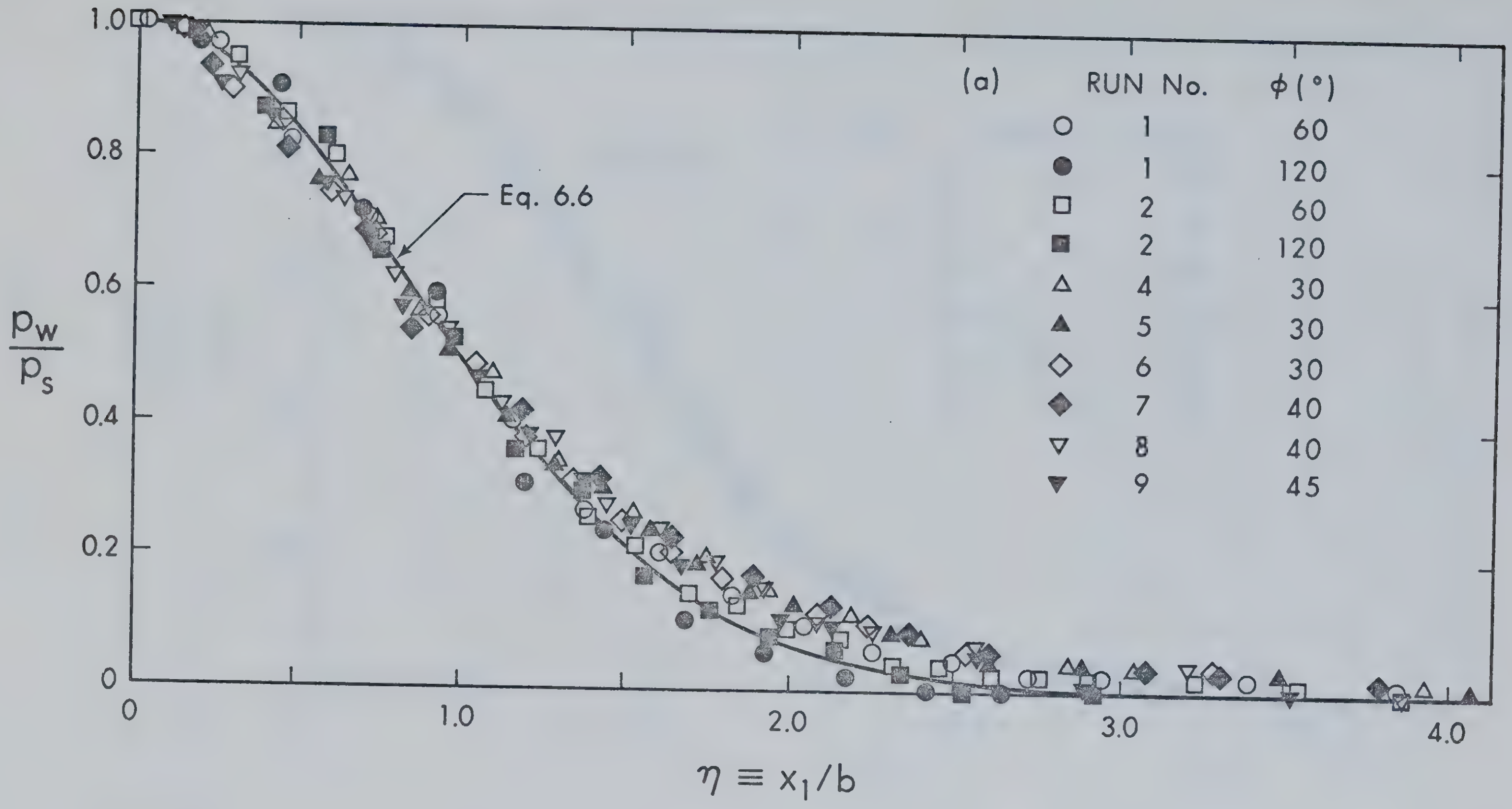

FIGURE 6.4 WALL PRESSURE SIMILARITY

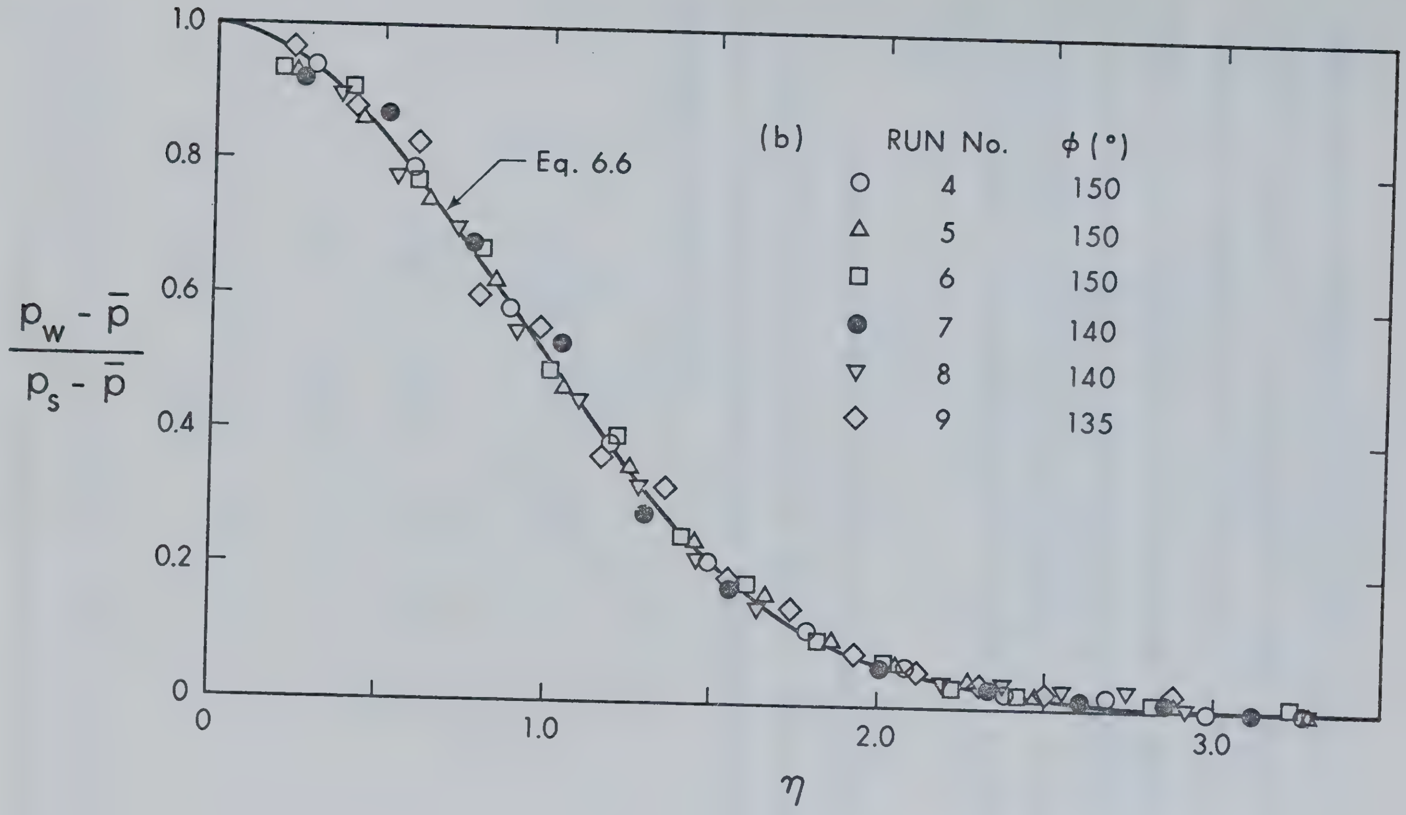

FIGURE 6.4 CONTINUED

Equation 6.6 is also plotted in Figure 6.4(a) and is seen to describe the data adequately for $\eta \lesssim 1.6$, being somewhat low for $\eta \gtrsim 1.6$. This type of similarity has also been reported by Kamoi and Tanaka (24). However, it cannot apply when the profile takes on negative values. If $\overline{p}$ is the minimum value of the profile ($\overline{p} < 0$), then Figure 6.4(b) shows that similarity is preserved if $(p_w - \overline{p})/(p_s - \overline{p})$ is plotted against $\eta = x_1/b$. Here b is defined to be the value of x_1 where $p_w - \overline{p} = \frac{1}{2}(p_s - \overline{p})$.

Complete prediction of the wall pressure requires, in addition, knowledge of the quantities p_s, b, $\overline{p}$ and s. With the same assumptions as in the previous section, these quantities can be shown by dimensional analysis to be:

$$\frac{p_s}{\rho U_o^2/2} \frac{H}{d} = g_1(\phi) \tag{6.7}$$

$$\frac{b}{H} = g_2(\phi) \tag{6.8}$$

$$\frac{s}{H} = g_3(\phi) \tag{6.9}$$

$$\frac{\overline{p}}{p_s} = g_4(\phi) \tag{6.10}$$

The stagnation pressure, p_s, is shown to agree with the formulation of Equation 6.7 in Figure 6.5. Schauer and Eustis (14) gave the relation:

$$\frac{p_s}{\rho U_o^2/2} \frac{H}{d} = 8 \sin \phi \tag{6.11}$$

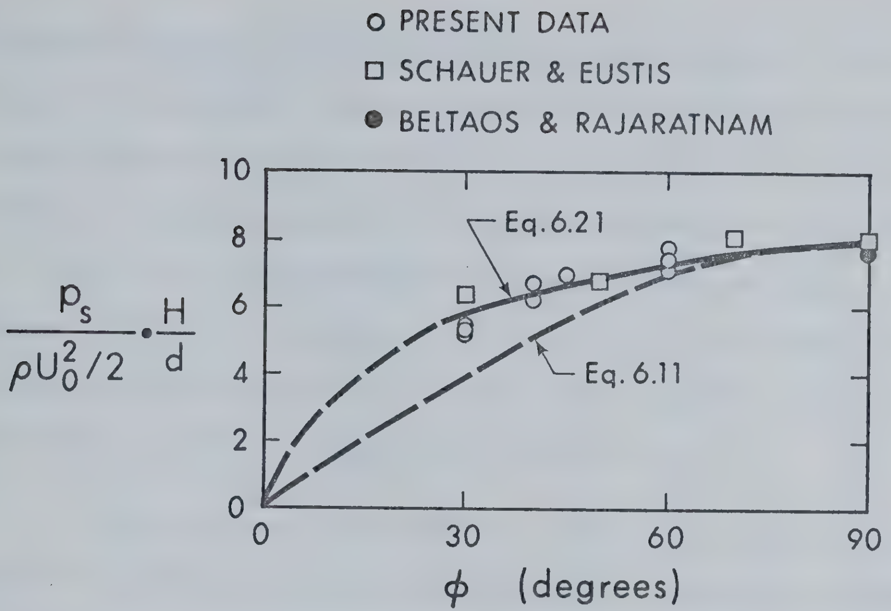

FIGURE 6.5 STAGNATION PRESSURE

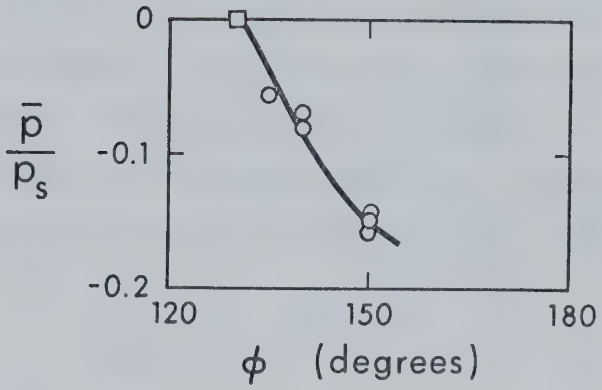

FIGURE 6.6 MINIMUM PRESSURE

which was derived by equating the integral of wall pressure to the normal component of momentum. However, the derivation was based on the assumption of symmetric wall pressure distribution, which does not allow for skewness or negative pressures for the lower values of ϕ and, therefore, it is only a crude approximation of reality as shown in Figure 6.5. Figure 6.6 shows the variation of $\overline{p}/p_s$ with ϕ. It is seen that negative pressures do not occur in the range $\phi \lesssim 130°$, whereas at $\phi = 150°$, $\overline{p}$ becomes a significant fraction of p_s.

The variation of the relative length scale, b/H, is shown in Figure 6.7. (The present data were obtained for values of H/d equal to 45.5 and 68.2, whereas the data of Schauer and Eustis were obtained for the values of H/d equal to 20, 30 and 40. The data of Kamoi and Tanaka were taken at H/d = 12 and 16.) In the range $30° \leq \phi \leq 90°$, b/H is seen to change very slightly. However, for $\phi > 90°$ the variation of b/H with ϕ is more significant, and the following empirical relation was found to be in reasonable agreement with data:

$$\frac{b_\phi}{b_{180-\phi}} = \left(\frac{180 - \phi}{90}\right)^{\frac{1}{4}} \quad ; \ \phi \geq 90° \qquad (6.12)$$

Figure 6.8 shows the relative eccentricity, s/H, of the stagnation point as a function of ϕ. Schach (45) has given the ideal flow solution for an impinging jet of finite width. The resulting expression for the eccentricity s is of a very complex nature and is shown graphically in Figure 6.9, where d_p denotes the width of the jet at an infinite distance from the wall. In the range $30° \leq \phi \leq 90°$ this relation is almost linear, i.e.:

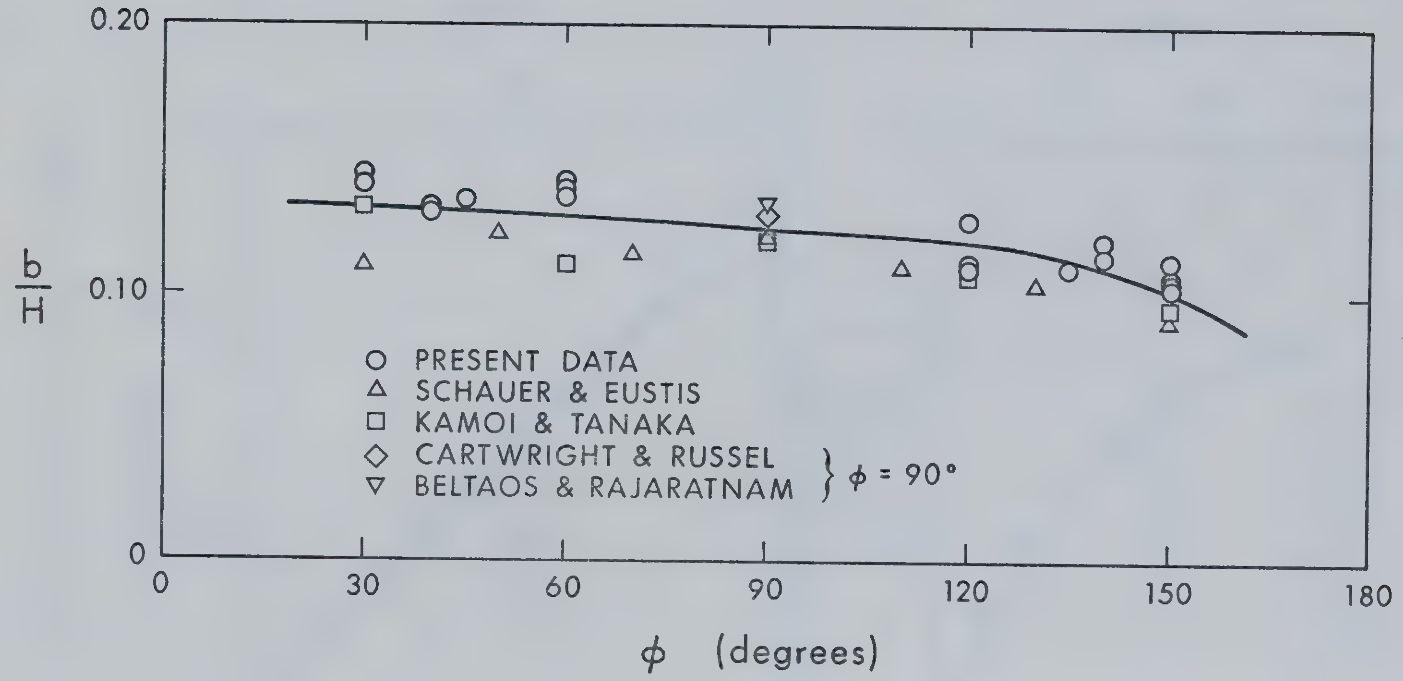

FIGURE 6.7 LENGTH SCALE FOR WALL PRESSURE

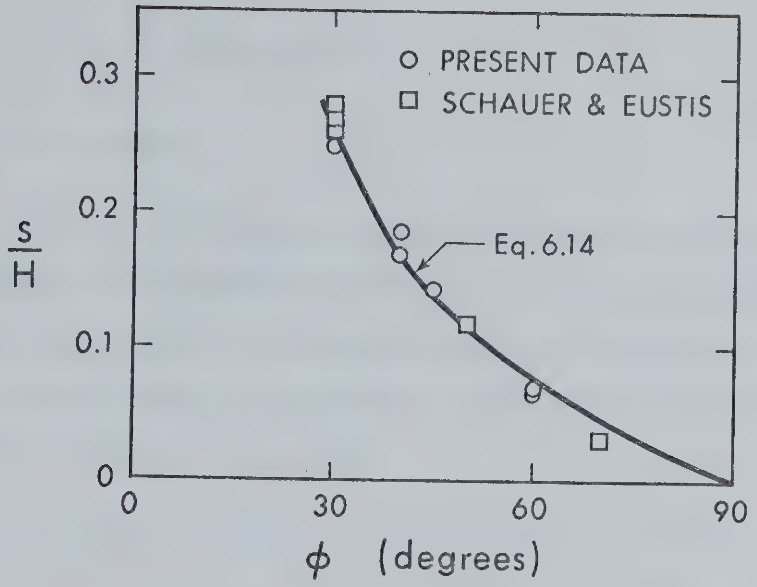

FIGURE 6.8 ECCENTRICITY OF STAGNATION POINT

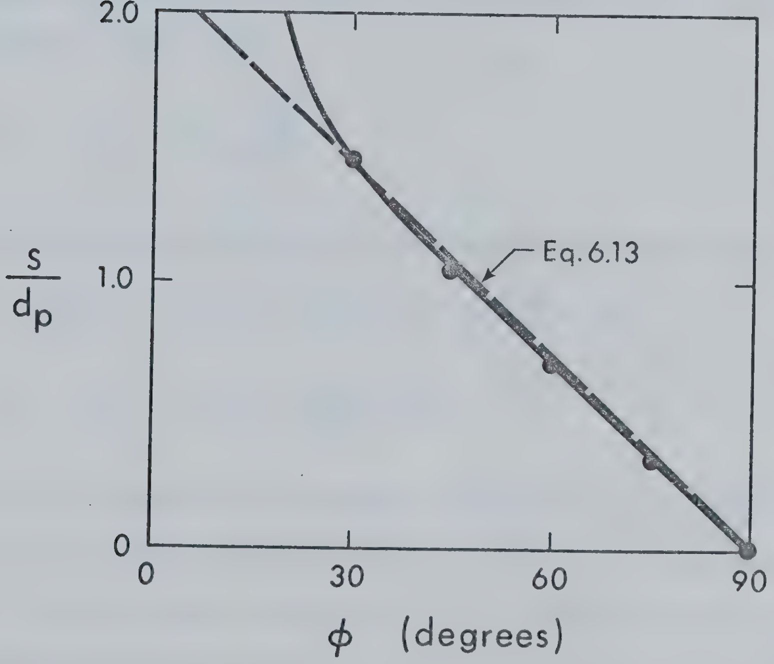

FIGURE 6.9 ECCENTRICITY FOR POTENTIAL JET

$$\frac{s}{d_p} = 2.15(1 - \frac{\phi}{90}) \qquad (6.13)$$

where ϕ is in degrees.

In order to use this equation for the present results, it is required that the corresponding potential jet has the same initial momentum and produces the same stagnation pressure as the real jet. Letting U be the velocity at infinity of the potential jet, then the following relations must be satisfied:

$$\rho U_o^2 d = \rho U^2 d_p \quad ; \quad p_s = \rho U^2/2$$

Using these conditions and the approximate expression for p_s (Equation 6.11) it can be shown that:

$$\frac{s}{H} \propto \frac{1 - \frac{\phi}{90}}{\sin \phi}$$

The experimental data indicate that this relation is satisfactory, the constant of proportionality being equal to 0.194, i.e.:

$$\frac{s}{H} = 0.194(1 - \frac{\phi}{90})/\sin \phi \qquad (6.14)$$

With the above results, it is possible to predict the wall pressure up to the point where the minimum pressure, $\bar{p}$, occurs. An approximate prediction of pressure beyond this point can be derived by assuming that this pressure is essentially due to a point vortex located a distance a above the wall. If Γ is the strength of the vortex, the wall pressure p_w at a distance ℓ from the projection of the vortex on the wall, is

given by (see Appendix D, Section D.3):

$$\frac{p_w}{\bar{p}} = [1 + (\frac{\ell}{a})^2]^{-2} \qquad (6.15)$$

If ℓ_2 is the value of ℓ where $\frac{p_w}{\bar{p}} = \frac{1}{2}$:

$$\frac{p_w}{\bar{p}} = [1 + 0.41(\frac{\ell}{\ell_2})^2]^{-2} \qquad (6.16)$$

The available data have shown that Equation 6.16 is a reasonable approximation. If $\bar{\eta}$, η_2 are the values of η where the minimum pressure, $\bar{p}$, and its one-half value occur, the present data indicate that $\bar{\eta} \cong 3.1$ and $\eta_2 \cong 5.1$. Since $\ell = (\eta - \bar{\eta})b$, Equation 6.16 can also be written as:

$$\frac{p_w}{\bar{p}} = [1 + 0.1025(\eta - \bar{\eta})^2]^{-2} \qquad (6.17)$$

It is now possible to derive an Equation for the stagnation pressure, p_s, by equating the integral of the wall pressure to the normal component of the initial momentum of the jet:

$$\int_{-\infty}^{\infty} p dx_1 = \rho U_o^2 d \sin \phi \qquad (6.18)$$

Using the previous expressions, it is possible to show (see Appendix D, Section D.4) that the above equation reduces to:

$$\frac{p_s}{\rho U_o^2/2} \frac{H}{d} = \frac{2 \sin \phi}{\left(\frac{b_1 + b_2}{H}\right) + 4.55\beta\left(\frac{b_2}{H}\right)} \qquad (6.19)$$

where β is the ratio $\overline{p}/p_s$ and b_1, b_2 are the values of b for the positive and negative sides of x_1 respectively. Note that this notation was introduced in order to restrict ϕ in the range of values less than 90°, since p_s is the same for supplementary angles. In this notation, the empirical relation expressed by Equation 6.12 can also be written as:

$$\frac{b_2}{b_1} = \left(\frac{\phi}{90}\right)^{1/4} \quad ; \quad \phi \leq 90° \tag{6.20}$$

Introducing this into Equation 6.19, the stagnation pressure becomes:

$$\frac{p_s}{\rho U_o^{\,2}/2} \; \frac{H}{d} = \frac{2 \sin \phi}{\frac{b_1}{H}\left\{1 + \left(1 + 4.55\frac{\overline{p}}{p_s}\right) \sqrt[4]{\frac{\phi}{90}}\right\}} \tag{6.21}$$

With the aid of the graphs of Figures 6.6 and 6.7, the above is plotted in Figure 6.5 and is seen to agree with the data reasonably well. This serves as a check of the presented results on pressure distribution.

It remains to determine the extent of the impingement region along the wall. Letting $\overline{x}_1$ denote the end of the impingement region, $\overline{x}_1$ could be defined as that value of x_1 where $|p| = 0.02\, p_s$. When negative pressures occur $\overline{x}_1$ will not be single valued. Hence, an additional restriction is imposed on $\overline{x}_1$, i.e., it should be the largest value of x_1 satisfying the above condition. The results show that $\overline{x}_1/H$ depends upon ϕ, as indicated in the following table.

$\phi(°)$	$\overline{x}_1/H$
30	0.490
45	0.400
60	0.345
90	0.310
120	0.275
133.5	0.355
150	0.700

TABLE 6.2 EXTENT OF IMPINGEMENT REGION

The value of $\overline{x}_1/H$ increases for decreasing ϕ in the range ($\phi < 130°$), owing to the "flattening" of the pressure profile and to increasing values of b. This trend is reversed in the range $\phi > 130°$, owing to the occurrence of negative pressures which cause the impingement region to be considerably longer than it would be in their absence. It is noteworthy that in this latter range ($\phi > 130°$) values of $\overline{x}_1/H$ predicted from Equation 6.17 are in good agreement with tabulated values which were determined directly from the data.

6.3.2.2 Wall Shear Stress

Typical wall shear stress variations are shown in Figure 6.10. When $\phi < 90°$ measurements with a Preston tube present no difficulty. However, when $\phi > 90°$, it is not possible to use an ordinary probe because the inclined nozzle leaves little room for equipment. A special probe was built to accommodate this configuration as shown in the following sketch. However, the length of the suspended part of the probe becomes enormous and measurement is not as accurate as with an

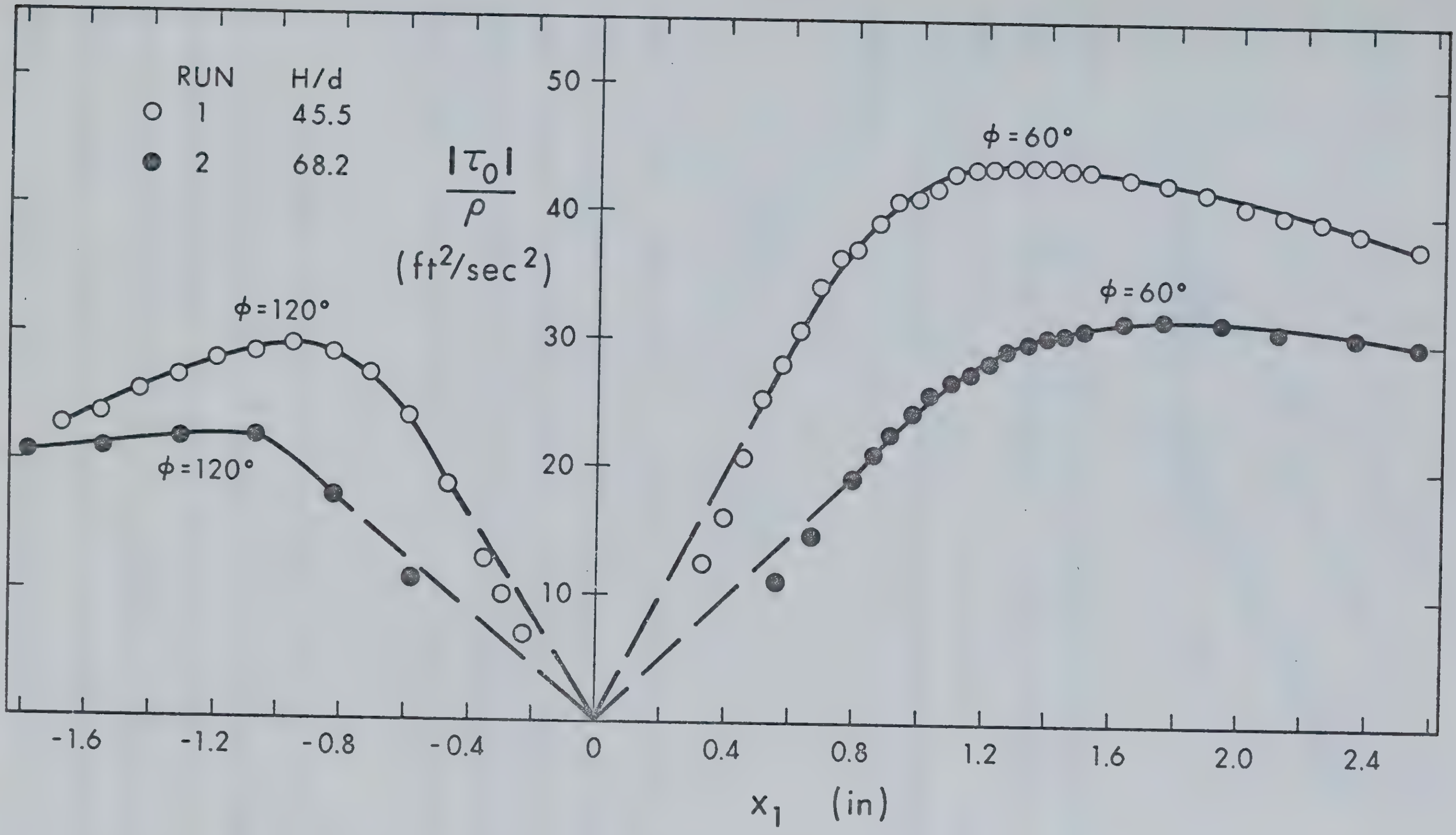

FIGURE 6.10 WALL SHEAR STRESS

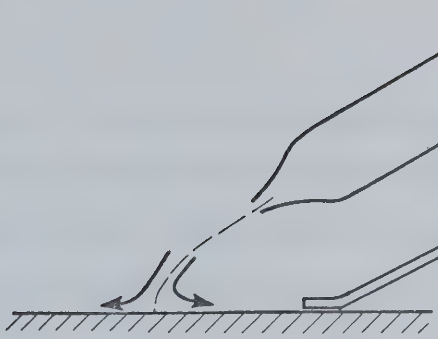

ordinary probe. This consideration is demonstrated clearly in Figure 6.10. Considering the shear stress τ_o to be positive for $x_1 > 0$, then it will be negative for $x_1 < 0$, and naturally τ_o must vary with x_1 in a continuous manner. Therefore, the following condition must be satisfied:

$$\left(\frac{d\tau_o}{dx_1}\right)_{x_1 \to 0^+} = \left(\frac{d\tau_o}{dx_1}\right)_{x_1 \to 0^-}$$

where $x_1 \to 0^+$ means that x_1 approaches zero from positive values. Hence, in the graphs of Figure 6.10 the slopes of $|\tau_o|/\rho$ for supplementary angles of impingement should be identical. Inspection shows that this is not the case, the deviations increasing with decreasing ϕ. Thus, shear stress measurements for $\phi > 90°$ must be regarded as approximate.

In order to predict the wall shear stress the same reasoning will be applied as that used in Chapter IV. It is firstly assumed that the stagnation streamline intersects the wall at right angles. This is not unreasonable in view of previous considerations (see Section 6.3.2.1). If the equations of motion are written in a curvilinear system (t_1, t_2) where t_1 is distance along the stagnating streamline and t_2 is distance

perpendicular to it, then some curvature terms will arise. However, since the stagnation streamline intersects the wall at right angles, the curvature terms will vanish very near the wall and the coordinate system (t_1, t_2) will coincide with the system (y, x_1) shown in Figure 6.1. Using similar reasoning as in Chapter IV, one could write:

$$\frac{d\tau_o}{dx_1} = \left(\frac{\partial p}{\partial y}\right)_{y = o} \tag{6.22}$$

(See also Appendix D, Section D.1.2)

For the case of normal impingement, it was found (26) that pressure distributions were geometrically similar with scales p_c and b_p, where p_c was the centerline value and b_p was the value of x_1 where $p/p_c = 0.5$. Assuming this to hold when $\phi \neq 90°$, with p_c being the value of pressure on the stagnating streamline, one could write:

$$p = p_c g(\eta_p) \quad ; \quad \eta_p = x_1/b_p \quad ; \quad g = e^{-k\eta_p^2} \quad ; \quad k = 0.693 \tag{6.23}$$

Using Equations 6.22 and 6.23 it is possible to show that (see Appendix D, Section D.1.2):

$$\tau_o/\tau_{om} = \mathrm{erf}(\sqrt{k}\,\eta) - C_1 \eta g(\eta) \tag{6.24}$$

$$\frac{\tau_{om}}{\rho U_o^2/2} \frac{H}{d} = h(\phi) \tag{6.25}$$

where τ_{om} is the maximum value of τ_o and C_1 is a coefficient which depends on ϕ. The functions C_1 and h are left to be determined empirically. Obviously, Equation 6.24 cannot be expected to hold when

negative pressures occur. Figure 6.11 shows the data plotted according to the formulation of Equation 6.24. It appears that a single curve can describe these data well, choosing $C_1 = 0.2$. The variation of C_1 with ϕ can be obtained directly from the data, using Equation 6.24 and working backwards. This would show that C_1 does vary somewhat with ϕ. However, the term associated with C_1 in Equation 6.24 represents a small correction and for prediction purposes, an average value of C_1 is sufficient.

When negative pressures occur ($\phi > 130°$) the above analysis is not valid. This is demonstrated in Figure 6.12, where data for $\phi = 150°$ are only crudely approximated by Equation 6.24. Considering the maximum shear stress, τ_{om}, dimensional analysis will show that:

$$\frac{\tau_{om}}{\rho U_o^2/2} \frac{H}{d} = \overline{h}(\phi, R_H) \tag{6.26}$$

where $R_H \equiv R_o \sqrt{\frac{H}{d}}$. However, the effect of viscosity on τ_{om} appears to be negligible, as was also found in Chapter IV, so that Equation 6.26 agrees in essence with theoretical predictions (Equation 6.25). This is verified in Figure 6.13 where data, covering a range of R_H from about 20,000 to about 270,000, define a single curve. In the range $\phi > 90°$, an increasing error should be expected to be inherent in the data of Figure 6.13, according to previous considerations. A correction can be applied if it is assumed that the error is proportional to the measured value of shear stress. For the case $\phi = 120°$, this correction amounts to about 20% of the measured value as shown in Figure 6.13. It

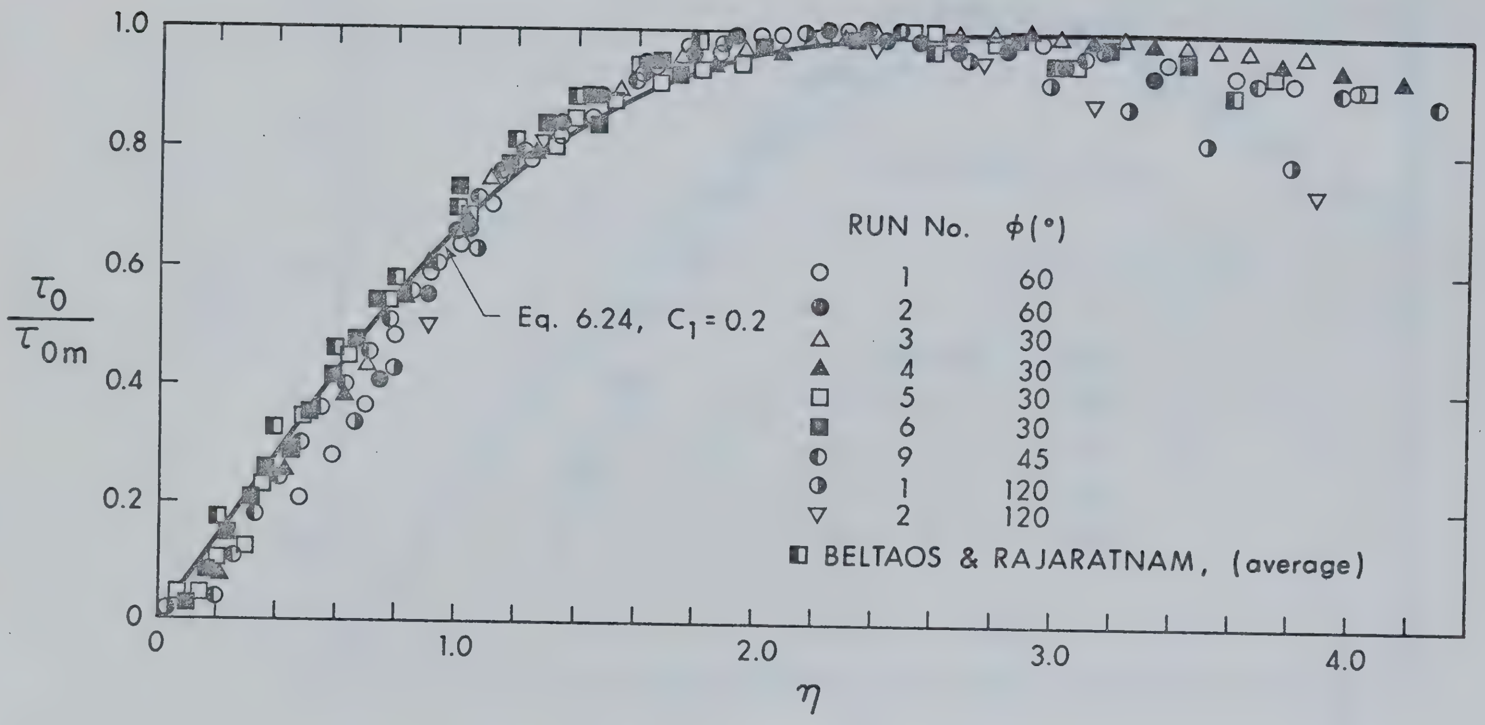

FIGURE 6.11 WALL SHEAR SIMILARITY, IMPINGEMENT REGION $\phi < 130°$

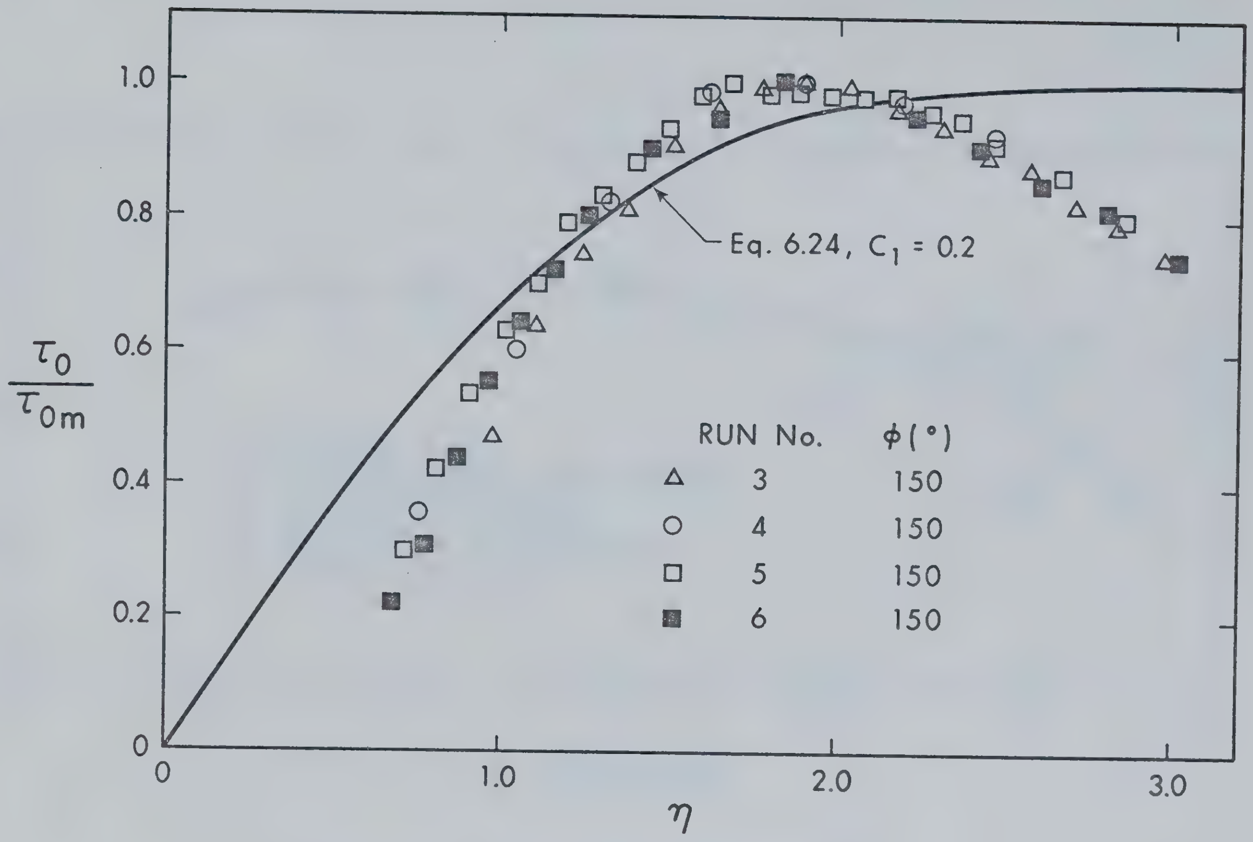

FIGURE 6.12 WALL SHEAR ϕ > 130°

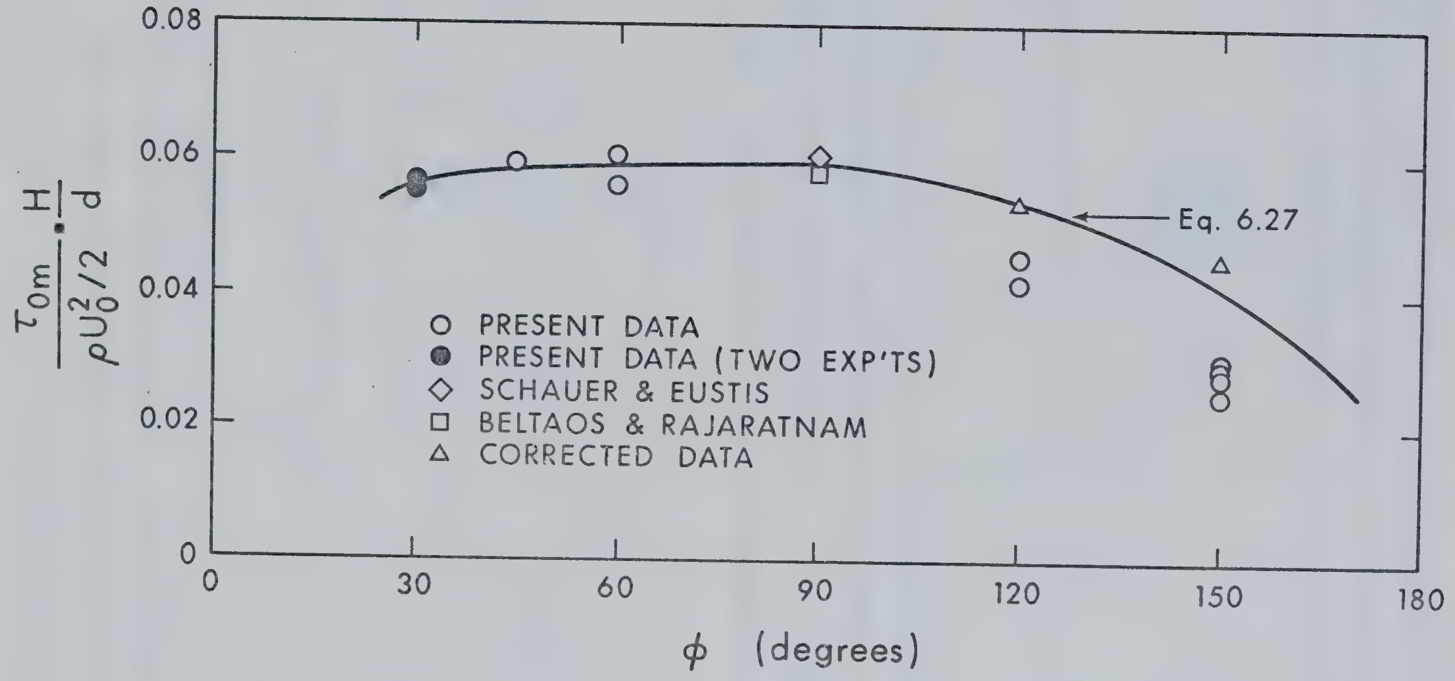

FIGURE 6.13 MAXIMUM WALL SHEAR STRESS

can be shown (Appendix D, Section D.1.2, Equation D.28) that the maximum shear stress at the side of negative x_1 is related to the corresponding value at the side of positive x_1 by the equation:

$$\frac{(\tau_{om})_2}{(\tau_{om})_1} = \frac{b_2}{b_1} \tag{6.27}$$

This is shown plotted in Figure 6.13, where it appears to agree with the corrected data.

Finally, owing to the presence of strong pressure gradients, the present measurements of wall shear stress are likely to involve errors greater than 6% (see Chapter III) when η is less than a limiting value, η_c. This depends on ϕ and is tabulated below.

ϕ(°)	η_c
30	1.9
60	2.0
90	2.1
120	2.2
150	2.4

TABLE 6.3 VALUES OF η_c

6.3.2.3 Maximum velocity, u_m

Begining at the stagnation point, a boundary layer grows at the wall. If the value of longitudinal velocity at the edge of the boundary layer is denoted by u_m, Figure 6.14 shows typical variations

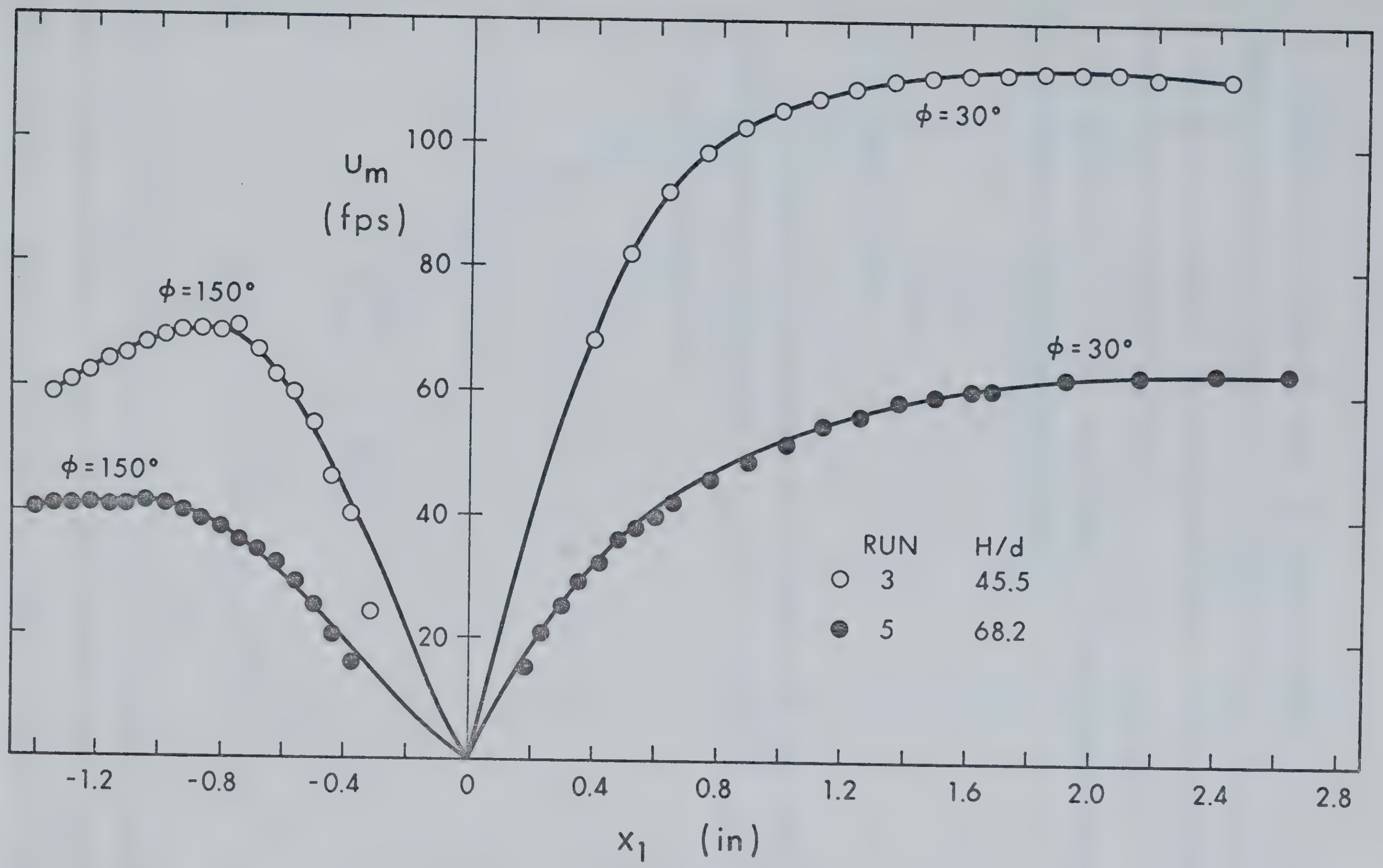

FIGURE 6.14 TYPICAL VARIATION OF u_m, IMPINGEMENT REGION

of this quantity. It is seen that u_m increases from zero at the stagnation point, to a maximum value and then decreases continuously. Regarding the accuracy of the data in the range $\phi > 90°$, considerations similar to these with respect to wall shear are valid. If u_{max} is the maximum value of u_m, then Figure 6.15 shows that profiles of u_m are geometrically similar in the sense:

$$\frac{u_m}{u_{max}} = f_u(\eta) \tag{6.28}$$

in the range $\phi < 130°$.

Beltaos (25) and Beltaos and Rajaratnam (26) have shown that in the case of normal impingement, u_m can be predicted by application of Bernoulli's equation, i.e.:

$$\frac{\rho u_m^2}{2} + p_w = p_s \quad ; \quad \phi = 90° \tag{6.29}$$

This can also be written as:

$$\frac{u_m}{u_{max}} = 1 - \left(\frac{p_w}{p_s}\right)^{1/2}$$

or

$$\frac{u_m}{u_{max}} = [1 - \exp(- 0.693\eta^2)]^{1/2} \tag{6.30}$$

Equation 6.30 is known to be valid for $\phi = 90°$. However, since Equation 6.28 holds for all ϕ less than 130°, it follows that $f_u(\eta)$ has the form given by Equation 6.30. This is plotted in Figure 6.15 and is seen to describe the data reasonably well. Yet, in the range $\phi > 130°$,

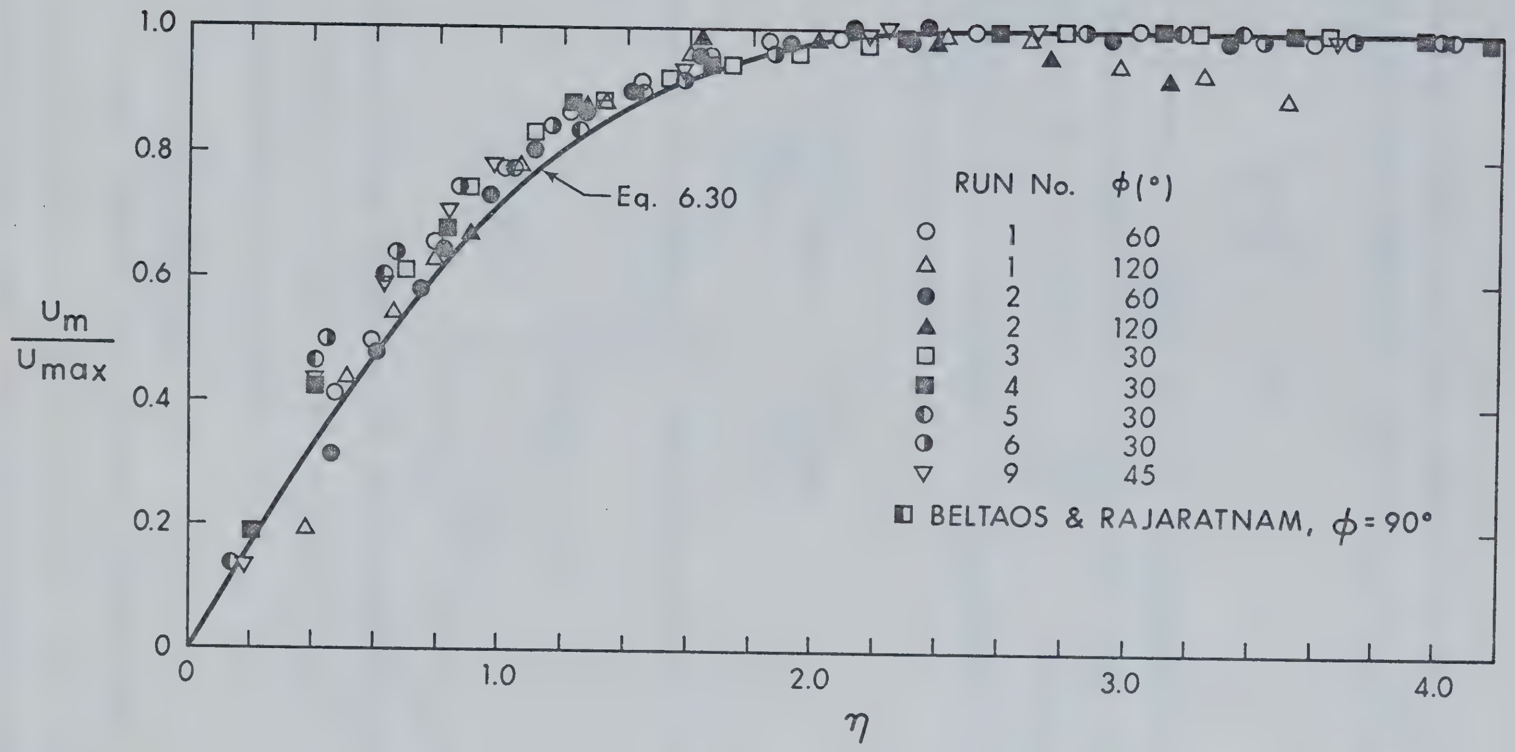

FIGURE 6.15 SIMILARITY OF u_m, $\phi < 130°$

this equation is only a rough approximation to the data, as seen in Figure 6.15a. From dimensional considerations, it can be shown that:

$$\frac{u_{max}}{U_o}\sqrt{\frac{H}{d}} = \bar{f}(\phi) \tag{6.31}$$

and this is verified in Figure 6.16. It is noteworthy that for $\phi \leq 90°$, $\bar{f}(\phi)$ is approximately a constant equal to 2.8. Since u_m is a continuous function of x_1, the value of $\left(\frac{du_m}{dx_1}\right)_{x_1 = 0}$ must be the same for supplementary angles of impingement. Using Equations 6.30 and 6.31, this condition can be expressed as:

$$\frac{(u_{max})_{180-\phi}}{(u_{max})_{\phi}} = \frac{(b)_{180-\phi}}{(b)_{\phi}} \tag{6.32}$$

This together with Equation 6.12, leads to the following summary for u_{max}:

$$\frac{u_{max}}{U_o}\sqrt{\frac{H}{d}} = \begin{cases} 2.8, \text{ for } \phi \leq 90° \\ 2.8 \left(\frac{180 - \phi}{90}\right)^{1/4}, \text{ for } \phi \geq 90° \end{cases} \tag{6.33}$$

This is shown plotted in Figure 6.16. The discrepancy between predicted values and data in the range $\phi > 90°$, is likely to be due to the inaccuracy of measurements in this range.

6.3.3 Wall Jet Region

A short distance after the end of the impingement region, the flow assumes the familiar pattern of the wall jet. As no measurements were performed in this region, this section is mainly an attempt to re-

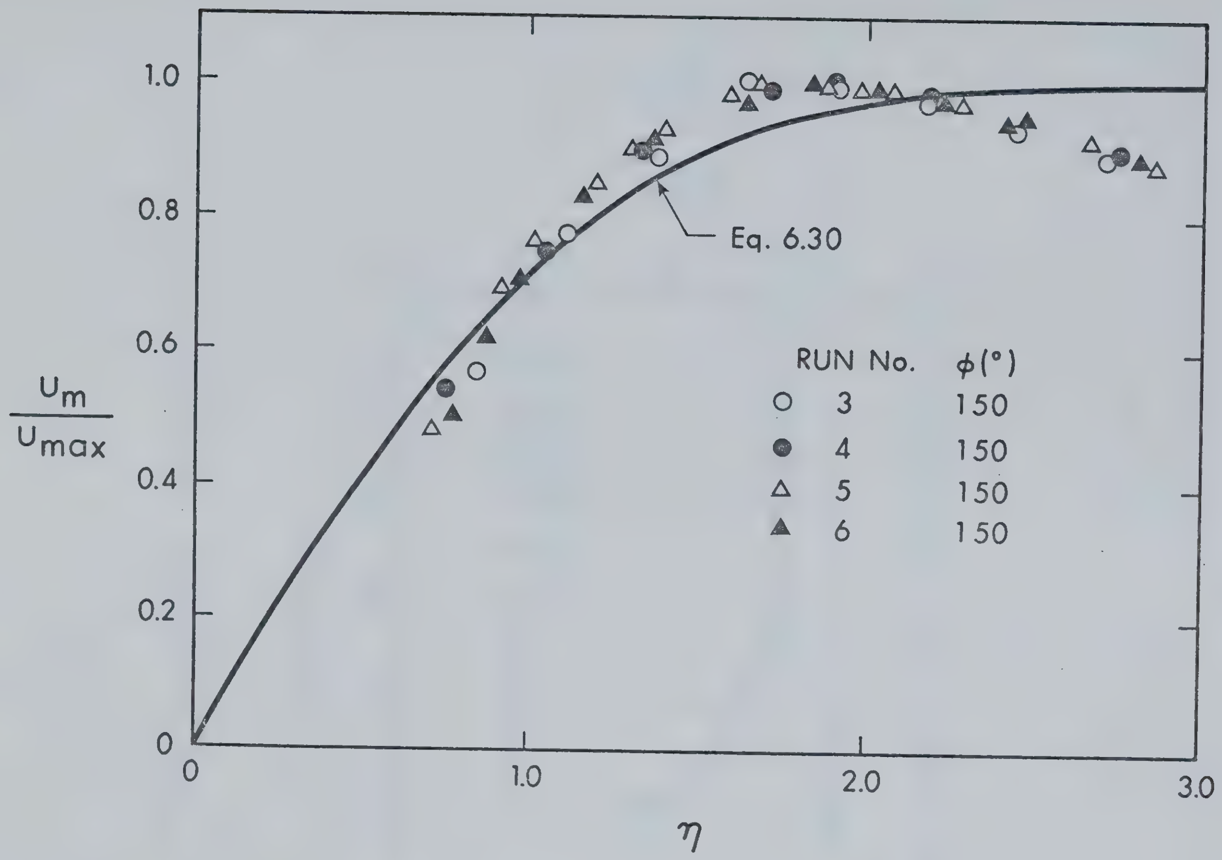

FIGURE 6.15a SIMILARITY OF u_m, $\phi > 130°$

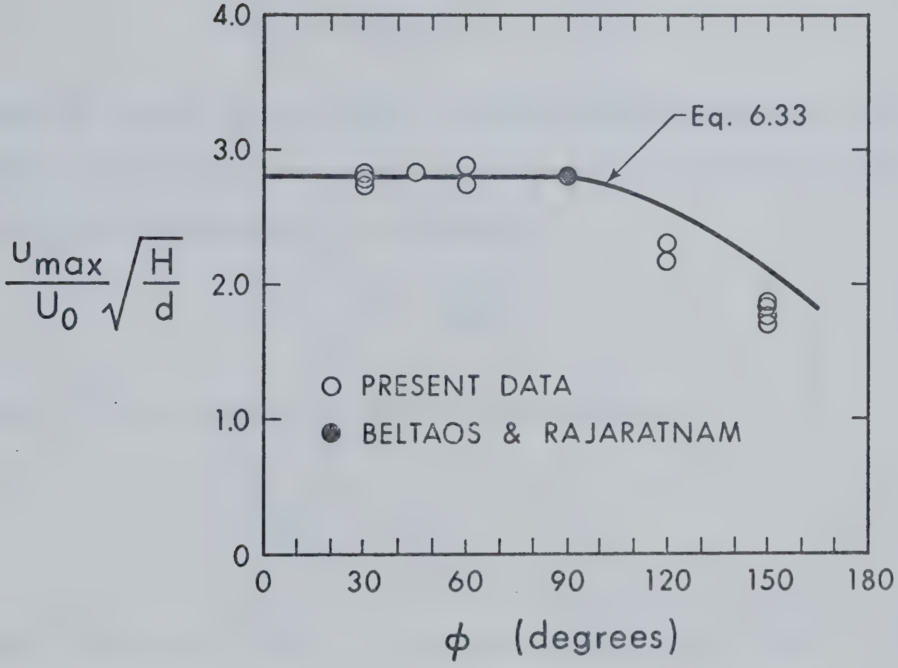

FIGURE 6.16 EVALUATION OF u_{max}

analyze existing data on the basis of the general theoretical considerations presented in Chapter II. The similarity of velocity profiles verified for $\phi \neq 90°$ by Schauer and Eustis (14), leads to the following (see Chapter II):

$$\begin{aligned} \delta_2 &= C_2 \bar{x} \\ u_m &= C_m \bar{x}^{\,a} \end{aligned} \qquad (6.34)$$

where the overbar denotes that x is measured from a virtual origin and not necessarily from the intersection of jet centerline and wall. Furthermore, the exponent a is given by:

$$a = -\frac{1}{2}\left(1 + \frac{C_f}{2FC_2}\right) \qquad (6.35)$$

where F is a constant representing the quantity:

$$\int_0^\infty \left(\frac{u}{u_m}\right)^2 d\left(\frac{y}{\delta_2}\right)$$

equal to about 0.7, and C_f is the local skin friction factor $\tau_o / \frac{\rho u_m^2}{2}$.

Consider first the skin friction factor C_f. According to previous considerations (Chapter II) this should be independent of x. The data of Schauer and Eustis (14) were re-analyzed and are plotted in Figure 6.17, in the form u_*/u_m vs x/H. These data were obtained for values of R_o between 39,000 and 43,000. For ϕ varying between 30° and 130°, and H/d between 20 and 40, it is seen that u_*/u_m and, therefore, C_f is indeed independent of x/H, H/d and ϕ. Thus, for an average value of $R_o \cong 41{,}000$, $C_f \cong 0.0054$. Since C_f is a

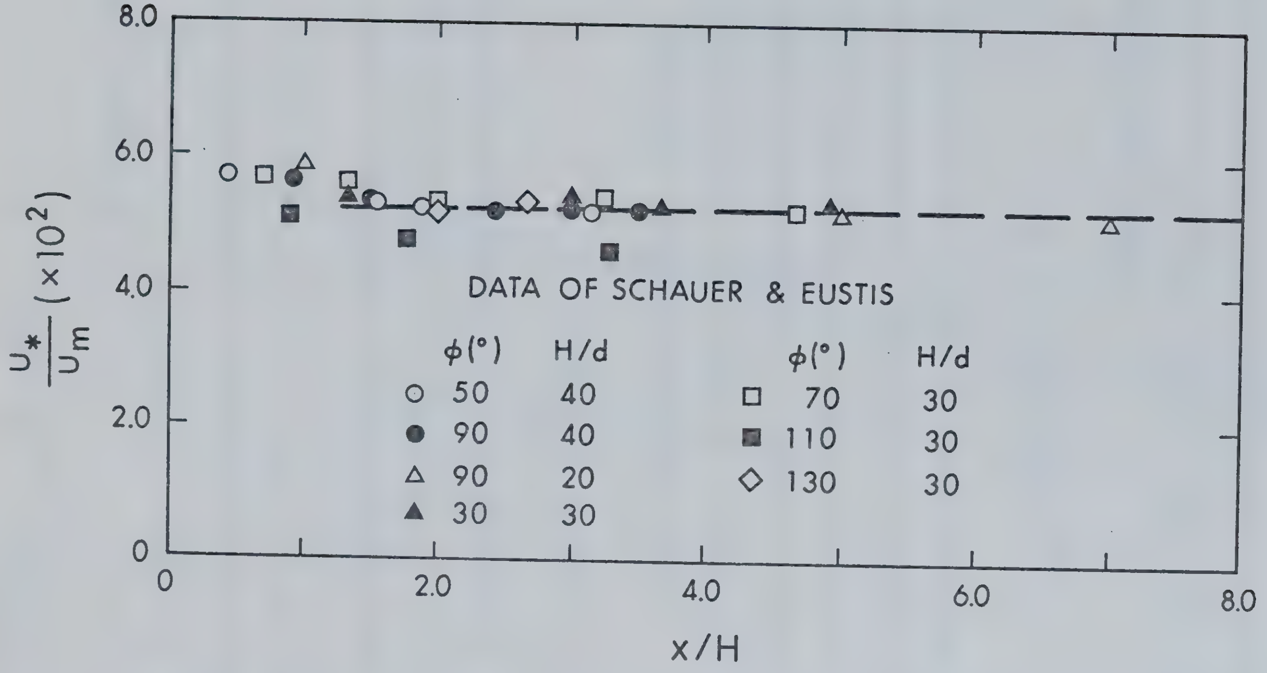

FIGURE 6.17 CONSTANCY OF FRICTION FACTOR

function of only R_o, earlier results, reported in (25) and (26) for $\phi = 90°$, as well as data for the classical wall jet ($\phi = 0°$), should apply. The available experimental results are plotted in Figure 6.18. For the case of a classical wall jet, Sigalla (32) proposed the following Blasius-type relation:

$$C_f = 0.0565 \left(\frac{u_m \delta}{\nu}\right)^{-0.25}$$

Using his results on u_m and δ, it was found that $(u_m \delta/\nu)^{0.25} = R_o^{0.25}$. $F(x/d)$, where $F(x/d)$ is a mild function, varying from 0.67 to 0.75 in the range of measurements, i.e., from $x/d = 15$ to 65. Considering that Sigalla's measurement of τ_o involved an error of about 15%, it is permissible to assume that $F(x/d)$ is constant with an average value of 0.71. With this, the above expression becomes:

$$C_f = 0.0790\, R_o^{-1/4} \quad \text{(Sigalla, re-analyzed)} \qquad (6.36)$$

This relation was obtained for an estimated range of R_o of $\sim 10^5$ to $\sim 3 \times 10^5$, and it is plotted in Figure 6.18, where it is seen to be somewhat steeper than the general trend of the data points.

Also for the case of a classical wall jet, Myers et al (33) have reported measurements of wall shear stress for values of R_o in the range 7,100 to 56,500. An average relationship for C_f can be derived from their results as:

$$C_f = 0.01525\, R_o^{-1/12} \quad \text{(Myers et al, re-analyzed)} \qquad (6.37)$$

This is also plotted in Figure 6.18, together with three data points

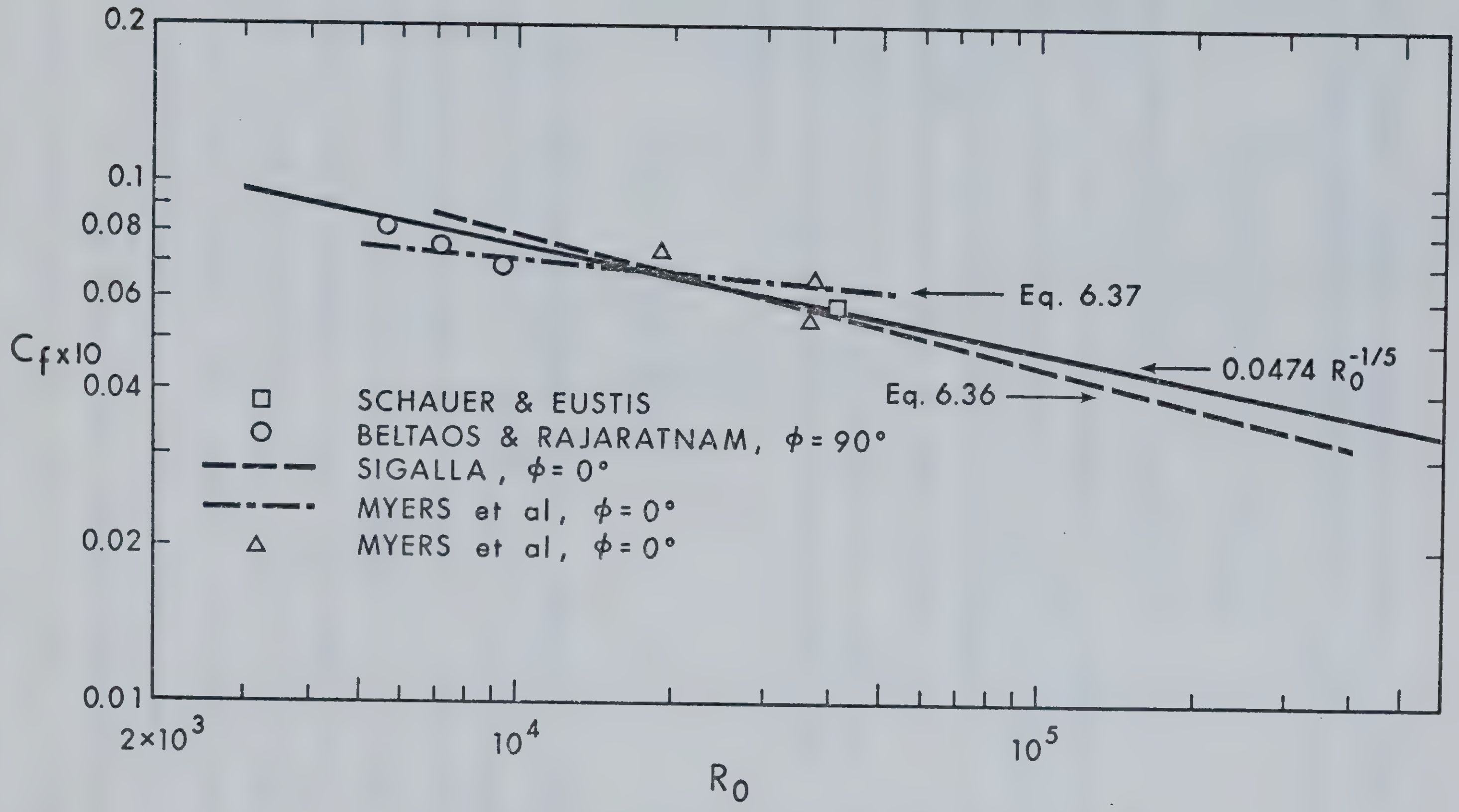

FIGURE 6.18 LOCAL SKIN FRICTION FACTOR, WALL JET REGION

computed directly from their tabulated measurements. The solid line drawn in Figure 6.18 is an average of all the data and has the equation:

$$C_f = 0.0474\, R_o^{-1/5} \qquad \text{(average)} \qquad (6.38)$$

Consider now the length scale δ_2. Equations 6.34 state that δ_2 varies linearly with x. The coefficient C_2, describing the gradient $d\delta_2/dx$ is not expected to depend upon ϕ or H/d, if account is taken of the derivations leading to Equation 6.34 (see Chapter II, Section 2.2). The data of Schauer and Eustis are shown in Figure 6.19. It is seen that a single straight line fits the data well, even though ϕ was varied from 30° to 130° and H/d was varied from 20 to 40. The equation of this line is:

$$\frac{\delta_2}{H} = 0.089\left(\frac{x}{H} + 1.2\right) \qquad (6.39)$$

i.e., $C_2 = 0.089$ and the virtual origin is located at a distance of 1.2H before the origin of x. For the case of normal impingement, ($\phi = 90°$), Cartwright and Russel (18) reported $C_2 = 0.056$ for R_o in the order of 10^5. The virtual origin was located at $x = -2.5H$. For the classical wall jet, Sigalla (32) gives $C_2 = 0.065$ for R_o in the order of 10^5, with the virtual origin at $x = -0.5d$. The results of Schwarz and Cosart (31) for $\phi = 0°$, show C_2 to decrease from 0.085 at $R_o = 13{,}500$ to 0.06 at $R_o = 41{,}600$, with the virtual origin being between $x = -7.2d$ and $-15.6d$. These considerations indicate that there exists a certain relationship between C_2 and R_o, and that generally C_2 decreases for increasing R_o. However, it is not possible

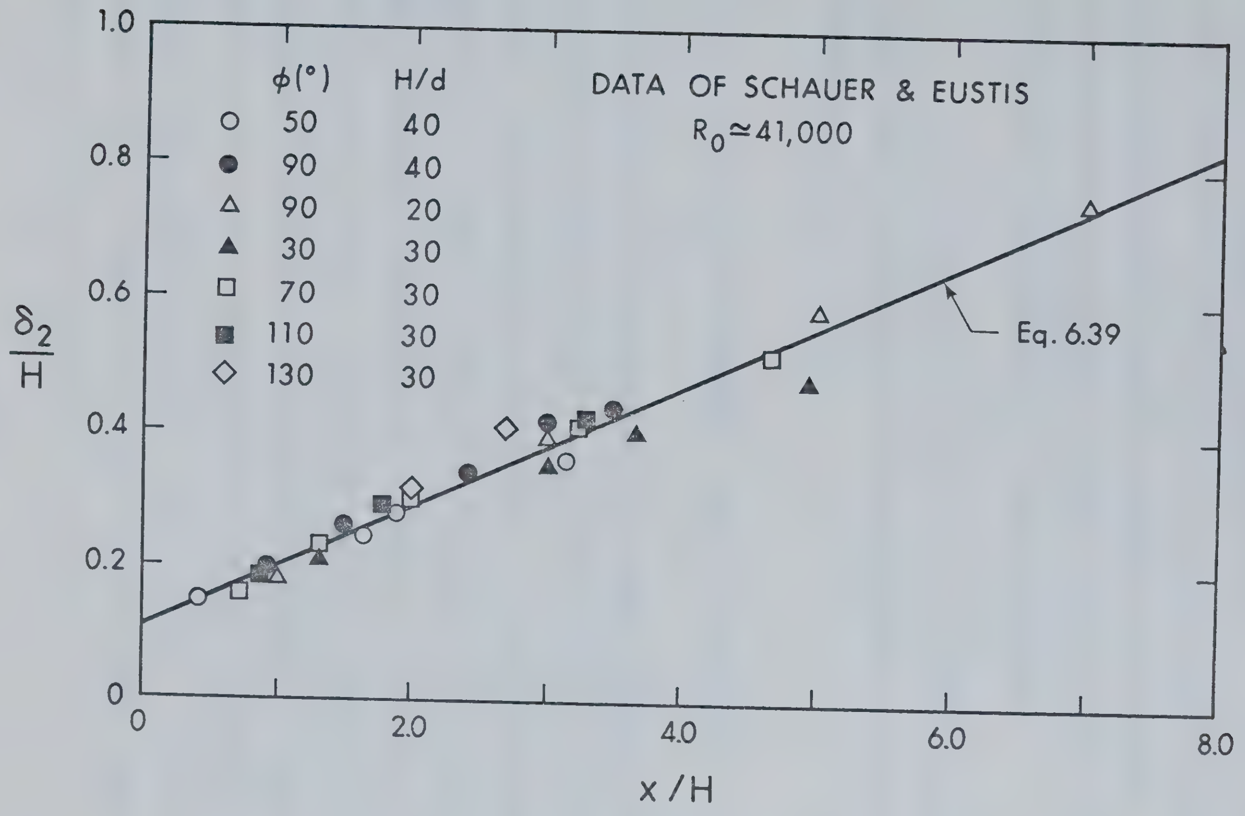

FIGURE 6.19 LENGTH SCALE, WALL JET REGION

at present to establish the relation between C_2 and R_o because C_2 is also dependent on conditions at the nozzle, which vary among different investigations and cannot be accounted for at present. The location of the virtual origin appears to depend only upon nozzle conditions, as no consistent variation with R_o could be detected.

An overall average value of C_2 is 0.0765, whereas the virtual origin seems to be located at an average distance of 1.35H before the origin of x, i.e.:

$$\frac{\delta_2}{H} = 0.0765 \left(\frac{x}{H} + 1.35\right) \qquad \text{(average)} \qquad (6.40)$$

For the case $\phi = 0°$, the quantity H becomes undefined, however, here the virtual origin is located at an average distance of 10d before the nozzle. The theoretical prediction for u_m is given by Equations 6.34 and 6.35. To obtain an estimate of the exponent, a, consider the term $\frac{C_f}{2FC_2}$ appearing in Equation 6.35. Taking $F \simeq 0.7$ and $C_2 \simeq 0.0765$ this becomes $C_f/0.107$. If this is less than, say, 0.06, it could be neglected in comparison to unity and the exponent, a, will be simply equal to -0.5. This condition will be satisfied so long as $C_f \lesssim 0.0064$ which in turn yields the condition $R_o \gtrsim 20{,}000$. In most practical problems, R_o is likely to be larger than this value, hence in what remains it will be assumed that $a \simeq -0.5$, and:

$$u_m = C_m \bar{x}^{-0.5} \qquad (6.41)$$

From dimensional considerations, it is easy to show that:

$$\frac{u_m}{U_o}\sqrt{\frac{H}{d}} = f(\frac{x}{H}, \phi)$$

which, in view of Equation 6.41, becomes:

$$\frac{u_m}{U_o}\sqrt{\frac{H}{d}} = \frac{C_u(\phi)}{\sqrt{x/H}}$$

or

$$\frac{u_m}{U_o} = \frac{C_u(\phi)}{\sqrt{x/d}} \qquad (6.42)$$

where $C_u(\phi)$ is a function of ϕ. Thus, the preceding approximation with respect to the exponent a has made it possible to show that H does not affect u_m. The data of Schauer and Eustis were re-analyzed and are shown plotted in Figure 6.20, in the form $(U_o/u_m)^2$ vs x/d. Equation 6.42 states that when the data are plotted in this form, straight lines would result. This is shown to be true in Figure 6.20, and the slopes of the resulting straight lines are related to C_u. For the case of normal impingement, Cartwright and Russel (18) gave the relation $u_m \propto x^{-0.39}$. However, when this was re-analyzed it was shown that in the range of x/d in which their data were obtained, Equation 6.42 was valid with $C_u = 2.41$.

Values of C_u are plotted against ϕ in Figure 6.21 where it is seen that the data points define a single curve, a fact that supports the conclusion $C_u = C_u(\phi)$. This function is now predicted as follows. It has been shown earlier that in Equation 6.35, the term $C_f/2FC_2$ could be neglected for $R_o \gtrsim 20,000$. Recalling that Equation 6.35 is a

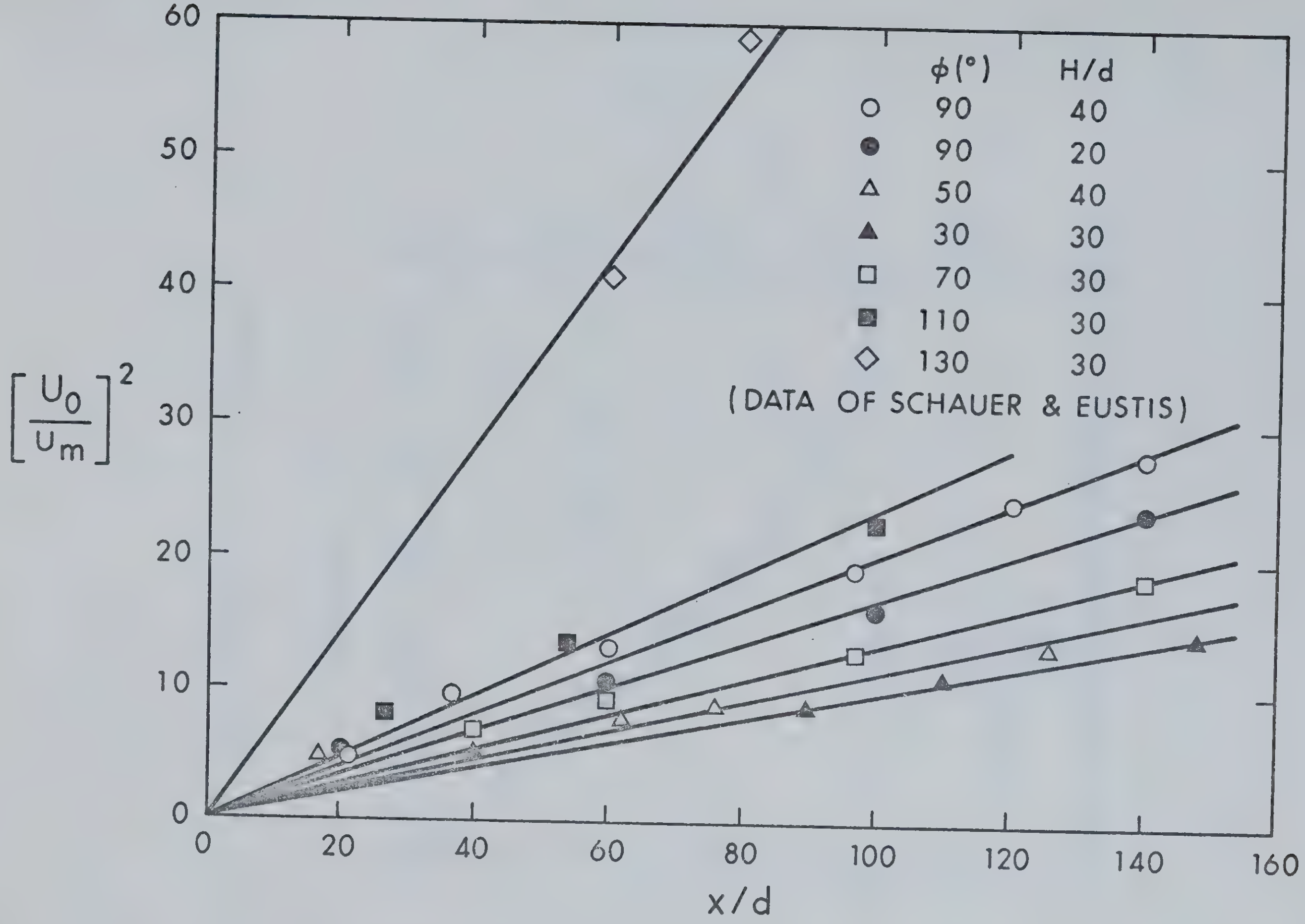

FIGURE 6.20 VELOCITY SCALE, WALL JET REGION

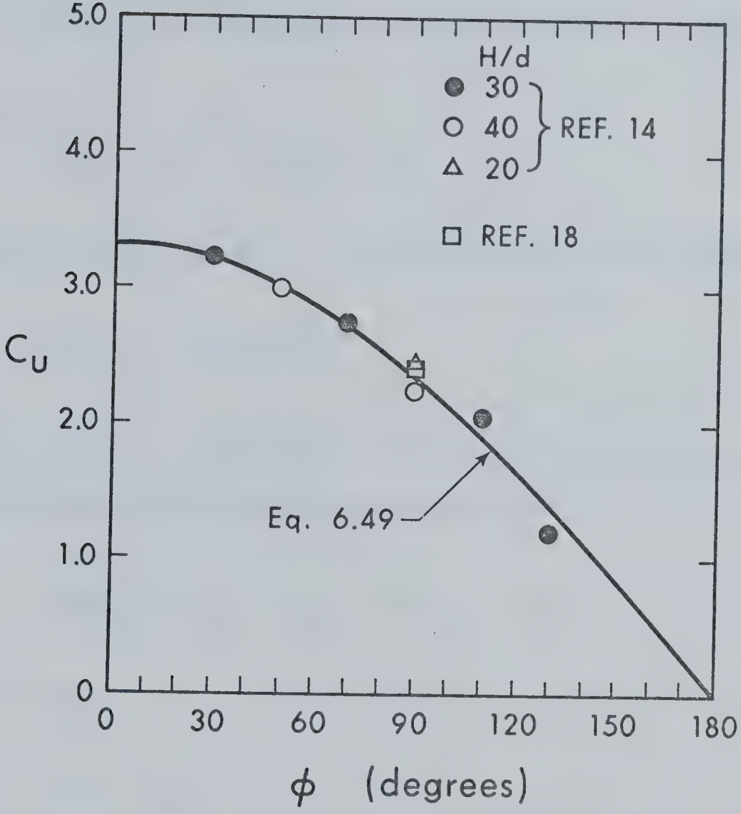

FIGURE 6.21 THE FUNCTION $C_u(\phi)$

result of the integral momentum equation (Chapter II, Section 2.2) and noting that this term represents frictional effects, it is reasonable to assume that frictional forces could be neglected from the momentum equation. If M_1 is the momentum of the wall jet in the direction of positive x and M_2 is the momentum in the direction of negative x, then:

$$M_1 - M_2 = \rho U_o^2 d \cos \phi \qquad (6.43)$$

But in general $M = \int_0^\infty \rho u^2 dy$, or taking similarity into account:

$$M = \rho F C_u^2 C_2 U_o^2 d \qquad (6.44)$$

Letting C_{u1} and C_{u2} correspond to the positive and negative x respectively, Equation 6.43 can be re-written as:

$$\rho d U_o^2 C_2 F (C_{u1}^2 - C_{u2}^2) = \rho U_o^2 d \cos \phi \qquad (6.45)$$

or the equivalent:

$$C_{u1}^2 - C_{u2}^2 = m^2 \cos \phi \qquad (6.46)$$

where $m^2 = \frac{1}{FC_2}$. Note that if ϕ is taken less than 90°, then C_{u1} coincides with $C_u(\phi)$ whereas C_{u2} will coincide with $C_u(180° - \phi)$. One more relation between C_{u1} and C_{u2} can be obtained if it is assumed that the momenta in the two wall jets (which are preserved quantities if friction is neglected) are in the same ratio, as in the corresponding case of a potential jet. If it is recognized that this ratio of momenta is determined by the flow conditions in the neighbour-

hood of the stagnation point, where the flow is locally of stagnation type, then this assumption does not appear unreasonable. This assumption will yield (44):

$$\frac{C_{u1}^{2}}{C_{u2}^{2}} = \frac{1 + \cos\phi}{1 - \cos\phi} \tag{6.47}$$

Solving Equations 6.46 and 6.47:

$$0° \le \phi \le 90° \;; \quad \left\{ \begin{array}{l} C_{u1} = m\sqrt{(1 + \cos\phi)/2} \\ \\ C_{u2} = m\sqrt{(1 - \cos\phi)/2} \end{array} \right. \tag{6.48}$$

To evaluate m consider the case $\phi = 0°$. This represents the classical wall jet for which $C_{u1} \simeq 3.32$ (29), and naturally $C_{u2} = 0$. It follows that $m = 3.32$. Furthermore, since C_{u2} could also be taken as the value of C_{u1} for the supplementary of ϕ, Equations 6.48 could be reduced to a single equation, i.e.:

$$C_u(\phi) = \sqrt{5.5(1 + \cos\phi)} \tag{6.49}$$

This is shown to describe the data adequately in Figure 6.21. Note that the chosen value of 3.32 for m would give a value of $C_2 \cong 1/0.7 \times 11 = 0.13$. This is not in agreement with the average value of 0.0765 obtained earlier (Equation 6.40) and the discrepancy is attributed to virtual origin effects. Substituting Equation 6.49 into Equation 6.42, the velocity scale is finally given by:

$$\frac{u_m}{U_o} = \left[\frac{5.5(1 + \cos\phi)}{x/d}\right]^{\frac{1}{2}} \tag{6.50}$$

6.4 Summary

The problem of oblique impingement of plane turbulent jets has been studied in this chapter. It was established that the free jet region extends up to 70% of the inclined impingement height, H, regardless of the angle of impingement. The wall pressure and wall shear stress, as well as the maximum velocity near the wall were studied in detail in the impingement region. A semi-empirical method, based on similarity properties, was developed to predict the wall pressure and velocity. The wall shear stress was predicted by the same method, as in the previous chapters, properly modified to account for the effects of obliqueness. The extent of this region along the wall was established from wall pressure considerations and it was found to be a portion of H that depends on the angle of impingement.

The wall jet region was studied utilizing previous experimental results. The analysis was carried out in accordance with the theoretical considerations of Chapter II. It was shown that the local skin friction factor depends only upon the Reynolds number R_o, and an average empirical equation was proposed which covers the entire range of experimental results ($5600 \leq R_o \lesssim 300{,}000$). The length scale was shown to vary linearly with x, however, the coefficient C_2 describing its gradient was found to depend upon the Reynolds number. At present, it is not possible to establish this relation because of the presence of significant nozzle effects which vary among different investigators. A satisfactory theoretical method was developed to predict the relative velo-

city scale u_m/U_o, which was shown to be proportional to $(x/d)^{-0.5}$, the coefficient of proportionality C_u being a function of only ϕ. This function was determined with the aid of the momentum integral equation and an analogy drawn from the corresponding case of a potential impinging jet.

CHAPTER VII - OBLIQUE IMPINGEMENT OF CIRCULAR TURBULENT JETS

7.1 Introduction

The oblique impingement of plane turbulent jets was studied in the previous chapter. Another configuration that is also of considerable practical importance, is the oblique impingement of circular turbulent jets. At first sight, it may appear that this problem is a generalization of the normal impingement of circular jets involving the same escalation of difficulty as when passing from the normal to oblique impingement of plane jets. This, however, is only a crude representation of reality. When dealing with plane jets, the oblique impingement involves only one parameter in addition to those describing the normal impingement, i.e., the angle of impingement ϕ. If a circular jet impinges at an angle different than 90° the flow remains axisymmetric only in the free-jet region. Therefore, in order to describe the impingement and wall-jet regions, it is necessary to introduce an extra space co-ordinate. This could be distance measured perpendicularly to the plane of symmetry (i.e., the plane containing the jet centerline and normal to the wall), or it could be a polar angle measured from the trace of the symmetry plane on the wall. Thus, when passing from normal to oblique impingement of circular jets, two new variables must be introduced, and this makes the problem more difficult than any other studied previously. Yet, the understanding gained in previous chapters will be helpful in this case.

It appears that no information is available for the impinge-

ment region, whereas the wall jet region has been studied earlier by Yakovlevskii and Krasheninnikov (27). Their work includes experimental and analytical results regarding the velocity field in the wall-jet region. The analysis is of the integral type and makes use of a number of rather arbitrary assumptions, such as conservation of flow rate and kinetic energy in the impingement region. Furthermore, an arbitrary physical model is introduced to represent the wall jet. This consists of the assumption that the wall jet is produced by a cylindrical nozzle of variable thickness. The analysis yields complex equations that are difficult to solve.

The objectives in this chapter are, therefore, two-fold. One is to study wall pressure and shear stress in the impingement region, and the second to obtain additional experimental data in the wall-jet region so as to complement those of (27). Furthermore, a relatively simple analytical approach is presented, based on the general theoretical considerations of Chapter II, which results in simple analytical expressions for the velocity field and the wall shear stress.

Consider now a circular turbulent jet impinging obliquely as shown in Figure 7.1. The wall pressure in excess of ambient will be denoted simply by p_w, the stagnation pressure is p_s and it occurs at the stagnation point, S, which is removed from the intersection of jet centerline and wall (point 0) by a distance s. For convenience, two co-ordinate systems will be used. In the impingement region, it was generally found more convenient to use the Cartesian co-ordinate system (x, y, z), whereas the wall-jet region was found easier to study

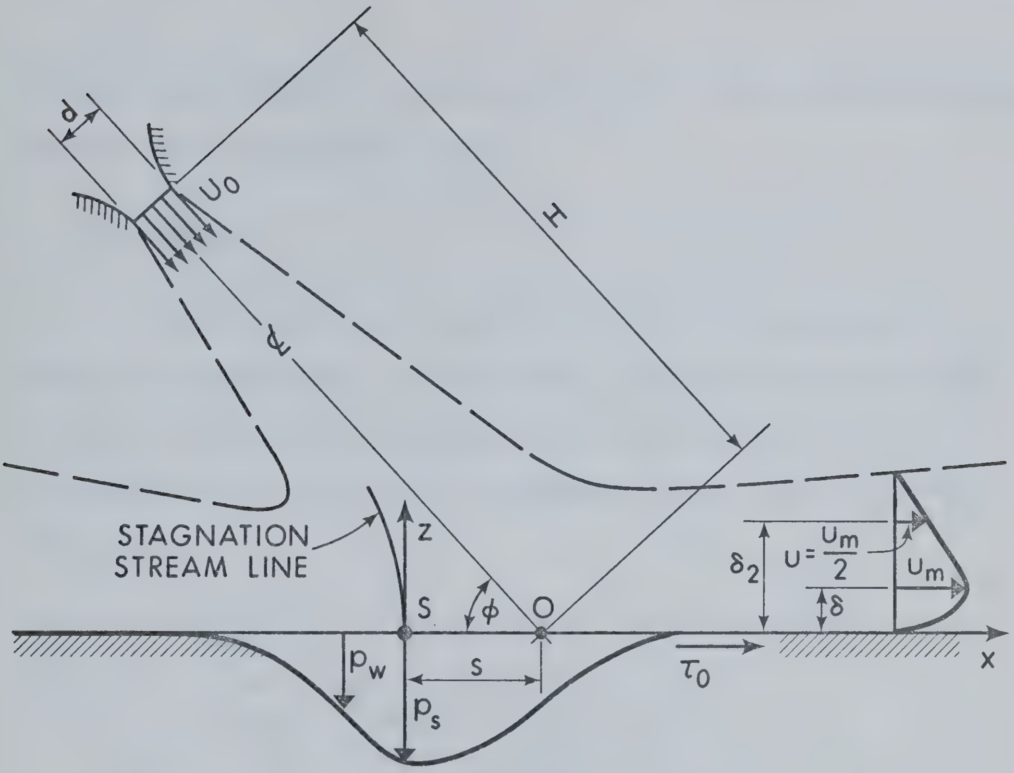
d
U0
H
℄
STAGNATION STREAM LINE
z
S
φ
O
δ2
u = Um/2
Um
δ
pw
s
ps
τ0
x

(a) Section through symmetry plane

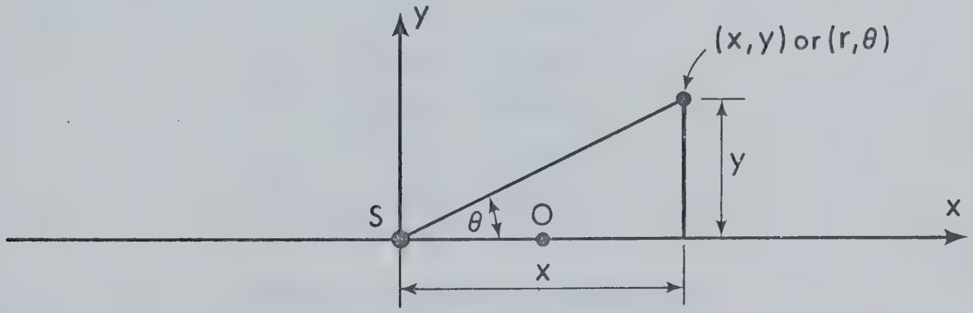
y
(x,y) or (r,θ)
y
S
θ
O
x
x

(b) Plan view

FIGURE 7.1 DEFINITION SKETCH

by using the cylindrical co-ordinates (r, θ, z). Note that both systems originate at the stagnation point S.

7.2 Experiments

The experimental set-up has been described in Chapter III. A total of nine experiments were performed, whose particulars are listed in Table 7.1. The nozzle Reynolds number, R_o, was varied from 35,000 to 100,000, whereas the relative impingement height, H/d, was between 15.5 and 47.

Run No.	H/d	R_o	$\phi(°)$
1	39.25	34,700	60
2	15.5	89,600	60
3	20.0	89,600	30
4	46.5	34,700	30
5	47	34,700	45
6	19.45	89,600	45
7	20.3	89,600	20
8	17.5	100,000	20
9	35.8	34,700	20

TABLE 7.1 RANGE OF EXPERIMENTS

Wall shear stress was measured using a Preston tube (Chapter III) of 0.046 in. outside diameter. As the line of action of shear stress is not generally known before-hand, measurements were performed only in instances where its line of action could be accurately estimated.

7.3 Analysis and Results

7.3.1 Impingement Region

The objective in this section is to study the wall pressure and shear stress. Measurement of wall pressure is straight-forward (Chapter III) even though it is fairly laborious. However, regarding the wall shear stress, a major difficulty is present, i.e., the direction of shear stress is not known at an arbitrary point on the wall. Considering the "limiting" or "wall" streamlines, the shear stress will act along the tangent of the wall streamline passing through the given point. Intuitively, it appears reasonable to assume that the wall streamlines are a family of curves orthogonal to the contours of equal wall pressure. Before this can be assumed, however, a better justification must be furnished. For a three-dimensional boundary layer, the equations of motion at the wall (z = 0) reduce to (46):

$$\left(\frac{\partial p}{\partial x}\right)_{z=o} = \mu \left(\frac{\partial^2 u}{\partial z^2}\right)_{z=o} \qquad (7.1)$$
$$\left(\frac{\partial p}{\partial y}\right)_{z=o} = \mu \left(\frac{\partial^2 v}{\partial z^2}\right)_{z=o}$$

whereas the components of the wall shear stress are given by:

$$\tau_{ox} = \mu \left(\frac{\partial u}{\partial z}\right)_{z=o} \qquad (7.2)$$
$$\tau_{oy} = \mu \left(\frac{\partial v}{\partial z}\right)_{z=o}$$

In Equations 7.1 and 7.2, p is the static pressure above ambient,

u, v are the velocity components in the x and y-directions respectively and μ is the viscosity of the fluid.

If the velocity profile is assumed to be collateral in the immediate vicinity of the wall, as is usually the case (46), then for a range of very small, but finite, values of z, the ratio v/u remains constant on the vertical through any given point (x, y, 0). Quantitatively this is expressed as:

$$v = \beta u \quad ; \quad \beta = \beta(x, y) \quad ; \quad \text{for} \quad 0 \leq z \leq z_o$$

with z_o being a small but finite length. This immediately implies that:

$$\left(\frac{\partial v}{\partial z}\right)_{z=o} = \beta\left(\frac{\partial u}{\partial z}\right)_{z=o} \quad \text{and} \quad \left(\frac{\partial^2 v}{\partial z^2}\right)_{z=o} = \beta\left(\frac{\partial^2 u}{\partial z^2}\right)_{z=o}$$

Substituting into Equations 7.1 and 7.2, it is easy to show that:

$$\frac{(\partial p/\partial y)_{z=o}}{(\partial p/\partial x)_{z=o}} = \beta = \frac{\tau_{oy}}{\tau_{ox}}$$

which shows that the total wall shear stress τ_o is in the same direction as the vector $(\nabla p)_{z=o}$ which in turn is orthogonal to the equal-pressure contour passing rhough the point (x, y, o). This then shows that the wall streamlines and the wall shear stresses are orthogonal to the equal-pressure contours. This conslusion will prove useful in the remaining part of this chapter.

7.3.1.1 Wall Pressure

Typical wall pressure contours are shown in Figure 7.2, for $\phi = 60°$ and 30°. It is seen that the contour shapes deviate increasingly from the circular pattern of normal impingement, as ϕ decreases. This, in turn, shows that wall streamlines will no longer be linear with the only exception of the streamline on the symmetry plane which is the x-axis. An interesting feature of these plots is the absence of negative values of pressure at the side of negative x. This is in apparent contrast with the observations for the plane jet (Chapter VI) where negative pressures did occur. Yet, this does not constitute a contradiction. It is well known that if an isolated vortex tube forms within a mass of fluid, it must end either on flow boundaries (solid or free surfaces), or it must close upon itself, i.e., forming a vortex ring. In the case of plane jets the occurrence of negative pressures was attributed to the formation of a straight-line vortex which ended on the sidewalls of the experimental set-up (see Chapter III). In the case of the circular jet, a vortex can close only upon itself, thus forming a vortex ring surrounding the jet. However, from the side of positive x there is no reason why concentrated vorticity should occur and, therefore, it is impossible for the ring to form, which explains the absence of negative pressure in this case.

In order to predict the wall pressure, an inductive, semi-empirical approach will be employed. Consider firstly the case of normal impingement, $\phi = 90°$. At a given point (x, y) or (r, θ) the wall pressure is $p_w(x, y) = p_w(r)$ because, due to symmetry, $\partial p/\partial\theta = 0$.

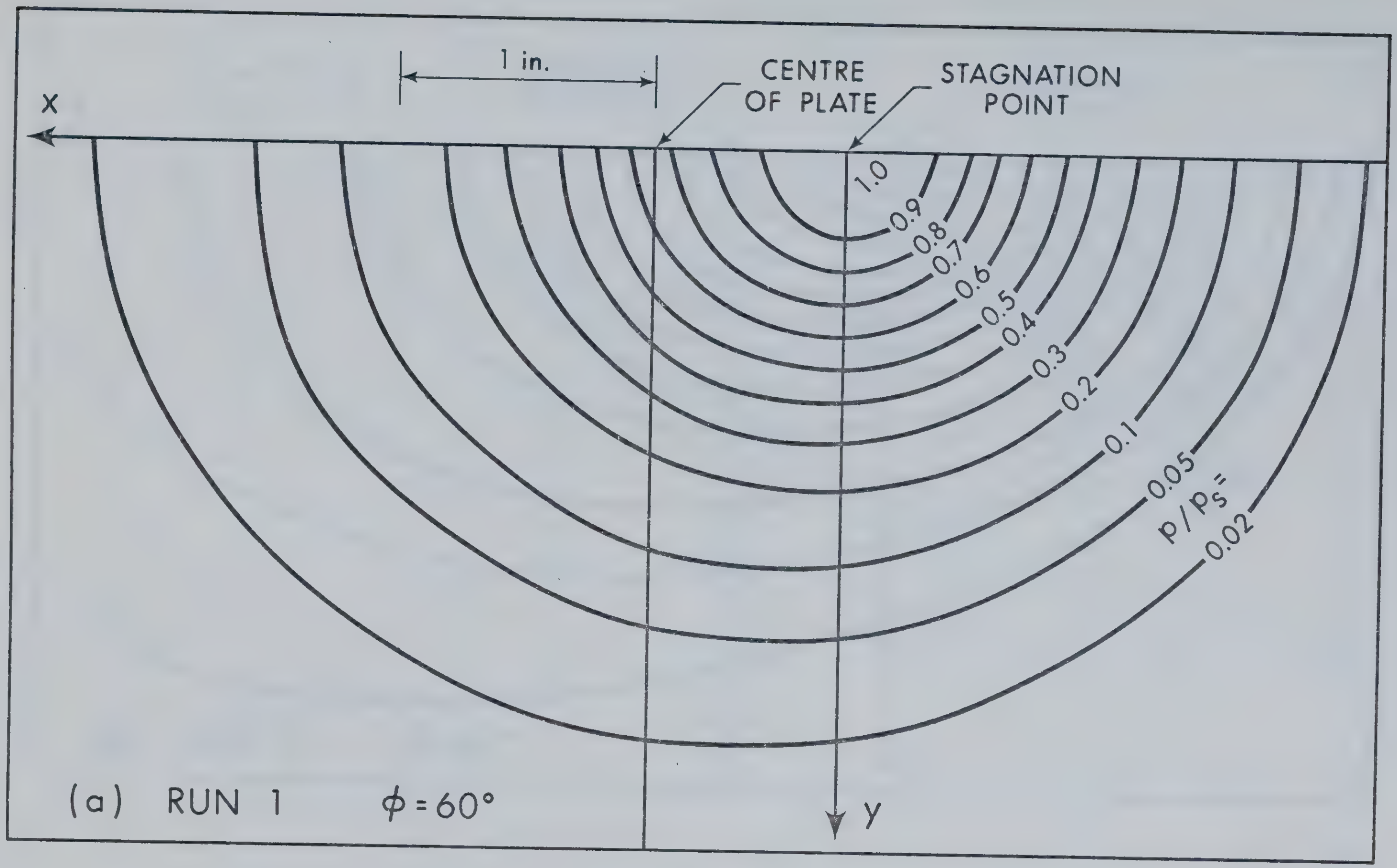

FIGURE 7.2 WALL PRESSURE CONTOURS

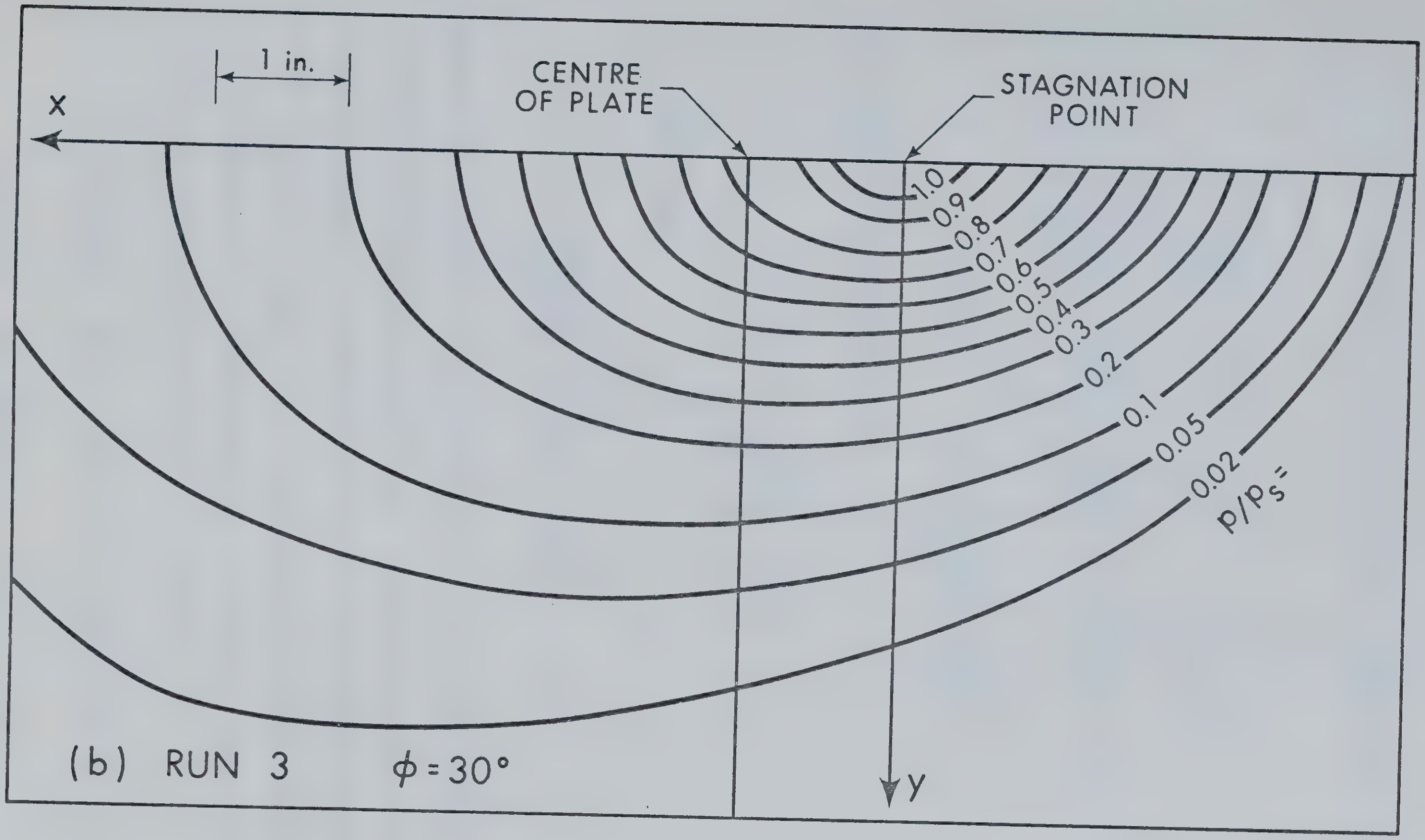

FIGURE 7.2 CONTINUED

It was found (Chapter IV) that the radial pressure profiles are similar, i.e.:

$$\frac{p_w}{p_s} = g(\eta) = e^{-k\eta^2} \quad ; \quad k = .693 \tag{7.3}$$

where $\eta = r/b$ and b is the value of r where $p_w = \frac{1}{2} p_s$. Equation 7.3 implies that:

$$p_w(x,\ y) = p_s \exp\left[-\ k\left(\frac{x^2}{b^2} + \frac{y^2}{b^2}\right)\right] \tag{7.4}$$

The pressure on the x-axis is:

$$p_w(x,\ o) = p_s \exp\left[-\ k\left(\frac{x^2}{b^2}\right)\right] \tag{7.5}$$

It follows that:

$$\frac{p_w(x,\ y)}{p_w(x,\ o)} = \exp\left[-\ k\left(\frac{y}{b}\right)^2\right] \tag{7.6}$$

Equation 7.6 states that, in the case of normal impingement, pressure profiles along lines parallel to the y-axis are similar if the maximum value of pressure is used (which occurs at $y = o$) as pressure scale and if b is used as length scale. This property of similarity is retained for all values of ϕ as Figures 7.3 [(a) to (c)] show. In these figures the following convention was adopted:

$$p_1 \equiv p_w(x,\ o) \text{ for } x > 0 \quad ; \quad p_2 \equiv p_w(x,\ o) \text{ for } x < 0$$

$$\zeta \equiv y/b \quad ; \quad b = \text{value of } y \text{ where } p = \frac{1}{2} p_{1,2}$$

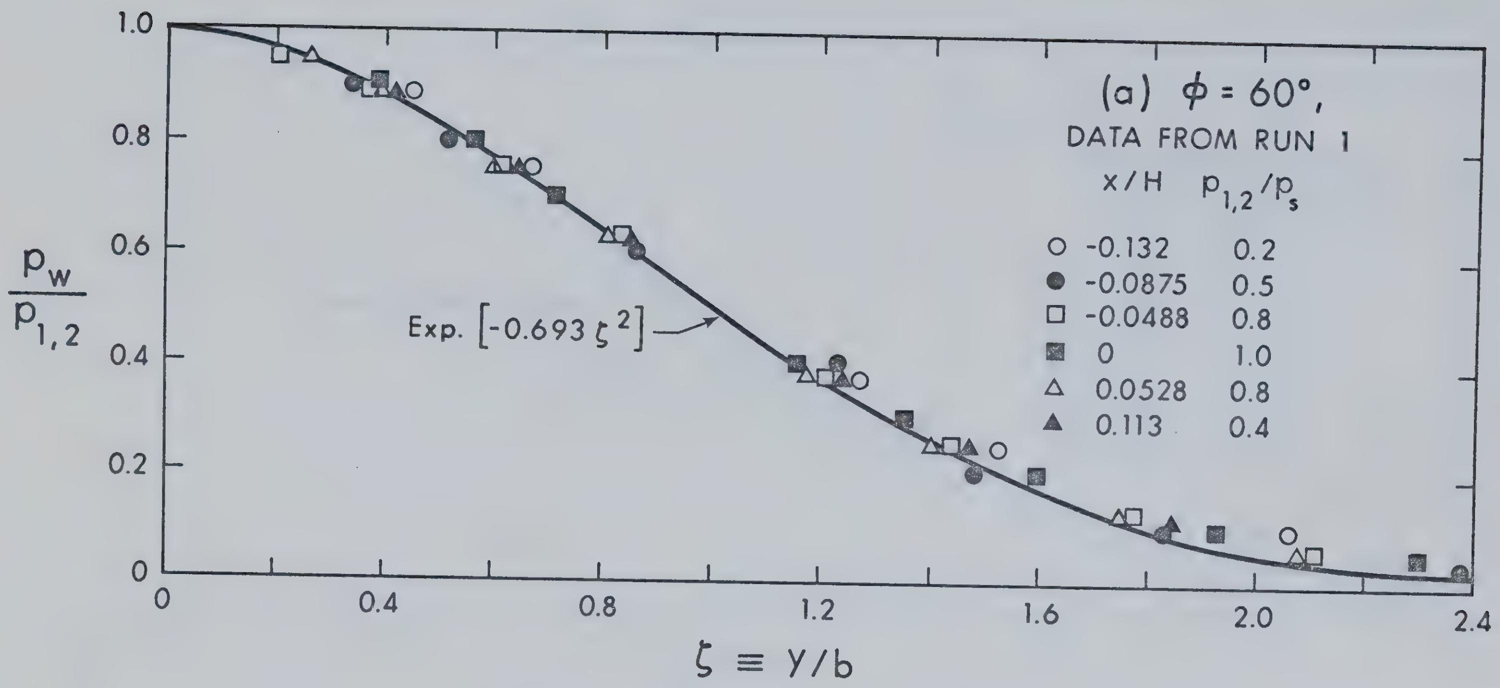

FIGURE 7.3 WALL PRESSURE SIMILARITY

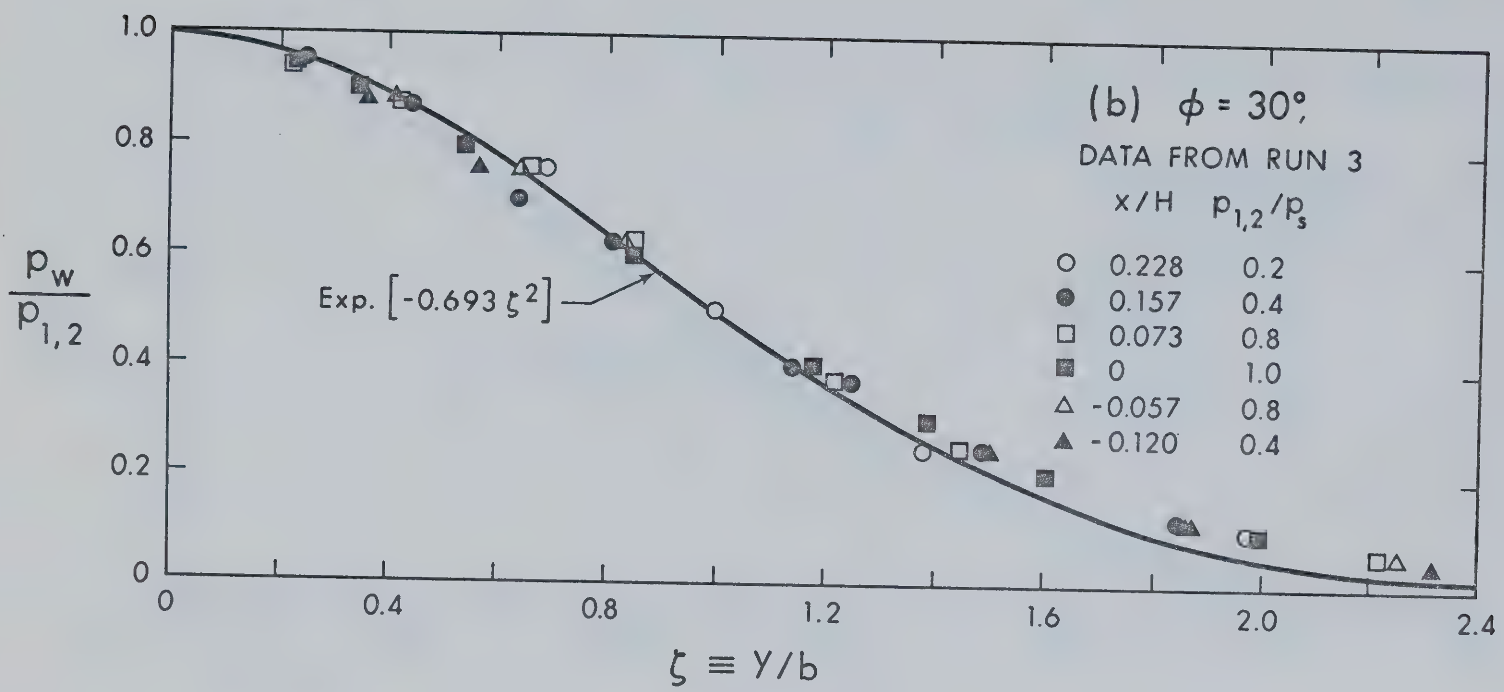

FIGURE 7.3 CONTINUED

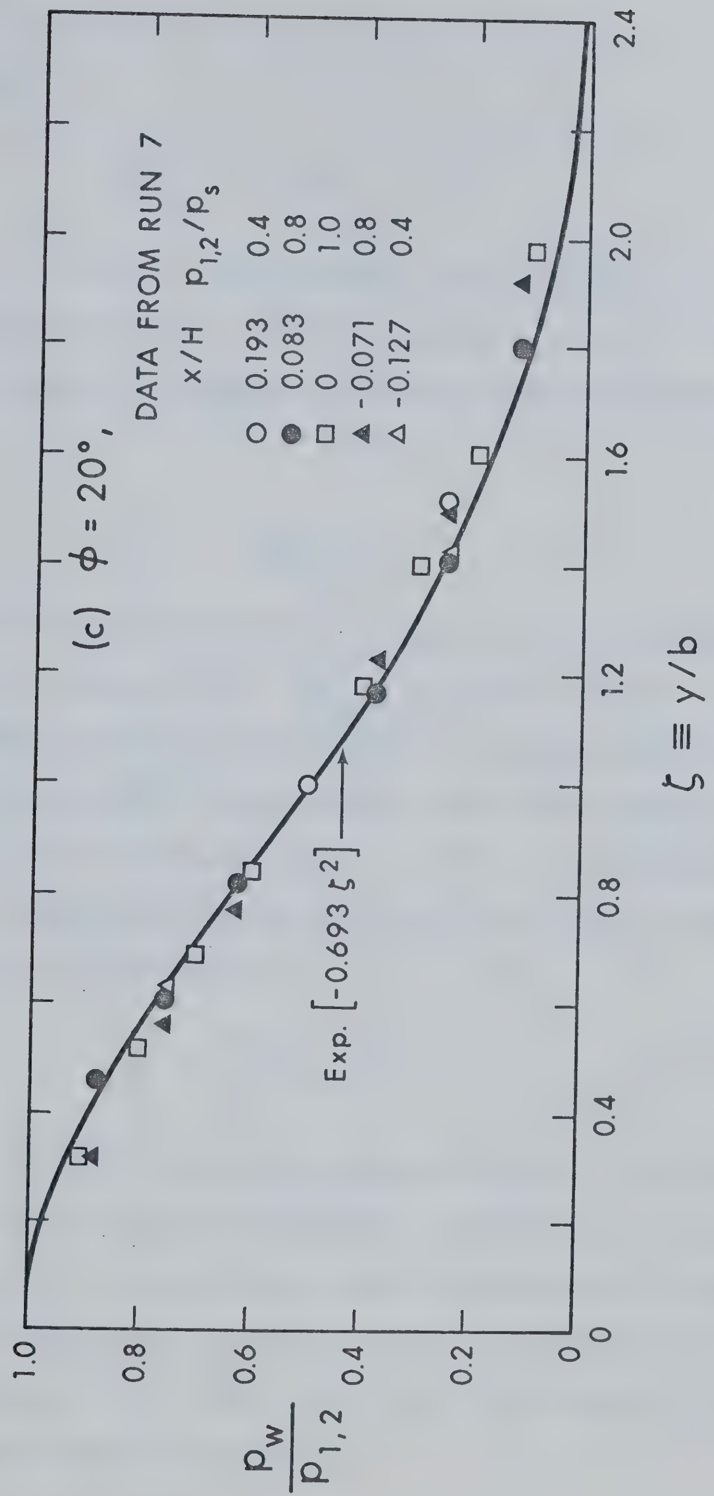

FIGURE 7.3 CONTINUED

Hence:

$$\frac{p_w}{p_{1,2}} = g(\zeta) = e^{-k\zeta^2} \tag{7.7}$$

where $k = 0.693$. Here, however, the length scale b is not constant, but it varies with x as shown in Figures 7.4 [(a) to (c)]. Assuming large heights of impingement, it can be shown by dimensional analysis that:

$$\frac{b}{H} = f_b(\frac{x}{H}, \phi) \tag{7.8}$$

The data are seen (Figure 7.4) to agree with the formulation of Equation 7.8. When $\phi = 90°$, $(\frac{b}{H})_{90} = f_b(\frac{x}{H}, 90°) = \text{const}$, i.e., f_b is a straight line parallel to the x-axis. The data indicate that the linearity of b/H is preserved for angles other than 90°, however, the slope of the line depends upon ϕ. If b_3 is the value of b at $x = 0$ (associated with the profile on the y-axis), the above considerations can be expressed as:

$$\frac{b}{H} = \frac{b_3}{H} + \alpha \frac{x}{H} \tag{7.9}$$

where $\frac{b_3}{H}$ and α are both functions of only ϕ and, therefore, they can easily be evaluated empirically. Regarding the principal pressures p_1 and p_2, these are also similarly distributed, much like in the case of plane jets, as shown in Figures 7.5 [(a) to (c)]. Defining η as $|x|/b_{1,2}$, $b_{1,2}$ being the value of $|x|$ where $p_{1,2} = \frac{1}{2} p_s$, the principal pressures are given by:

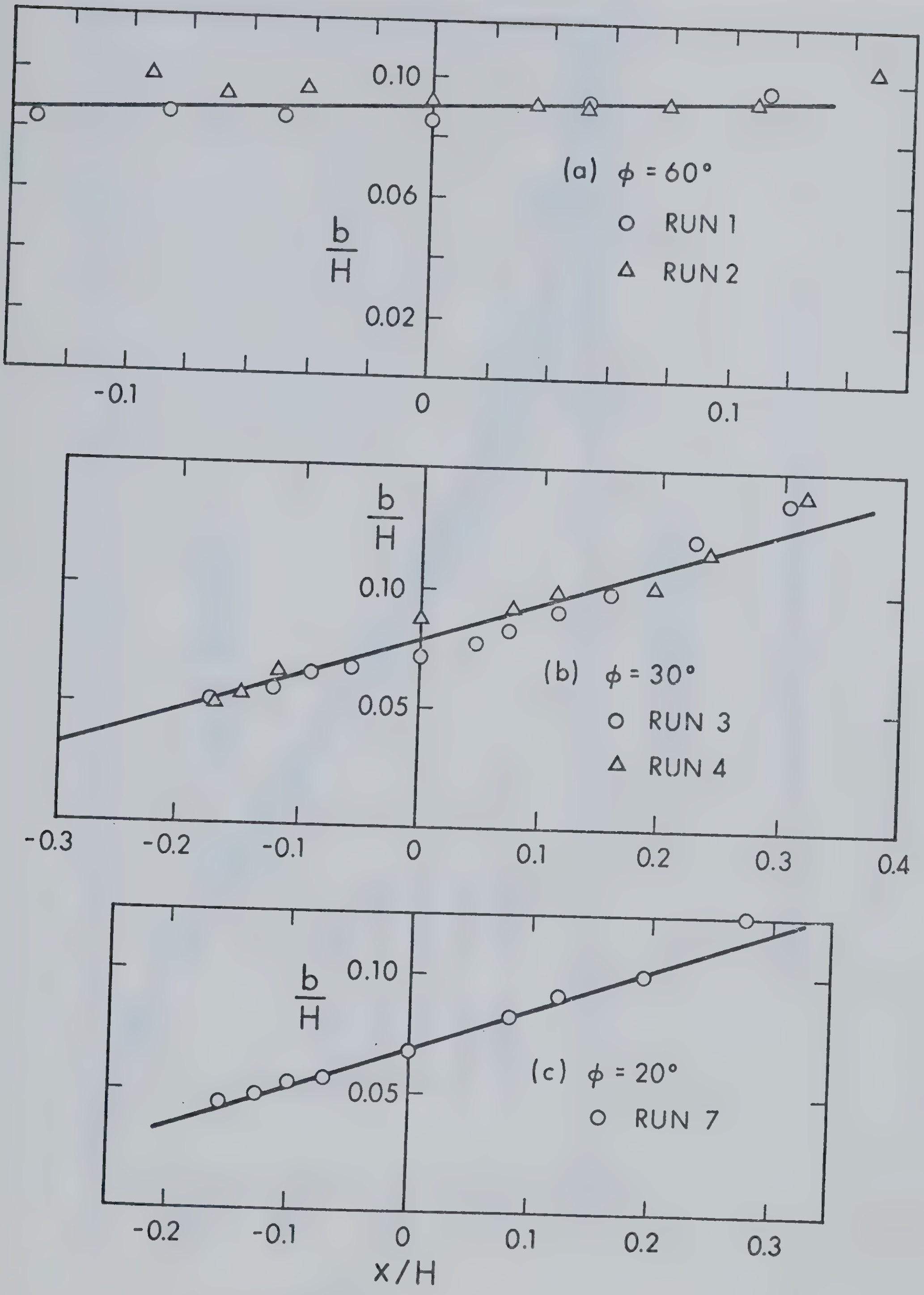

FIGURE 7.4 LENGTH SCALE b

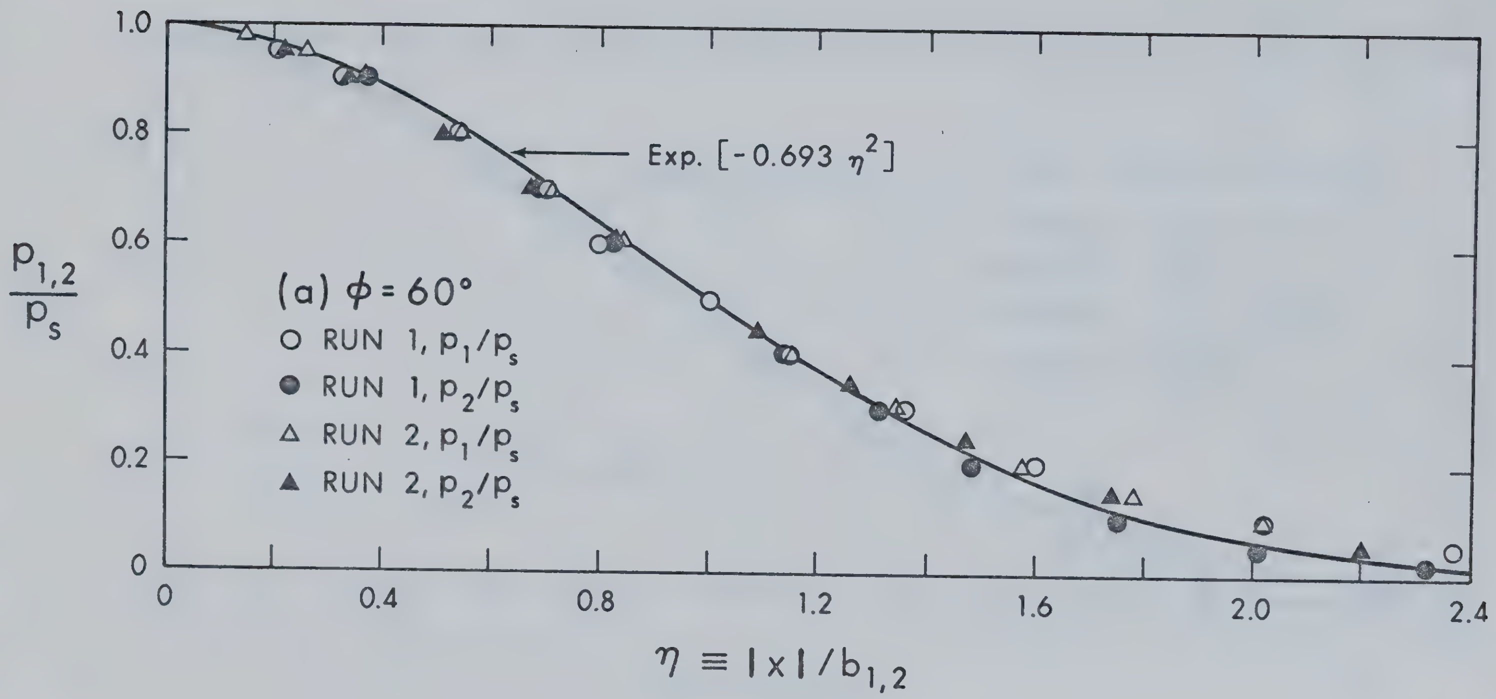

FIGURE 7.5 SIMILARITY OF SYMMETRY PLANE WALL PRESSURE

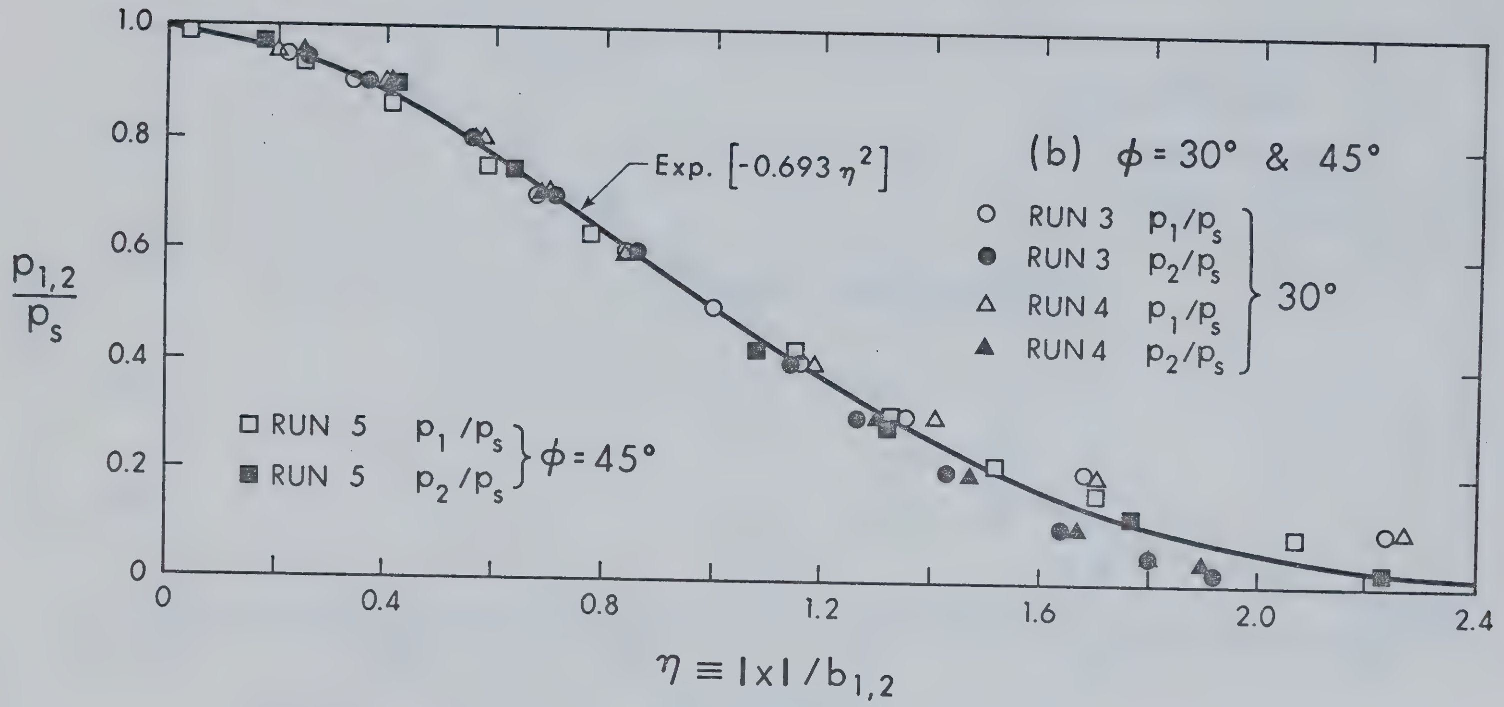

FIGURE 7.5 CONTINUED

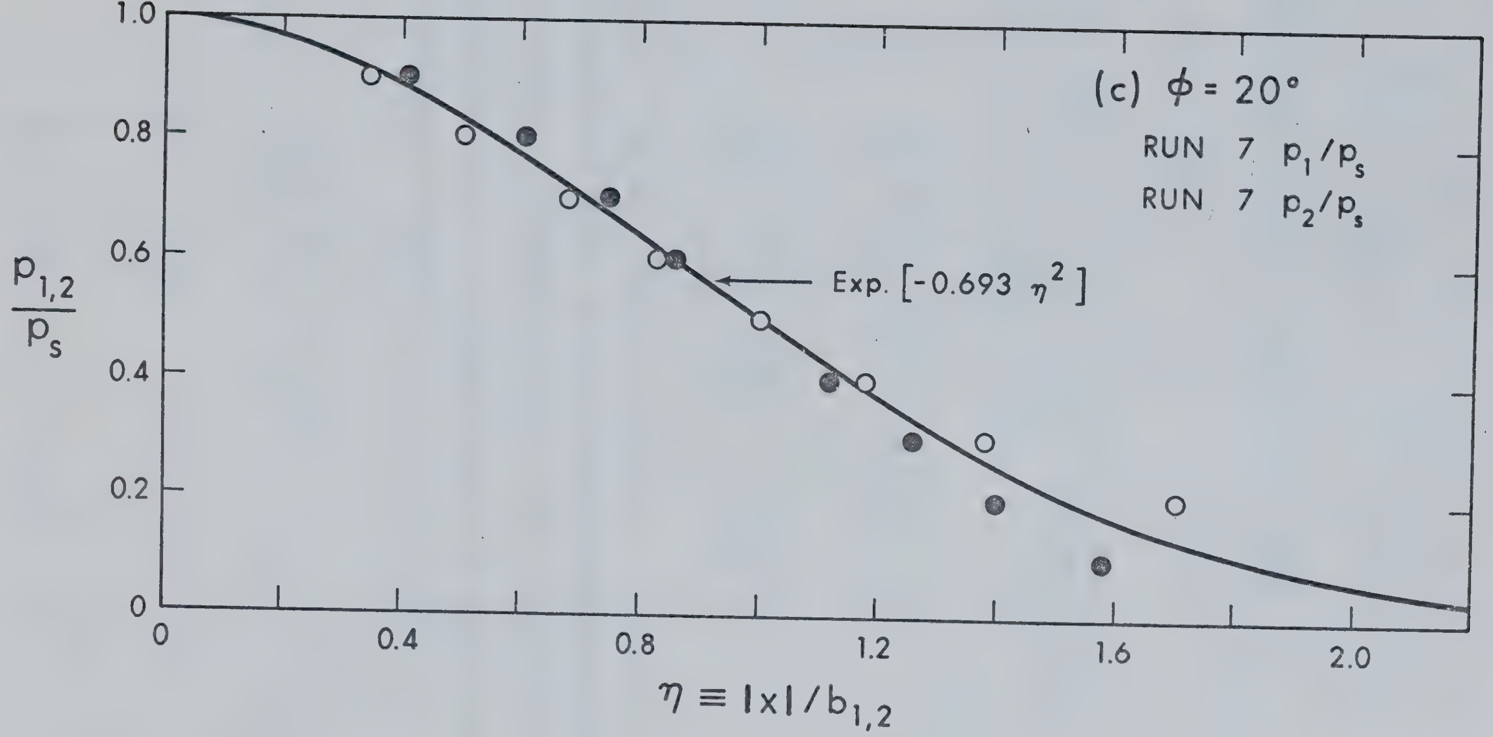

FIGURE 7.5 CONTINUED

$$\frac{p_{1,2}}{p_s} = g(\eta) = e^{-k\eta^2} \qquad (7.10)$$

By dimensional analysis it is easy to show that:

$$\frac{b_{1,2}}{H} = f_{1,2}(\phi) \qquad (7.11)$$

It is now possible to derive a general expression for the pressure at any point (x, y) on the wall as follows:

$$\frac{p_w}{p_s} = \frac{p_w}{p_{1,2}} \frac{p_{1,2}}{p_s} = g(\zeta)g(\eta)$$

or

$$\frac{p_w}{p_s} = \exp\left[-k\left(\frac{x^2}{b_{1,2}^2} + \frac{y^2}{b^2}\right)\right] \qquad (7.12)$$

In Equation 7.12, b_1 should be used when $x > 0$ and b_2 when $x < 0$. On the basis of the above, the wall pressure can be predicted entirely if the following quantities are known: The eccentricity s, the stagnation pressure p_s, the length scales b_1, b_2, b_3 and the slope α. By dimensional analysis, it is easy to show that:

$$\frac{p_s}{\rho U_o^2/2} \left(\frac{H}{d}\right)^2 = f_p(\phi)$$

$$\frac{s}{H} = f_s(\phi) \qquad (7.13)$$

$$\frac{b_i}{H} = f_i(\phi) \quad ; \quad i = 1,2,3$$

$$\alpha = \alpha(\phi)$$

The first two formulations are verified in Figures 7.6 and 7.7 where the data for different values of R_o and H/d are shown to define single curves. Similarly, the expressions involving the length scales are verified in Figure 7.8, whereas values of α are plotted against ϕ in Figure 7.9.

Qualitatively, the variations of s and p_s are similar to those obtained for plane jets (Chapter VI). However, here the relative eccentricity s/H is about one-half that of the plane case. The relative length scale b_1/H increases with decreasing values of ϕ, like in the plane case, but its rate of increase is considerably larger. In contrast with the plane case, the relative scale b_2/H increases with decreasing ϕ. This is attributed to the inability of the jet to develop concentrated vorticity at the side of negative x. Yet, as b_1 is always greater than b_2, the pressure profiles on the symmetry plane are generally skew, the skewness increasing as ϕ decreases, much like in the plane case. This is clearly demonstrated in Figure 7.10, where the ratio b_2/b_1 is plotted against ϕ. This ratio is indicative of the degree of skewness of the pressure distribution and is termed the "skewness index". It is now possible to derive some useful expressions related to properties of the wall pressure distribution. The equal-pressure contour of value $p_w/p_s = 1/m$ can be obtained using Equation 7.12:

$$\frac{1}{m} = \exp\left[-k\left(\frac{x^2}{b_{1,2}^2} + \frac{y^2}{b^2}\right)\right]$$

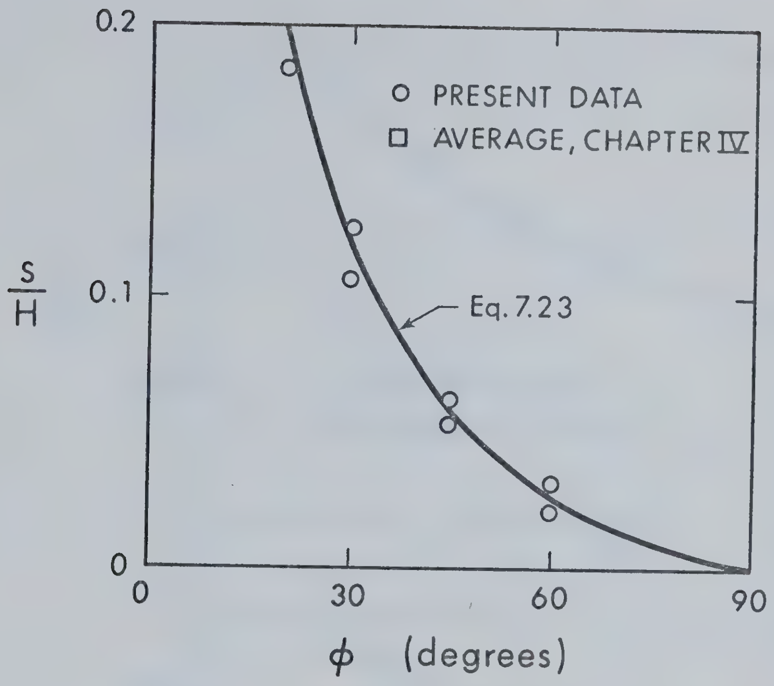

FIGURE 7.6 ECCENTRICITY OF STAGNATION POINT

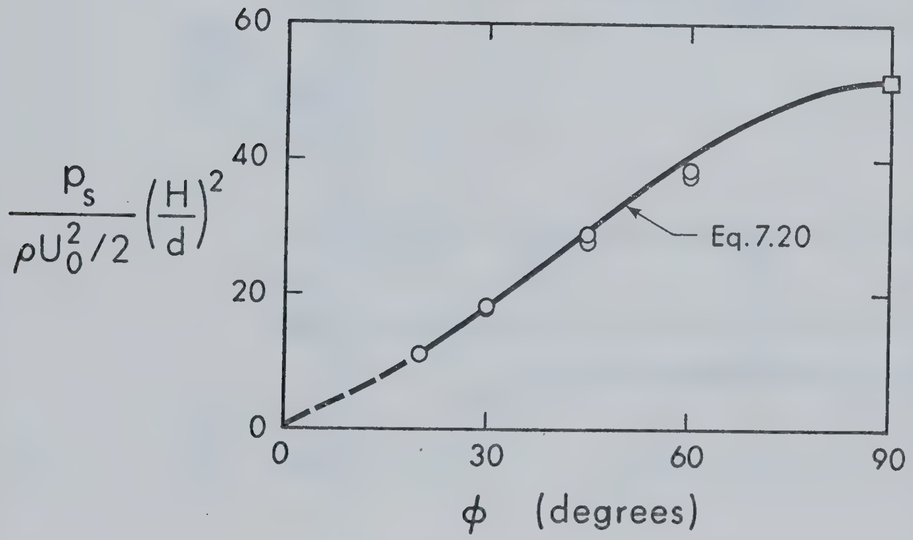

FIGURE 7.7 STAGNATION PRESSURE

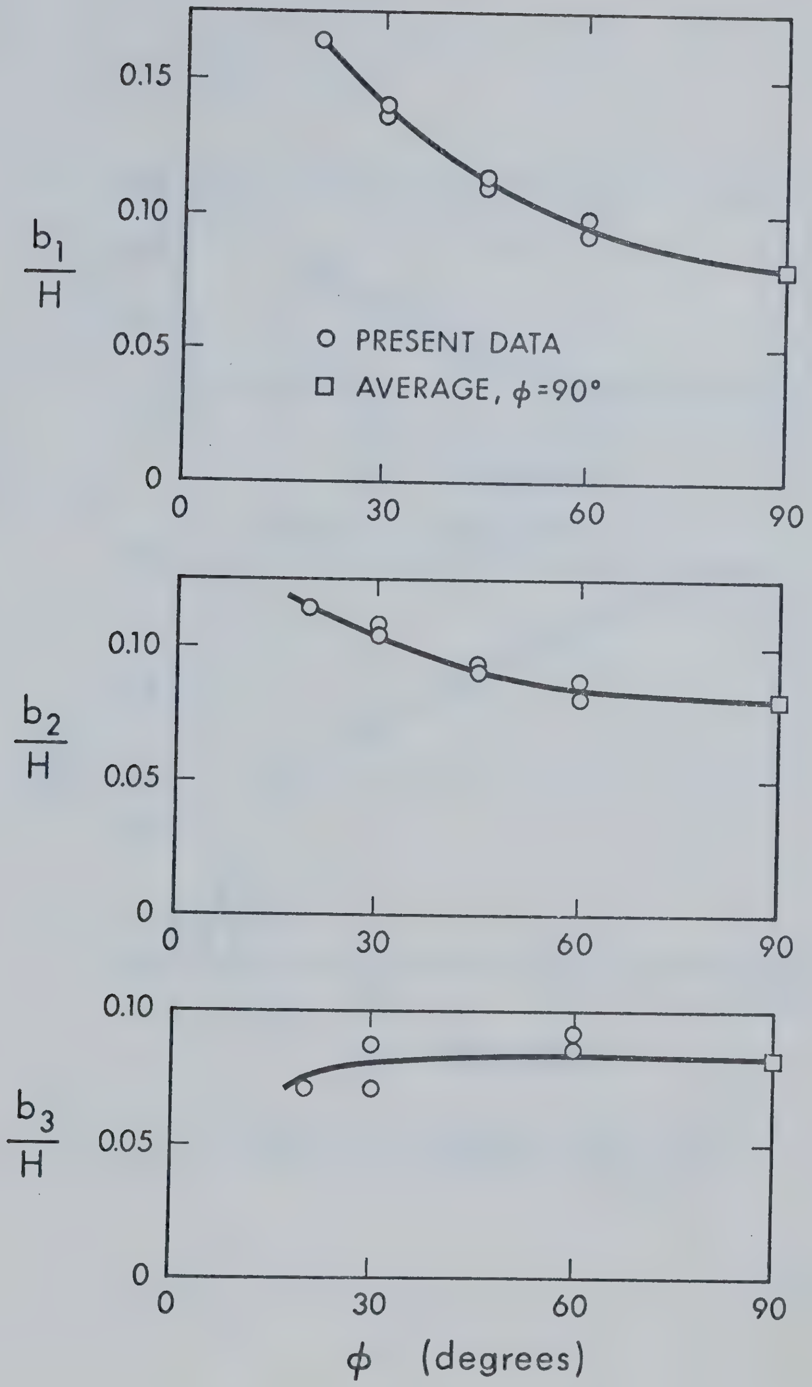

FIGURE 7.8 LENGTH SCALES b_1, b_2, b_3

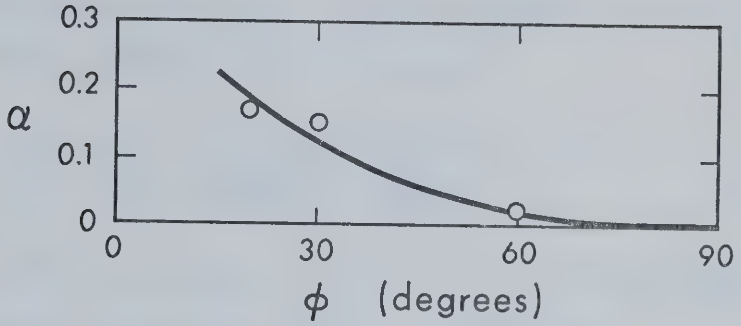

FIGURE 7.9 VARIATION OF α

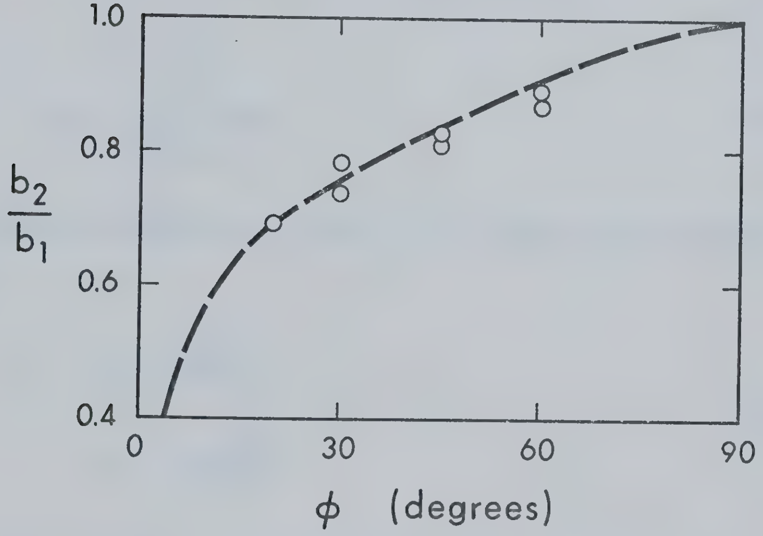

FIGURE 7.10 SKEWNESS INDEX b_2/b_1

or
$$y = \pm b\sqrt{\frac{\ell nm}{k} - \frac{x^2}{b_j^{\,2}}} \quad ; \quad j = 1,2$$

which is symmetric about the x-axis. Dropping the minus sign for convenience, and using Equation 7.9, this becomes:

$$\frac{y}{H} = \left(\frac{b_3}{H} + \alpha\,\frac{x}{H}\right)\sqrt{\frac{\ell nm}{k} - \left(\frac{x/H}{b_j/H}\right)^2} \tag{7.14}$$

where $j = 1$ when $x > 0$ and $j = 2$ when $x < 0$. If a_m is the area of the contour $p_w/p_s = 1/m$, then a_m is given by:

$$a_m = 2\int_{x_2}^{x_1} y\,dx \tag{7.15}$$

where $x_{1,2}$ are the values of x where this contour intersects the x-axis, i.e.:

$$\begin{aligned} x_1 &= b_1\sqrt{\frac{\ell nm}{k}} \\ x_2 &= -\,b_2\sqrt{\frac{\ell nm}{k}} \end{aligned} \tag{7.16}$$

Using the available results and making some obvious approximations, Equation 7.15 can be reduced to (see Appendix D, Section D.5):

$$a_m \simeq \frac{\pi}{2}\left(\frac{\ell nm}{k}\right) b_3\,(b_1 + b_2) \tag{7.17}$$

The area of the contour $p_w/p_s = 1/2$ is then:

$$a_2 \simeq \frac{\pi}{2}\, b_3\,(b_1 + b_2) \tag{7.18}$$

since $k = \ln 2 = .693$. Hence, the ratio a_m/a_2 equals $\ln m/k$. When $p_w/p_s = 1/m$, this can be written as:

$$\frac{p_w}{p_s} = e^{-k \frac{a}{a_2}} \tag{7.19}$$

Equation 7.19 states that the wall pressure is similarly distributed if it is referred to the area a of the contour which a certain value of p determines. The scale of pressure is p_s and the scale of area is a_2, i.e., the value of a when $p_w = \frac{1}{2} p_s$. This could be easily checked for the case $\phi = 90°$. It follows that the property of similarity with respect to contour areas is preserved for all ϕ. Contour areas were obtained directly from the data (with a planimeter) and Equation 7.19 is verified in Figure 7.11. This result makes integration of wall pressure very simple. The total pressure force acting on the wall, P_w, will be:

$$P_w = \int_o^\infty p da = a_2 p_s \int_o^\infty (\frac{p}{p_s}) \, d \, (\frac{a}{a_2})$$

or

$$P_w = \frac{a_2 p_s}{k}$$

Equating P_w to the normal component of the initial momentum of the jet:

$$\frac{1}{k} \, a_2 p_s = \rho \, \frac{\pi d^2}{4} \, U_o^{\,2} \sin \phi$$

Using Equation 7.18, this becomes, after some manipulation:

$$\frac{p_s}{\rho U_o^{\,2}/2} \, (\frac{H}{d})^2 = \frac{k \sin \phi}{\bar{b}_3 (\bar{b}_1 + \bar{b}_2)} \tag{7.20}$$

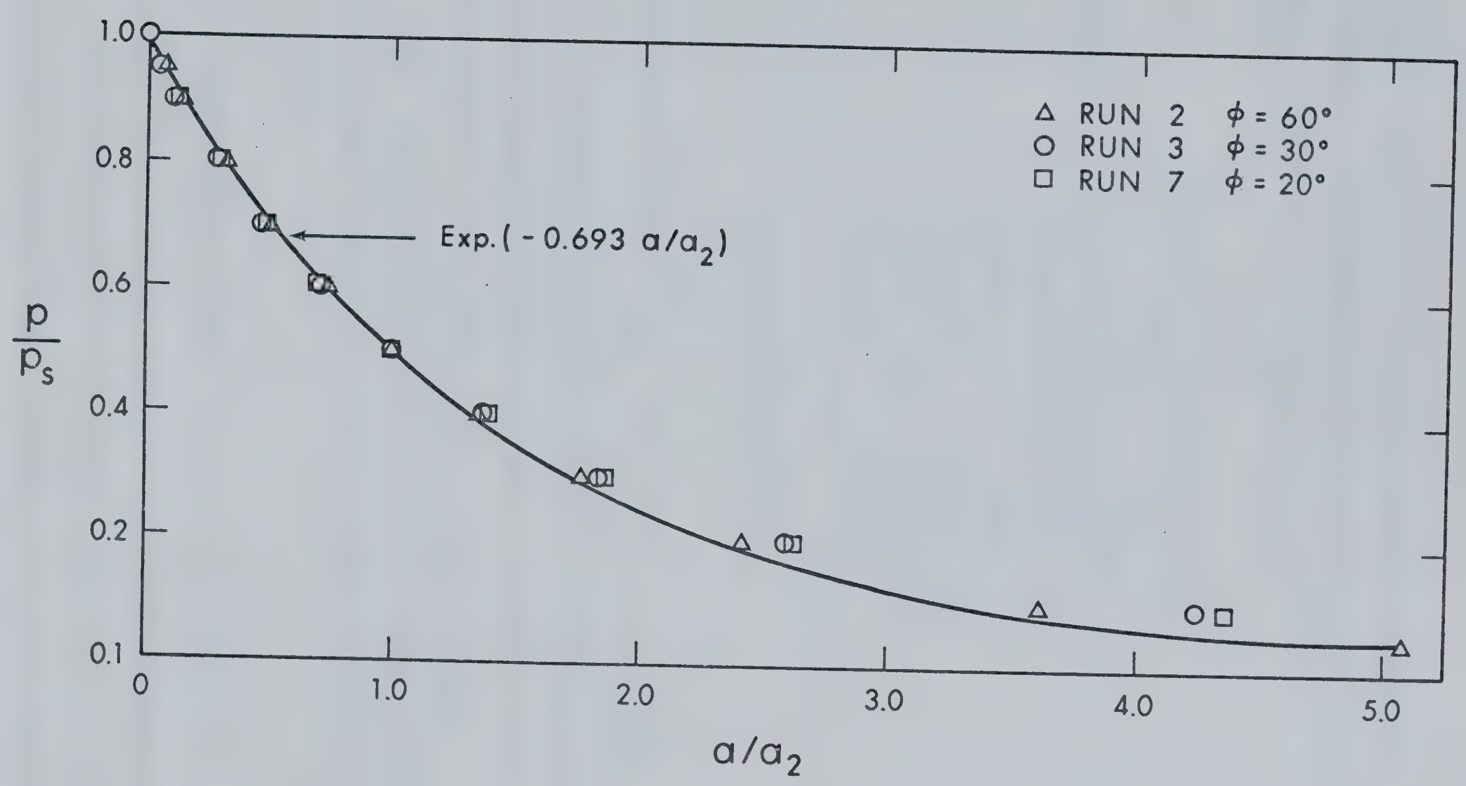

FIGURE 7.11 SIMILARITY IN TERMS OF CONTOUR AREAS

where $\overline{b}_i \equiv b_i/H$; $i = 1,2,3$. When $\phi = 90°$, $\overline{b}_1 = \overline{b}_2 = \overline{b}_3 = \overline{b}_{90}$ and $\sin\phi = 1$. The present data (Chapter IV) gave $\overline{b}_{90} = 0.078$. A summary of available data is tabulated below.

Source	$\overline{b}_{90}$
Poreh & Cermak	0.075
Tani & Komatsu	0.088
Hrycak et al	0.089
Bradbury	0.077
Present data	0.078
Average	0.0814

TABLE 7.2 VALUE OF $\overline{b}_{90}$

Using an average value of $\overline{b}_{90} = 0.0814$, the value of $\frac{p_s}{\rho U_o^2/2}\left(\frac{H}{d}\right)^2$ at $\phi = 90°$ is predicted to be 52.2 which is in excellent agreement with the average experimental value of 52 obtained in Chapter IV. The empirical curves of Figure 7.8 were drawn so that they pass through $\overline{b} = 0.0814$ at $\phi = 90°$. Using these curves, Equation 7.20 can be evaluated and is plotted in Figure 7.7 where it is seen to agree well with the experimental results.

Considering the eccentricity s of the stagnation point, it is not possible to derive an expression from potential flow considerations, owing to the fact that no potential solutions can be found for flows that are not axisymmetric. However, s can be predicted if it is assumed to be proportional to a characteristic linear dimension of the

wall pressure distribution. Such a dimension is the distance x_c of the center of gravity of the wall pressure distribution from S. This is given by:

$$x_c P_w = \int_{-\infty}^{\infty} \int_{-\infty}^{\infty} xp\,dx\,dy \tag{7.21}$$

This equation can be reduced to (see Appendix D, Section D.6):

$$\frac{x_c}{H} = \frac{\bar{b}_1 - \bar{b}_2}{\sqrt{\pi k}} + \frac{\alpha}{2k} \; \frac{\bar{b}_1^{\,3} + \bar{b}_2^{\,3}}{\bar{b}_3(\bar{b}_1 + \bar{b}_2)} \tag{7.22}$$

Taking a factor of proportionality of 2.9, indicated by the experimental results, the eccentricity s becomes:

$$\frac{s}{H} = 2.9\,\frac{x_c}{H} \tag{7.23}$$

This equation is shown plotted in Figure 7.6 and is seen to be an adequate description of the data.

With the information already available it is possible, in principle, to derive an equation for the family of curves that are orthogonal to equal-pressure contours. These curves will represent the wall streamlines, as was pointed out earlier, and inspection of the available relations shows that a derivation of their equations would be rather laborious. The end of the impingement region could be taken as the contour $p_w/p_s = 1/m$ with m being a large number so that $p_w/p_s \to 0$. For example, m could be taken equal to 50, so that $p_w/p_s = 0.02$. It is reasonable to assume that beyond the impingement region, the wall

streamlines are linear, retaining the direction they had when crossing the limiting pressure contour. Inspection of the pressure contours indicates that these straight lines intersect the x-axis at different points,i.e., there is no single focus of streamlines. These considerations are in agreement with photographic evidence presented in (45) for the case of a potential impinging jet. Yakovlevskii and Krasheninnikov (27) state that in the wall jet region the streamlines are straight and originate at the point 0 (Figure 7.1). This implies a single focus of streamlines. This apparent disagreement with the present conclusion can be explained as follows. Even though the streamlines originate at different points on the x-axis, the distance of these points from 0 or S remains finite and is of the order of the distance 0S(= s). This distance, however, is about an order of magnitude less than H. Measurements in the wall-jet region are made for distances r at least of the order of H, hence it makes little difference whether a measurement of velocity is made by orienting a probe towards S or 0 or any other point in-between.

7.3.1.2 Wall Shear Stress

Measurements of wall shear stress in the impingement region were performed, as a rule, only along lines where the direction of shear stress could be estimated reasonably well. The x-axis constitutes such a line and typical shear stress measurements on this locus are shown in Figure 7.12. The quantity τ_{o*} is a normalized value of the shear stress τ_o defined as $\tau_{o*} \equiv \tau_o d_o{}^2/4\rho\nu^2$ where d_o is the outside diameter of the Preston tube (.046 in.). In Figure 7.12, the data

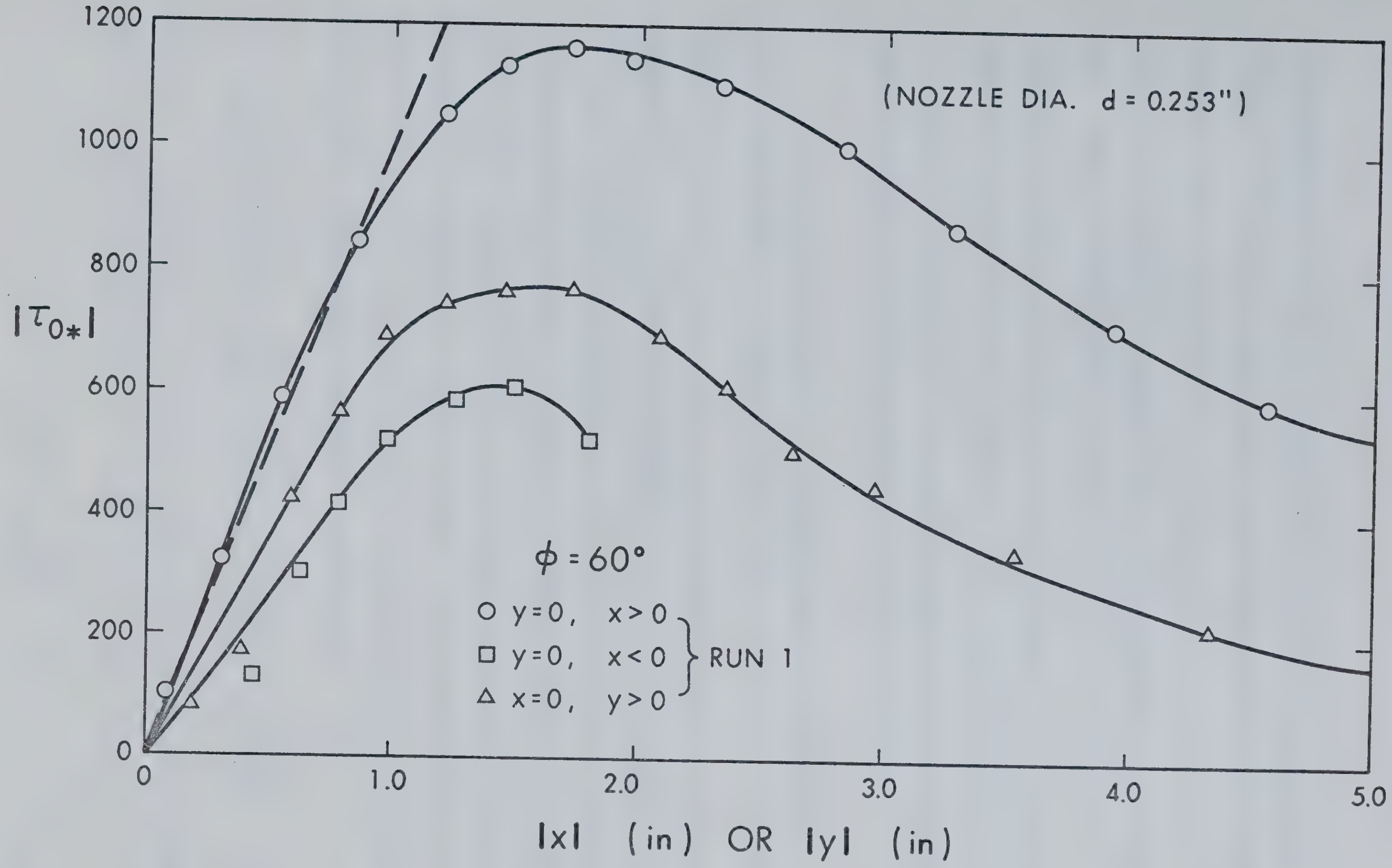

FIGURE 7.12 WALL SHEAR STRESS MEASUREMENTS

for the case $x = 0$, $y > 0$ indicate measurements along the y-axis. For the case $\phi = 60°$, the y-axis was almost perpendicular to the pressure contours, hence such measurement was permissible. Owing to probe interference with the flow, the data for $x < 0$ are mostly of qualitative value. This is demonstrated clearly in Figure 7.12 where the continuity condition $(d\tau_o/dx)_{x \to o^+} = (d\tau_o/dx)_{x \to o^-}$ is not satisfied. It may be noted that values of shear stress along the x-axis are the most important from the practical point of view, because they indicate maximum $(x > 0)$ and minimum $(x < 0)$ variations.

In order to predict τ_o consider again the equation of motion in the z-direction. Strictly speaking, a curvilinear frame of reference should be used (x_1, y_1, z_1) where z_1 is distance along the stagnating streamline, x_1 is distance perpendicular to it on the symmetry plane and y_1 is distance permendicular to the symmetry plane. However, if the stagnating streamline is assumed to intersect the wall at right angles, it is permissible to use the Cartesian system (x, y, z) or the system (r, θ, z) if z is kept very small. The Reynolds equation of motion in the z-direction is (after some manipulation of the equation given in (47), and using cylindrical co-ordinates):

$$v_r \frac{\partial v_z}{\partial r} + \frac{v_\theta}{r}\frac{\partial v_z}{\partial \theta} + v_z \frac{\partial v_z}{\partial z} = \frac{1}{\rho}\frac{\partial \sigma_z}{\partial z} + \frac{1}{\rho r}\frac{\partial (r\tau_{rz})}{\partial r} + \frac{1}{\rho r}\frac{\partial \tau_{\theta z}}{\partial \theta} \qquad (7.24)$$

where σ_z, τ_{rz} and $\tau_{\theta z}$ are total (laminar plus turbulent) normal and shearing stresses respectively. In particular, σ_z is given by:

$$\sigma_z = -\bar{p} - \rho\overline{v_z'^2} + 2\mu \frac{\partial v_z}{\partial z} \qquad (7.25)$$

where the overbar denotes time average and the prime denotes fluctuating value. At the wall (z = 0) the inertial terms vanish and Equation 7.24 becomes:

$$-\left(\frac{\partial\sigma_z}{\partial z}\right)_0 = \left[\frac{1}{r}\frac{\partial(r\tau_{rz})}{\partial r}\right]_0 + \left[\frac{1}{r}\frac{\partial\tau_{\theta z}}{\partial\theta}\right]_0 \tag{7.26}$$

Much like in the previous chapters, here again the viscous component of σ_z will be assumed to be negligible in comparison to the other terms. Furthermore, it is assumed that the measured pressure p is approximately equal to $\overline{p} + \rho\overline{v_z'^2}$ Hence, Equation 7.26 is finally reduced to:

$$\left(\frac{\partial p}{\partial z}\right)_0 = \frac{1}{r}\frac{\partial(r\tau_{or})}{\partial r} + \frac{1}{r}\frac{\partial\tau_{o\theta}}{\partial\theta} \tag{7.27}$$

where τ_{or} and $\tau_{o\theta}$ are the components of τ_o in the r and θ directions respectively. This equation will now be solved for the cases $\theta = 0°$ and $180°$, i.e., along the x-axis. In this case $r = x$ and since the flow approaches axisymmetric properties near the symmetry plane, terms involving $\frac{\partial}{\partial\theta}$ will vanish. Denoting $(\tau_{or})_{\theta=0,\pi}$ as τ_o, Equation 7.27 becomes:

$$\frac{d(x\tau_o)}{dx} = x\left(\frac{\partial p}{\partial z}\right)_{\substack{z=o\\y=o}} \tag{7.28}$$

This can be reduced to (see Appendix D):

$$\frac{\tau_o}{\tau_{om}} = q_m[g_1(\eta) - \sigma_m g_2(\eta)] \tag{7.29}$$

where $g_1(\eta) = \frac{1 - g(\eta)}{\eta}$; $g_2(\eta) = \eta g(\eta)$ and q_m, σ_m are functions

of η_m, the value of η where the maximum shear stress, τ_{om}, occurs. These functions are shown graphically in Figure 7.13. Furthermore, η_m is a function of ϕ and:

$$C_* \equiv \frac{\tau_{om}}{\rho U_o^2} \left(\frac{H}{d}\right)^2 = h(\phi) \tag{7.30}$$

The functions $\eta_m = \eta_m(\phi)$ and $h(\phi)$ are left to be determined empirically. In Appendix D, Section D.1.1, Equation D.17 and Equation D.18, it is further shown that η_m has the same value for both semi-axes ($x < 0$ and $x > 0$) and that if $\tau_{om}^{(1)}$, $\tau_{om}^{(2)}$ are the values of τ_{om} for the semi-axes $x > 0$ and $x < 0$ respectively, then, in order to satisfy continuity of τ_o at $x = 0$, the ratio $\tau_{om}^{(2)}/\tau_{om}^{(1)}$ must equal the skewness index:

$$\frac{\tau_{om}^{(2)}}{\tau_{om}^{(1)}} = \frac{b_2}{b_1} \tag{7.31}$$

The variation of η_m with ϕ is evaluated empirically in Figure 7.14. Using this graph, and the auxiliary plots of Figure 7.13, Equation 7.29 was applied to the cases $\phi = 60°$, $45°$ and $30°$, and the results are compared with experimental data in Figure 7.15(a) to (c). It is seen that theory is in good agreement with experiments in the main portion of the impingement region. It was pointed out earlier that when $x < 0$, significant errors are involved in measurements of τ_o. If it is assumed that this error is proportional to the magnitude of τ_o, then the curves τ_o/τ_{om} will be reliable in the range $x < 0$, as they involve only relative values. Regarding the friction coefficient C_* defined

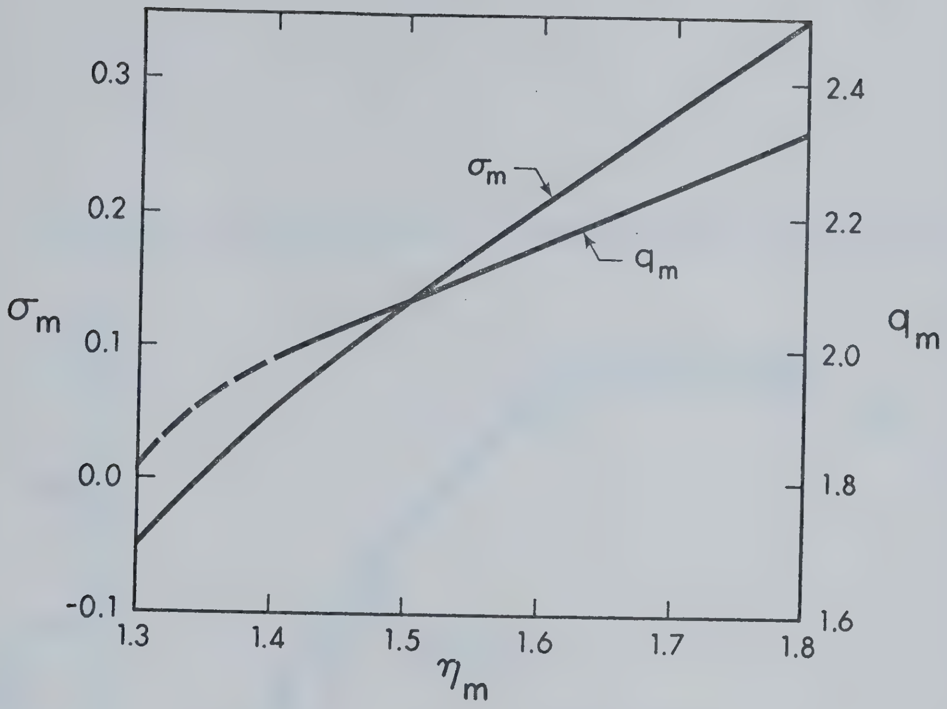

FIGURE 7.13 AUXILIARY FUNCTIONS σ_m, q_m

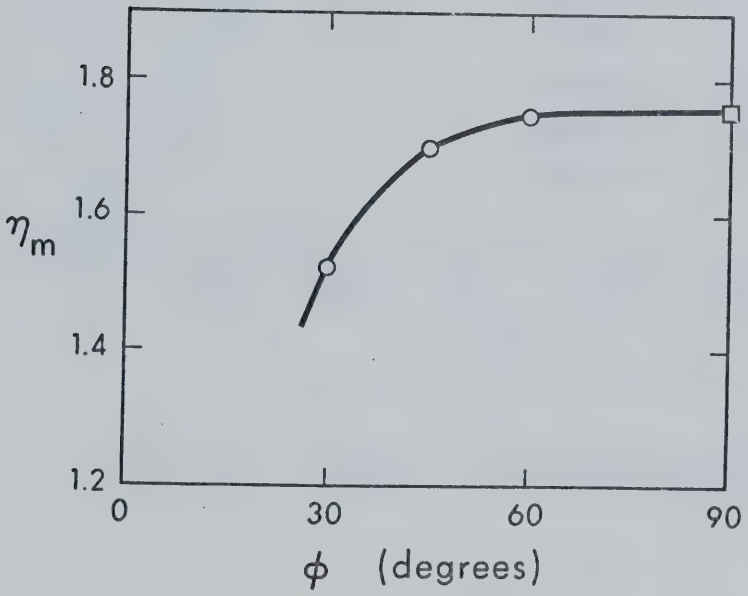

FIGURE 7.14 LOCUS OF MAXIMUM WALL SHEAR, SYMMETRY PLANE

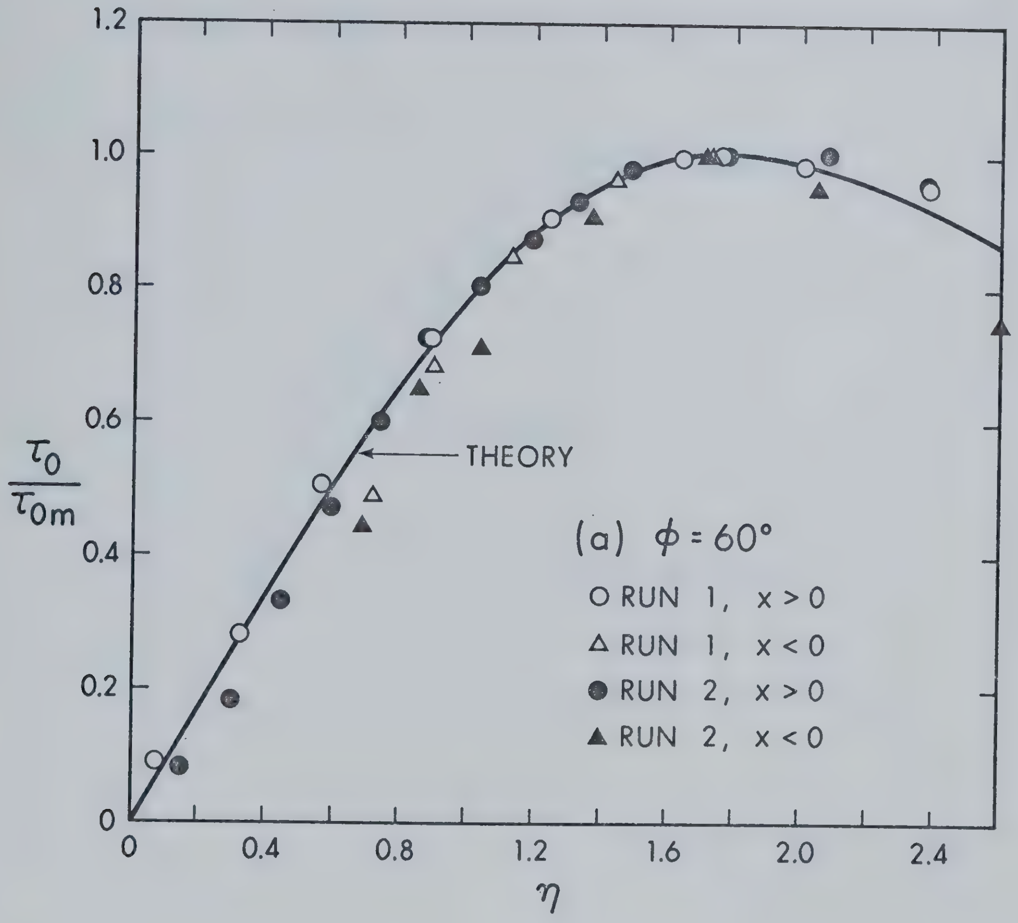

FIGURE 7.15 SIMILARITY OF WALL SHEAR, SYMMETRY PLANE

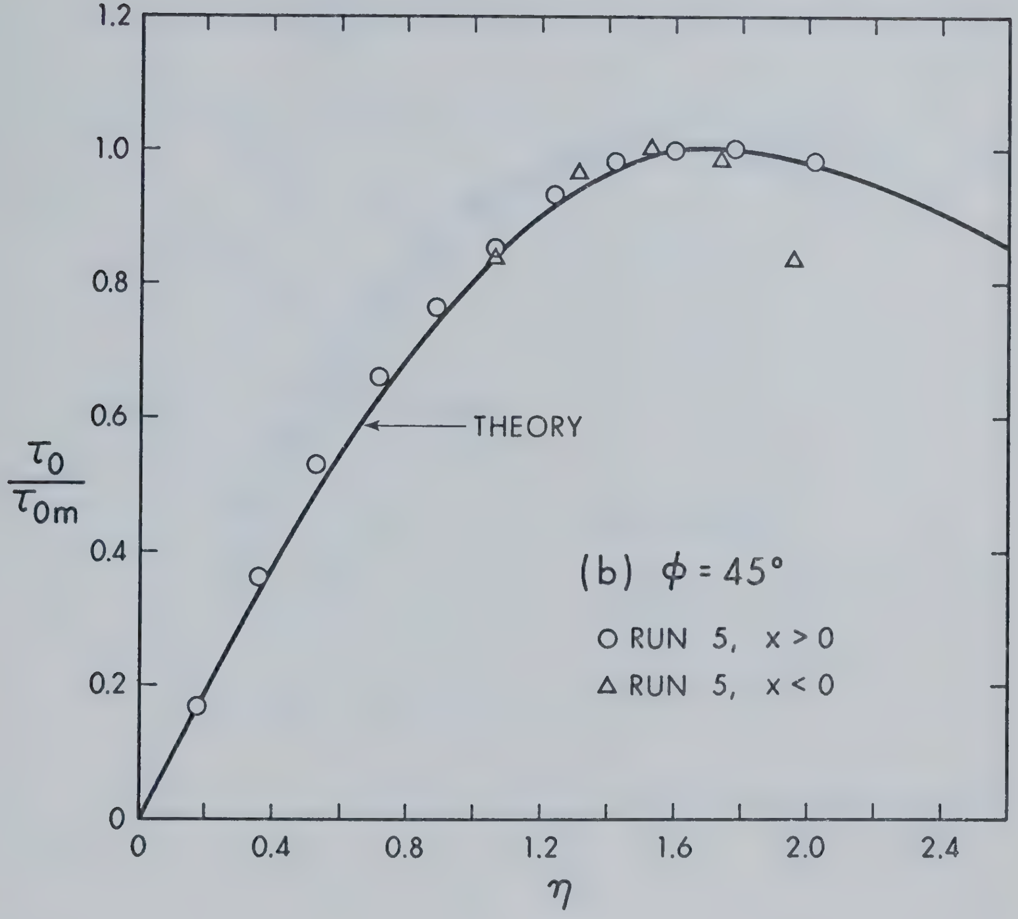

FIGURE 7.15 CONTINUED

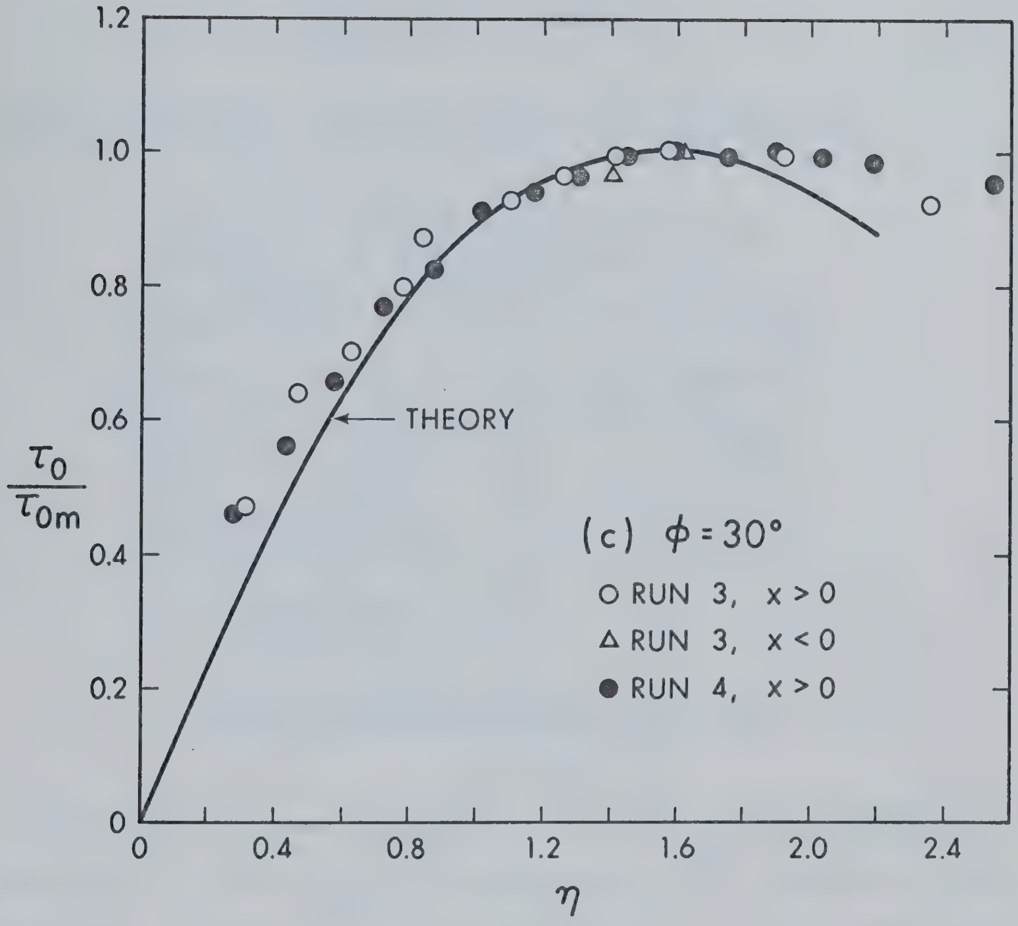

FIGURE 7.15 CONTINUED

in Equation 5.30, only the data for $x > 0$ are reliable. Dimensional analysis will indicate that:

$$C_* \equiv \frac{\tau_{om}}{\rho U_o^2} \left(\frac{H}{d}\right)^2 = \bar{h}(\phi, R_o) \qquad (7.32)$$

The available data, for $x > 0$ $(C_*^{(1)})$ are tabulated below.

Source	R_o	H/d	$\phi(°)$	$C_*^{(1)}$
Run 1	34,700	39.25	60	0.179
Run 2	89,600	15.50	60	0.163
Run 3	89,600	20.00	30	0.154
Run 4	34,700	46.50	30	0.168
Run 5	34,700	47.00	45	0.181
Ch. IV	40×10^3 to 180×10^3	18 to 66	90	0.160

TABLE 7.3 MAXIMUM SHEAR STRESS ($x > 0$)

As was the case at normal impingement, there seems to be no consistent variation of C_* with R_o. At the same time, $C_*^{(1)}$ appears to be independent of the angle ϕ, as was the tendency in the case of plane jets (Chapter VI), and therefore an average value will be adopted, i.e.:

$$C_*^{(1)} = 0.166 \qquad (7.33)$$

Regarding $C_*^{(2)}$, the value of C_* when $x < 0$, Equation 7.31 provides a useful guide. Figure 7.16 shows this plotted (using Figure 7.10)

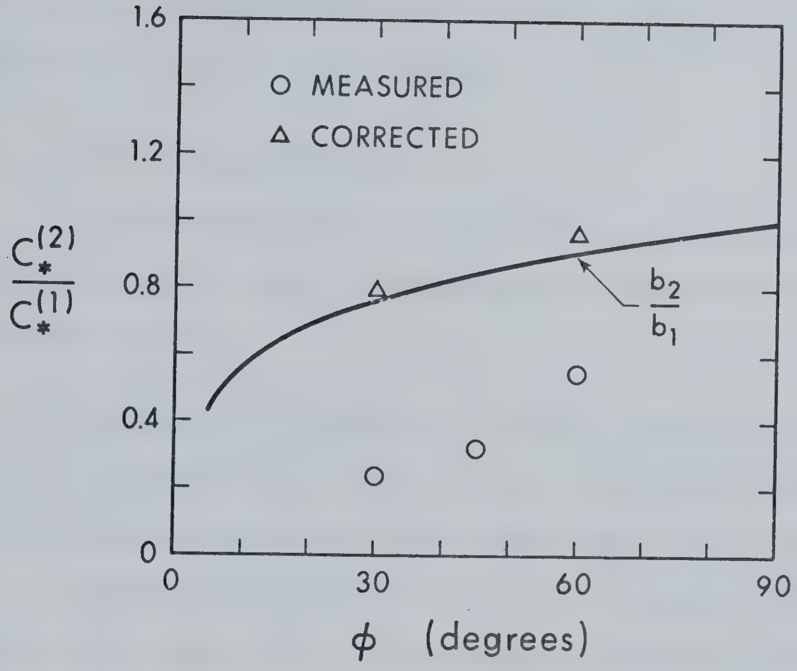

FIGURE 7.16 EVALUATION OF $C_*^{(2)}$

together with the measured data. It is seen that there is no agreement but this does not necessarily disprove the analysis, as the data are unreliable in this range. If it is assumed that the error is proportional to the magnitude of the wall shear stress, it is possible to apply a correction based on the requirement of continuous shear stress variation at $x = 0$. The corrected values are also shown in Figure 7.16 and they are much closer to the theoretical curve.

7.3.2 Wall Jet Region

A short distance after the end of the impingement region, the flow assumes a pattern similar in many respects to the type of flow known as the wall jet.

On the basis of considerations stated at the end of Section 7.3.1.1, it is permissible to assume that for all practical purposes, the flow takes place along radial lines originating at the stagnation point S. Yakovlevskii and Krasheninnikov (27) assumed the origin to be at the intersection of the jet centerline and the wall. Considering that measurements in this region are made at radial distances that are at least an order of magnitude larger than the eccentricity, s, this difference is immaterial. Furthermore, it will be assumed that no significant skewness occurs in the boundary layer. This assumption is implicit in (27) even though it is not stated explicitly. It is evident that skewness is likely to increase for decreasing values of the angle of impingement, so that this assumption can be adopted with the qualification that it may be unrealistic for the smaller values of ϕ.

Yakovlevskii and Krasheninikov (27) reported that profiles of the radial velocity component are geometrically similar in the usual manner of wall jets. However, their experimentation was limited in the range $45° \leq \phi \leq 90°$. In order to further explore similarity, measurements were performed for the rather extreme case $\phi = 20°$, at polar angles $\theta = 0°$ and 45°. If u is the radial component of velocity and u_m is its maximum value in the vertical, plots of u/u_m vs z/δ_2 are shown in Figure 7.17. The results confirm similarity of profiles at this low value of ϕ. A summary of average data is presented graphically in Figure 7.18 together with the classical wall jet profile. Experimental results are in good agreement among themselves, even though agreement with theory is only fair. It is reasonable to expect that skewness would cause the profiles to deviate from similarity, so that it may be concluded that at least in the range $20° \leq \phi \leq 90°$ skewness effects are not significant.

Consider now the following analysis. Neglecting viscous stresses, the Reynolds equation of motion in the radial direction is (47):

$$v_r \frac{\partial v_r}{\partial r} + \frac{v_\theta}{r}\frac{\partial v_r}{\partial \theta} + v_z \frac{\partial v_r}{\partial z} - \frac{v_\theta^2}{r} = -\frac{1}{\rho}\frac{\partial p}{\partial r} - \frac{\partial \overline{v_r'^2}}{\partial r} - \frac{\overline{v_r'^2}}{r} + \frac{\overline{v_\theta'^2}}{r} +$$

$$+ \frac{1}{r}\frac{\partial(-\overline{v_r'v_\theta'})}{\partial \theta} + \frac{\partial}{\partial z}\left(-\overline{v_r'v_z'}\right) \qquad (7.34)$$

Neglecting further the pressure gradients and the quantity:

$$\frac{\overline{v_\theta'^2} - \overline{v_r'^2}}{r} \quad \text{and setting} \quad \tau_{r\theta} = -\rho\,\overline{v_r'v_\theta'}$$

and $\tau_{rz} = -\rho\,\overline{v_r'v_z'}$

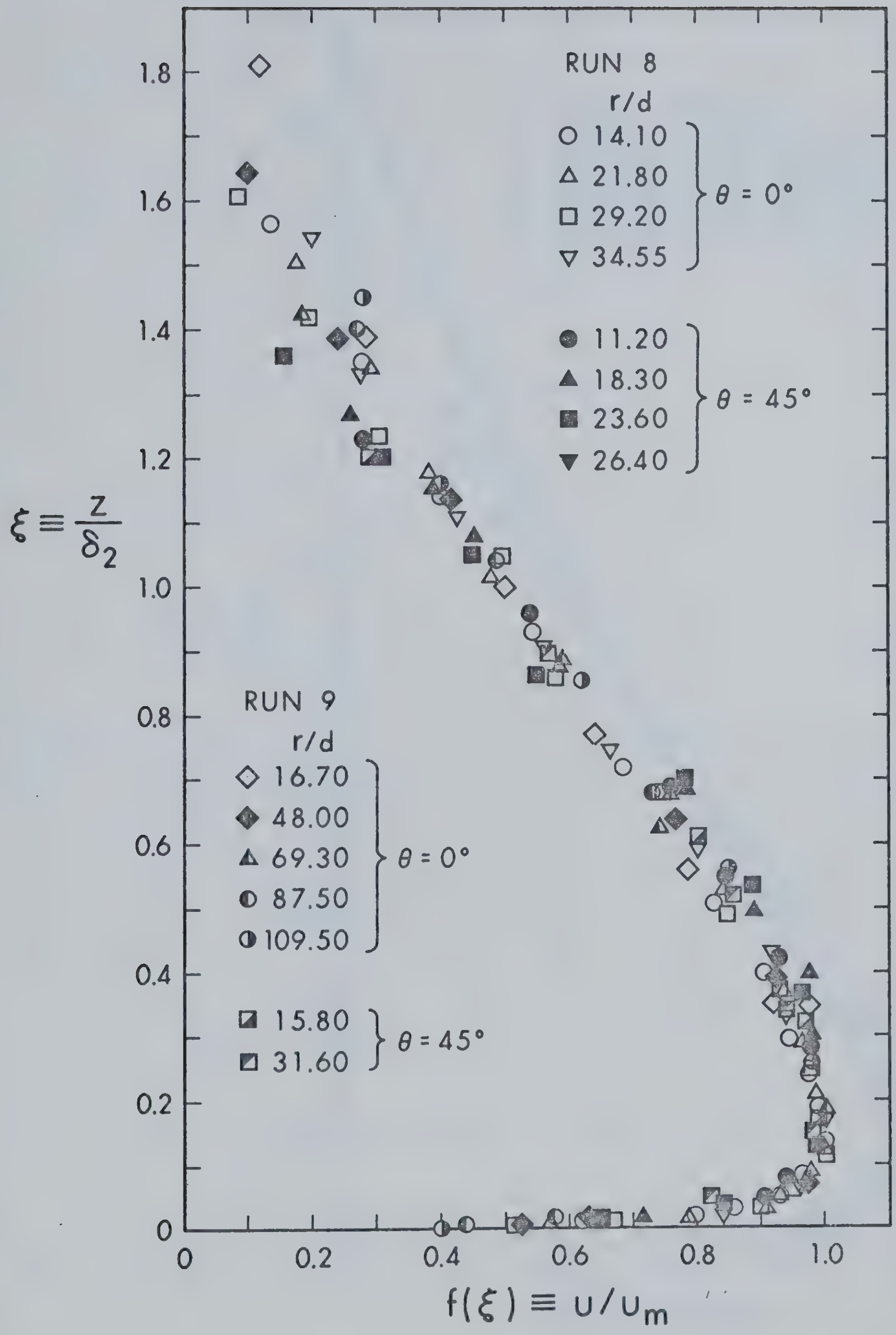

FIGURE 7.17 WALL JET SIMILARITY

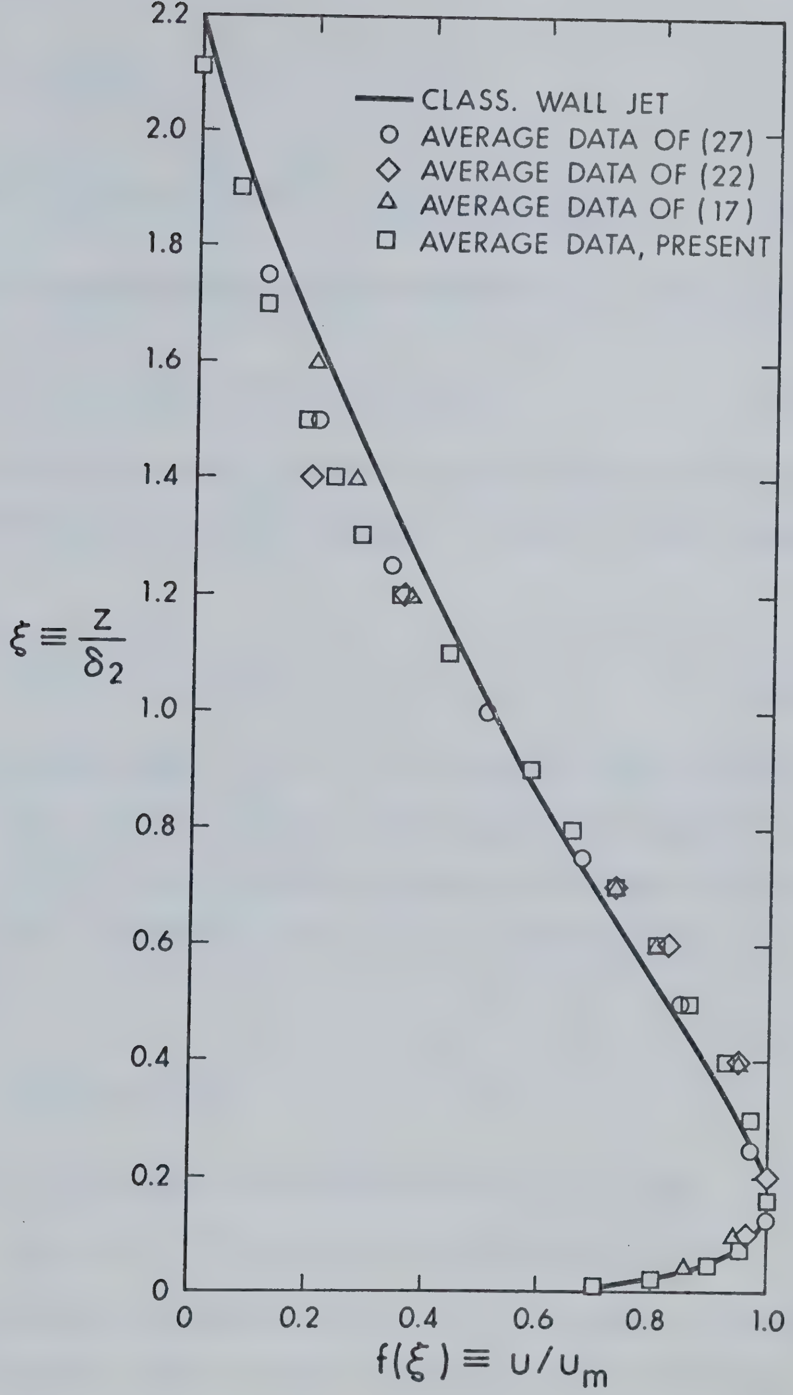

FIGURE 7.18 WALL JET SIMILARITY - SUMMARY

this equation becomes:

$$v_r \frac{\partial v_r}{\partial r} + \frac{v_\theta}{r}\frac{\partial v_r}{\partial \theta} + v_z \frac{\partial v_r}{\partial z} - \frac{v_\theta^2}{r} = \frac{1}{\rho r}\frac{\partial \tau_{r\theta}}{\partial \theta} + \frac{1}{\rho}\frac{\partial \tau_{rz}}{\partial z} \qquad (7.35)$$

Introducing the usual boundary-layer approximations, it is assumed that:

$$\frac{\partial}{\partial r} \ll \frac{\partial}{\partial z} \quad \text{and} \quad v_z \ll v_r \qquad (7.36)$$

Furthermore, since in the wall jet region the radial direction is almost the same with the direction of a streamline, it could be further assumed that:

$$\frac{\partial}{r\partial \theta} \ll \frac{\partial}{\partial z} \quad \text{and} \quad v_\theta \ll v_r \qquad (7.37)$$

In addition to these, since $v_\theta \ll v_r$, it could be assumed that the stress $\tau_{r\theta} = \tau_{\theta r}$ which acts between radial planes is much smaller than the stress $\tau_{rz} = \tau_{zr}$ which is produced mainly by the dominant velocity gradient $(\partial v_r/\partial z)$. Considering also the first of relations 7.37, it follows that:

$$\frac{\partial \tau_{r\theta}}{r\partial \theta} \ll \frac{\partial \tau_{rz}}{\partial z}$$

Hence, $\partial \tau_{r\theta}/r\partial\theta$ could be neglected from Equation 7.35. Since $\frac{\partial v_r}{\partial r} \sim \frac{v_r}{r}$, the term v_θ^2/r could be neglected in comparison to $v_r \frac{\partial v_r}{\partial r}$. Furthermore, the angular velocity v_θ is at most of the order of v_z which together with the first of relations 7.37 indicates that $v_\theta \frac{\partial v_r}{r\partial \theta} \ll v_z \frac{\partial v_r}{\partial z}$. Therefore, Equation 7.35 can be reduced to:

$$v_r \frac{\partial v_r}{\partial r} + v_z \frac{\partial v_r}{\partial z} \cong \frac{1}{\rho} \frac{\partial \tau_{rz}}{\partial z} \tag{7.38}$$

Consider now the time-average equation of continuity (47):

$$\frac{1}{r}\frac{\partial}{\partial r}(rv_r) + \frac{\partial v_\theta}{r\partial\theta} + \frac{\partial v_z}{\partial z} = 0 \tag{7.39}$$

Since $v_\theta \lesssim v_z$ and $\frac{\partial}{r\partial\theta} << \frac{\partial}{\partial z}$ this reduces to:

$$\frac{\partial(rv_z)}{\partial z} + \frac{\partial(rv_r)}{\partial r} = 0 \tag{7.40}$$

These equations (7.38 and 7.40) appear to be the same with those governing axisymmetric flows. Yet, the flow is not assumed to be axisymmetric because angular variations cannot be neglected, even though they do not appear in the governing differential equation. In view of these, the flow in this region could be labeled as "quasi-axisymmetric", because even though it is not axisymmetric, it does retain some properties of the axisymmetric radial wall jet. It is now convenient to employ a more familiar notation, i.e., v_r, v_z are designated as u and w respectively. Then, Equations 7.38 and 7.40 become:

$$u\frac{\partial u}{\partial r} + w\frac{\partial u}{\partial z} = \frac{1}{\rho}\frac{\partial \tau}{\partial z} \tag{7.41}$$

$$\frac{\partial(ru)}{\partial r} + \frac{\partial(rw)}{\partial z} = 0 \tag{7.42}$$

where τ is written instead of τ_{rz}. The similarity relation is:

$$\frac{u}{u_m} = f(\xi) \quad ; \quad \xi \equiv \frac{z}{\delta_2} \tag{7.43}$$

These relations are identical with the starting equations of the conventional axisymmetric wall jet. Assuming similarity of shear stresses $\tau = \rho u_m^2 g_\tau(\xi)$, and proceeding as in Chapter II, it is possible to derive the following:

$$\frac{\delta_2}{u_m}\frac{\partial u_m}{\partial r}[f^2 - f'F] - \frac{\delta_2}{r}f'F - \frac{\partial \delta_2}{\partial r}f'F = g_\tau(\xi) \qquad (7.44)$$

Where

$$F(\xi) = \int_o^\xi f(\xi)d\xi \qquad (7.45)$$

This relation implies that:

$$\frac{\delta_2}{u_m}\frac{\partial u_m}{\partial r} = C_1 \qquad (7.46)$$

$$\frac{\delta_2}{r} = C_2 \qquad (7.47)$$

$$\frac{\partial \delta_2}{\partial r} = C_3 \qquad (7.48)$$

where the constants C_1, C_2, C_3 must be universal since the functions f, F and g are the same regardless of R_o, H/d or ϕ. Equations 7.47 and 7.48 require that:

$$\delta_2 = C_2 r \qquad (7.49)$$

and Equations 7.46 and 7.49 lead to:

$$u_m = k(\theta)r^a \qquad (7.50)$$

where a is an exponent and $k(\theta)$ is a function of θ. The integral momentum equation, together with Equations 7.49 and 7.50 will yield:

$$a = -\left(1 + \frac{C_f}{4C_2F_1}\right) \qquad (7.51)$$

where C_f is the local skin-friction factor $\tau_o / \frac{\rho u_m^2}{2}$, τ_o is the wall shear stress in the r-direction, and F_1 is a constant equal to $\int_o^\infty f^2 d\xi$. The skin-friction factor C_f can be shown to depend only upon R_o, using the same arguments as in Chapter II, i.e.:

$$C_f = C_f(R_o) \qquad (7.52)$$

The quantity $u_*/u_m = \sqrt{C_f/2}$ is plotted against r/d for different values of ϕ, θ and H/d in Figure 7.19. It is seen that u_*/u_m does not depend on r/d. Values of C_f obtained from this graph are tabulated below. Inspection shows that the only dependence of C_f is indeed on the Reynolds number, R_o.

Run No	R_o	H/d	ϕ(°)	θ(°)	C_f
1	34,700	39.25	60	0 90 180	0.0101 0.0116 0.0106
2	89,600	15.5	60	0 90	0.0087 0.0090
3	89,600	20.0	30	0	0.0082
4	34,700	46.5	30	0	0.01095
5	34,700	47.0	45	0	0.01095

TABLE 7.4 SKIN-FRICTION FACTOR

Data from Table 7.4 are plotted in Figure 7.20, together with the empiri-

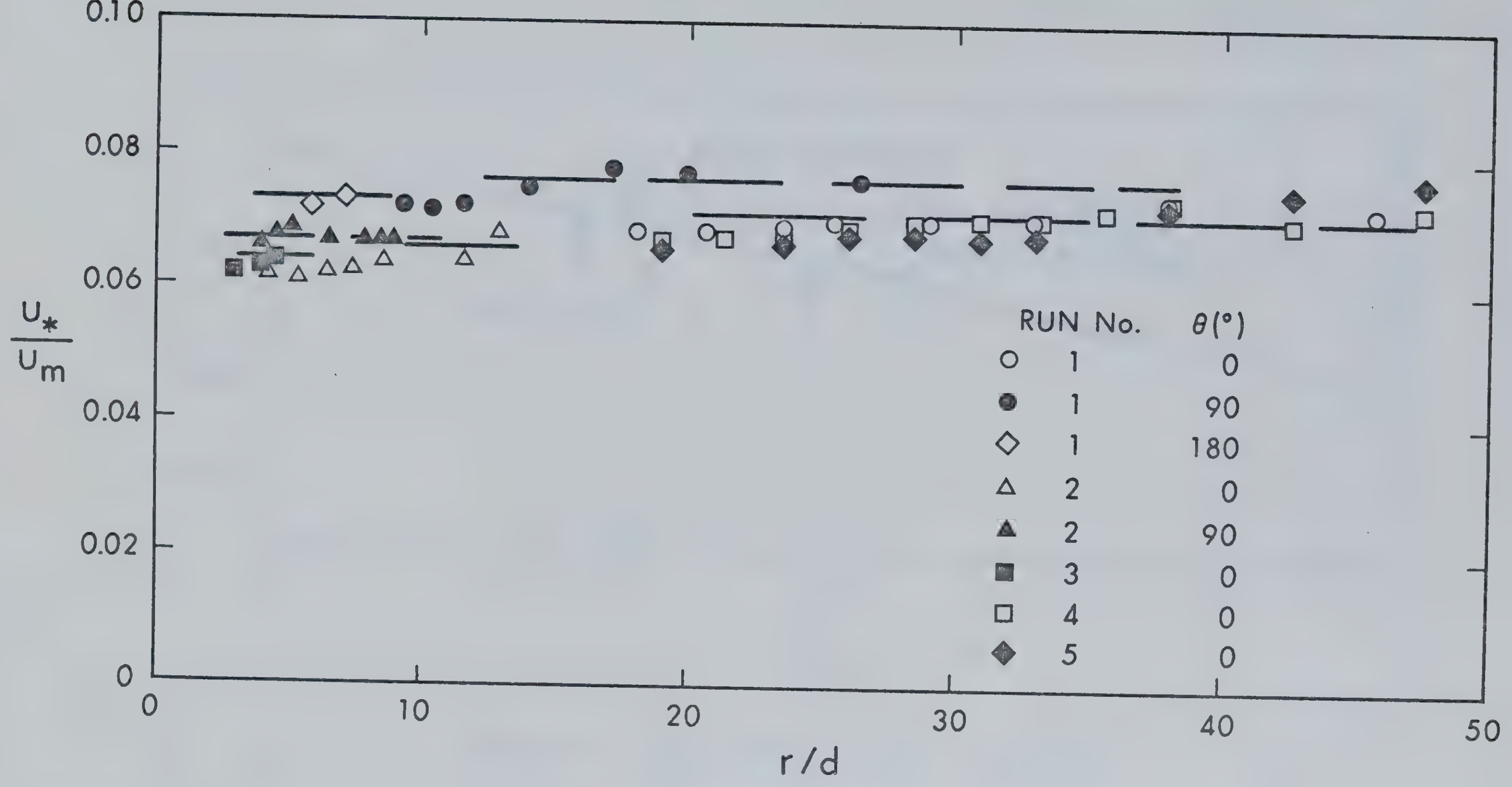

FIGURE 7.19 CONSTANCY OF u_*/u_m

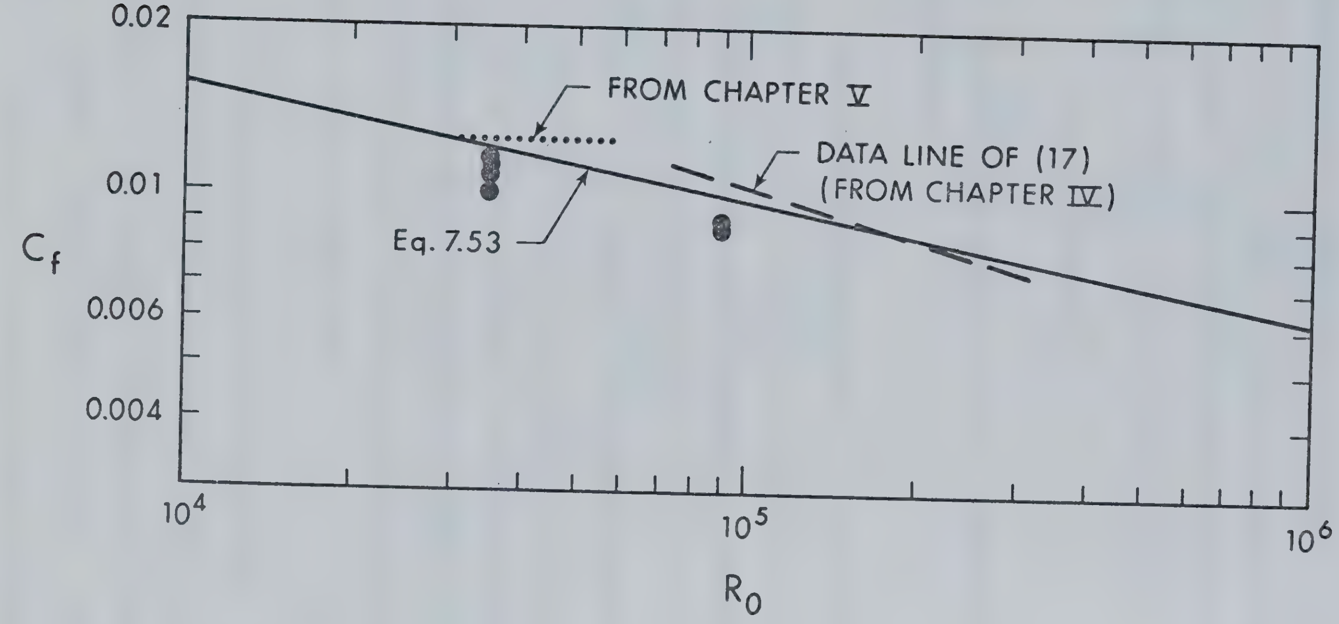

FIGURE 7.20 SKIN FRICTION FACTOR - WALL JET

cal equation for C_f arrived at in Chapter IV. It appears that the exponent -0.3 of R_o gives a variation somewhat steeper than the general trend of the data. Hence, the following relation is proposed, using an exponent of -1/5 as in the case of plane jets, i.e.:

$$C_f = 0.0980\, R_o^{-\frac{1}{5}} \tag{7.53}$$

Figure 7.20 shows that Equation 7.53 is a reasonable average of the available results.

Regarding the length scale δ_2, it was shown earlier that it grows linearly with r, at a rate that should be a universal constant, apart from some Reynolds number dependence. Yakovlevskii and Krasheninikov (27) reported experimental data for $\phi = 45°$, $60°$ and $90°$, $H/d = 3.5$ and 10 and $\theta = 0°$ and $90°$, at a value of Reynolds number, $R_o = 69{,}000$. The length scale δ_2 was found to grow linearly with r at a slope of 0.075, which is close to 0.0792 and 0.0765 that were established in Chapters IV and V respectively. The present results for the case $\phi = 20°$ are shown in Figure 7.21, and they are described adequately by a straight line of slope 0.0755.

It remains to evaluate the velocity scale u_m. Consider first the exponent a in Equation 7.50. Strictly speaking, this is always less than -1 as Equation 7.51 indicates. Using $C_2 \simeq 0.075$ and $F_1 \simeq 0.7$, the term $C_f/4F_1C_2$ becomes $C_f/0.21$. This will be less than, say 0.06, so long as C_f is less than 0.0126, a condition that will be satisfied so long as $R_o \gtrsim 20{,}000$. In this range, it could therefore be assumed that $a \simeq -1$, i.e., $u_m \propto \frac{1}{r}$. The velocity scale, u_m, is

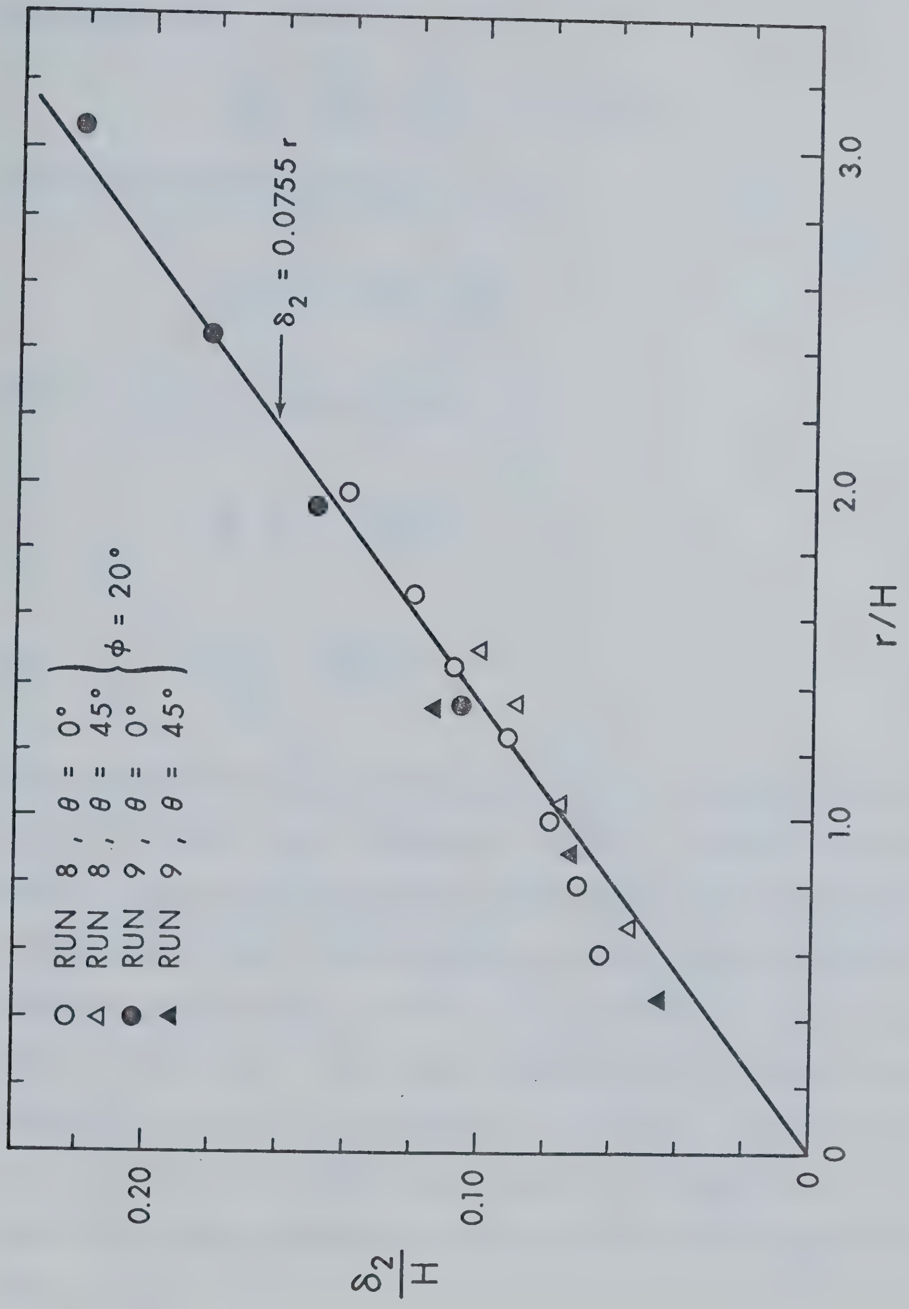

FIGURE 7.21 LENGTH SCALE IN WALL JET

also given by:

$$u_m = f(\rho, \rho U_o{}^2 d^2, H, \phi, r, \theta)$$

which by dimensional analysis becomes:

$$\frac{u_m}{U_o} \frac{H}{d} = \overline{f}(\phi, \theta, \frac{r}{H}) \tag{7.54}$$

Since $u_m \propto \frac{1}{r}$, it follows that:

$$\frac{u_m}{U_o} \frac{H}{d} = \frac{h(\phi, \theta)}{r/H}$$

or

$$\frac{u_m}{U_o} = \frac{h(\phi, \theta)}{r/d} \tag{7.55}$$

which implies that u_m is independent of H. Furthermore, if U_o/u_m is plotted against r/d for fixed ϕ and θ , straight lines should result. This is shown in Figures 7.22 (a) and (b) where the data define straight lines after a certain distance from the stagnation point. Note also that data with same ϕ and θ but different values of H/d, fall along the same line. The virtual origin seems to be located at the stagnation point, with the exception of the case $\phi = 20°$, $\theta = 45°$. The slopes of these straight lines equal the reciprocal of h. The data of (27) were re-analyzed in the same manner and it was again found that $u_m \propto \frac{1}{r}$.

Experimental values of $h(\phi, \theta)$ are tabulated on the following page, together with values of r_o/H, r_o being the value of r where

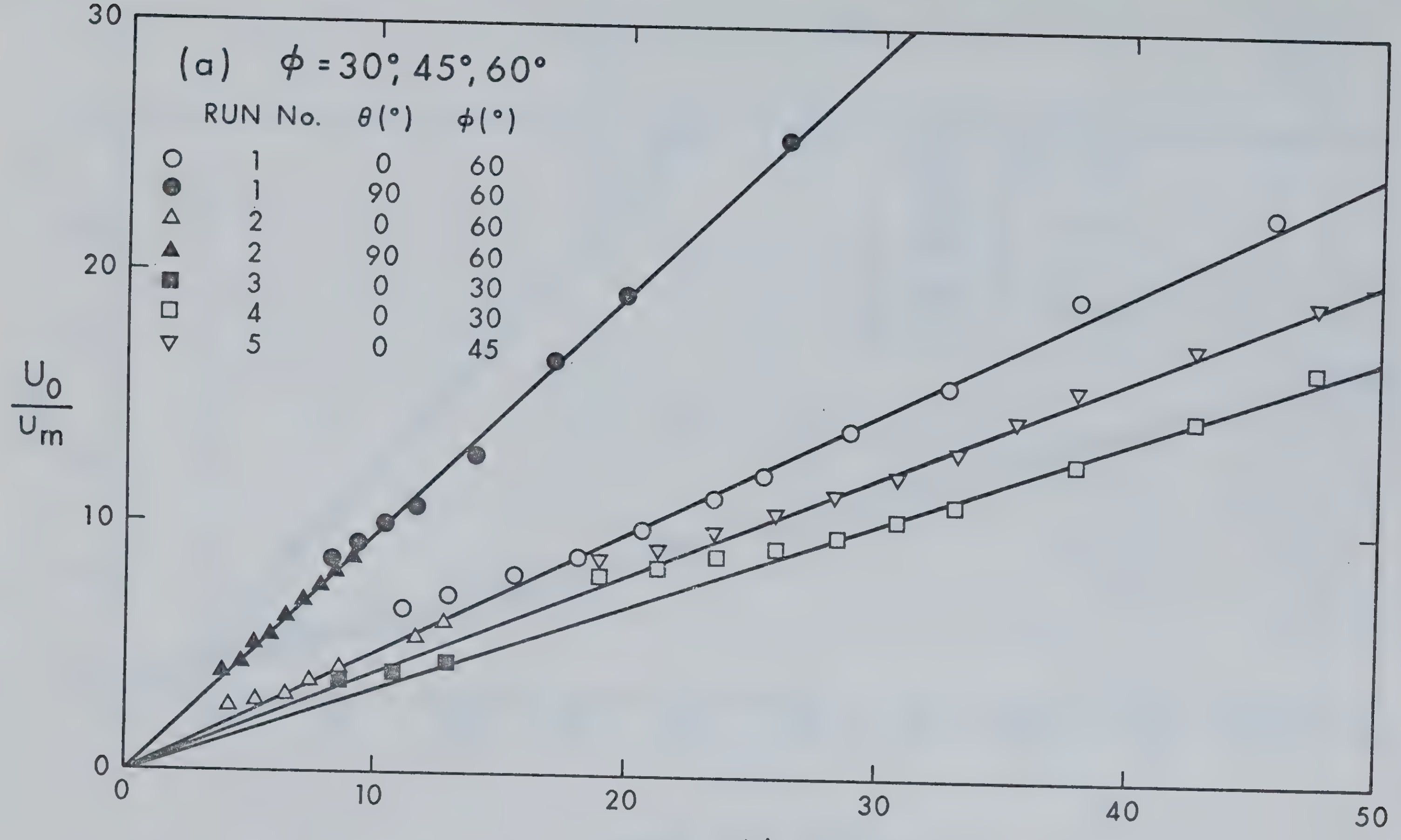

FIGURE 7.22 VELOCITY SCALE IN WALL JET

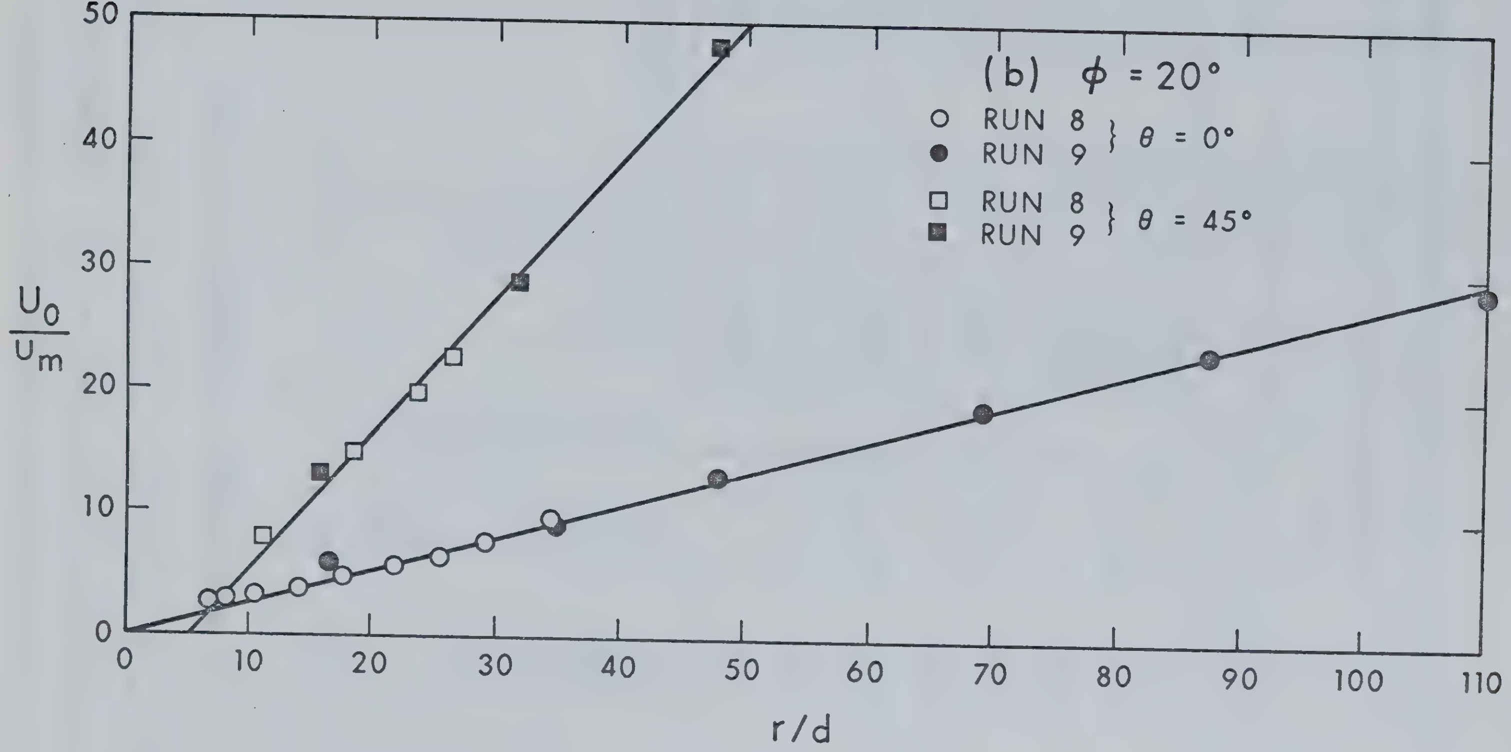

FIGURE 7.22 CONTINUED

u_m begins to obey Equation 7.55, and it can be thought of as the beginning of the wall jet region (see also Chapter IV).

Source	H/d	R_o	ϕ(°)	θ(°)	$h(\phi, \theta)$	r_o/H
Run 1	39.25	34,700	60	0	2.05	.447
Run 1	39.25	34,700	60	90	1.04	-
Run 1	39.25	34,700	60	180	.695	-
Run 2	15.5	89,600	60	0	2.05	.420
Run 2	15.5	89,600	60	90	1.04	-
Run 3	20.0	89,600	30	0	2.94	.625
Run 3	20.0	89,600	30	90	.45	-
Run 4	46.5	34,700	30	0	2.94	.590
Run 5	47.0	34,700	45	0	2.48	.533
Run 5	47.0	34,700	45	180	0.40	-
Run 8	17.5	100,000	20	0	3.72	.800
Run 8	17.5	100,000	20	45	0.90	.800
Run 9	35.8	34,700	20	0	3.72	.84
Run 9	35.8	34,700	20	45	0.90	.56
Yakovlevskii & Krasheninnikov (27)	3.5	69,200	90	any	1.19	.34
	10	"	90	any	1.54	.36
	3.5	"	60	0	2.03	-
	3.5	"	60	180	.495	-
	10	"	60	0	2.01	.43
	10	"	60	180	.704	.31
	3.5	"	45	0	2.25	-
	3.5	"	45	45	1.41	-
	3.5	"	45	90	.69	-
	3.5	"	45	135	.40	-
	3.5	"	45	180	.35	-
	10	"	30	0	2.77	.53
	10	"	30	180	.20	-

TABLE 7.5 EXPERIMENTAL VALUES OF $h(\phi, \theta)$

This table shows that h depends only upon ϕ and θ according to theory. The quantity r_o/H can also be shown to depend only upon ϕ and θ. This appears to be the trend, however, the data on r_o are

not as consistent. It remains now to evaluate the function $h(\phi, \theta)$. Consider first the particular cases $\theta = 0°$ and $\theta = 180°$. These cases are of particular interest because they represent maximum and minimum values of h for a given ϕ. Let:

$$\begin{aligned} h_1 &\equiv h(\phi, 0°) \\ h_2 &\equiv h(\phi, 180°) \end{aligned} \qquad (7.56)$$

A relation between h_1 and h_2 can be obtained from momentum considerations, as follows. Consider an elementary control volume determined by two planes intersecting at the centerline of the jet and whose traces on the wall form a small angle $\Delta\theta$ about the x-axis, as shown in Figure 7.23.

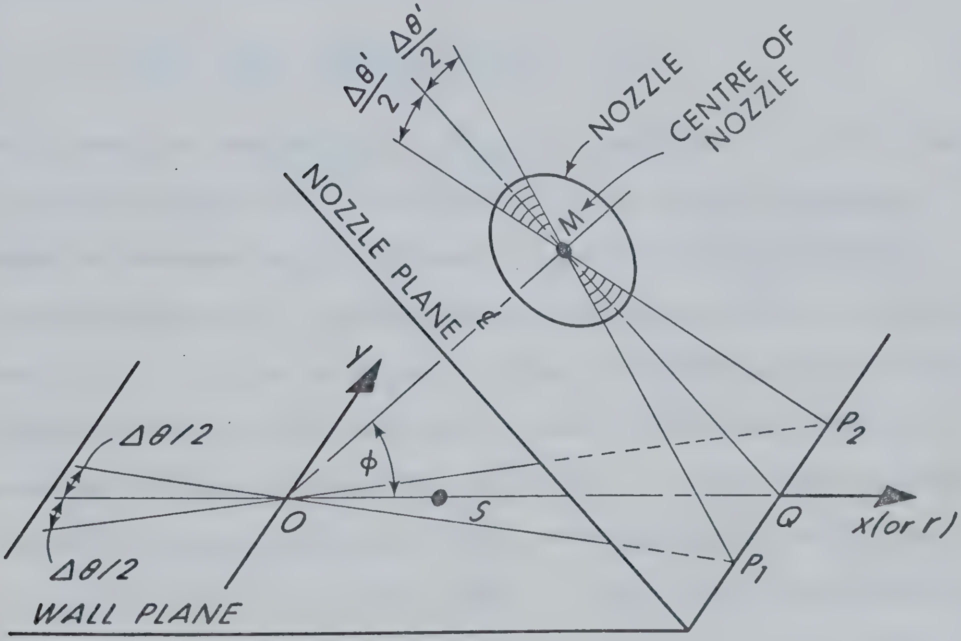
Δθ'/2
Δθ'/2
NOZZLE
CENTRE OF NOZZLE
M
NOZZLE PLANE
℄
Y
Δθ/2
Δθ/2
φ
O
S
P2
Q
P1
x(or r)
WALL PLANE

FIGURE 7.23 CONTROL VOLUME

The planes are OP_1M and OP_2M whereas the plane MP_1P_2 is the plane defined by the outlet section of the nozzle. The angles OMQ, OQP_1 and OQP_2 are all right angles. If the angle ϕ is not very small, then the elementary momentum in either direction of the x-axis will be:

$$dM = \int_o^\infty \rho u^2 r \Delta\theta dz = \rho\Delta\theta u_m{}^2 \delta_2 r F_1$$

or, using Equations 7.49 and 7.55:

$$dM_{1,2} = \rho F_1 C_2 \Delta\theta h_{1,2}^2 U_o{}^2 d^2 \tag{7.57}$$

which shows that dM is preserved. Regarding the term $h_{1,2}$ this should be understood to be h_1 when $x > 0$ and h_2 when $x < 0$. The same applies to $dM_{1,2}$. The difference:

$$dM_1 - dM_2 = \rho F_1 C_2 U_o{}^2 d^2 \Delta\theta (h_1{}^2 - h_2{}^2) \tag{7.58}$$

will equal the x-projection of dM_o, the momentum at the nozzle contained within the angle $\Delta\theta^1$ (see Figure 7.23). Strictly speaking, in order to evaluate $dM_{1,2}$, distance r should be measured from the stagnation point S. However, when ϕ is not very small, $s/H \lesssim 0.1$, and if r/H is taken sufficiently large, no significant error will be introduced. Another objection may be raised because some momenta may be entering the control volume near the point O, owing to the bending of streamlines there. These are assumed to be negligible, which is not unreasonable if ϕ is not very small. Finally, frictional forces are neglected, and this is reasonable for $R_o \gtrsim 20{,}000$ (see also Chapter IV).

The elementary momentum, dM_o is:

$$dM_o = 2 \frac{\Delta\theta^1}{2\pi} \rho U_o^2 \frac{\pi d^2}{4}$$

hence:

$$\rho F_1 C_2 U_o^2 d^2 \Delta\theta (h_1^2 - h_2^2) = \frac{1}{4} \rho \pi d^2 U_o^2 \Delta\theta^1 \cos\phi$$

which reduces to:

$$h_1^2 - h_2^2 = K_1 \left(\frac{\Delta\theta^1}{\Delta\theta}\right) \cos\phi \qquad (7.59)$$

where $K_1 = \frac{1}{4F_1 C_2}$. If $\Delta\theta$, $\Delta\theta^1$ are very small, $\Delta\theta \approx \tan\Delta\theta$, hence, (from Figure 7.23):

$$\frac{\Delta\theta}{\Delta\theta^1} = \frac{\Delta\theta\ /2}{\Delta\theta^1/2} = \frac{\frac{QP_1}{OQ}}{\frac{QP}{MQ}} = \frac{MQ}{OQ} = \sin\phi \qquad (7.60)$$

Thus, Equation 7.59 becomes:

$$h_1^2 - h_2^2 = K_1 \frac{\cos\phi}{\sin\phi} \qquad (7.61)$$

One more relation between h_1 and h_2 is obtained by considering the elementary flow rate, dQ between two planes normal to the wall, located

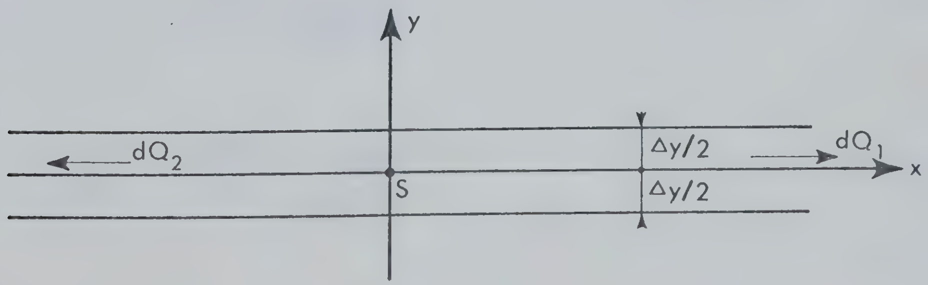

at a small distance $\Delta y/2$ on either side of the x-axis (see sketch on previous page).

$$dQ = \int_0^\infty u\Delta y dz = \Delta y \int_0^\infty u dz = \Delta y u_m \delta_2 \underbrace{\int_0^\infty (\frac{u}{u_m}) d(\frac{y}{\delta_2})}_{F_2}$$

i.e., $$dQ_{1,2} = \Delta y F_2 C_2 (U_o d) h_{1,2}$$

and $$\frac{dQ_2}{dQ_1} = \frac{h_2}{h_1} \qquad (7.62)$$

Note that dQ on the strip Δy is preserved, i.e., it is independent of r. Furthermore, the flow in this strip has the properties of the symmetry plane and approximates a two-dimensional condition. Hence, it is assumed that dQ_2/dQ_1 is equal to the ratio of flow rates from a corresponding plane jet of ideal fluid, i.e., (44):

$$\frac{dQ_2}{dQ_1} = \frac{h_2}{h_1} = \frac{1 - \cos\phi}{1 + \cos\phi} \qquad (7.63)$$

The experimental results, taken from Table 7.5 confirm Equation 7.63, as shown in Figure 7.24. Solving Equations 7.61 and 7.63, h_1 and h_2 are given by:

$$h_1 = \frac{\sqrt{K_1}}{2} \frac{1 + \cos\phi}{\sqrt{\sin\phi}} \qquad (7.64)$$

$$h_2 = \frac{\sqrt{K_1}}{2} \frac{1 - \cos\phi}{\sqrt{\sin\phi}} \qquad (7.65)$$

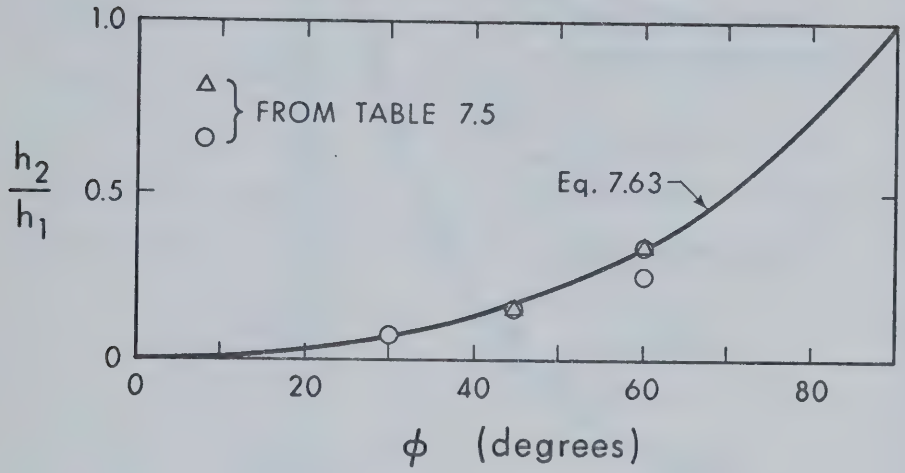

FIGURE 7.24 VERIFICATION OF EQUATION 7.63

Data on h_1 and h_2 are plotted in Figure 7.25. When $\phi = 90°$, $h_1 = h_2 = h_{90}$. The average value of h_{90} in Chapter IV was found to be 1.0. The data of (27) indicate $h_{90} = 1.19$. Furthermore, it appears that the experimental data of Figure 7.25 will be best described if h_{90} is taken as 1.10 which is also an average between 1.0 and 1.19. Moreover, the definition of $K_1 \equiv \frac{1}{4F_1C_2}$ will give $h_{90} = \frac{1}{2\sqrt{4F_1C_2}} \cong 1.08$, if F_1 is taken as 0.7 and C_2 as 0.077 which is an average between the value 0.079 found in Chapter IV and 0.075 found in this Chapter. Thus, Equations 7.64 and 7.65 become:

$$h_1 = 1.10 \frac{1 + \cos\phi}{\sqrt{\sin\phi}} \tag{7.66}$$

$$h_2 = 1.10 \frac{1 - \cos\phi}{\sqrt{\sin\phi}} \tag{7.67}$$

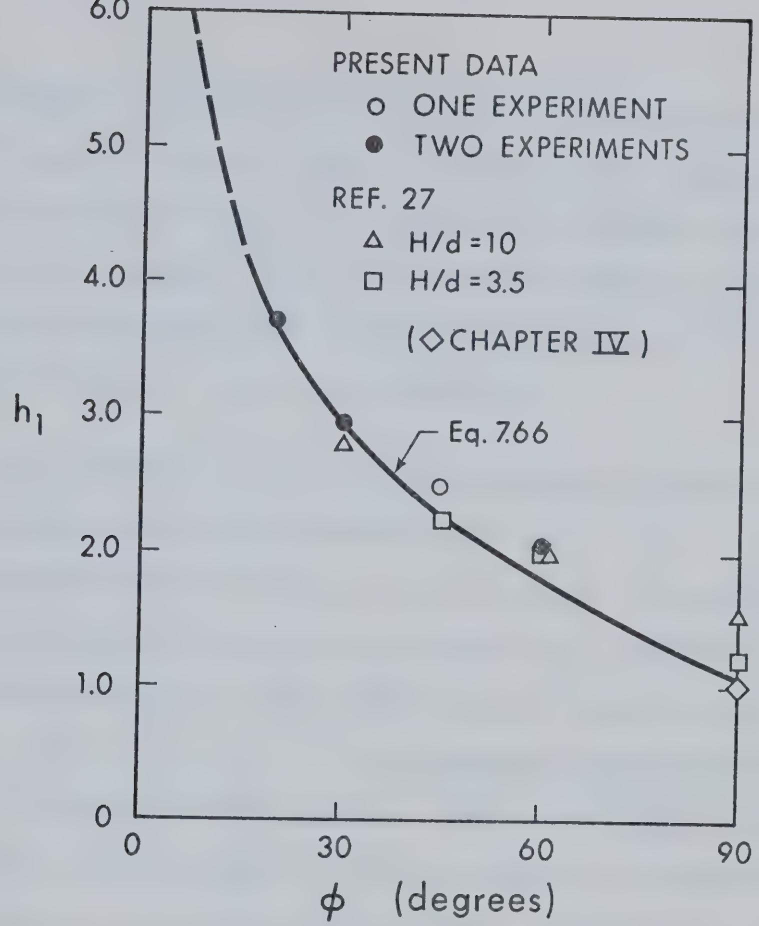

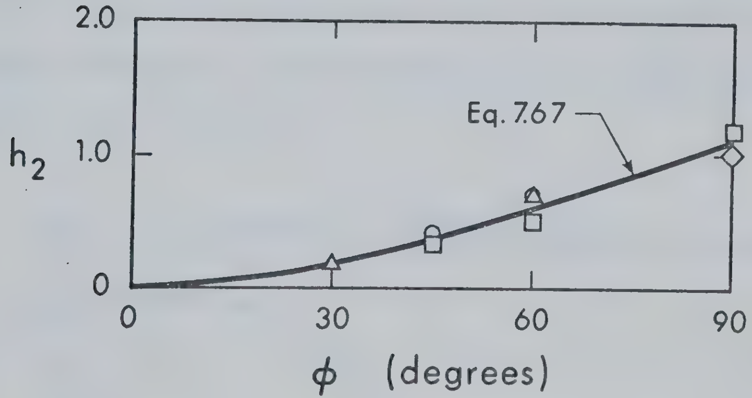

FIGURE 7.25 THE FUNCTIONS h_1 AND h_2

These are plotted in Figure 7.25 and are seen to describe the data adequately at least for $20° \leq \phi \leq 90°$. Considering the limiting case $\phi = 0°$, it is seen that $\lim\limits_{\phi \to 0} h_2 = 0$, which is in agreement with physical considerations. However, $\lim\limits_{\phi \to 0} h_1 = \infty$, which is physically unacceptable. This is attributed to the fact that for very small ϕ, the formulation of Equation 7.59 is no longer valid.

The function $h(\phi, \theta)$ can now be predicted in general, as follows. Consider the locus of points on the plane $z = 0$, for which the maximum velocity in the vertical, u_m, is constant. These loci will be called "isotachs" as they are lines of equal u_m, even though they are not, strictly speaking, such. Some contours of equal u_m are presented in (27), for $\phi = 45°$, and they appear to be almost elliptical in shape. It will be assumed, therefore, that for any angle the isotachs are elliptical. For the case $\phi = 90°$, the isotachs are circles which indicates that if a, b are the long and short semi-axes of the ellipse, then the ratio b/a must be unity when $\phi = 90°$ and it should decrease for decreasing values of ϕ. Consider then one such ellipse as shown in Figure 7.26.

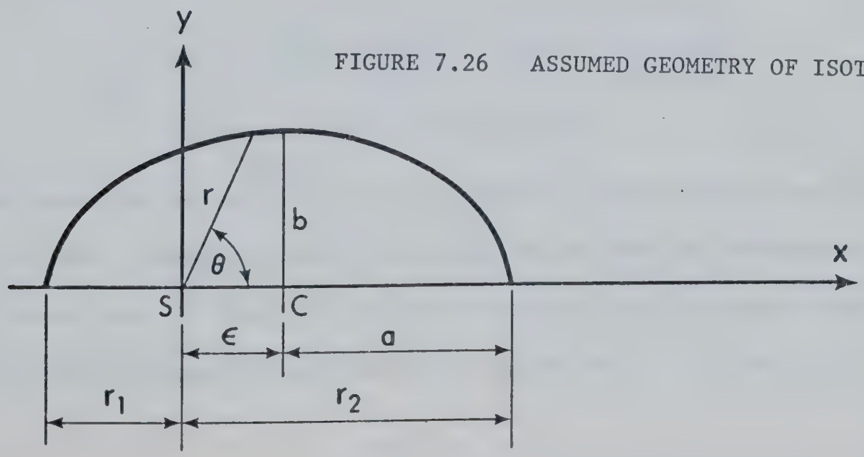

FIGURE 7.26 ASSUMED GEOMETRY OF ISOTACHS

This ellipse will be completely defined if the semi-axes a, b and the eccentricity ε from the stagnation point are specified. Obviously, at $\phi = 90°$, $a = b$ and $\varepsilon = 0$. For the following analysis it is only necessary to assume that at least one isotach is an ellipse. For any point (r, θ) on the periphery of the ellipse, u_m/U_o is constant, i.e.:

$$\frac{h}{r} = \text{const} = \frac{h_1}{r_1} = \frac{h_2}{r_2} \tag{7.68}$$

The equation of the ellipse is:

$$\left(\frac{x - \varepsilon}{a}\right)^2 + \left(\frac{y}{b}\right)^2 = 1 \tag{7.69}$$

Furthermore, $r_1 = a + \varepsilon$, $r_2 = a - \varepsilon$ and $\dfrac{r_2}{r_1} = \dfrac{1 - (\varepsilon/a)}{1 + (\varepsilon/a)} = \dfrac{h_2}{h_1}$.

Recalling Equation 7.63, it follows that:

$$\frac{\varepsilon}{a} = \cos\phi$$

Since (Equation 7.68) $\dfrac{h}{h_1} = \dfrac{r}{r_1}$, Equation 7.69 can be solved to yield (see Appendix D, Section D.7):

$$\frac{h}{h_1} = \frac{\cos\phi\cos\theta + \sqrt{\cos^2\theta + \left(\frac{a}{b}\right)^2 \sin^2\phi \sin^2\theta}}{(1 + \cos\phi)\left[\cos^2\theta + \left(\frac{a}{b}\right)^2 \sin^2\theta\right]} \tag{7.70}$$

This equation was derived on the assumption that at least one isotach is elliptical. However, using this relation and working backwards it can be shown that all isotachs will be elliptical with the same value of b/a. It is now necessary to establish the variation of b/a with ϕ.

Consider the case $\phi = 90°$. Then:

$$\frac{u_m}{U_o} = \frac{h_{90}}{r/d} = \frac{2h_{90}}{\sqrt{A/A_o}} \qquad (7.71)$$

where A is the area of the isotach $\frac{u_m}{U_o} = \text{const}$ (πr^2) and A_o is the area of the nozzle $(\pi d^2/4)$. It is reasonable to expect that this law, expressed in terms of isotach areas will be generally valid, i.e., for $\phi \neq 90°$. (A similar property was discovered earlier with respect to wall pressures in the impingement region.)

For elliptical isotachs:

$$A = \pi ab = \pi(\frac{b}{a}) (\frac{a}{r_1})^2 r_1^2$$

Using some obvious geometrical relations and Equation 7.68, it is possible to show that:

$$\frac{A}{A_o} = \frac{b}{a} (1 + \frac{h_2}{h_1})^2 (\frac{r_1}{d})^2 \qquad (7.72)$$

On this isotach: $\frac{u_m}{U_o} = \frac{h}{r/d} = \frac{h_1}{r_1/d}$; using Equation 7.72 it follows that:

$$\frac{u_m}{U_o} = \frac{h_1 \sqrt{\frac{b}{a}} [1 + \frac{h_2}{h_1}]}{\sqrt{A/A_o}} \qquad (7.73)$$

Comparing with Equation 7.71:

$$(h_1 + h_2) \sqrt{\frac{b}{a}} = 2h_{90}$$

or, by Equations 7.66 and 7.67:

$$\frac{b}{a} = \sin\phi \tag{7.74}$$

Substituting Equations 7.74 and 7.66 into Equation 7.70, h is given finally as:

$$h(\phi, \theta) = \frac{1.10}{\sqrt{\sin\phi}} \cdot \frac{1 + \cos\phi\cos\theta}{\cos^2\theta + \frac{\sin^2\theta}{\sin^2\phi}} \tag{7.75}$$

Experimental results are available for $\theta = 45°$, $90°$ and $135°$. Consider first $\theta = 90°$. Then:

$$h(\phi, 90°) = 1.10\ (\sin\phi)^{3/2} \tag{7.76}$$

When $\theta = 45°$ or $135°$, Equation 7.75 becomes:

$$h(\phi, \substack{45° \\ 135°}) = \frac{2.20}{\sqrt{\sin\phi}} \quad \frac{1 \pm .707\cos\phi}{1 + (\sin\phi)^{-2}} \tag{7.77}$$

These are shown plotted together with available experimental data in Figure 7.27. It is seen that agreement is reasonably good with the exception of the smaller values of ϕ. The variation of the function $h(\phi, \theta)$ is illustrated more clearly in Figure 7.28 where h is plotted against θ for fixed values of ϕ.

Finally, consider the beginning of the wall jet region, r_o. It is easy to show that r_o/H is a function of ϕ and θ only. Adequate data to define this function exist only for $\theta = 0°$. If r_i denotes the end of the impingement region, this quantity can be found

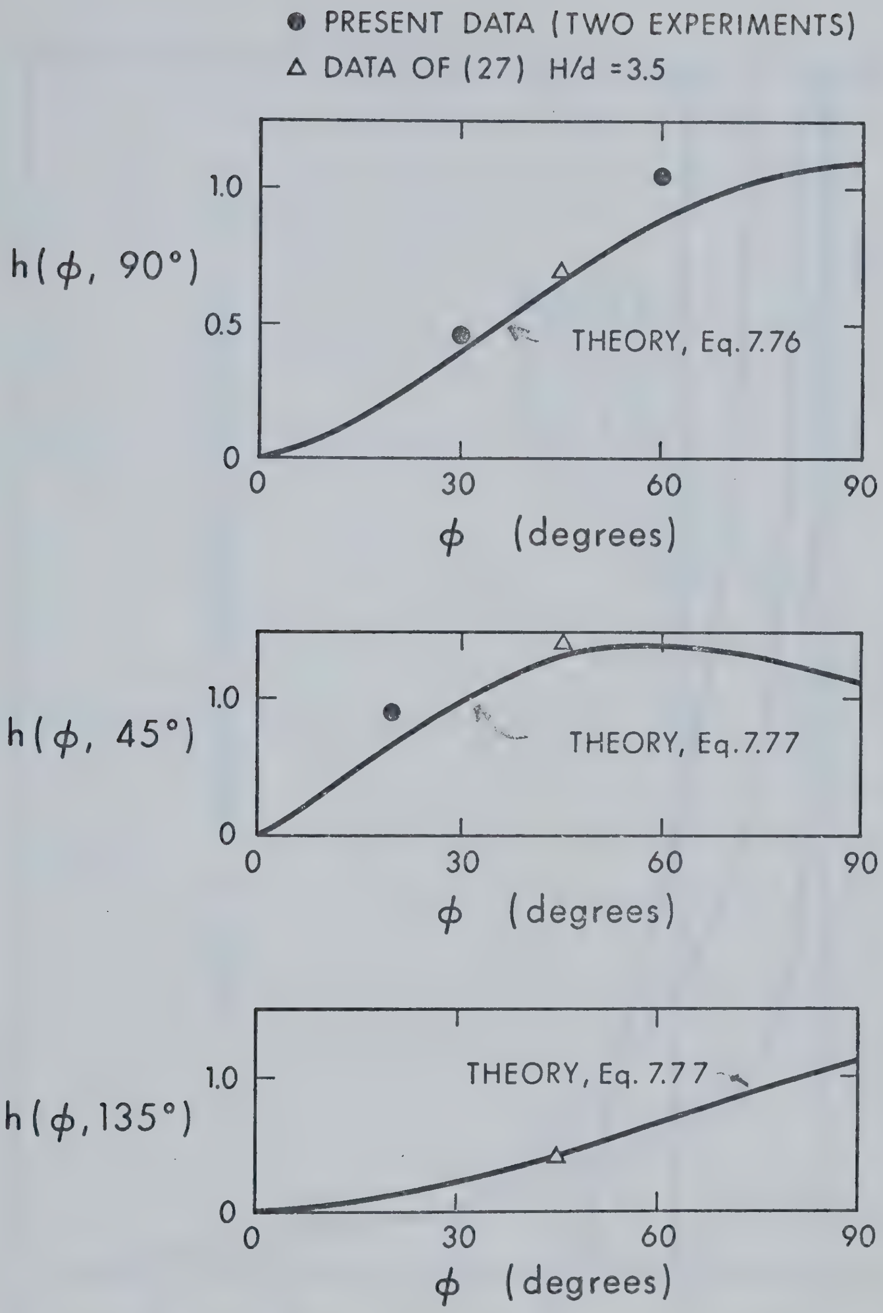

FIGURE 7.27 COMPARISON OF THEORY WITH EXPERIMENT

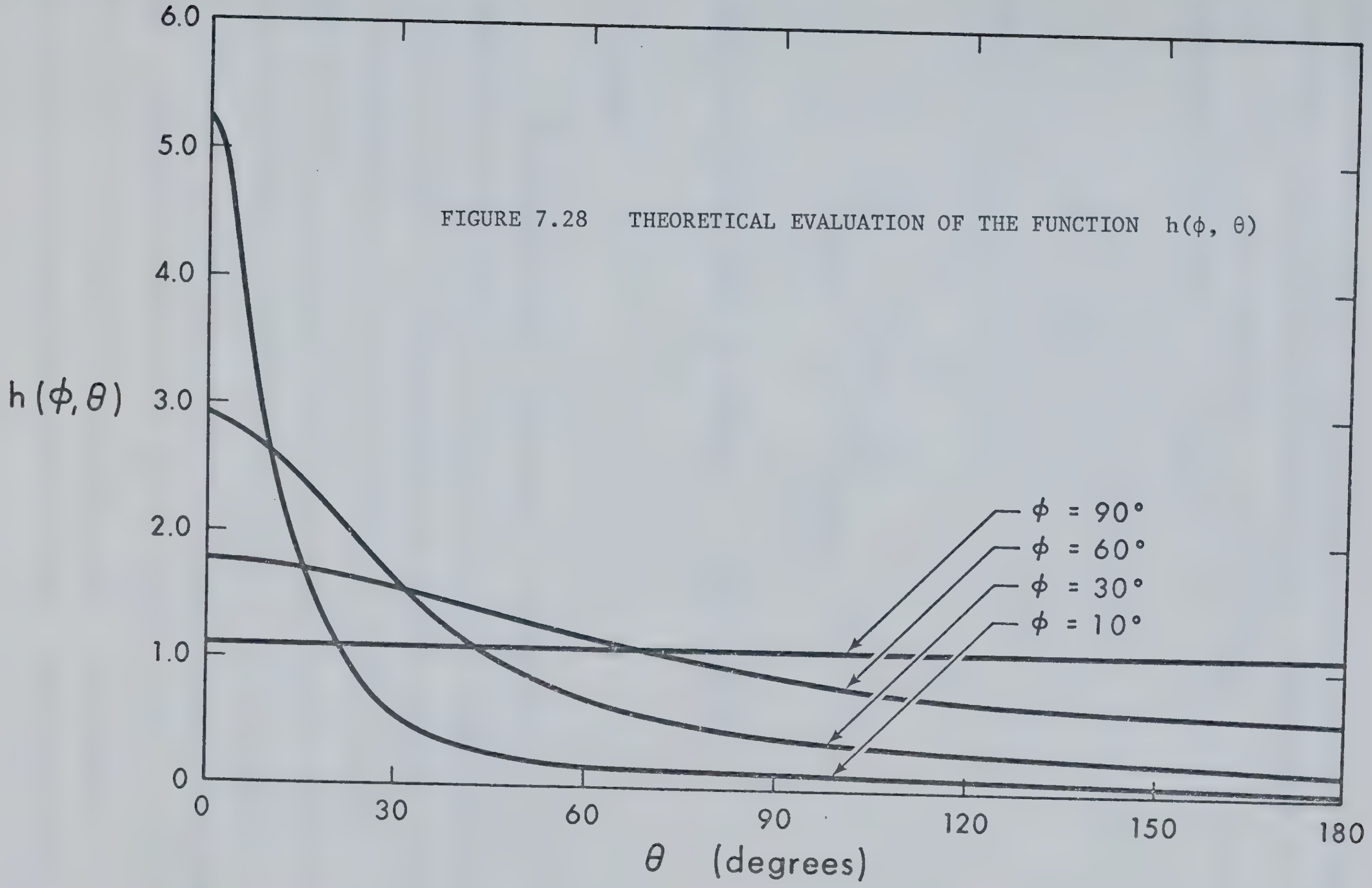

FIGURE 7.28 THEORETICAL EVALUATION OF THE FUNCTION h(ϕ, θ)

from the pressure similarity curve and the values of b/H (Figures 7.5 and 7.8). It was found that the ratio r_o/r_i is independent of ϕ when $\theta = 0°$ and is equal to 1.9. If it is assumed that this property holds for other values of θ, then:

$$\frac{r_o}{r_i} = f(\theta)$$

Applying this relation at $\phi = 90°$:

$$\left(\frac{r_o}{r_i}\right)_{\phi=90°} = f(\theta) = \left(\frac{r_o}{r_i}\right)_{\substack{\phi=90° \\ \theta=0°}} = f(0) = 1.9$$

which implies that $f(\theta)$ is actually a constant, equal to 1.9.

7.4 Summary

An advanced case of impingement on smooth walls has been considered in this chapter. This is the oblique impingement of circular turbulent jets. In the impingement and wall-jet regions, the flow is three-dimensional, i.e., it is necessary to use three space coordinates for its description. The wall pressure has been predicted by means of an inductive, semi-empirical approach. Wall shear stress in the impingement region is generally very difficult to measure and predict owing to uncertainty regarding its line of action. However, the direction of wall shear is known in a particular case, i.e., along the intersection of the symmetry plane with the wall. Measurements showed

general agreement with theoretical considerations based on the same approach as that used in previous chapters.

For prediction of flow properties in the wall jet region, a theory has been developed, which is based on boundary-layer simplifications of the Reynolds equations of motion. It was shown that the flow in the wall jet can be considered to be quasi-axisymmetric. This means that flow takes place practically along radial lines, with shearing stresses between radial planes being negligible. The length scale grows linearly on each radial, at a universal slope. The local skin friction factor C_f remains constant along each radial. Moreover, it does not depend on any other parameter of the problem $(H/d, \phi, \theta)$ but upon the nozzle Reynolds number, R_o. Using all available data, it has been possible to derive an average empirical expression for C_f which indicates that $C_f \propto R_o^{-1/5}$, much like in the corresponding case of plane jets (Chapter VI). Thus, the wall shear stress can be calculated if the velocity scale, u_m, is known. It was shown that $u_m \propto 1/r$. However, there exist significant variations of u_m in the angular direction. These were predicted by assuming the contours of equal u_m to be elliptical in shape, based on data presented in (27) and on available knowledge regarding normal impingement (Chapters IV and V). It was again verified that considerations of whether the height of impingement is "large" or "small" do not influence the wall jet region.

CHAPTER VIII - CIRCULAR TURBULENT JET IN AN OPPOSING, INFINITE STREAM

8.1 Introduction

The impingement of turbulent jets upon solid boundaries has been studied in the preceding chapters. However, impingement is not necessarily associated with solid boundaries. For example, one could conceive of two streams impinging against each other at an infinite variety of geometrical configurations. In this chapter, the impingement of a circular turbulent jet against an infinite uniform stream will be considered. This constitutes a simple geometrical configuration, however, there is relatively little information in literature with respect to this problem.

Jets in counterflow are used as aerodynamic stabilizers in afterburners or turbojet engines. For the hydraulic engineer, this problem is of interest with respect to efficient dilution of effluent discharges. Furthermore, this problem represents a limiting case of the more general problem of jets issuing in streams. Depending upon the angle between the original directions of the jet and the stream, many different configurations are obtained. For example, jets in co-flow and jets in cross-flow are the configurations associated with the angles 0° and 90° respectively. Jets in counterflow occur when this angle is 180°.

Basic mean flow characteristics are shown in the definition sketch, Figure 8.1. The jet issues from a nozzle of diameter d with

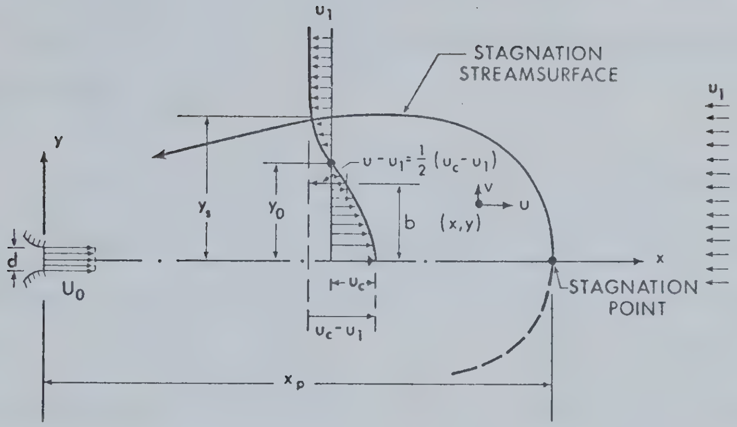

FIGURE 8.1 DEFINITION SKETCH

initial velocity U_o, against an infinite, uniform, stream of velocity u_1 ($u_1 < 0$). A stagnation point forms on the centerline at a distance x_p from the nozzle. This distance is called the "penetration length" and could be considered to be a quantity analogous to the height, H, associated with impingement on solid boundaries. It was shown in the previous chapters that H was a "key" prarmeter for the quantitative treatment of the problem. Thus, it is not unreasonable to speculate that in the present problem, x_p will also be an important parameter. There is a physical difference, however. Whereas for impingement on solid boundaries, H is an imposed (or, independent) parameter, here the penetration length is a dependent quantity. Treatment of problems in terms of dependent quantities is somewhat unorthodox, however, it can be perfectly logical under certain circumstances. Other things being

constant, x_p will be a single-valued function of the stream velocity u_1. This implies that, mathematically, one could treat either parameter as independent.

Returning to Figure 8.1, if u, v are the time-average components of velocity in the longitudinal (x) and radial (y) directions respectively, knowledge of the flow field amounts to knowing the function $u = u(x, y)$, since $v = v(x, y)$ can be obtained by integrating the equation of continuity. As it is common in jet flows, longitudinal velocity profiles at different distances from the outlet can be reduced to a single similarity curve if proper choice of velocity and length scales is made (28). The problem then reduces to predicting the similarity functions and the variations of the scales.

The first contribution to this problem appears to be a brief paper by Arendt et al, Rouse (48) in 1956. Experimental results were presented in a dimensionless form suggested by dimensional analysis. These results were rather approximate because only the magnitude of velocity was measured, its direction being estimated by a trial-and-error procedure. The correct choice of determining parameters of the problem was pointed out, and it allowed derivation of a very simple expression for the penetration length. Sui and Ivanov in 1959 (49) and Sui in 1961 (50) proposed, after extensive experimentation, empirical formulae and nomograms for predicting the velocity and length scales and the similarity function. Timma (51) dealt mainly with similarity of velocity profiles and the dependence of the penetration length upon initial conditions. Ilizarova and Ginevskii (52) reported

some experimental results and Ginevskii (53) gave a complex theoretical treatment, which however, is mostly of qualitative value. Sekundov (54) presented an integral analysis for predicting the penetration length and the velocity scale. The resulting expressions are rather complex and confirmation was only partial, since comparison with experiment was made only with respect to the penetration length. Measurements of the mean flow and turbulent correlations were reported by Rao (55). The experimental data with respect to turbulent correlations are, however, rather crude, as is pointed out by the author. For example, the turbulent shear stress was found to have a large negative value on the centerline, which is impossible as it must vanish at this location because of symmetry. In the following sections it will be shown that the time-average velocity field can be predicted by means of simple equations based on theoretical arguments combined with empirically established assumptions.

8.2 Experiments

Careful search of the Russian literature (Refs. 49 to 54) disclosed that a wealth of experimental data with respect to the mean flow was already available. Therefore, only one experiment was conducted to serve as an additional, independent check on the available results. Details of the experimental set-up and techniques have been described in Chapter III. The values of U_o and u_1 for this experiment were 248 and -23 fps respectively.

8.3 Analysis and Results

In what follows, it will be assumed that this problem is analogous to impingement at large heights. By this is meant that the penetration length should be sufficiently large so that the main portion of the flow in the jet can be assumed to originate from a point source of momentum. Arendt et al, Rouse (48) have shown that this assumption leads to the result $x_p/d \propto \lambda$, if λ is defined to be the speed ratio, $U_o/|u_1|$. The constant of proportionality was reported [(48),(55)] to be about 2.4, which means that if x_p/d is required to be, say, larger than 10, λ will have to be larger than about 4. A more precise determination of this limit will be considered later, but these values give an idea of the range in which the present study will be valid. Assuming then a "large" penetration length, it is possible to distinguish again three flow regions (Figure 8.1). Firstly, in a region beginning at the nozzle and extending up to some distance before the stagnation point, one could expect the flow to have considerable similarities with the free jet. The region close to and upstream of the stagnation point is an impingement region where the v-component of velocity takes on large values while the static pressure rises above the ambient. Finally, the region downstream of the stagnation point can be assumed to be occupied by approximately potential flow. This is clearly demonstrated in the experiments of Rao (55) where it is shown that the turbulent correlations become very small as the stagnation point is approached. Transitions between these regions cannot be precluded.

8.3.1 Velocity Similarity Function

A typical variation of u in the radial direction is shown schematically in Figure 8.1. From a maximum value of u_c on the centerline, u decreases continuously, approaching the free-stream velocity u_1 as y increases. If u_m is the centerline value of $u - u_1$ $(u_m \equiv u_c - u_1)$ then, similarity can be expected to be in the form $(u - u_1)/u_m = f(\eta)$, where $\eta \equiv y/b$ and b is that value of y where $u - u_1 = \frac{1}{2} u_m$. This is shown in Figure 8.2 where the present data and those of Sui and Ivanov (49) define a single curve. In this figure the quantity D/d which appears in the legend denotes the relative dimension of the opposing stream with respect to the nozzle diameter, d. The conventional free-jet similarity function $(f = e^{-0.693\eta^2})$ is also plotted in Figure 8.2 and is seen to be adequate only in the range $0 \leq \eta \lesssim 1.2$. For $\eta \gtrsim 1.2$, the data give considerably higher values of f, which in turn shows that in this case the jet expands faster than a free jet. Inspection of the legend indicates that these profiles are in the range $x/x_p \lesssim 0.73$. No data are available near or beyond the stagnation point, as measurements with conventional equipment are practically impossible close to the stagnation point. In order to obtain an understanding of the flow field beyond the stagnation point, it is reasonable to assume that it can be approximated by the potential flow solution for a three-dimensional point source of strength m in a uniform stream, u_1. The source is located on the centerline at a distance x_o from the stagnation point. This distance will be initially unspecified, but it must be such that

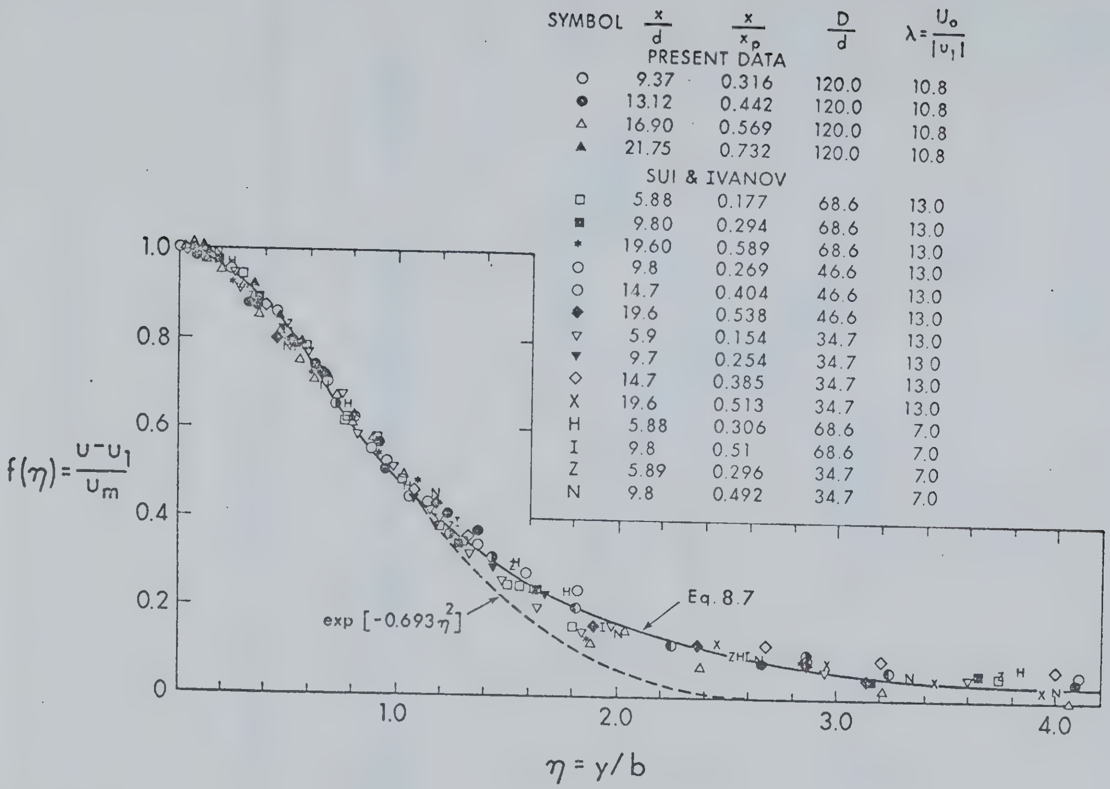

FIGURE 8.2 SIMILARITY OF VELOCITY PROFILES

the shape of the stagnation stream surface is reproduced as closely as possible near the stagnation point.

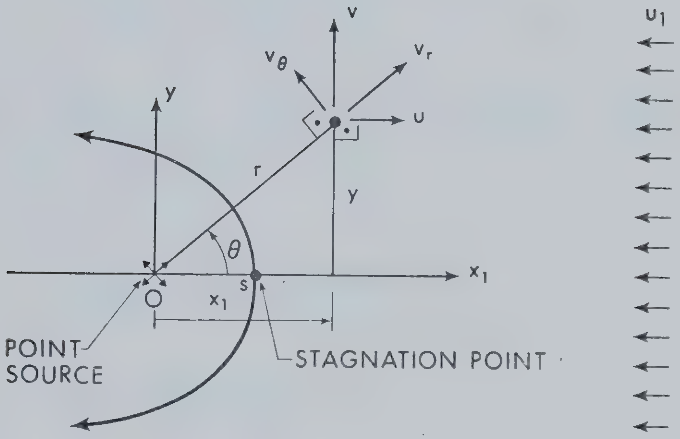
v
v_θ
v_r
u_1
y
u
r
y
θ
x_1
O
x_1
S
POINT SOURCE
STAGNATION POINT

FIGURE 8.3 THREE DIMENSIONAL POINT SOURCE IN A UNIFORM STREAM

With reference to Figure 8.3, the potential flow solution yields (56):

$$v_r = \frac{k}{r^2} - |u_1| \cos \theta$$

$$v_\theta = |u_1| \sin \theta \tag{8.1}$$

where $k = m/4\pi$. From these, it is possible to find an expression for $u - u_1$, i.e.:

$$u - u_1 = k \cos \theta / r^2 \tag{8.2}$$

At $$y = 0 \quad ; \quad u_m = u_c - u_1 = k/x_1^2 \tag{8.3}$$

where x_1 is distance along the centerline measured from the point source. It follows that:

$$\frac{u - u_1}{u_m} = \left(\frac{x_1^2}{x_1^2 + y^2}\right)^{3/2} \tag{8.4}$$

If b is the value of y where $(u - u_1)/u_m = \frac{1}{2}$, and $\eta = y/b$, the above can be reduced to:

$$\frac{u - u_1}{u_m} = [1 + 0.59\eta^2]^{-3/2} \tag{8.5}$$

with $$b = \sqrt{0.59}\ x_1 \tag{8.6}$$

This ascertains that similarity holds even beyond the stagnation point. It is now reasonable to assume that similarity exists throughout the flow field with a universal similarity function given by Equation 8.5, i.e.:

$$\frac{u - u_1}{u_m} = f(\eta) = [1 + 0.59\eta^2]^{-3/2} \tag{8.7}$$

This is verified in Figure 8.2 where it is seen that this function describes the data adequately even when η becomes as large as 4.0. It is not hard to explain this agreement in the range $x/x_p < 1$. For small values of η, where the flow is of the turbulent jet nature, the gaussian law is adequate. For large values of η, the flow becomes

almost potential (as can be verified in (55) where turbulent intensities tend to zero for increasing values of y), and Equation 8.7 is more appropriate. As these two functions practically coincide when $\eta \lesssim 1.2$, Equation 8.7 can be used for all η. It is of interest to note here that a conventional approach, i.e., assuming an eddy viscosity model for the shear stress, and then using similarity considerations to reduce the equation of motion to an ordinary differential equation, is not fruitful. The main reason for this appears to be the lack of similarity in the distribution of the radial component of velocity v and the turbulent shear stress τ. This can be seen if v is evaluated from the equation of continuity and substituted into the equation of motion, using $\tau = \rho u_m^2 g(\eta)$. Such substitution will indicate some restrictions upon the quantities b, u_m, u_1, which in turn can be shown to lead to absurdum.

This limitation was not realized by Ginevskii (53), who implicitly assumed similarity of shear stress distributions and obtained the shear stress by a polynomial approximation satisfying some obvious boundary conditions. The function $f(\eta)$ describing the velocity profile was then derived by means of an eddy viscosity model. This lack of similarity is the reason for the somewhat unconventional approach employed in the present work.

8.3.2 Velocity Scale

For a turbulent jet propagating in an infinite, uniform stream, and for a large penetration length, it is reasonable to assume that (see

also Rouse (48):

$$x_p = f_1(M_o, \rho, u_1) \tag{8.8}$$

where M_o $(\equiv \rho\pi d^2 U_o{}^2/4)$ is the initial momentum of the jet. With the same assumptions, u_m will be given by:

$$u_m = f_2(M_o, \rho, u_1, x)$$

which by means of Equation 8.8 reduces to:

$$u_m = f_3(M_o, \rho, x, x_p)$$

or:

$$\frac{u_m}{U_o} \frac{x_p}{d} = f_4(\frac{x}{x_p}) \tag{8.9}$$

Experimental data are plotted in this form in Figure 8.4, where it is seen that, excepting the values $\lambda = 2$ and 3, they define a single curve. Thus, it appears that the present formulation is correct for $\lambda \gtrsim 4$, which checks out with previous approximate considerations. Considering now the quantitative form of Equation 8.4, it is known that for a free jet $u_m \propto 1/x$. Also, for jets in co-flow, Tani and Kobashi (57) found that $u_m \propto 1/x$. It can easily be verified that here u_m varies also as $1/x$ for $x/x_p \lesssim 0.7$, i.e.:

$$\frac{u_m}{U_o} \frac{x_p}{d} = \frac{5.83}{x/x_p} \quad ; \quad x/x_p \lesssim 0.70 \tag{8.10}$$

This is shown plotted in Figure 8.4. Note that Equation 8.10 can also

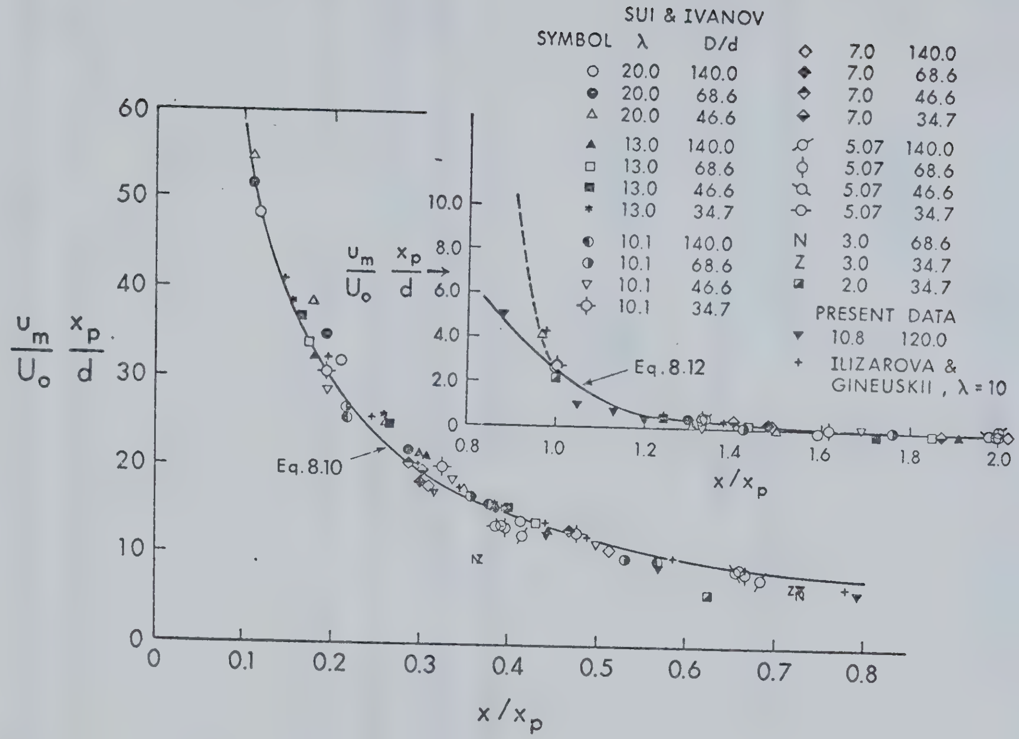

FIGURE 8.4 VELOCITY SCALE VARIATION

be written as:

$$\frac{u_m}{U_o} = \frac{5.83}{x/d} \tag{8.11}$$

which is the familiar law of axial velocity decay in free jets. For $x/x_p > 1.0$, Equation 8.3 should apply. By plotting:

$$\left(\frac{u_m}{U_o} \frac{x_p}{d}\right)^{-\frac{1}{2}} \quad \text{vs.} \quad x/x_p$$

it was found that a straight line, intersecting the axis at $x/x_p = 0.8$, described the data reasonably well. Thus:

$$\frac{u_m}{U_o} \frac{x_p}{d} = \frac{0.104}{(x_1/x_p)^2} \quad ; \quad x/x_p > 1.0 \tag{8.12}$$

where $x_1 = x - 0.8\, x_p$. This relation is verified in Figure 8.4. In the range $0.7 \leq x/x_p \leq 1.0$, a smooth transition joins the laws of Equations 8.10 and 8.12. Comparing Equation 8.12 to Equation 8.3, the required strength m of the point source was found to be (Appendix D, Section D.8):

$$m/Q_o \simeq 4.3\,\lambda \tag{8.13}$$

where $Q_o (\equiv \pi d^2 U_o/4)$ is the initial discharge of the jet. A complete prediction of u_m requires knowledge of the penetration length, x_p, which is evaluated in the following section.

8.3.3 Penetration Length

Recalling Equation 8.8 and applying dimensional reasoning, x_p

is given by:

$$x_p/d = C_p \lambda$$

where C_p is a constant. An experimental value of $C_p = 2.4$ was given in (48). Applying Equation 8.9 at $x/x_p = 1$, where $u_m = u_1$, it can be shown that $C_p = f_4(1.0)$. From Figure 8.4, an average value of C_p is 2.6. Hence:

$$x_p/d \simeq 2.6 \lambda \qquad (8.14)$$

When λ becomes less than about 4, the above reasoning will not be valid and in this case it could be shown that $x_p/d = \phi_1(\lambda)$, where $\phi_1(\lambda)$ is not necessarily a linear function.

8.3.4 Length Scale

Using dimensional arguments similar to those leading to Equation 8.9, it can be shown that:

$$b/x_p = f_5(x/x_p) \qquad (8.15)$$

This formulation is substantiated in Figure 8.5 where the data define a single curve while λ is varied between 7 and 20. The corresponding variation of a free jet is also shown for comparison.

To develop a quantitative expression for the function f_5, consider the locus $u = 0$, i.e., $y = y_o$. Sekundov (54) arrived at an expression for the gradient dy_o/dx, which was too complex to permit integration and it was assumed, with some indirect justification, that

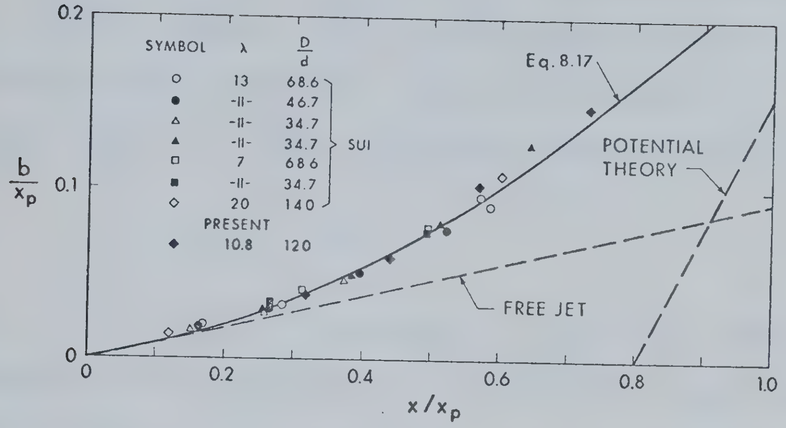

FIGURE 8.5 LENGTH SCALE VARIATION

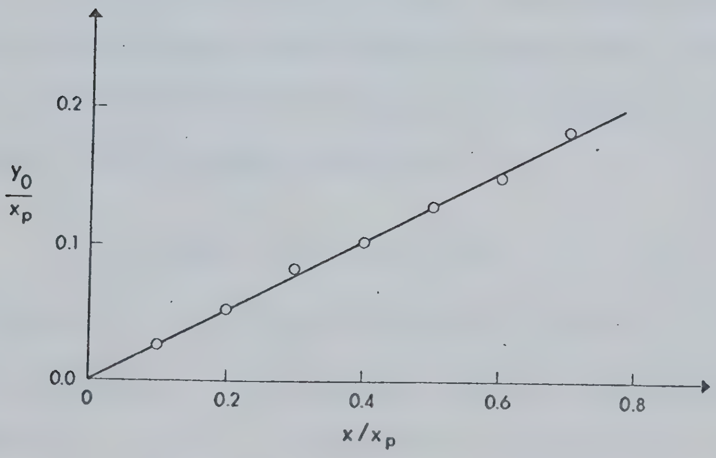

FIGURE 8.6 LINEARITY OF y_o/x_p

dy_o/dx is a constant. The results available here permit a direct test of this assumption. If $\eta_o = y_o/b$ then $f(\eta_o) = - u_1/u_m$ and $\eta_o = f^{-1}(- \frac{u_1}{u_m})$. Further, $y_o/x_p = \eta_o b/x_p$. Using average data from Figures 8.4 and 8.5, values of y_o/x_p were calculated and they are shown plotted in Figure 8.6, which confirms the linearity of y_o, in the range $x/x_p < 0.7$. Thus, the following empirical relation is adopted:

$$y_o = 0.26\ x \tag{8.16}$$

When $\lambda \to \infty$, the flow becomes that of a free jet. In that case, Equation 8.16 will represent the locus of points $u/u_m \approx 0.01$, i.e., the locus where u is almost equal to zero. Using the definition of y_o and Equations 8.7, 8.10 and 8.16, it is easy to show that:

$$\frac{b}{x_p} = 0.2\ \xi \left[\left(\frac{2.24}{\xi} \right)^{2/3} - 1 \right]^{-1/2} \tag{8.17}$$

where ξ is substituted for x/x_p. This relation is verified in Figure 8.5 at least in the range of available data, $x/x_p < 0.73$. For $x/x_p > 1.0$, the potential variation of b will be $b = \sqrt{0.59}\ x_1$ (Sec. 8.3.1), which can also be written as:

$$b/x_p = 0.77\ (\xi - 0.8) \tag{8.18}$$

In Figure 8.7, the relations expressed by Equations 8.17 and 8.18 are shown graphically. It is seen that the two functions have a point of tangency at $\xi = 1.4$, a property that justifies use of Equation 8.17 for $\xi \leq 1.4$, and use of Equation 8.18 for $\xi \geq 1.4$.

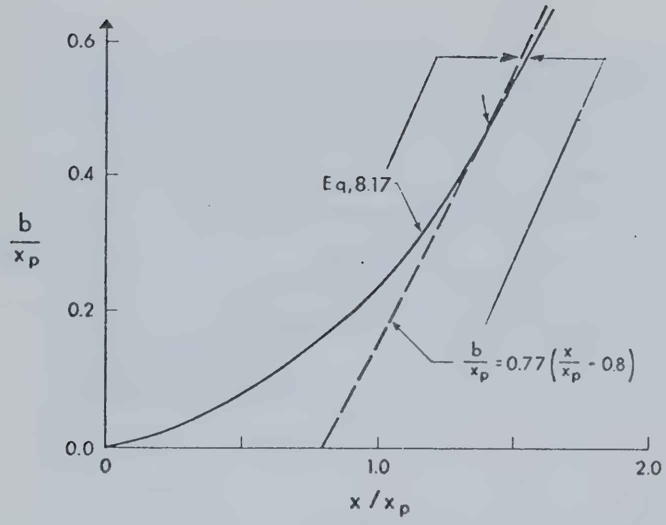

FIGURE 8.7   LENGTH SCALE - GENERALIZATION

8.3.5 Geometry

It is now possible to construct the generalized geometry of the flow field. As an example, two loci will be considered in this section, i.e., the locus $y = y_o$ $(u = 0)$ and the stagnation stream-surface, $y = y_s$ (Figure 8.1).

The locus $y = y_o$ can be found using the definition of y_o and the present findings regarding similarity of velocity profiles and the variation of the scales. Calculated values are shown plotted in Figure 8.8. It is seen that y_o reaches a maximum value of about $0.18\ x_p$ at $x/x_p \simeq 0.77$. Ginevskii's (53) theoretical development predicts this to be $0.11\ x_p$, i.e., about 40% less.

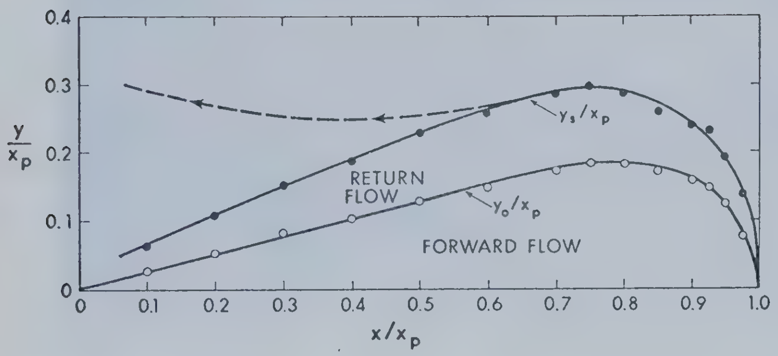

FIGURE 8.8 FLOW GEOMETRY

If y_s is the radius of the stagnation streamsurface, then y_s can be determined from the definition of this surface, i.e.:

$$\int_0^{y_s} 2\pi y u dy = 0$$

From this equation it can easily be shown that (see Appendix D, Section D.9) y_s/x_p depends only upon x/x_p, and calculated values are shown plotted in Figure 8.8. It is seen that y_s reaches a maximum value of about 0.29 x_p at $x/x_p \simeq 0.75$.

It should be emphasized that these loci must be regarded as time-averaged. Instantaneous configurations are shown in the photographs of Figure 8.9. (These photographs were taken using ordinary dye injected together with a water jet. The set-up was installed in a 1.5 ft. wide laboratory flume and it was used for vizualization purposes only.) In theory, the stagnation streamsurface envelops the entire

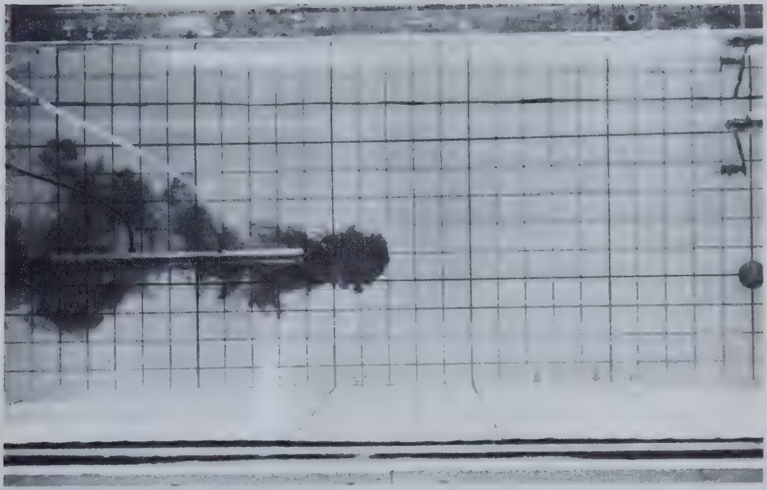

Speed Ratio = 10.7, Jet Reynolds no. = 2500

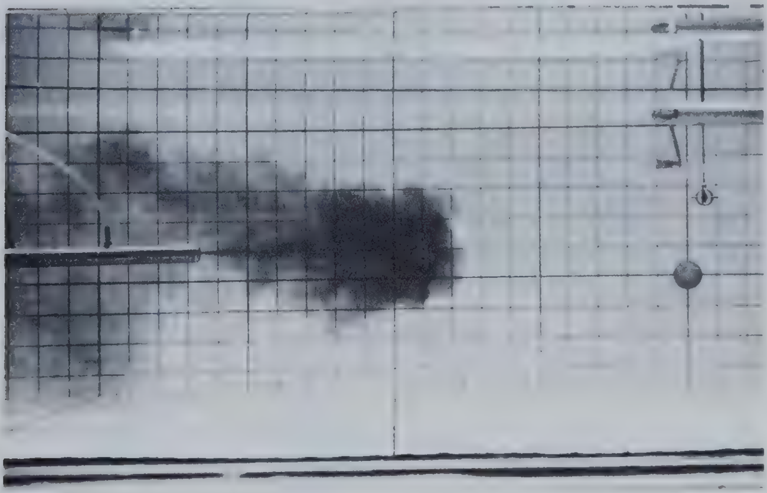

Speed Ratio = 27.2, Jet Reynolds no. = 6800

FIGURE 8.9 VISUALIZATION

flow originating from the jet. However, this is not true in the present case owing to turbulent exchange, so that the enveloping curve would be considerably higher than the stagnation streamsurface (broken line, Figure 8.8). This effect can also be seen in the photographs of Figure 8.9, and it is obviously beneficial from the practical point of view, where maximum diffusion is usually desirable.

8.3.6 The Question of Infinitely Wide Streams

In reality, infinitely wide streams do not exist. Therefore, it is necessary to consider the question as to what stream dimension can be considered to be infinite. If D is the lateral dimension of the opposing stream, and d_s is the maximum diameter of the stagnation streamsurface, then the ratio D/d_s gives an indication of the degree of contraction of the opposing stream, due to the developing counterjet. Assuming the opposing stream to be circular in cross section, the discharge Q will be $Q = \pi D^2 u_1/4$. At the section where d_s occurs, the velocity u_s (assumed to be uniform) will be larger than u_1 and it will be given by:

$$\frac{u_s}{u_1} = \frac{1}{1 - (\frac{d_s}{D})^2} \qquad (8.19)$$

If D/d_s is greater than, say, 3.3, then u_s/u_1 will be always less than 1.10 which means that the development of the jet will hardly be affected by the size of the stream. An indirect confirmation of this limit is presented in Figure 8.10, where the relative penetration length

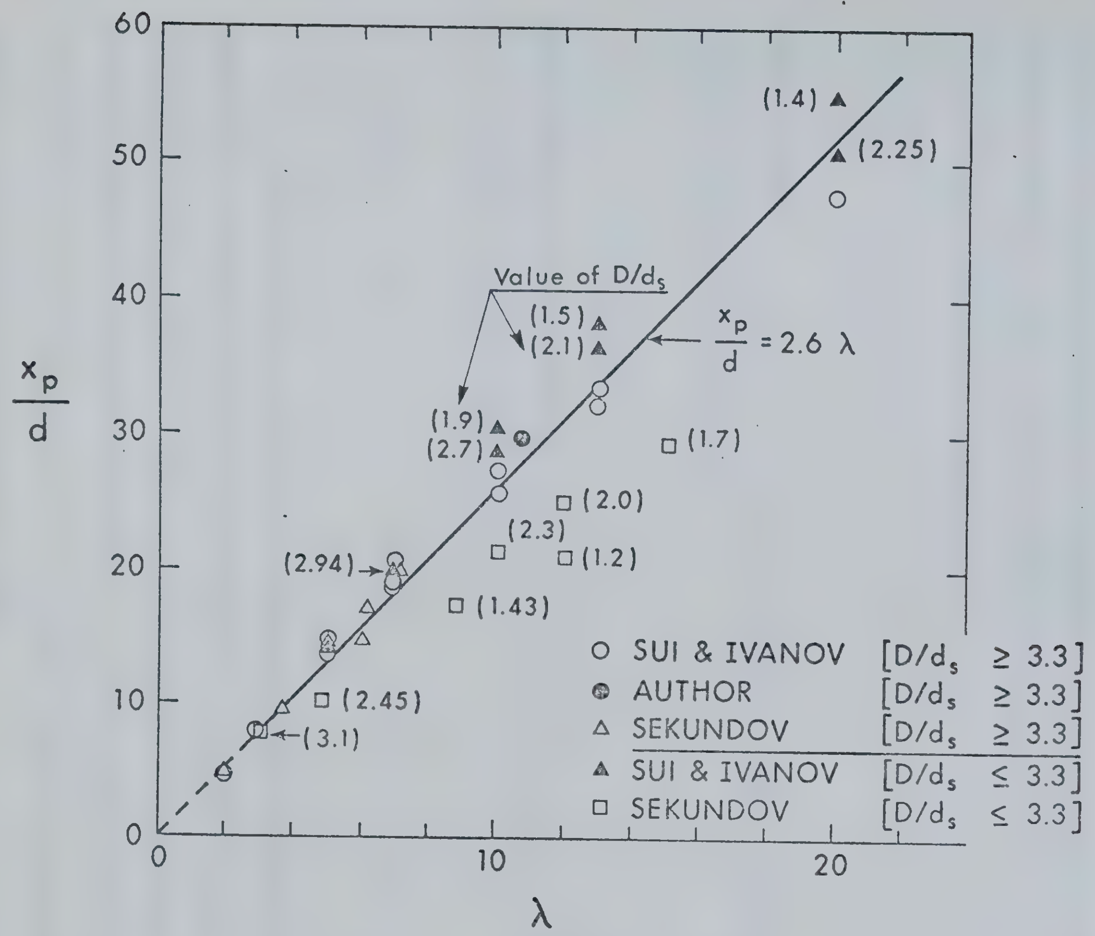

FIGURE 8.10 PENETRATION LENGTH

is plotted against λ. If the stream can be considered to be infinite, then x_p/d should obey Equation 8.14. Otherwise the size D will be an important parameter. It is seen by inspection that our prediction is reasonable, even though it is difficult to establish precisely the limiting value of D/d_s in this manner. Since $d_s \simeq 2 \times 0.29\ x_p$, this criterion can also be written as:

$$\frac{D}{x_p} \gtrsim 1.9 \tag{8.20}$$

which is close to $D/x_p \gtrsim 2.0$, given by Sekundov (54). The above relation can also be written as:

$$\frac{D}{d} \gtrsim 5\ \lambda \tag{8.21}$$

which implies that the limiting value of D in terms of the jet size d is dependent upon the speed ratio λ.

8.4 Summary

The problem of a circular counterjet has been treated in this chapter from the point of view of impinging jets. It was observed firstly that the penetration length could be used as an independent variable instead of the stream velocity u_1. Thus, dimensional analysis was carried out in analogy with previous chapters using the penetration length in the role of the impingement height.

The velocity similarity function was predicted by combining potential flow theory with turbulent jet knowledge. The velocity scale

was found to vary as in a free jet in the range $x/x_p \lesssim 0.7$, whereas it conformed to potential flow considerations for $x/x_p \gtrsim 1.0$. The length scale was found to grow considerably faster than in a free jet and it was predicted by utilizing the empirical observation that the locus of points where $u = 0$, is a straight line. Finally, the question of infinity was considered and it was shown that a stream size D can be treated as infinite, if D/x_p is larger than about 1.9.

CHAPTER IX - SUMMARY

The flow characteristics of turbulent impinging jets have been studied both experimentally and analytically. Starting with the relatively simple geometry of a circular jet impinging normally on a smooth wall, the study was extended step-by-step so as to include relatively complex geometrical configurations such as the oblique impingement of circular jets.

With a view to practical application to scouring problems, emphasis was placed in predicting wall pressures and shearing stresses in the impingement region and a satisfactory semi-empirical method of analysis has been proposed. Some preliminary considerations of the scouring problem (Appendix A) have shown promise with respect to predicting scouring processes on the basis of the present findings.

Flow characteristics of the wall jet region have also been considered. It was shown that a simple analytical approach can predict flow properties reasonably well so long as the nozzle Reynolds number is larger than about 20,000. Confirmation was provided by a re-analysis of experimental data of previous investigations and by data collected by the author.

Further, the problem of a circular counterjet was studied as being essentially an impingement problem and a simple semi-empirical method has been proposed to predict the time-average velocity field.

Finally, in the course of this study it was shown that when the impinging jet is not fully developed when approaching the stagnation point, the physics of the problem changes drastically in the impingement region. A limited study in this direction (axisymmetric case) has been performed in order to furnish some fundamental understanding of the difference from the fully developed impingement. This could provide the foundation for further work on more complex geometries, which was not pursued here, owing to rather limited practical interest of this type of flow.

The present work was confined to study of time-average quantities. However, the importance of turbulent fluctuations cannot be underestimated. In view of the current trend of attacking sediment transport problems in terms of probabilistic arguments, it is evident that turbulence measurements in the impingement region are desirable and expecially with respect to wall pressures.

Experiments with rough walls are also desirable, since mobile beds are usually rough. However, the difficulty may arise of how would wall pressure and shear stress be defined in the case of rough boundaries. This is commonly overcome by averaging over an area that includes a large number of roughness elements. Is it then correct to express forces on roughness elements in the manner introduced in Appendix A? Research in this direction (see also Chao & Sandborn (58)), would be an excellent contribution to the field of sediment transportation. The impinging jet provides a good means of doing so, because of the simultaneous existence of shear stresses and pressure gradients,

thus affording an opportunity to relate forces on roughness elements to the local (areal average) values of pressure and shear stress. It is known at present that local scour is caused by two kinds of singularities. One is the impinging jet, the other is the vortex located near a boundary. It appears reasonable to speculate that an approach similar to the present could be fruitful with respect to the vortex starting, say, with a simple rectilinear vortex located near a smooth boundary.

REFERENCES

1. Rouse, H. "Criteria for Similarity in the Transportation of Sediment". Hydraulics Conference, Proc. pp. 33-49, 1939. (Iowa University, Studies in Engineering, Bulletin 20).

2. Doddiah, D., Albertson, M.L. and Thomas, R. "Scour from Jets". Minnesota International Hydraulic Convention, September 1953.

3. Sarma, K.V.N. "A Note on a Simple Empirical Formula for Scour under Jets". J. of the Irrigation and Power, Volume 22, No. 4, October 1965, p. 528.

4. Sarma, K.V.N. and Sivasankar, R. "Scour Under Vertical Circular Jets". J. of the Institution of Engineers (India), C.E.D., Volume XLVIII, No. 3, November 1967.

5. Sarma, K.V.N. "Existence of Limiting Scour Depth". J. of the Institution of Engineers (India), C.E.D., Volume XLVIII, No. 1, September 1967.

6. Poreh, M. and Hefez, E. "Initial Scour and Sediment Motion Due to an Impinging Submerged Jet". Proc., IAHR, 12th. Congress, 1967, Volume 3, p. 9.

7. Johnson, G. "The Effects of Entrained Air on the Scouring Capacity of Water Jets". Proc., IAHR, 12th. Congress, 1967, Volume 3, p. 218.

8. Tsuchiya, Y. "Concerning the Scour Limit Resulting from Vertical Water Jets". Kyodai Bosai Kenkyujo Nenpo (Kyoto University Disaster Prevention Research Institute Annual Report), No. 6, July 1963, pp. 278-311.

9. Murray, R.I., Nelson, L.E. and Steven, J.R., (P.G. Hubbard - Adviser) "Deflection of a Jet by a Normal Wall". Seven Exploratory Studies in Hydraulics, by Hunter Rouse, J. of the Hydraulic Division, ASCE, August 1956.

10. Bradshaw, P. and Love, E.M. "The Normal Impingement of a Circular Air Jet on a Flat Surface", ARC, R and M No. 3205, 1959.

11. Poreh, M. and Cermak, J.E. "Flow Characteristics of a Circular Submerged Jet Impinging Normally on a Flat Boundary". Proc. 6th Midwestern Conference on Fluid Mechanics, pp. 198-212, 1959.

12. Mathieu, J. "Contribution a l'Etude Aerothermique d'un Jet Plan Evoluant en Presence d'une Paroi". Doctor of Science Thesis, University of Grenoble, October 1959.

13. Vidal, R.J. "Aerodynamic Processes in the Downwash-Impingement Problem". J. of the Aerospace Sciences, September 1962.

14. Schauer, J.J. and Eustis, R.H. "The Flow Development and Heat Transfer Characteristics of Plane Turbulent Impinging Jets". Technical Report 3, Department of Mech. Eng., Stanford University, October 1963.

15. Tani, I. and Komatsu, Y. "Impingement of a Round Jet on a Flat Surface". Edited by Henry Goertler, Proc. of the 11th. International Congress of Applied Mechanics, Munich, Germany, pp. 672-676, 1964.

16. Cola, R. "Energy Dissipation of a High Velocity Vertical Jet Entering a Basin". 11th IAHR Congress, Volume 1, Leningrad, 1965.

17. Poreh, M. Tsuei, Y.G. and Cermak, J.E. "Investigation of a Turbulent Radial Wall Jet". J. of Applied Mechanics, June 1967, pp. 457-463.

18. Cartwright, W.G. and Russell, P.J. "Characteristics of a Turbulent Slot Jet Impinging on a Plane Surface". Proc., Inst. Mech. Engrs., 1967-68, Vol. 182, Pt 3H, Paper 32.

19. Wolfshtein, M. "Some Solutions of the Plane Turbulent Impinging Jet". J. of Basic Engineering, ASME, December 1970, pp. 915-922.

20. Skifstad, J.G. "Aerodynamics of Jets Pertinent to VTOL Aircraft". J. of Aircraft, AIAA, May-June 1970, Volume 7, No. 3.

21. Gauntner, J.W., Livingood, J.N.B. and Hrycak, P. "Survey of Literature on Flow Characteristics of a Single Turbulent Jet Impinging on a Flat Plate". U.S. NASA, TN-D-5652, 1970.

22. Hrycak, P., Lee, D.T., Gauntner, J.W. and Livingood, J.N.B. "Experimental Flow Characteristics of a Single Turbulent Jet Impinging on a Flat Plate". U.S. NASA, TN-D-5690, 1970.

23. Bradbury, L.J.S. "The Impact of an Axisymmetric Jet onto a Normal Ground". Aeronautical Quarterly, May 1972, pp. 141-147.

24. Kamoi, A. and Tanaka, H. "Measurements of Wall Shear Stress, Wall Pressure and Fluctuations in the Stagnation Region Produced by Oblique Jet Impingement". Fluid Dynamics Measurements, Conference Papers, Volume 1, 1972, pp. 217-227.

25. Beltaos, S. "Normal Impingement of Plane Turbulent Jets on Smooth Walls". M.Sc. Thesis, Department of Civil Engineering, The University of Alberta, Edmonton, Canada, 1972.

26. Beltaos, S. and Rajaratnam, N. "Plane Turbulent Impinging Jets". J. of Hydraulic Research, IAHR, Volume 11, No. 1, 1973, pp. 29-59.

27. Yakovlevskii, O.V. and Krasheninnicov, S. Yu. "Spreading of a Turbulent Jet Impinging on a Flat Surface". Fluid Dynamics (Faraday Press translation of Izv. AN SSSR. Mekhanika Zhidkostei; Gaza), Volume 1, No. 4, July-August 1966, p. 136.

28. Abramovich, G.N. "The Theory of Turbulent Jets". Tech. Editing by L.H. Schindel, the M.I.T. Press, Massachussetts Institute of Technology, Cambridge, Massachussetts, 1963.

29. Rajaratnam, N. "Introduction to Turbulent Jets". (in Prep.) Department of Civil Engineering, the University of Alberta, Edmonton, Canada.

30. Glauert, M.B. "The Wall Jet". J. of Fluid Mechanics, 1, 1956, p. 625.

31. Schwartz, W.H. and Cosart, W.P. "The Two-Dimensional Turbulent Wall Jet". J. of Fluid Mechanics, Volume 10, 1961, pp. 481-495.

32. Sigalla, A. "Measurements of Skin Friction in a Plane Turbulent Wall Jet". J. Royal Aeronautics Society, London, Volume 62, 1961.

33. Myers, G.E., Schauer, J.J. and Eustis, R.H. "The Plane Turbulent Wall Jet, Part I - Jet Development and Friction Factor". Technical Report No. 1, Department of Mechanical Engineering, Stanford University, June 1961.

34. Rajaratnam, N. "Plane Turbulent Wall Jets on Rough Boundaries". Technical Report, Department of Civil Engineering, the University of Alberta, Edmonton, Canada, June 1965. (Also published in Water Power, London, England, April-May-June 1967.)

35. Rajaratnam, N. and Subramanya, K. "An Annotated Bibliography on Turbulent Wall Jets". Technical Report, Department of Civil Engineering, The University of Alberta, Edmonton, Canada, 1967.

36. Schlichting, H. "Boundary Layer Theory". McGraw-Hill Book Co., New York, 6th. Edition, 1968.

37. Wolfshtein, M. "A Theory for Turbulent Stagnation Flow". T.A.E. Report No. 106, Department of Aeronautical Eng., Technion-Israel, Institute of Technology, Haifa, Israel, February 1970.

38. Beltaos, S. "Non-Rotating Pitot Cylinder". Technical Report, Department of Civil Engineering, The University of Alberta, Edmonton, Canada, 1972.

39. Preston, J.H. "The Determination of Turbulent Skin Friction by Means of Pitot Tubes". J. of the Royal Aeronautical Society, London, England, Volume 58, February 1954, pp. 109-121.

40. Patel, V.C. "Calibration of the Preston Tube and Limitations on its Use in Pressure Gradients". J. of Fluid Mechanics, Volume 23, pp. 185-208, 1965.

41. Hill, B.J. "Measurement of Local Entrainment Rate in the Initial Region of Axisymmetric Turbulent Air Jets". J. of Fluid Mechanics, Volume 51, Part 4, 1972, p. 773.

42. Squire, H.B. and Trouncer, J. "Round Jets in a General Stream". A.R.C. Technical Report, R. & M. 1974, January 1944.

43. Kuhn, R.E. "An Investigation to Determine Conditions Under which Downwash from VTOL Aircraft will Start Surface Erosion from Various Types of Terrain, U.S. NASA, TN-D-56, September 1959.

44. Batchelor, G.K. "An Introduction to Fluid Dynamics". Cambridge (England) University Press, 1967.

45. Schach, W. "Umlenkung eines freien Flussigkeitsstrahles an einer ebenen Platte, Ing. Archiv 5(1934), p.245.

46. Nash, J.F. and Patel, V.C. "Three Dimensional Turbulent Boundary Layers". Atlanta, Scientific and Business Consultants, 1972.

47. Loitsianskii, L. "Mechanics of Liquids and Gases". Oxford, New York, Pergamon Press (1st. English Edition), 1966.

48. Arendt, J., Babcock, H.A. and Schuster, J.C. (H. Rouse, Adviser). "Penetration of a Jet into a Counterflow". Seven Exploratory Studies in Hydraulics by Hunter Rouse, J. of Hydraulic Division, August 1956.

49. Sui, Kh.N. and Ivanov, Yu.V. "The Investigation of the Development of a Circular Jet in the Initial Region of an Opposing Stream of Large Dimensions" (In Russian). Eesti NSV teadusteakadeemia, Tallin, Toimetised, Isvestia Fuusika-matemaatick-ja technikateaduste seeria, Seeria fiziko-matimaticheskikh nauk, Volume 8, No. 2, 1959, pp. 78-83.

50. Sui, Kh.N. "The Investigation of the Development of Circular and Planar Jets in Parallel and Opposing Streams" (In Russian). Same Journal as in Ref. 49, Volume 10, No. 3, 1961, pp. 215-223.

51. Timma, E. "Turbulent Circular and Planar Jets Developing in an Opposing Stream" (In Russian). Same Journal as in Ref. 49, Volume 11, No. 4, 1962, pp. 253-262.

52. Ilizarova, L.I. and Ginevskii, A.S. "The Experimental Investigation of Jets in an Opposing Stream" (In Russian). Promyshlennaia Aerodynamika (Tsentral'nyi aero-gidro-dinamicheskii institut imeni Prof. N.E. Zhukovskogo), Moskow, No. 23, 1962.

53. Ginevskii, A.S. "Turbulent Jet Streams with Reverse Liquid Flows", (In Russian). Same Reference as above.

54. Sekundov, A.N. "The Propagation of a Turbulent Jet in an Opposing Stream", from a collection of papers on Turbulent Jets of Air, Plasma and Real Gas, Edited by G.N. Abramovich, Moscow Aviation Institute, Translated from Russian, Consultants Bureau, New York, 1969.

55. Rao, T.R.K. "Investigation of the Penetration of a Jet into a Counterflow". M.Sc. Thesis, Department of Mechanics and Hydraulics, State University of Iowa, February 1958.

56. Streeter, V.L. "Fluid Dynamics". New York, McGraw-Hill, 1948.

57. Tani, I and Kobashi, Y. "Experimental Studies on Compound Jets". Proc. 1st. Japan National Congress for Applied Mechanics, 1951.

58. Chao, J.L. and Sandborn, V.A. "Study of Static Pressure along a Rough Boundary". J. of Hydraulic Division, ASCE, March 1965, pp. 193-203.

59. Chiu, V.M.H. "The Scour Hole Created by an Air Jet". Project 500 Final Report, Department of Civil Engineering, The University of Alberta, Edmonton, Canada, 1973.

60. Paintal, A.S. "Concept of Critical Shear Stress in Loose Boundary Open Channels". J. of Hydraulic Research, IAHR, Volume 9, 1971, p. 91.

61. Paintal, A.S. "A Stochastic Model of Bed Load Transport". J. of Hydraulic Research, IAHR, Volume 9, 1971, p. 527.

62. Yalin, M.S. "Mechanics of Sediment Transport". Pergamon Press, Oxford, New York, Toronto, Sydney, 1972.

APPENDIX A - A CRITERION FOR SCOUR

A.1 Introduction

In this section it is shown how the knowledge gained so far can be applied to the scour problem. When a turbulent jet impinges on an erodible boundary, scour may or may not occur. The first task, associated with scour from jets is, therefore, to determine the conditions under which scour will take place. This question can be put into several forms. For example, given the geometry and velocity of the jet and given the properties of the erodible bed material, determine whether scour will or will not take place. Or, given the geometry and velocity of the jet, determine the properties of the bed material so that scour will not occur. If scour is expected to take place, the next task is to determine its magnitude and geometry and their development with time.

In this Appendix, which serves as an illustration of practical application of the present results, only the first question will be considered for the relatively simple case of circular turbulent jets impinging normally on a boundary consisting of cohesionless material of uniform size D. The answer to this question will form a criterion for scour.

A.2 Theoretical Considerations

A criterion for scour has been proposed earlier by Poreh and Hefez (6), based on dimensional reasoning. If M_o is the initial

momentum of the jet and H is the initial impingement height and D the size of the uniform bed material, then if everything else is kept constant and M_o is allowed to vary, there will be a value of M_o below which no scour will occur. Poreh and Hefez wrote the following dimensional relation for the critical value of M_o:

$$M_o = f(\rho, \gamma_s, D, H, \nu)$$

where ρ, ν are the density and kinematic viscosity of the fluid respectively, and γ_s is the submerged specific weight of the bed material, i.e., $\gamma_s = \rho g(s - 1)$ if s is the specific gravity of the bed material with respect to the particular fluid.

By dimensional analysis, the above relation can be reduced to:

$$\frac{H^3 \gamma_s}{M_o} = G \left(\frac{\sqrt{M_o/\rho}}{\nu}, \frac{D}{H} \right) \qquad (A.1)$$

Since $M_o = \rho \frac{\pi d^2}{4} U_o^2$, this can also be written as:

$$\frac{H^3 g(s - 1)}{d^2 U_o^2} = G_1 \left(R_o, \frac{D}{H}\right) \qquad (A.2)$$

Experiments with air jets impinging on sand beds, showed that the influence of the Reynolds number, R_o, was negligible* and for the range of

---

* This is not surprising in view of our previous findings on smooth walls. It was established earlier that even for smooth walls, shear stress and pressure did not depend on R_o. Since erodible walls are rough, it may be expected that the scouring forces will not depend on R_o for a stronger reason.

experimentation (D/H = .00029 to .0022), the following empirical relation was found adequate:

$$\frac{H^3 g(s - 1)}{d^2 U_o^{\ 2}} = 12.8 \frac{H}{D} \tag{A.3}$$

which can be further reduced to:

$$\frac{H/d}{U_o/\sqrt{gD(s - 1)}} = 3.58 \tag{A.4}$$

Tsuchiya (8) considered the same problem. His approach, however, was based on questionable theoretical derivations so that it was not possible to obtain any consistent criterion, such as the above.

Consider now the following simplified theoretical model, which makes use of the critical shear stress concept. The total tractive force on a bed particle will consist of two components, one due to the shear stress τ_o and another due to the pressure gradient, dp/dr, i.e.:

$$T = \tau_o a_1 - \Delta p_w a_2$$

where T is the tractive force and a_1 is a horizontal area representing the "area of influence" for the particular grain. Obviously, $a_1 = c_1 D^2$ with the constant c_1 being a coefficient which depends upon the degree of packing of the bed material. The quantity Δp_w represents the pressure difference between the front and back sides of the particles, whereas a_2 is a vertical area representing the effective area of projection of the grain. Much like a_1, this area will be $a_2 = c_2 D^2$. If τ_e is an equivalent, or total, shear stress, which

incorporates pressure gradient effects, it will be equal to T/a_1, i.e.:

$$\tau_e = \tau_o - \frac{a_2}{a_1} \Delta p_w$$

or
$$\tau_e = \tau_o - \alpha D \frac{dp_w}{dr} \qquad (A.5)$$

where $\alpha = \text{const} = c_2/c_1$. This derivation is ordinarily valid for uniform bed materials with grains of spherical shape. Since the constant α depends mainly upon the shape of the individual grain and the degree of packing of the bed material, allowances can be made to extend this equation to non-uniform materials of shapes other than spherical. Furthermore, it is obvious that this analysis will be realistic so long as the grains are very small in comparison to the width of the impingement region. If r_* denotes the radial extent of this region, it is reasonable to restrict particle sizes so that D is less than, say, one-tenth of r_*, i.e.:

$$D \lesssim 0.1\, r_* \qquad (A.6)$$

For a smooth wall and large impingement heights, $r_* \simeq 0.2\, H$ (Chapter IV). When the wall is rough this value is likely to change. Since roughness tends to intensify turbulence, it is reasonable to expect that r_* will decrease with increasing D. When D becomes equal to or greater than r_* then the pressure difference Δp_w will be simply equal to p_s. Obviously, most practical situations will be such that condition A.6 is satisfied.

If τ_c is the critical shear stress associated with the par-

ticular combination of fluid and sediment, then a condition for non-scouring will be:

$$\max \quad \tau_e \leq \tau_c \tag{A.7}$$

Considering large impingement heights, it was shown in Chapter IV that:

$$\tau_o = \tau_{om}\, g(\lambda) \quad ; \quad p_w = p_s\, f(\lambda) \quad ; \quad \lambda = r/H$$

with:

$$\frac{\tau_{om}}{\rho U_o^2} \left(\frac{H}{d}\right)^2 = C_* = 0.16$$

$$\frac{p_s}{\rho U_o^2} \left(\frac{H}{d}\right)^2 = K_p = 26$$

When the wall is rough, the functions g and f as well as the coefficients C_* and K_p will generally depend upon the relative roughness D/H, so that:

$$\lim_{D/H \to 0} C_* = 0.16 \quad ; \quad \lim_{D/H \to 0} K_p = 26 \quad ; \quad \lim_{D/H \to 0} g(\lambda) = g_o(\lambda)$$

and $$\lim_{D/H \to 0} f(\lambda) = f_o(\lambda)$$

where g_o, f_o represent the forms occuring for smooth walls.

Using these relations, it is possible to reduce Equation A.5 to the form:

$$\tau_e = \rho U_o^2 \left(\frac{d}{H}\right)^2 \left[C_* g(\lambda) - \alpha K_p \frac{D}{H} \frac{df}{d\lambda}\right] \tag{A.8}$$

The quantity inside the brackets is a function of both λ and D/H. Denoting this by $F(\lambda, D/H)$, the above equation becomes:

$$\tau_e = \rho U_o^2 (\frac{d}{H})^2 F(\lambda, \frac{D}{H}) \tag{A.9}$$

The maximum of τ_e will occur at $\lambda = \lambda_m$, while λ_m is determined from:

$$\left[\frac{\partial F}{\partial \lambda}\right]_{\lambda=\lambda_m} = 0 \tag{A.10}$$

which implies that $\lambda_m = \lambda_m(\frac{D}{H})$. It follows that:

$$\max \tau_e = \rho U_o^2 (\frac{d}{H})^2 G(\frac{D}{H}) \tag{A.11}$$

where G is a new function which depends only upon D/H.

Considering now the critical shear stress, τ_c, the well-known Shields' diagram gives the normalized critical shear, $\tau_c/\rho g(s - 1)D$, as a function of the particle Reynolds number, $u_* D/\nu$. However, the influence of viscosity is of little consequence in most practical situations, i.e.:

$$\tau_c = \beta \rho g(s - 1)D \tag{A.12}$$

where β is a constant. This condlusion is also supported by the results of Poreh and Hefez (6), where no viscous effects could be detected as was pointed out earlier.

Substituting Equations A.11 and A.12 into Equation A.7 the

condition for non-scouring can be expressed as:

$$\frac{H/d}{U_o/w_*} \geq \sqrt{\frac{G(\frac{D}{H})}{\beta}} \qquad (A.13)$$

where w_* has been substituted for the quantity $\sqrt{g(s-1)D}$, which has the dimensions of velocity, and is related to the fall velocity of a single particle in still fluid. Taking the limit when $D/H \to 0$, then τ_e will not contain the pressure gradient term and at the same time $C_* \simeq 0.16$. Hence, at the limit:

$$\frac{H/d}{U_o/w_*} \geq \sqrt{\frac{0.16}{\beta}} \quad ; \quad (\frac{D}{H} \to 0) \qquad (A.14)$$

This relation will hold for the smaller values of D/H, and it is obviously independent of this parameter. This explains the empirical finding of Poreh and Hefez (Equation A.4), whose experiments were for D/H always less than 0.002.

Considering now the larger values of D/H, i.e., $D/H \geq r_*/H$, obviously this will represent impingement on a relatively smooth, but curved wall. To evaluate forces on a particle it will now be necessary to integrate τ_o and p on the surface of the grain. These forces will now be proportional to τ_{om} and p_s which in turn are proportional to $\rho U_o^2 d^2/H^2$. It follows that in this case the criterion of non-scour will simply be:

$$\frac{H/d}{U_o/w_*} \geq \text{const} \quad ; \quad D \geq r_* \qquad (A.15)$$

Since r_* is likely to decrease with D/H, the condition $D \geq r_*$ will

be satisfied at a value of D/H which will be less than 0.2, i.e., of the order of 0.1. The criterion of Equation A.13 can also be obtained by dimensional analysis, as in Equation A.2, neglecting viscous effects. Analogous results can be obtained when the height of impingement is small. Using the results of Chapter V, it is possible to show that in this case:

$$\tau_e = \frac{\rho U_o^2}{2}\left[C_{fm} h_\tau(\bar{r}) - \alpha \frac{D}{d} \frac{dh_p}{d\bar{r}}\right] \tag{A.16}$$

where $h_\tau(\bar{r}) = \frac{\tau_o}{\tau_{om}}$; $h_p(\bar{r}) = p_w/p_s$; $\bar{r} = r/d$; $C_{fm} = \frac{\tau_{om}}{\rho U_o^2/2} \simeq 0.007$

Thus, the criterion for non-scouring will be:

$$\frac{w_*}{U_o} \geq \sqrt{\frac{G_1(\frac{D}{d})}{\beta}} \tag{A.17}$$

whereas when $D/d \to 0$, this will reduce to:

$$\frac{w_*}{U_o} \geq \sqrt{\frac{C_{fm}}{\beta}} \quad ; \quad (\frac{D}{d} \to 0) \tag{A.18}$$

And when $D/d \geq r_*/d$:

$$\frac{w_*}{U_o} \geq \text{const} \quad (D \geq r_*) \tag{A.19}$$

A.3 Comparison with Experiments

Experimental results are available from three different sources. (i) Poreh and Hefez (6). Data were obtained with air jets impinging on

sand beds in the range $0.00029 \leq D/H \leq 0.0022$ ($0.23\text{ mm} \leq D \leq 0.90\text{ mm}$).

(ii) Tsuchiya (8). Data were obtained with water jets impinging on sand beds in the following ranges of parameters:

$$\begin{aligned} 0.4435\text{ mm} &\leq D \leq 15.0\text{ mm} \\ 3{,}840 &\leq R_o \leq 58{,}600 \\ 10 &\leq H/d \leq 80 \\ 0.00222 &\leq D/H \leq 0.0375 \end{aligned}$$

Critical velocities were obtained by keeping other parameters constant, while varying the velocity U_o and recording the relative amount of sediment that moved. The critical velocity was defined to be that value of U_o at which 0.5% of sediment in the impingement area of the boundary was dislodged.

(iii) Chiu (59). Data were obtained for air jets impinging on a nearly uniform sand bed of median size $D = 0.26$ mm. Other parameters were in the following ranges:

$$\begin{aligned} 16.6 &\leq H/d \leq 50.28 \\ 8{,}780 &\leq R_o \leq 42{,}800 \\ 0.000804 &\leq D/H \leq 0.00243 \end{aligned}$$

In these experiments, the bed was allowed to be scoured and the final maximum (or equilibrium) scour depth was measured. This was plotted against U_o in each case (keeping other parameters constant) and the value of U_o corresponding to zero scour depth was obtained by extrapolation. This extrapolation was considered to be fairly reliable because the scour depth varied with U_o linearly (excepting the very high values of U_o).

Experimental data from the above sources have been re-analyzed and they are plotted in the form suggested by Equation A.13 in Figure A.1.

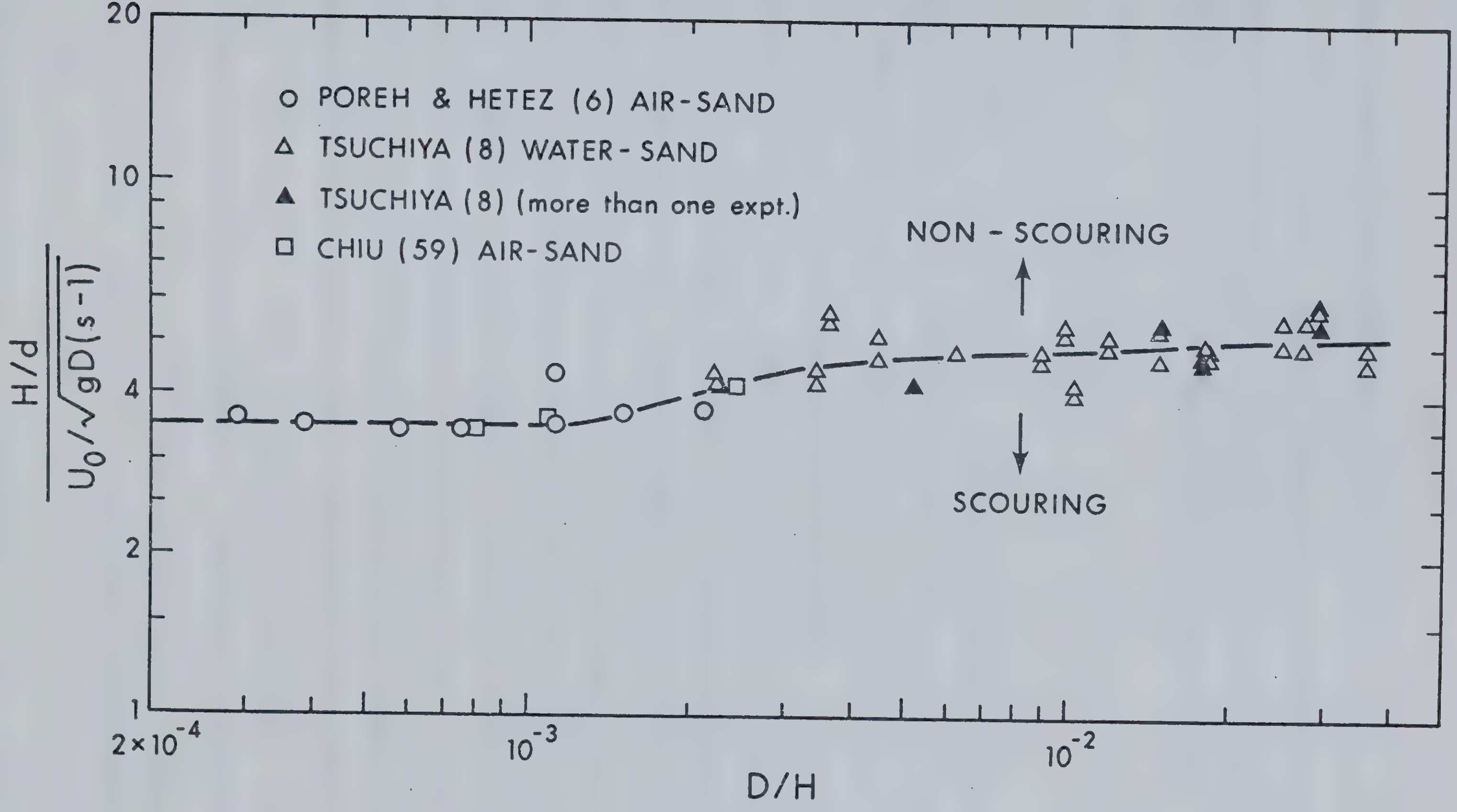

FIGURE A.1 A SCOUR CRITERION

The data exhibit considerable scatter which, however, is not uncommon for scour experiments. Thus, our formulation is reasonably well verified and for practical purposes the average curve drawn through the data could be used to obtain limiting values of the parameter:

$$\frac{H/d}{U_o/\sqrt{gD(s-1)}}$$

For the lower values of D/H ($D/H \lesssim 0.0012$) this parameter remains constant, as was predicted earlier, with an average value of 3.5. Substituting this into Equation A.14, the corresponding value of β will be 0.013. A conventional value from Shields' diagram would be about 0.04. There are two reasons for the discrepancy. Firstly, Shields' value was obtained for plane flow, whereas the present data are for axisymmetric flow. This difference, however, is not expected to account for the present variation of 300%. The following second reason appears to be more satisfactory and lies in the definition of the critical condition. Shields' diagram was obtained by plotting shear stress versus rate of transport and extrapolating to zero rate of transport. Later experimental and theoretical studies (see for example Paintal (60) and (61) and Yalin (62)), showed that some transport takes place even when $\tau_o \rightarrow 0$. This situation can be explained if the turbulent nature of the flow is considered. Turbulence is responsible for the existence of a certain, however small, probability of movement, which in turn, causes some transport to occur over long periods of time. Using theoretical derivations of Paintal (61) for plane flows, the corresponding probabilities of movement for $\beta = 0.013$ and 0.04

respectively are 10^{-8} and 10^{-6}.

Another interesting feature in Figure A.1 is the tendency of the data to become independent of D/H as D/H increases, in agreement with previous considerations. Finally, it is noteworthy that no significant differences exist between air-sand and water-sand data, even though these represent an over thousand-fold variation in submerged specific weight of sediment. In the phenomenon of sediment transportation there exists a quantitative difference between transport by air and transport by water. This is due to the fact that in the former case, $(s - 1) \sim 1{,}000$ whereas in the latter case $(s - 1) \sim 1.0$. Thus, fall velocities are much greater in air. This implies that saltating particles, strike the bed with much greater momentum in air than in water, a fact that contributes to increase transport. When dealing with initiation of motion, however, very little transport occurs and movement is mostly by rolling, so that the above factor is absent. This explains why no quantitative difference exists between air-sand and water-sand data in Figure A.1.

Using $\beta = 0.013$, the criterion for scour for small impingement heights will be:

$$\frac{U_o}{w_*} = \sqrt{\frac{0.013}{C_{fm}}} \qquad (A.20)$$

The quantity C_{fm} varies slightly with nozzle Reynolds number, and for R_o between 31,000 and 54,000 (Chapter V) has an average value of 0.007, which gives:

$$\frac{U_o}{w_*} \simeq 1.4 \qquad (A.21)$$

In practice, almost always U_o is much larger than w_* so that scour will almost always occur for small impingement heights.

A.4 Summary

A simple application to the scour problem associated with impinging jets has been presented in this Appendix. It was shown that the question of whether or not scour occurs, can be answered by examining a single dimensionless parameter which expresses the erosive capacity of the jet. Experiments confirmed theoretical predictions over a wide range of the specific weight of bed material with respect to the surrounding fluid.

APPENDIX B - ERROR ANALYSIS OF PITOT CYLINDER TECHNIQUE

The Non-Rotating Pitot Cylinder Technique is based on the assumption that the pressure readings taken from the three orifices of the probe (see Figure 3.7) are related to the local static and dynamic pressures p_o and p_v respectively by the equations:

$$p_i = p_o + K_i p_v \quad ; \quad i = 1,2,3 \tag{B.1}$$

where K_i are three calibration factors which depend on the angle ϕ (see Figure 3.7). Calibration of the instrument was carried out in a uniform stream, i.e., p_o and p_v have the same value in all three locations 1,2,3 of the orifices. However, if there exist gradients of p_o and p_v in the direction normal to the axis of the probe, then it is reasonable to assume that:

$$p_i = p_{oi} + K_i p_{vi} \quad ; \quad i = 1,2,3 \tag{B.2}$$

where p_{oi} and p_{vi} are the values corresponding to the locations of the orifices. Assuming constant gradients between 1 and 3, the following relations apply:

$$\begin{aligned} p_{o3} &= p_{o2} + \Delta \frac{dp_o}{dx} \quad ; \quad p_{o1} = p_{o2} - \Delta \frac{dp_o}{dx} \\ p_{v3} &= p_{v2} + \Delta \frac{dp_v}{dx} \quad ; \quad p_{v1} = p_{v2} - \Delta \frac{dp_v}{dx} \end{aligned} \tag{B.3}$$

where the gradients $\frac{dp_o}{dx}$, $\frac{dp_v}{dx}$ are evaluated at the central orifice, 2, x denotes distance normal to the probe axis, and Δ is the distance

between successive orifices.

The first step after measurement of p_1, p_2, p_3 is to compute the factor:

$$K = \frac{p_1 - p_2}{p_3 - p_2} \quad ; \quad \phi < 0$$

$$\text{or:} \quad K = \frac{p_3 - p_2}{p_1 - p_2} \quad ; \quad \phi > 0 \tag{B.4}$$

from which the value of ϕ can be obtained from the appropriate graph. Using Equations B.2 and B.3, K will be given by:

$$K = \frac{(K_1 - K_2) - \frac{\Delta}{p_{v2}}\left[\frac{dp_o}{dx} + K_1 \frac{dp_v}{dx}\right]}{(K_3 - K_2) + \frac{\Delta}{p_{v2}}\left[\frac{dp_o}{dx} + K_3 \frac{dp_v}{dx}\right]} \tag{B.5}$$

If $\frac{dp_o}{dx}$ and $\frac{dp_v}{dx}$ are both zero, then $K = (K_1 - K_2)/(K_3 - K_2)$, and this can be assumed to be the "true" value of K at the location of orifice 2 where the measurement applies. The extra terms in Equation B.5 will be responsible for the introduction of a certain error. As "true" distributions of p_o, p_v are not known before hand, the measured values (which are obtained on the assumption that gradient terms are negligible) will be used to obtain an estimate of the errors introduced because of gradient terms. In order to apply a correction to K, it is necessary to add terms equal in magnitude and opposite in sign to the gradient terms on both the nominator and the denominator of the fraction. Hence, a corrected value of K will be:

$$K = \frac{p_1 - p_2 + \Delta\left[\frac{dp_o}{dx} + K_1\frac{dp_v}{dx}\right]}{p_3 - p_2 - \Delta\left[\frac{dp_o}{dx} + K_3\frac{dp_v}{dx}\right]} \tag{B.6}$$

The values of p_1, p_2, p_3, K_1, K_3 appearing in Equation B.6 should, strictly speaking, be "true" values. These, however, are not known before hand and, therefore, as a first approximation the measured values can be used. For the case of impingement at small heights, where gradients are most intense, error estimates will be provided for two profiles. One is in the free-jet region where $dp_o/dx = 0$ and the other in the impingement region, where both dp_o/dx and dp_v/dx are different from zero. Letting h denote corresponding manometer height and considering that here $\Delta = 0.0141$ in, Equation B.6 becomes:

$$K = \frac{h_1 - h_2 + 0.0141\left[(\frac{dh_v}{dx})K_1 + \frac{dh_o}{dx}\right]}{h_3 - h_2 - 0.0141\left[(\frac{dh_v}{dx})K_3 + \frac{dh_o}{dx}\right]} \tag{B.7}$$

The analysis of error is performed in Tables B.1 and B.2, where r denotes radial distance and the subscript c denotes corrected values.

It is seen by inspection that these errors are generally within acceptable limits, with the exception of large values of distance from the center, where the percent error is magnified owing to the very small magnitudes of h_v and h_o. Thus, excepting regions where h_v and h_o become very small, the error in static pressure is less than 3.5% whereas it is less than about 4.0% for the dynamic pressure. Since $v \propto \sqrt{p_v}$, the error in velocity measurement will be less than 2%.

Radial Station (in)	h_v	ϕ(°)	K	K_c	ϕ_c	$(h_v)_c$	$e(p_v)$ %	$e(\phi)$ (°)	h_o	$(h_o)_c$	$e(p_o)$ %
0.30	161.7	- 2.7	.82	.82	- 2.7	161	+ .435	0			
0.35	134.5	- 4.5	.72	.72	- 4.4	135.6	- .81	- 0.1			
0.40	107.5	- 5.75	.65	.655	- 5.6	108.7	- 1.1	- 0.15			
0.45	79.25	- 7.2	.583	.587	- 7.0	81.0	- 2.16	- 0.2			
0.50	53.4	- 8.5	.525	.543	- 7.9	55.5	- 3.8	- 0.6			
0.55	35.0	- 9.3	.48	.493	- 9.0	36.3	- 3.6	- 0.3			
0.60	22.6	- 10.0	.45	.465	- 9.7	23.3	- 3.0	- 0.3			
0.70	9.26	- 11.3	.40	.42	- 10.75	9.63	- 3.8	- 0.55			

TABLE B.1 ERROR ANALYSIS, $dp_o/dx = 0$

(Data from investigation of Chapter V)

12.015	108	+ 1.5	.893	.96	+ 0.5	108.2	- .111	+ 1.0	78	77.4	+ .775
12.10	125.8	+ 2.7	.817	.865	+ 1.8	125.4	+ .32	+ 0.9	61.2	61.4	- .325
12.20	137	+ 5.3	.668	.685	+ 5.0	136.5	+ .366	+ 0.3	46	47	- 2.13
11.95	123	0	.993	.95	+ 0.6	122.7	+ .245	- 0.6	62.5	62.8	- .48
11.90	129.5	- 0.9	.932	.955	- 0.5	129.7	- .154	- 0.4	56	55.8	+ .36
11.85	133	- 2.5	.829	.85	- 2.1	133.5	- .375	- 0.4	49	48.5	+ 1.03
11.80	136	- 4.2	.731	.75	- 3.8	136	0	- 0.4	44	44	0.0
11.75	136	- 5.9	.638	.655	- 5.6	135.6	+ .293	- 0.3	38	39	- 2.56
11.70	126.5	- 7.7	.555	.573	- 7.3	127.3	- .629	- 0.4	32	31	+ 3.45
11.65	112.5	- 9.7	.466	.49	- 9.1	113.5	- .880	- 0.6	27	25	+ 8.0
11.60	97.1	- 11.5	.393	.42	- 10.75	.98	- .92	- 0.75	20	18	+ 11.1
11.55	77.3	- 13.6	.317	.35	- 12.5	79.7	- 3.01	- 1.1	14	11	+ 27.2
11.50	56.8	- 15.3	.250	.29	- 14.2	57.2	- .70	- 1.1	11	9.5	+ 15.8
11.45	41.1	- 17.3	.175	.23	- 15.8	42.7	-3.75	- 1.5	7	5	+ 40.0
11.40	30.1	- 18.5	.138	.20	- 16.6	30.8	-2.27	- 1.9	5	3.2	+ 56.2

TABLE B.2 ERROR ANALYSIS, $dp_o/dx \neq 0$

The error of the angle ϕ is generally less than about 1°, becoming as large as 2° in regions where p_o, p_v tend to zero.

APPENDIX C - ANNULAR SHEAR LAYER

Consider an annular turbulent shear layer, originating at x = 0, as shown in Figure C.1.

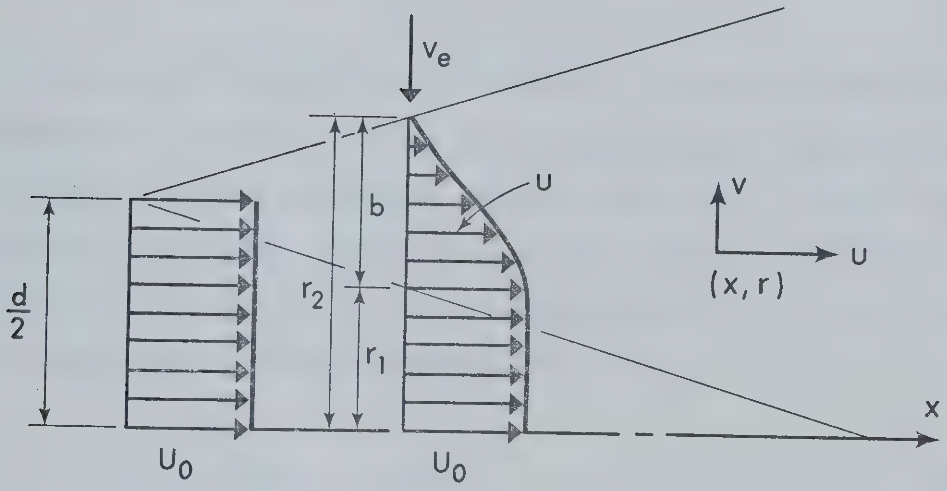

FIGURE C.1 DEFINITION SKETCH

The Reynolds equation of motion in the x-direction is (neglecting laminar stresses in comparison to $\tau = -\rho\overline{u'v'}$):

$$u\frac{\partial u}{\partial x} + v\frac{\partial u}{\partial r} = -\frac{1}{\rho}\frac{\partial p}{\partial x} + \frac{1}{\rho r}\frac{\partial (r\tau)}{\partial r} \qquad \text{(C.1)}$$

and the longitudinal component of velocity, u is given by:

$$u = \begin{cases} U_o & \text{for} \quad r \le r_1 \\ U_o f(\eta) & \text{for} \quad r \ge r_1 \end{cases} \tag{C.2}$$

where $\eta \equiv (r - r_1)/b$, $b = r_2 - r_1$, r_2 being the value of r where $u = 0$, and the function $f(\eta)$ is closely approximated by (28):

$$f(\eta) = (1 - \eta^{3/2})^2 \tag{C.3}$$

The conventional approach in these problems is to pursue a similarity analysis (29). However, in this case it can easily be shown that conventional similarity assumptions [such as $v/U_o = f_1(\eta)$, $\tau/\rho U_o^2 = g(\eta)$] will lead to absurdum. Therefore, an integral analysis is preferable. Multiplying Equation C.1 by r and integrating from $r = 0$ to $r = r_2$, and neglecting the pressure gradient term:

$$\int_o^{r_2} ru^2 dr = \frac{1}{8} d^2 U_o^2 \tag{C.4}$$

But $$\int_o^{r_2} ru^2 dr = \underbrace{\int_o^{r_1} rU_o^2 dr}_{A} + \underbrace{\int_{r_1}^{r_2} ru^2 dr}_{B}$$

$$A = \frac{1}{2} U_o^2 r_1^2 \tag{C.5}$$

$$B = \int_o^1 (\eta b + r_1) U_o^2 f^2(\eta) b d\eta =$$

$$= U_o^2 b^2 \int_o^1 \eta f^2 d\eta + U_o^2 b r_1 \int_o^1 f^2 d\eta$$

Using Equation C.3, this becomes:

$$B = 0.065\, U_o^2 b^2 + 0.313\, U_o^2 r_1 b \tag{C.6}$$

Thus Equation C.4 can be written as:

$$\overline{r_1}^2 + 0.13\, \overline{b}^2 + 0.626\, \overline{b}\, \overline{r_1} - \frac{1}{4} = 0 \tag{C.7}$$

where the overbar is used to denote non-dimensionalized quantities with respect to d (i.e., $\overline{r_1} = r_1/d$ etc.). It is then possible to express $\overline{r_1}$ in terms of $\overline{b}$ by solving the quadratic, i.e.:

$$\overline{r_1} = \sqrt{0.25 - 0.0325\, \overline{b}^2} - 0.313\, \overline{b} \tag{C.8}$$

This is plotted in Figure C.2 where it is seen that it can very accurately be approximated by the linear relation:

$$\overline{r_1} \simeq 0.50 - 0.338\, \overline{b} \tag{C.9}$$

One more relation between r_1 and b can be obtained if the entrainment data of Hill (41) are used. Let Q be the total flow-rate through the jet. Then, Hill's entrainment coefficient C_2 is defined as:

$$C_2 = \frac{d}{Q_o} \frac{dQ}{dx} \quad \text{(incompressible flow)} \tag{C.10}$$

But $Q = \int_o^{r_2} 2\pi r u dr$, which after manipulation, can be written as:

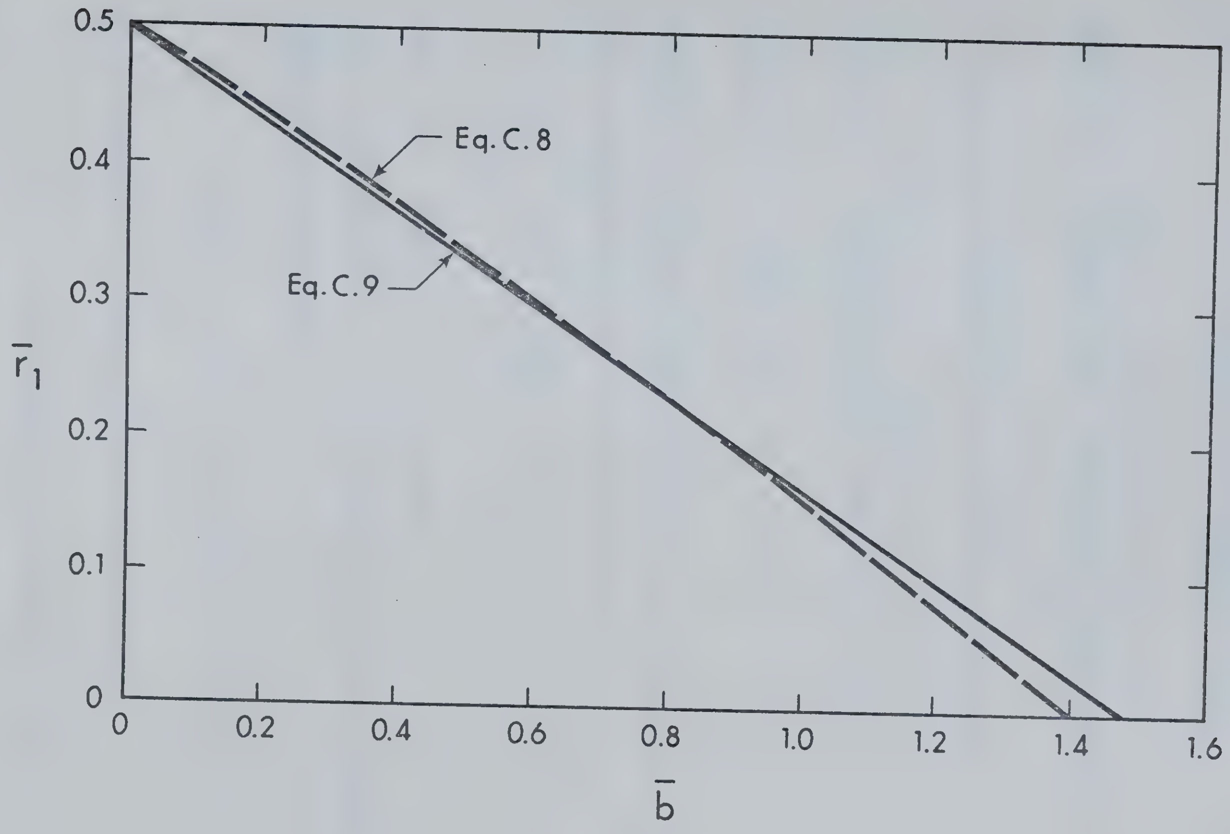

FIGURE C.2 RELATION BETWEEN $\overline{r}_1$ AND $\overline{b}$

$$Q = \pi \left\{ U_o r_1^2 + 2K_1 U_o b^2 + 2K_2 U_o b r_1 \right\} \qquad (C.11)$$

where $K_1 = \int_o^1 \eta f d\eta = 0.13$ and $K_2 = \int_o^1 f d\eta = 0.45.$

It follows that Equation C.10 can also be written as:

$$\frac{d}{d\bar{x}} \left\{ \overline{r_1}^2 + 2K_1 \bar{b}^2 + 2K_2 \bar{b}\, \overline{r_1} \right\} = \frac{1}{4} C_2 \qquad (C.12)$$

(Since $Q_o = \frac{\pi d^2}{4} U_o$).

The data of Hill (41) indicate that for small values of $\bar{x} = x/d$, C_2 can be approximated by a straight line, i.e.:

$$C_2 \simeq \alpha + \beta \bar{x} \quad ; \quad \bar{x} \lesssim 5\text{-}6 \qquad (C.13)$$

with $\alpha = 0.083 \quad ; \quad \beta = 0.036.$

Substituting Equation C.13 into Equation C.12 and integrating, we obtain after some manipulation:

$$4\, \overline{r_1}^2 + 1.04\, \bar{b}^2 + 3.6\, \bar{b}\, \overline{r_1} = \alpha\, \bar{x} + \frac{1}{2} \beta\, \bar{x}^2 + 1 \qquad (C.14)$$

Using Equation C.9, this can also be written as:

$$\bar{b}^2 + 1.57\, \bar{b} - [0.297\, \bar{x} + 0.064\, \bar{x}^2] = 0 \qquad (C.15)$$

which yields:

$$\bar{b} = \frac{1}{2} [\phi(\bar{x}) - 1.57] \qquad (C.16)$$

with $$\phi(\overline{x}) \equiv \sqrt{2.46 + 1.19\,\overline{x} + 0.256\,\overline{x}^2} \qquad (C.17)$$

The function $\phi(\overline{x})$ is shown graphically in Figure C.3, where it is seen that it can very accurately be approximated by the straight line:

$$\phi(\overline{x}) \cong 1.57 + 0.45\,\overline{x} \qquad (C.18)$$

Using this relation and Equations C.9 and C.16 the scales r_1 and b are given by:

$$\overline{b} = 0.225\,\overline{x} \qquad (C.19)$$

$$\overline{r_1} \cong 0.50 - 0.077\,\overline{x} \qquad (C.20)$$

If $b_{1/2}$ is the value of $r - r_1$ where $u = \frac{1}{2} U_o$ then Equation C.3 will show that $b_{1/2} = 0.442\,b$ which implies that:

$$\overline{b_{1/2}} = 0.10\,\overline{x} \qquad (C.21)$$

Considering now the entrainment velocity, v_e, this can be predicted as follows:

$$2\pi r_2 v_e = \frac{dQ}{dx}$$

Hence: $\overline{v_e} = \dfrac{v_e}{U_o} = \dfrac{C_2}{8\,\overline{r_2}}$ which by means of previous findings can be written as:

$$\overline{v_e} = \frac{0.083 + 0.036\,\overline{x}}{8(0.71 + 0.12\,\overline{x})} \qquad (C.22)$$

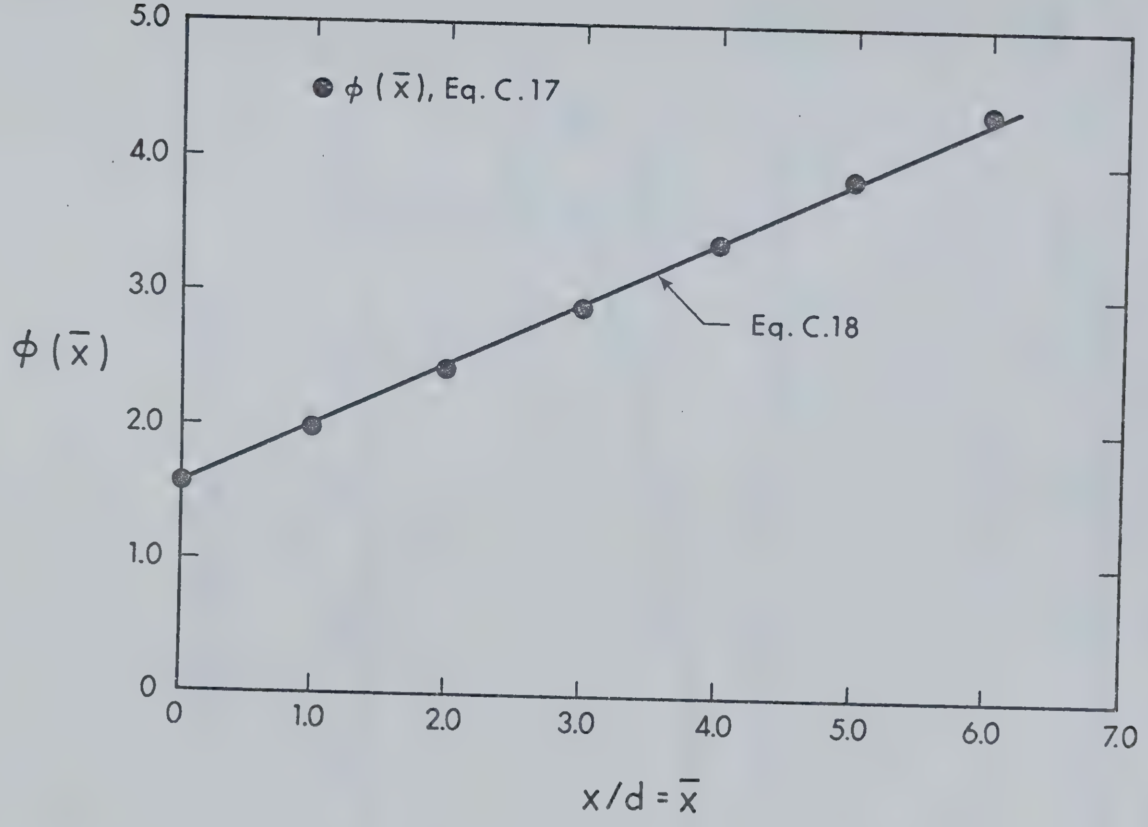

FIGURE C.3 THE FUNCTION $\phi(\bar{x})$

This is shown plotted in Figure C.4, where it is seen that $\overline{v}_e$ increases with $\overline{x}$, approaching a constant value of about 0.025. Thus, for $\overline{x} \gtrsim 5.0$, i.e, for the transition and for the fully developed jet, one could assume $\overline{v}_e \simeq \text{const} = .025$.

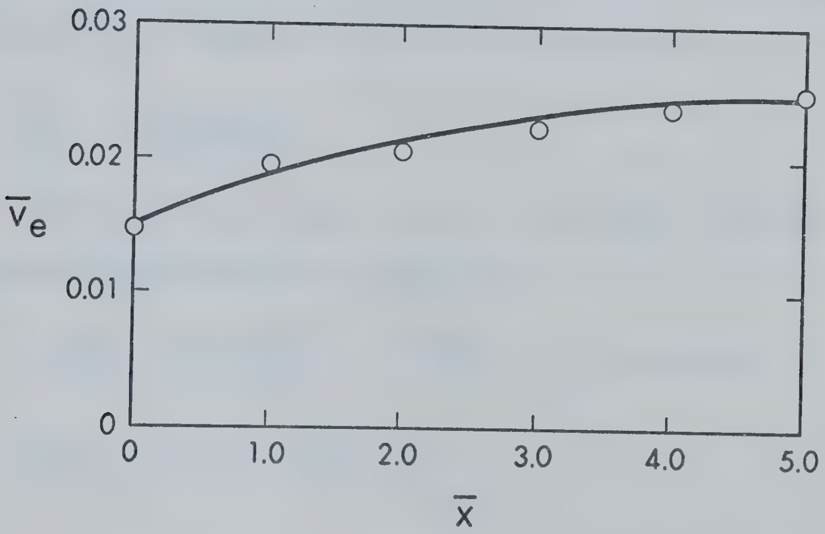

FIGURE C.4 ENTRAINMENT VELOCITY

APPENDIX D - DERIVATIONS

D.1 Prediction of Wall Shear Stress in Impingement Region

Wall shear stress in the impingement region is predicted in general by applying at the wall the equation of motion in the direction normal to the wall. Then the local pressure gradient normal to the wall is related to the shear gradient along the wall. The pertinent equations are different for plane and circular jets.

D.1.1 Circular Jet

The total normal stress is $\sigma_x = -p + 2\mu \frac{\partial u}{\partial x}$. Firstly, it is shown that the viscous term is negligible.

$$2\mu \frac{\partial u}{\partial x} = \frac{2\mu}{r} \frac{\partial (ru)}{\partial x} = -\frac{2\mu}{r} \frac{\partial (rv)}{\partial r} \qquad \text{(by continuity)}$$

But

$$\frac{\partial (rv)}{\partial r} \sim \frac{d}{dr} (rv_m) \sim \left\{\frac{d}{dr} [rv_m]\right\}_{r=0} \tag{D.1}$$

where v is velocity paramell to the wall and v_m is its maximum in a given vertical occuring at the edge of the boundary layer. When $r \rightarrow 0$ it is reasonable to assume that $p_w + (\rho u_m^2/2) = p_s$ (as is also shown in Chapter IV). This relation leads to Equation 4.35 which can be used to evaluate $[\frac{d}{dr} (rv_m)]_{r=0}$ and Equation D.1 becomes:

$$\frac{1}{r} \frac{\partial}{\partial r} (rv) \sim \sqrt{228\ K_p}\ \frac{U_o d}{H^2} \tag{D.2}$$

At the same time, $p \sim p_w \sim p_s$. Hence it will suffice to show that:

$$(2\mu)\ 2\ \sqrt{228\ K_p}\ \frac{U_o d}{H^2} \ll p_s$$

or, after some obvious manipulations:

$$R_o \gg 4\sqrt{\frac{228}{K_p}} = 11.8 \qquad (D.3)$$

which is always satisfied for a turbulent jet. The above considerations apply to normal impingement. In the case of oblique impingement, similar reasoning can be applied for wall shear stresses on the symmetry plane. In this case the angular gradient is zero and, therefore, the continuity equation will be identical with that of axisymmetric impingement. Using the results of Chapter VII, the condition to be satisfied will be:

$$R_o \gg \frac{4\ \sqrt{2k/K_p}}{(b/H)} \qquad (D.4)$$

where now K_p and b/H depend on the angle of impingement height. The right-hand side in (D.4) will be less than about 20 if the angle of impingement, ϕ is greater than 10°, which implies that (D.4) will always be satisfied in this range.

A similar development can also be applied to the case of small impingement heights (Chapter V). Here $p_s = \rho U_o^2/2$ and the necessary conditions (using results from Chapter V) will read:

$$R_o \gg 10 \qquad (D.5)$$

which again is always satisfied.

The starting equation for prediction of wall shear stress will be:

$$\frac{d}{dr}(r\tau_o) = r\left(\frac{\partial p}{\partial z}\right)_{z=0} \tag{D.6}$$

where z is distance from the stagnation point measured along the normal to the wall. This relation applies for normal impingement as well as for oblique along the symmetry plane (see also Chapters IV, V and VII). Assuming similarity of pressure profiles:

$$p = p_c\, f(\eta) \quad ; \quad \eta \equiv r/b_p \quad ; \quad f = e^{-k\eta^2} \quad ; \quad k = .693$$

Differentiating:

$$\frac{\partial p}{\partial z} = \frac{\partial p_c}{\partial z} f(\eta) - \frac{p_c}{b_p}\frac{\partial b_p}{\partial z}\eta f'(\eta)$$

and $$\left(r\frac{\partial p}{\partial z}\right)_{z=0} = b_{pw}\left(\frac{\partial p_c}{\partial z}\right)_0 \eta f - p_s\left(\frac{\partial b_p}{\partial z}\right)_0 \eta^2 f' \tag{D.7}$$

Using Equation D.7, and integrating Equation D.6, the wall shear stress will be given by:

$$\frac{\tau_o}{p_s} = \frac{1}{2k}\left[\frac{b_{pw}}{p_s}\left(\frac{\partial p_c}{\partial z}\right)_0 + 2\left(\frac{\partial b_p}{\partial z}\right)_0\right]\left(\frac{1-f}{\eta}\right) - \left(\frac{\partial b_p}{\partial z}\right)_0 \eta f$$

Letting $g_1(\eta) = \frac{1-f}{\eta}$ and $g_2(\eta) = \eta f$, this can be written more briefly as:

$$\frac{\tau_o}{p_s} = \frac{1}{2k}\left[\frac{b_{pw}}{p_s}\left(\frac{\partial p_c}{\partial z}\right)_0 + 2\left(\frac{\partial b_p}{\partial z}\right)_0\right] g_1(\eta) - \left(\frac{\partial b_p}{\partial z}\right)_0 g_2(\eta) \tag{D.8}$$

For the case of large impingement heights, dimensional reasoning will show that:

$$\frac{p_c}{p_s} = h_1\left(\frac{z}{H}, \phi\right) \quad \text{and} \quad \frac{b_p}{H} = h_2\left(\frac{z}{H}, \phi\right)$$

It follows that $\left(\frac{\partial p_c}{\partial z}\right)_0 = h_3(\phi)\,\frac{p_s}{H}$ and $\left(\frac{\partial b_p}{\partial z}\right)_0 = h_4(\phi)$, where

$$h_3(\phi) = \left[\frac{\partial h_1}{\partial(z/H)}\right]_{z/H=0} \quad \text{and} \quad h_4(\phi) = \left[\frac{\partial h_1}{\partial(z/H)}\right]_{z/H=0}$$

With these, Equation D.8 becomes:

$$\frac{\tau_o}{p_s} = \frac{1}{2k}\left[\frac{b_{pw}}{H}\,h_3(\phi) + 2h_4(\phi)\right] g_1(\eta) - h_4(\phi)\,g_2(\eta) \qquad \text{(D.9)}$$

If η_m is the value of η where the maximum value of τ_o occurs, then this maximum, τ_{om}, is given by:

$$\frac{\tau_{om}}{p_s} = \frac{1}{2k}\left[\frac{b_{pw}}{H}\,h_3(\phi) + 2h_4(\phi)\right] g_1(\eta_m) - h_4(\phi)\,g_2(\eta_m) \qquad \text{(D.10)}$$

Letting $\alpha(\phi)$ and $\beta(\phi)$ represent the coefficients of g_1 and g_2 in Equations D.9 and D.10:

$$\begin{aligned} \frac{\tau_o}{p_s} &= \alpha\, g_1(\eta) - \beta\, g_2(\eta) \\ \frac{\tau_{om}}{p_s} &= \alpha\, g_1(\eta_m) - \beta\, g_2(\eta_m) \end{aligned} \qquad \text{(D.11)}$$

Also, since η_m is a locus of maximum:

$$\alpha\, g_1'(\eta_m) - \beta\, g_2'(\eta_m) = 0 \qquad \text{(D.12)}$$

Letting $\sigma_m = \frac{g_1'(\eta_m)}{g_2'(\eta_m)} = \frac{\beta}{\alpha}$ and $q_m = [g_1(\eta_m) - \sigma_m\, g_2(\eta_m)]^{-1}$ the above can also be written as:

$$\begin{aligned} \frac{\tau_o}{\tau_{om}} &= q_m\, [g_1(\eta) - \sigma_m\, g_2(\eta)] \\ \tau_{om} &= p_s\, \alpha\, [g_1(\eta_m) - \sigma_m\, g_2(\eta_m)] = \frac{\alpha p_s}{q_m} \end{aligned} \qquad \text{(D.13)}$$

which implies that:

$$C_* = \frac{\tau_{om}}{\rho U_o^2} \left(\frac{H}{d}\right)^2 = h(\phi) \qquad \text{(D.14)}$$

The quantities q_m and σ_m depend on η_m and Figure 7.13 (Chapter V) shows these functions graphically. The variation of η_m with the angle of impingement ϕ, is left to be obtained empirically.

In the case of normal impingement, $\eta_m \simeq 1.76$ which gives $q_m = 2.295$ and $\sigma_m = 0.32$. Using also the result $b_{pw}/H = 0.078$, τ_o/τ_{om} will be given as:

$$\frac{\tau_o}{\tau_{om}} = 0.18\, \frac{1 - e^{-114\lambda^2}}{\lambda} - 9.43\, \lambda\, e^{-114\lambda^2} \qquad \text{(D.15)}$$

where $\lambda = r/H$. This is identical to Equation 4.31 in Chapter IV.

Consider now the case of oblique impingement. It is reasonable to assume that the length scales defining the wall pressure (b_1, b_2 and b_3)

approach a constant ratio between themselves as the wall is approached, i.e., for small values of z, $b_2/b_1 = c_1$ and $b_3/b_1 = c_2$ so that c_1 and c_2 are independent of z. This implies that:

$$\frac{(\partial b_2/\partial z)_o}{(\partial b_1/\partial z)_o} = c_1 = \left(\frac{b_2}{b_1}\right)_o \qquad \text{(D.16)}$$

and similarly for b_3.

Consider now the coefficients α and β:

$$\alpha = \frac{1}{2k}\left[\left(\frac{b_{pw}}{H}\right) h_3(\phi) + 2\beta\right] \quad ; \quad \beta = \left(\frac{\partial b_p}{\partial z}\right)_o$$

Hence:
$$\frac{\alpha}{\beta} = \frac{1}{2k}\left[\frac{(b/H)_o}{\beta} h_3(\phi) + 2\right] = \frac{1}{\sigma_m}$$

Letting the subscripts 1 and 2 denote quantities related to the sides of positive and negative x respectively, it can immediately be verified that $[h_3(\phi)]_1 = [h_3(\phi)]_2$. At the same time, Equation D.16 ascertains that:

$$\left[\frac{(b/H)_o}{\beta}\right]_1 = \left[\frac{(b/H)_o}{\beta}\right]_2$$

and, therefore:

$$\left(\frac{\alpha}{\beta}\right)_1 = \left(\frac{\alpha}{\beta}\right)_2 \qquad \text{or} \qquad (\sigma_m)_1 = (\sigma_m)_2$$

Since σ_m is a single-valued function of η_m the latter relation implies that:

$$(\eta_m)_1 = (\eta_m)_2 \qquad \text{(D.17)}$$

a relation that was verified experimentally (Chapter VII). From Equations D.13, it now follows that:

$$\frac{(\tau_{om})_2}{(\tau_{om})_1} = \frac{\alpha_2}{\alpha_1} = \frac{\beta_2}{\beta_1} = \frac{b_2}{b_1} \tag{D.18}$$

The condition of continuity of wall shear variation at $x = 0$, requires that (from Equation D.13):

$$\left[\frac{\tau_{om}}{b}\left\{\frac{d}{d\eta}\left(\frac{\tau_o}{\tau_{om}}\right)\right\}_{\eta=0}\right]_1 = \left[\frac{\tau_{om}}{b}\left\{\frac{d}{d\eta}\left(\frac{\tau_o}{\tau_{om}}\right)\right\}_{\eta=0}\right]_2$$

It can be easily checked that this is indeed satisfied by means of Equation D.18.

Consider now the case of small impingement heights. The steps leading to Equation D.8 are identical, therefore, Equation D.8 will be the starting equation in this case. In Chapter V it was shown that:

$$p_s = \rho U_o^2/2 \quad \text{and} \quad \frac{p}{\rho U_o^2/2} = f_5\left(\frac{z}{d}, \frac{r}{d}\right)$$

Therefore, $b_p/d = h_5(z/d)$, hence $\left(\frac{\partial b_p}{\partial z}\right) = \text{const.}$

Further, the term $\frac{b_{pw}}{p_s}\left(\frac{\partial p_c}{\partial z}\right)_o = \text{const}$, hence:

$$\frac{\tau_o}{p_s} = \alpha\, g_1(\eta) - \beta\, g_2(\eta) \tag{D.19}$$

where α and β are constants. Using a Gaussian approximation to p_w/p_s, $b_{pw}/d = 0.62$. Hence $\eta_m = \frac{1.15}{0.62} = 1.85$ which gives $q_m = 2.375$

and $\sigma_m = 0.385$. Thus the wall shear stress can finally be written as:

$$\frac{\tau_o}{\tau_{om}} = 1.47 \left\{ \frac{1 - e^{-1.8(r/d)^2}}{r/d} - \frac{r}{d} e^{-1.8(r/d)^2} \right\} \qquad (D.20)$$

which is identical to Equation 5.39 of Chapter V. The maximum wall shear stress will be simply:

$$\frac{\tau_{om}}{\rho U_o^2} = \text{const.}$$

D.1.2 Plane Jet

The total normal stress is again $\sigma_x = -p + 2\mu \frac{\partial v}{\partial y}$ (see Chapter VI for definition of symbols). From continuity:

$$\frac{\partial v}{\partial y} = -\frac{\partial u}{\partial x_1} \quad \text{and} \quad \frac{\partial u}{\partial x_1} \sim \frac{du_m}{dx_1} \sim \left(\frac{du_m}{dx_1}\right)_{x_1=0}$$

Assuming that near the stagnation point, the Bernoulli equation holds, it can be shown that:

$$\left(\frac{du_m}{dx_1}\right)_{x_1=0} = \frac{U_o}{b} \sqrt{\frac{d}{H}} \sqrt{kK_p}$$

with $$K_p = \left(p_s / \frac{\rho U_o^2}{2}\right) \frac{H}{d}$$

hence, it will suffice to show that (assuming $p \sim p_w \sim p_s$):

$$2\rho\nu \frac{U_o}{b} \sqrt{\frac{d}{H}} \sqrt{kK_p} << p_s$$

which leads to:

$$R_o \sqrt{\frac{H}{d}} \quad \gg \quad 15 \tag{D.21}$$

which will always be satisfied for a turbulent jet.

The starting equation for the prediction of wall shear stress is:

$$\frac{d\tau_o}{dx_1} = \left(\frac{\partial p}{\partial y}\right)_{y=0} \tag{D.22}$$

Using the relations of Equation 6.23:

$$\left(\frac{\partial p}{\partial y}\right)_o = \left(\frac{\partial p_c}{\partial y}\right)_o g(\eta_p) - \frac{p_s}{b}\left(\frac{\partial b_p}{\partial y}\right)_o \eta_p g'(\eta_p)$$

This relation satisfies identically the requirement of continuous shear stress distribution at $x_1 = 0$. Substituting into Equation D.22 and integrating:

$$\frac{\tau_o}{p_s} = \left[\frac{b}{p_s}\left(\frac{\partial p_c}{\partial y}\right)_o + \left(\frac{\partial b_p}{\partial y}\right)_o\right]\int_0^\eta g\,d\eta - \left(\frac{\partial b_p}{\partial y}\right)_o \eta g$$

which can also be written as:

$$\frac{\tau_o}{p_s} = \frac{1}{2}\sqrt{\frac{\pi}{k}}\left\{\frac{b}{p_s}\left(\frac{\partial p_c}{\partial y}\right)_o + \left(\frac{\partial b_p}{\partial y}\right)_o\right\} \operatorname{erf}(\sqrt{k}\eta) - \left(\frac{\partial b_p}{\partial y}\right)_o \eta g \tag{D.23}$$

From dimensional considerations, one could show that very near the wall p_c and b_p are given by:

$$p_o = p_s h_1 (\frac{y}{H}, \phi) \quad ; \quad b_p = H\, h_2 (\frac{y}{H}, \phi) \tag{D.24}$$

which indicate that the terms $\frac{b}{p_s} (\frac{\partial p_c}{\partial y})_o$ and $(\partial b_p/\partial y)_o$ depend only upon ϕ, i.e.:

$$\frac{1}{2} \sqrt{\frac{\pi}{k}} \left\{ \frac{b}{p_s} (\frac{\partial p_c}{\partial y})_o + (\frac{\partial b_p}{\partial y})_o \right\} = \alpha(\phi)$$

and $$(\frac{\partial b_p}{\partial y})_o = \beta(\phi)$$

Hence:

$$\frac{\tau_o}{p_s} = \alpha \mathrm{erf}(\sqrt{k}\eta) - \beta \eta g \tag{D.25}$$

The maximum value of τ_o occurs for $\eta \to \infty$, i.e.:

$$\frac{\tau_{om}}{p_s} = \alpha \left\{ \frac{\tau_{om}}{\rho U_o^2/2} \frac{H}{d} = h(\phi) \right\} \tag{D.26}$$

Dividing:

$$\frac{\tau_o}{\tau_{om}} = \mathrm{erf}(\sqrt{k}\eta) - \frac{\beta}{\alpha} \eta g \tag{D.27}$$

This is identical with Equation 6.26 of Chapter VI, if β/α is set equal to C_1. Using the subscripts 1 and 2 to denote the sides of positive and negative x_1 respectively, and reasoning in a manner similar to that of the previous section, it is possible to show that:

$$\frac{(\tau_{om})_2}{(\tau_{om})_1} = \frac{b_2}{b_1} \qquad (D.28)$$

D.2 Derivation of Equations 5.26 and 5.30

The equation of continuity is:

$$\frac{\partial(ru)}{\partial z} + \frac{\partial(rv)}{\partial r} = 0 \qquad (D.29)$$

Substituting Equation 5.25 and integrating:

$$rv = -\frac{1}{2}u'_c r^2 - \Delta u'_c r_1^2 \underbrace{\int_0^{\lambda} \phi\lambda d\lambda}_{F_2(\lambda)} + \Delta u_c r'_1 r_1 \underbrace{\int_0^{\lambda} \phi^1\lambda^2 d\lambda}_{F_1(\lambda)}$$

This can also be written as:

$$\frac{v/U_o}{r_1/d} = \frac{\Delta u_c}{U_o}\,\frac{r'_1 d}{r_1}\,\frac{F_1(\lambda)}{\lambda} - \frac{1}{2}\,\frac{u'_c d}{U_o}\,\lambda - \frac{\Delta u'_c d}{U_o}\,\frac{F_2(\lambda)}{\lambda} \qquad (D.30)$$

But $u_c = U_o f(\bar{z})$ and $r_1 = d\sigma[f(\bar{z})]^{-\frac{1}{2}}$ where σ is a function of H/d, related to C as defined in Equation 5.20. Since $u_m \simeq 1.15\, u_c$ it follows that $\Delta u_c = \beta U_o f(\bar{z})$; $\beta \simeq 0.15$. Substituting these into Equation D.30 and simplifying:

$$\frac{v/U_o}{r_1/d} = -\frac{1}{2} f'(\bar{z}) F(\lambda) \qquad (D.31)$$

where $F(\lambda) = \lambda + \beta\,(F_1 + 2F_2)\lambda^{-1}$. This equation is identical to

Equation 5.26. To evaluate $F(\lambda)$ it is necessary to find $F_1(\lambda)$ and $F_2(\lambda)$, which are related to $\phi(\lambda) = \lambda^2(2 - \lambda^2)$.

$$F_1(\lambda) = \int_0^\lambda \lambda^2 \phi' d = \int_0^\lambda 4(\lambda^3 - \lambda^5)d\lambda = \lambda^4 - \frac{2}{3}\lambda^6$$

$$F_2(\lambda) = \int_0^\lambda (2\lambda^3 - \lambda^5)d\lambda = \frac{\lambda^4}{2} - \frac{\lambda^6}{6}$$

$$F_1 + 2F_2 = 2\lambda^4 - \lambda^6.$$

Hence $F(\lambda) = \lambda + \beta(2\lambda^3 - \lambda^5)$ and $F(1) = 1 + \beta$ therefore:

$$\frac{v}{v_1} = \frac{F(\lambda)}{F(1)} = \frac{\lambda}{1 + \beta}\left[1 + \beta\,\lambda^2(2 - \lambda^2)\right] \qquad (D.32)$$

which is identical to Equation 5.30 with $\beta = 0.15$.

D.3 Derivation of Equation 6.15 (Chapter VI)

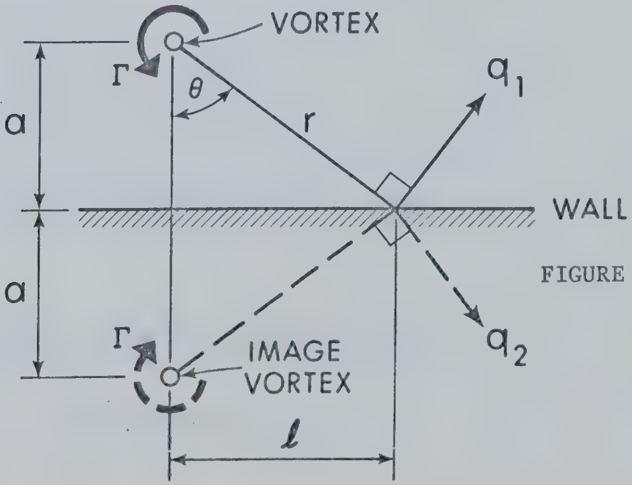

FIGURE D.1 VORTEX NEAR A WALL

With reference to Figure D.1, the velocity q_1 due to a vortex of strength Γ is:

$$q_1 = q_2 = \Gamma/2\pi r$$

The resultant velocity will be in the direction of the wall and has a magnitude of:

$$q = 2q_1 \cos\theta = 2\frac{\Gamma}{2\pi r} \cdot \frac{a}{r} = \frac{\Gamma}{\pi}\frac{a}{r^2}$$

Applying the Bernoulli equation (and using $r^2 = a^2 + \ell^2$):

$$p_w = -\frac{\rho\Gamma^2}{2\pi^2}\frac{a^2}{(a^2+\ell^2)^2} \tag{D.33}$$

The minimum pressure $\overline{p}$ will be:

$$\overline{p} = -\frac{\rho\Gamma^2}{2\pi^2 a^2} \tag{D.34}$$

Dividing Equation D.33 with D.34:

$$\frac{p_w}{\overline{p}} = [1 + (\frac{\ell}{a})^2]^{-2} \tag{D.35}$$

which is identical to Equation 6.15.

D.4 Derivation of Equation 6.19 (Chapter VI)

The starting equation is:

$$\int_{-\infty}^{\infty} p_w dx_1 = \rho U_o^2 d \sin \phi \tag{D.36}$$

But:

$$\int_{-\infty}^{\infty} p_w dx_1 = \underbrace{\int_{-\infty}^{-\bar{\eta}\, b_2} p_w dx_1}_{A} + \underbrace{\int_{-\bar{\eta}\, b_2}^{0} p_w dx_1}_{B} + \underbrace{\int_{0}^{\infty} p_w dx_1}_{C}$$

Consider each term separately:

$$A = \int_{-\infty}^{-\bar{\eta}\, b_2} p_w dx_1 = \bar{p} b_2 \int_{\bar{\eta}}^{\infty} \frac{p_w}{\bar{p}} d\eta = \bar{p} b_2 \int_{0}^{\infty} \left(\frac{p_w}{\bar{p}}\right) d(\eta-\bar{\eta})$$

Using Equation 6.17:

$$A = \bar{p} b_2 \int_{0}^{\infty} [1 + 0.1025 \ (\eta-\bar{\eta})^2]^{-2} \ d(\eta-\bar{\eta}) \ =$$

$$= \bar{p} b_2 \int_{0}^{\infty} (1 + 0.1025 \ \sigma^2)^{-2} \ d\sigma$$

where σ is a dummy variable.

Evaluating the integral, A is finally given by:

$$A = 2.45 \ \beta \ p_s b_2 \tag{D.37}$$

where $\beta = \bar{p}/p_s$. Consider now B:

$$B = \int_{-\bar{\eta}\, b_2}^{0} p_w dx_1 = p_s b_2 \int_{0}^{\bar{\eta}} \left(\frac{p_w}{p_s}\right) d\eta$$

Using the similarity property of Figures 4.5a and 4.5b:

$$\frac{p_w - \bar{p}}{p_s - \bar{p}} = g(\eta) = e^{-k\eta^2} \quad ; \quad k = 0.693 \qquad (D.38)$$

Equation D.38 holds for all η when $\bar{p} = 0$, but only in the range $0 \leq \eta \leq \bar{\eta}$ when $\bar{p} < 0$. Since B involves integration only in the interval $[0, \bar{\eta}]$ it follows that:

$$B = p_s b_2 \int_0^{\bar{\eta}} [\beta + (1 - \beta) g(\eta)] d\eta$$

or:

$$B = p_s b_2 \, [\beta(\bar{\eta} - 0) + (1 - \beta) \int_0^{\bar{\eta}} g(\eta) d\eta] \qquad (D.39)$$

Since $g(\eta)$ is almost zero for $\eta \geq \bar{\eta}$, the above can also be written as:

$$B = p_s b_2 \, [(1 - \beta) \int_0^{\infty} g d\eta + \beta\bar{\eta}] \qquad (D.40)$$

Finally, C is given by:

$$C = p_s b_1 \int_0^{\infty} g d\eta \qquad (D.41)$$

and:

$$A + B + C = 2.45\beta p_s b_2 + p_s b_2 \, [\beta\bar{\eta} + (1 - \beta) \int_0^{\infty} g d\eta] +$$

$$+ p_s b_1 \int_0^\infty g d\eta =$$

$$= p_s \left\{ 2.45\beta b_2 + b_2 \int_0^\infty g d\eta + b_1 \int_0^\infty g d\eta + \beta b_2 \bar{\eta} - \beta b_2 \int_0^\infty g d\eta \right\}$$

Letting $F_p = \int_0^\infty g d\eta$:

$$A + B + C = p_s \left\{ \beta b_2 (2.45 + \bar{\eta} - F_p) + F_p (b_1 + b_2) \right\}$$

or using $\bar{\eta} = 3.1$:

$$p_s \left\{ \beta b_2 (5.55 - F_p) + F_p (b_1 + b_2) \right\} = \rho U_o^2 d \sin \phi$$

or:

$$\frac{p_s}{\rho U_o^2/2} \frac{H}{d} = \frac{2 \sin \phi}{\beta \frac{b_2}{H} (5.55 - F_p) + F_p \left(\frac{b_1 + b_2}{H}\right)} \tag{D.42}$$

when $\phi = 90°$; $b_1 = b_2 = b_{90}$ and $\beta = 0$, hence:

$$\left(\frac{p_s}{\rho U_o^2/2} \frac{H}{d} \right)_{90°} = \frac{2}{2 F_p (b_{90}/H)} = \frac{1}{F_p (b_{90}/H)}$$

Evaluating F_p to agree with the experimental result:

$$\left(\frac{p_s}{\rho U_o^2/2} \frac{H}{d} \right)_{90°} \simeq 8.0$$

F_p has to be taken equal to one which is in reasonable agreement with the theoretical value of 1.065. Using $F_p = 1.0$, Equation D.42 becomes:

$$\frac{p_s}{\rho U_o^2/2} \frac{H}{d} = \frac{2 \sin \phi}{\frac{b_1 + b_2}{H} + 4.55\beta \frac{b_2}{H}} \tag{D.43}$$

which is Equation 6.19.

D.5 Derivation of Equation 7.17 (Chapter VII)

The starting relation is:

$$a_m = 2 \int_{x_2}^{x_1} y dx \tag{7.15}$$

where y is given by Equation 7.14 and x_1, x_2 are defined in Equation 7.16. The above gives:

$$a_m = 2 \left[\int_{x_2}^{0} y dx + \int_{0}^{x_1} y dx \right] =$$

$$= 2 \left[b_2^2 \int_{x_2/b_2}^{0} \left(\frac{y}{b_2}\right) d\left(\frac{x}{b_2}\right) + b_1^2 \int_{0}^{x_1/b_1} \left(\frac{y}{b_1}\right) d\left(\frac{x}{b_1}\right) \right]$$

Let $\xi \equiv \frac{x}{b_j}$; $j = 1, 2$. Then:

$$\frac{y}{b_j} = \left(\frac{b_3}{b_j} + \alpha\xi\right) \left(\frac{\ell nm}{k} - \xi^2\right)^{1/2} \tag{D.44}$$

Further, if $\xi_o \equiv \sqrt{\ell nm/k}$, then:

$$x_1/b_1 = \xi_o \quad \text{and} \quad x_2/b_2 = -\xi_o$$

Using these and Equation D.44, a_m will be given by:

$$a_m = 2\left[b_2^2 \int_{-\xi_o}^{0} (\frac{b_3}{b_2} + \alpha\xi)[\xi_o^2 - \xi^2]^{1/2} d\xi + b_1^2 \int_{0}^{\xi_o} (\frac{b_3}{b_1} + \alpha\xi)\right.$$

$$\left. [\xi_o^2 - \xi^2] \, d\xi \right]$$

$$= 2\left\{b_2^2 \frac{b_3}{b_2} \int_{-\xi_o}^{0} \sqrt{\xi_o^2 - \xi^2} \, d\xi + b_1^2 \frac{b_3}{b_1} \int_{0}^{\xi_o} \sqrt{\xi_o^2 - \xi^2} \, d\xi + \right.$$

$$\left. + \alpha \left[b_2^2 \int_{-\xi_o}^{0} \xi(\xi_o^2 - \xi^2)^{1/2} d\xi + b_1^2 \int_{0}^{\xi_o} \xi(\xi_o^2 - \xi^2)^{1/2} d\xi\right]\right\}$$

Evaluating the integrals, this becomes:

$$a_m = 2\left\{\frac{\pi\xi_o^2}{4} b_3(b_2 + b_1) + \frac{\alpha\xi_o^3}{3} (b_1^2 - b_2^2)\right\} =$$

$$= \frac{\pi}{2} (\frac{\ell nm}{k}) b_3 (b_1 + b_2) + \frac{2}{3} \alpha \, (\frac{\ell nm}{k})^{3/2} (b_1^2 - b_2^2)$$

Calculations have shown that the second term can be neglected, owing ot the fact that α and $b_1^2 - b_2^2$ are both relatively small quantities. Therefore:

$$a_m \simeq \frac{\pi}{2} (\frac{\ell nm}{k}) b_3 (b_1 + b_2) \qquad \text{(D.45)}$$

which is Equation 7.17.

D.6 Derivation of Equation 7.22 (Chapter VII)

Consider firstly the integral:

$$\int_{-\infty}^{\infty}\int_{-\infty}^{\infty} x p_w dxdy = \int_{-\infty}^{\infty} x\left(\int_{-\infty}^{\infty} p_w dy\right)dx =$$

$$= \int_{-\infty}^{\infty} x p_{1,2}\, b\left[2\int_{0}^{\infty} \left(\frac{p_w}{p_{1,2}}\right) d\left(\frac{y}{b}\right)\right]dx =$$

$$= 2\int_{-\infty}^{\infty} x p_{1,2}\, b\left[\int_{0}^{\infty} e^{-k\zeta^2} d\zeta\right]dx =$$

$$\sqrt{\frac{\pi}{k}} \int_{-\infty}^{\infty} xb\, p_{1,2}\, dx =$$

$$= \sqrt{\frac{\pi}{k}}\left\{\int_{-\infty}^{0} xb\, p_2\, dx + \int_{0}^{\infty} xb\, p_1\, dx\right\} =$$

$$= \sqrt{\frac{\pi}{k}}\left\{b_2^3 p_s \int_{-\infty}^{0} \left(\frac{x}{b_2}\right)\left(\frac{b}{b_2}\right)\left(\frac{p_2}{p_s}\right) d\left(\frac{x}{b_2}\right) +\right.$$

$$\left. + b_1^3 p_s \int_{0}^{\infty} \left(\frac{x}{b_1}\right)\left(\frac{b}{b_1}\right)\left(\frac{p_1}{p_s}\right) d\left(\frac{x}{b_1}\right)\right\} =$$

$$= \sqrt{\frac{\pi}{k}}\, p_s \left\{b_2^3 \int_{-\infty}^{0} \eta e^{-k\eta^2} \left[\frac{b_3}{b_2} + \alpha\eta\right] d\eta +\right.$$

$$+ b_1^3 \int_0^\infty \eta e^{-k\eta^2} [\frac{b_3}{b_1} + \alpha\eta] d\eta \Big\} =$$

$$= p_s \sqrt{\frac{\pi}{k}} \Big\{ b_2^2 b_3 \int_{-\infty}^0 \eta e^{-k\eta^2} d\eta + b_1^2 b_3 \int_0^\infty \eta e^{-k\eta^2} d\eta +$$

$$+ \alpha b_2^3 \int_{-\infty}^0 \eta^2 e^{-k\eta^2} d\eta + \alpha b_1^3 \int_0^\infty \eta^2 e^{-k\eta^2} d\eta \Big\}$$

Evaluating the integrals this becomes:

$$\int_{-\infty}^\infty \int_{-\infty}^\infty x p_w dxdy = \sqrt{\frac{\pi}{k}} p_s \Big\{ \frac{b_3}{2k} (b_1^2 - b_2^2) + \frac{\alpha}{2k} \sqrt{\frac{\pi}{k}} (b_1^3 + b_2^3) \Big\}$$

Using Equation 7.21, this becomes:

$$x_c P_w = \sqrt{\frac{\pi}{k}} p_s \Big\{ \frac{b_3}{2k} (b_1^2 - b_2^2) + \frac{\alpha}{2k} \sqrt{\frac{\pi}{k}} (b_1^3 - b_2^3) \Big\}$$

But $P_w = \frac{a_2 p_s}{k} = \frac{\pi}{2} b_3 (b_1 + b_2) \frac{p_s}{k}$ hence, after simplification:

$$x_c = \frac{b_1 - b_2}{\sqrt{k\pi}} + \frac{\alpha}{2k} \frac{b_1^3 + b_2^3}{b_3 (b_1 + b_2)} \qquad (D.46)$$

which is Equation 7.22.

D.7 Derivation of Equation 7.70

The equation of the ellipse is:

$$(\frac{x - \varepsilon}{a})^2 + (\frac{y}{b})^2 = 1 \qquad (7.69)$$

In terms of polar co-ordinates, (r, θ) this can also be written as:

$$\left(\frac{r\cos\theta - \varepsilon}{a}\right)^2 + \left(\frac{r\sin\theta}{b}\right)^2 = 1 \qquad \text{(D.47)}$$

Expanding and introducing the ratio r/r_1 which equals h/h_1, this becomes:

$$\left(\frac{r}{r_1}\right)^2\left(\frac{r_1}{a}\right)^2\cos^2\theta + \left(\frac{\varepsilon}{a}\right)^2 - 2\left(\frac{r}{r_1}\right)\left(\frac{r_1}{a}\right)\left(\frac{\varepsilon}{a}\right)\cos\theta +$$

$$+ \left(\frac{r}{r_1}\right)^2\left(\frac{r_1}{a}\right)^2\left(\frac{a}{b}\right)^2\sin^2\theta = 1 \qquad \text{(D.48)}$$

But $r_1 = a + \varepsilon$, i.e., $r_1/a = 1 + (\varepsilon/a)$. Hence:

$$\left(\frac{r}{r_1}\right)^2\left\{\left(1 + \frac{\varepsilon}{a}\right)^2\cos^2\theta + \left(1 + \frac{\varepsilon}{a}\right)^2\left(\frac{a}{b}\right)^2\sin^2\theta\right\} -$$

$$- 2\left(\frac{r}{r_1}\right)\left(1 + \frac{\varepsilon}{a}\right)\left(\frac{\varepsilon}{a}\right)\cos\theta - \left(1 - \frac{\varepsilon^2}{a^2}\right) = 0$$

Further, dividing by $1 + (\varepsilon/a)$:

$$\left(\frac{r}{r_1}\right)^2\left(1 + \frac{\varepsilon}{a}\right)\left\{\cos^2\theta + \left(\frac{a}{b}\right)^2\sin^2\theta\right\} - 2\left(\frac{r}{r_1}\right)\left(\frac{\varepsilon}{a}\right)\cos\theta - \left(1 - \frac{\varepsilon}{a}\right) = 0$$

This relation can be solved for r/r_1 to give:

$$\frac{r}{r_1} = \frac{\frac{\varepsilon}{a}\cos\theta \pm \sqrt{\left(\frac{\varepsilon}{a}\right)^2\cos^2\theta + \left(1 + \frac{\varepsilon}{a}\right)\left(1 - \frac{\varepsilon}{a}\right)\left(\cos^2\theta + \frac{a^2}{b^2}\sin^2\theta\right)}}{\left(1 + \frac{\varepsilon}{a}\right)\left(\cos^2\theta + \frac{a^2}{b^2}\sin^2\theta\right)}$$

$$= \frac{\frac{\varepsilon}{a}\cos\theta \pm \sqrt{\cos^2\theta + (a/b)^2\sin^2\theta\,[1 - (\varepsilon/a)^2]}}{(1 + \varepsilon/a)[\cos^2\theta + (a/b)^2\sin^2\theta]} \qquad \text{(D.49)}$$

But $\varepsilon/a = \cos\phi$, hence:

$$\frac{r}{r_1} = \frac{\cos\phi\cos\theta \pm \sqrt{\cos^2\theta + (a/b)^2 \sin^2\theta \sin^2\phi}}{(1 + \cos\phi)[\cos^2\theta + (a/b)^2 \sin^2\theta]} \tag{D.50}$$

Since r/r_1 is a positive quantity only the "plus" sign is meaningful. Recalling that $r/r_1 = h/h_1$, Equation D.50 becomes identical to Equation 7.70.

D.8 Derivation of Equation 8.13

The distance x_o from the point source to the stagnation point is given by (56):

$$x_o = \sqrt{\frac{m}{4\pi|u_1|}} \tag{D.51}$$

But this was found to be equal to 0.2 x_p, hence:

$$m = 4\pi|u_1|(0.2)^2 x_p^2$$

Using Equation 8.14, this becomes:

$$m = 4\pi(0.2)^2(2.6)^2 d^2 U_o^2/|u_1|$$

or

$$\frac{m}{Q_o} = \frac{m}{\frac{\pi}{4} d^2 U_o} = 16(0.04)(2.6)^2\lambda$$

i.e.

$$\frac{m}{Q_o} = 4.3\ \lambda \tag{D.52}$$

which is Equation 8.13.

D.9 Stagnation Streamsurface, $y = y_s$.

The starting equation is:

$$\int_0^{y_s} 2\pi y u dy = 0 \qquad (D.53)$$

But $u = u_1 + u_m f(\eta)$ (Equation 8.7)

$$\int_0^{y_s} y u dy = b^2 \int_0^{\eta_s} \eta(u_m f + u_1) d\eta$$

where $\eta_s \equiv y_s/b$. Hence:

$$\int_0^{y_s} y u dy = b^2 \left\{ u_m \int_0^{\eta_s} \eta f d\eta + u_1 \int_0^{\eta_s} \eta d\eta \right\} = 0$$

Evaluating the integrals, this becomes:

$$\frac{u_m}{0.59} \left[1 - \frac{1}{\sqrt{1 + 0.59 \eta_s^2}} \right] = \frac{1}{2} |u_1| \eta_s^2$$

Letting $F(\eta) \equiv \eta^2 \left[1 - \frac{1}{1 + 0.59 \eta^2} \right]^{-1}$ and using Equations 8.9 and 8.14, this reduces to:

$$F(\eta_s) = 1.3 f_4(\frac{x}{x_p}) \qquad (D.54)$$

Hence $\eta_s = F^{-1} \left\{ 1.3 f_4(\frac{x}{x_p}) \right\} = G(\frac{x}{x_p})$

Since $y_s/x_p = \eta_s b/x_p$, it follows that:

$$\frac{y_s}{x_p} = \text{function of } \frac{x}{x_p} \text{ only} \tag{D.55}$$

This function can be evaluated easily using Equation D.54 and Equation 8.15.

B30102